THÈSE

En vue de l'obtention du

DOCTORAT DE L'UNIVERSITÉ DE TOULOUSE

Délivré par l'Université Toulouse 3 - Paul Sabatier

Présentée et soutenue par

Gaylor WAFFLARD-FERNANDEZ

Le 15 décembre 2020

Signatures observationnelles de la migration planétaire dans l'émission des poussières froides des disques protoplanétaires

---

Ecole doctorale : **SDU2E - Sciences de l'Univers, de l'Environnement et de l'Espace**

Spécialité : **Astrophysique, Sciences de l'Espace, Planétologie**

Unité de recherche :
IRAP - Institut de Recherche en Astrophysique et Planetologie

Thèse dirigée par
Clément BARUTEAU

Jury

M. Wilhelm KLEY, Rapporteur
M. Guillaume LAIBE, Rapporteur
M. François MENARD, Examinateur
Mme Claire MOUTOU, Examinatrice
M. Geoffroy LESUR, Examinateur
M. Clément BARUTEAU, Directeur de thèse

OBSERVATIONAL SIGNATURES OF PLANETARY MIGRATION IN THE COLD DUST EMISSION OF PROTOPLANETARY DISKS

GAYLOR WAFFLARD-FERNANDEZ

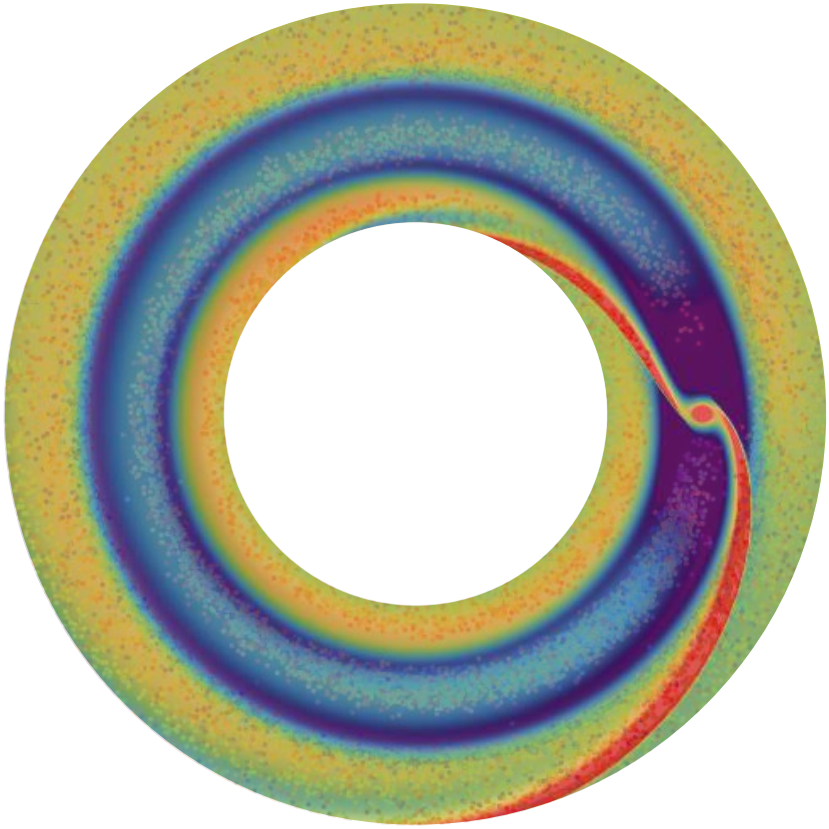

Institut de Recherche en Astrophysique et Planétologie
Université Toulouse III - Paul Sabatier, CNRS
31400, Toulouse, FRANCE

ABSTRACT

The subject of this PhD thesis is related to the orbital evolution of planets in a protoplanetary disk made of gas and dust around a young star (the first ten million years after the star's formation). The gravitational interaction between planets and the protoplanetary disk gas rapidly changes the distance between the planets and the star. This is known as planetary migration. Many studies have examined how the direction and speed of planetary migration depend on the planet's mass and the physical properties of the disk gas, with the aim to explain the orbital properties of exoplanets. Dust is most often discarded in this kind of studies because its mass content is much smaller than that of the gas and it should therefore have a negligible impact on planetary migration.

Yet, dust has gained considerable importance over the past few years owing to the rapidly growing number of multi-wavelength spatially resolved observations of the dust emission in protoplanetary disks. These observations show that dust emission, in particular the cold dust emission at radio wavelengths such as that probed by the ALMA interferometer, can feature structures (spirals, rings and gaps, crescent-shaped asymmetries...) that are very similar to those imparted by disk-planets interactions. For this reason, structures in the dust emission are often interpreted as signatures of the presence of hidden planets. These structures therefore stress the need to better understand how disk-planets interactions generally, and planetary migration more specifically, impact the dust emission in protoplanetary disks. This is the aim of my PhD thesis.

To reach this goal, I have carried out 2D and 3D hydrodynamical simulations modeling both the dust and gas of a protoplanetary disk where one or several planets form and migrate. The simulations results have been post-processed by dust and line radiative transfer calculations to compute synthetic maps of the disk emission that are directly comparable to observations. I show that the large-scale intermittent migration towards its star of a planet with a mass typically between those of Saturn and Jupiter is able to generate multiple rings of millimeter dust particles. These annular structures in the dust distribution take the form of bright and dark rings in the radio emission that resemble those observed in several disks. The intensity contrast between bright and dark rings is detectable with ALMA's current sensitivity. Other aspects explored in this thesis include the kinematic signatures of the presence of a massive planet in the gas emission of its disk, and the dust emission at the Lagrange points of a migrating planet.

RÉSUMÉ

Cette thèse porte sur l'évolution orbitale de planètes dans un disque protoplanétaire constitué de gaz et de poussières autour d'une jeune étoile (les dix premières millions d'années après la formation de l'étoile). L'interaction gravitationnelle entre les planètes et le gaz du disque protoplanétaire change rapidement la distance des planètes à leur l'étoile. C'est ce que l'on appelle la migration planétaire. De nombreuses études ont examiné comment la direction et la vitesse de cette migration planétaire dépendent de la masse de la planète et des propriétés physiques du gaz des disques, afin d'interpréter les propriétés orbitales des exoplanètes. Les poussières sont la plupart du temps négligées dans ce type d'études car elles représentent une masse très inférieure à celle du gaz dans les disques, et ont donc a priori moins d'impact sur la migration planétaire que le gaz.

Cependant, la poussière a connu un regain d'intérêt au cours des dernières années en raison du nombre croissant d'observations multi-longueurs d'onde spatialement résolues de l'émission de la poussière des disques protoplanétaires. Cette émission, en particulier l'émission de poussières froides telle qu'observée en radio par l'interféromètre ALMA, peut révéler des structures (spirales, anneaux sombres et brillants, asymétries en forme de croissant...) très similaires à celles engendrées par les interactions disque-planète. Pour cette raison, les structures dans l'émission des poussières sont souvent attribuées à la présence de planètes non-détectées. Ces structures soulignent donc la nécessité de mieux comprendre dans quelle mesure les interactions disque-planète en général, et la migration planétaire en particulier, jouent un rôle dans l'émission des poussières des disques protoplanétaires. Cette problématique constitue la pierre angulaire de mon travail de thèse.

Pour ce faire, j'ai réalisé des simulations hydrodynamiques 2D et 3D modélisant à la fois la poussière et le gaz d'un disque protoplanétaire dans lequel une ou plusieurs planètes se forment et migrent. Les résultats des simulations ont ensuite été post-traités par des calculs de transfert radiatif dans la poussière et le gaz afin de calculer des cartes synthétiques de l'émission du disque, directement comparables aux observations. Je montre en particulier que la migration intermittente à grande échelle d'une planète dont la masse est typiquement comprise entre celle de Saturne et celle de Jupiter est capable de générer des anneaux multiples de poussières millimétriques. Ces structures annulaires dans la distribution des poussières prennent en fait la forme d'anneaux sombres et brillants dans l'émission radio, qui ressemblent à ceux observés dans plusieurs disques. Le contraste d'intensité entre les anneaux sombres et brillants est détectable avec la sensibilité actuelle d'ALMA. D'autres aspects explorés dans cette thèse comprennent les signatures cinématiques de la présence d'une planète massive dans l'émission de gaz, et l'émission de poussières aux points de Lagrange d'une planète qui migre.

CONTENTS

List of figures ix

List of tables xiii

Avant-propos xv

1 OBSERVATIONAL CONTEXT 1
1.1 Multi-wavelength observations . . . 3
1.2 Important properties of protoplanetary disks . . . 7
1.2.1 Disk lifetimes . . . 7
1.2.2 Disk sizes . . . 8
1.2.3 Disk masses . . . 10
1.2.4 Disk temperatures . . . 11
1.2.5 Other valuable observations . . . 12

2 DYNAMICS OF PROTOPLANETARY DISKS 17
2.1 The life and death of protoplanetary disks . . . 19
2.1.1 Formation: from cloud to protoplanetary disk . . . 19
2.1.2 Equilibrium . . . 20
2.1.2.1 Centrifugal balance . . . 20
2.1.2.2 Vertical hydrostatic equilibrium . . . 21
2.1.2.3 Turbulent viscosity ν and α-parameter . . . 23
2.1.3 Accretion models . . . 24
2.1.4 Disk dispersal: from protoplanetary disk to stellar system . . . 27
2.2 Dust dynamics . . . 29
2.2.1 Aerodynamic drag force . . . 29
2.2.2 Radial drift . . . 30
2.2.3 Vertical settling . . . 33
2.2.4 Dust growth . . . 35
2.2.5 Dust properties . . . 38
2.3 Selected magneto-hydrodynamical instabilities . . . 40
2.3.1 Magneto-Rotational Instability . . . 41
2.3.2 Gravitational Instability . . . 41
2.3.3 Vertical Shear Instability . . . 43
2.3.4 Rossby Waves Instability and vortices . . . 44

Appendices 47
2.A Disk temperature . . . 47

3 PLANET FORMATION AND ORBITAL EVOLUTION 49
3.1 Linking protoplanetary disks to stellar systems . . . 51
3.2 Planet formation . . . 58

3.3 Planet migration . . . 61
3.3.1 Type-I migration . . . 62
3.3.1.1 The wake torque Γ_L . . . 64
3.3.1.2 The static corotation torque Γ_C . . . 65
3.3.1.3 Impact of self-gravity on the Lindblad torque . . . 68
3.3.2 Gap opening and the onset of type-II migration . . . 68
3.3.3 Type-III migration . . . 73
3.3.3.1 Dynamical corotation torque . . . 73
3.3.3.2 A coorbital deficit . . . 73
3.3.4 A short recap on planet migration . . . 76

4 DISK SUBSTRUCTURES AND HOW TO CREATE THEM 79
4.1 Statistics and biases . . . 81
4.1.1 General mechanisms... . . . 81
4.1.2 ... able to generate multiple rings . . . 82
4.2 Substructures in the dust . . . 83
4.3 How to create rings and crescent-like structures? . . . 87
4.3.1 Snowlines-related mechanisms . . . 90
4.3.2 The pressure maxima, these dust traps . . . 91
4.4 Substructures in the gas . . . 93
4.4.1 Global diagnostics . . . 94
4.4.2 Channel maps . . . 95
4.4.3 Velocity kinks . . . 97
4.5 What about the predicted signposts of planetary migration ? . . . 99

5 NUMERICAL METHODS 105
5.1 Hydrodynamical simulations: `Dusty FARGO-ADSG` and `FARGO3D` . . . 107
5.1.1 `Dusty FARGO-ADSG` . . . 107
5.1.1.1 Presentation of the code . . . 107
5.1.1.2 The grid . . . 110
5.1.1.3 The gas . . . 111
5.1.2 multifluid `FARGO3D` . . . 112
5.1.2.1 Initialization of the gas quantities . . . 112
5.1.2.2 A fiducial setup . . . 113
5.2 Radiative Transfer calculations: `RADMC3D` . . . 116
5.2.1 Dust radiative transfer . . . 116
5.2.2 Lines radiative transfer . . . 119
5.3 Python analysis tools . . . 121

Appendices 123
5.A Output step in `FARGO-ADSG/FARGO3D` . . . 123

6 INTERMITTENT PLANET MIGRATION AND FORMATION OF MULTIPLE DUST RINGS AND GAPS IN PROTOPLANETARY DISKS 125
6.1 Physical model and numerical methods . . . 127
6.2 Overview . . . 130
6.3 Uther simulation ($h_0 = 0.05$, $\alpha = 10^{-3}$) . . . 132

6.3.1 Coorbital vorticity-weighted deficit . . . 133
6.3.2 Dust spatial distribution . . . 138
6.3.3 Continuum emission . . . 142
6.4 Pendragon simulation ($h_0 = 0.06$, $\alpha = 10^{-4}$) . . . 144
6.4.1 Dust spatial distribution . . . 145
6.4.2 Continuum emission . . . 147
6.5 Parameter space and beyond the fiducial cases . . . 149
6.5.1 Initial gas surface density profile . . . 149
6.5.2 Self-Gravity . . . 155
6.5.3 Energy equation . . . 156
6.5.4 Resolution . . . 159
6.5.5 Dust backreaction . . . 160
6.5.6 Inner planet and resonance . . . 163
6.6 Longevity of the dust rings . . . 164
6.7 Geometrical spacing . . . 165

Appendices 169
6.A Mass of the circumplanetary disk . . . 169
6.B Additional results for fast and slow migration . . . 169
6.C A simple modification to the expression of the coorbital vortensity deficit for fast migration . . . 171

7 FURTHER OBSERVATIONAL DIAGNOSTICS OF PLANET FORMATION AND MIGRATION: ONGOING PROJECTS 173
7.1 Spectral index and dust size distribution . . . 175
7.2 Spotlighting the temporal evolution of substructures . . . 179
7.3 Velocity kinks due to the presence of a giant planet . . . 182
7.4 Orbital evolution of an outer low-mass planet in a disk with pre-formed annular substructures . . . 191
7.5 Dust dynamics and emission at the Lagrange points of a migrating planet 195
7.6 Preliminary work on intermittent runaway migration in 3D . . . 202
7.7 Tracking a group of particles . . . 206

8 CONCLUSION AND FUTURE PROSPECTS 209

Conclusion et perspectives 215

Bibliography 221

LIST OF FIGURES

Figure 1.1.1 Pre-ALMA sketch of a disk structure seen edge-on. 3
Figure 1.1.2 Dust thermal emission of large particles and scattered light from smaller particles in the DoAr25, IM Lup and MY Lup disks. 4
Figure 1.2.1 Disk fractions as a function of stellar age for different star-forming regions. 8
Figure 1.2.2 Comparison of disk sizes depending on the tracer observed. . . 9
Figure 1.2.3 Vertical contributions of four CO isotopologues used to probe the TW Hya disk. 10
Figure 1.2.4 Intensity-weighted velocity map and position velocity diagram showing the gas kinematics of the HD 163296 disk. 14
Figure 1.2.5 Detection of slow and fast winds in the disk DG Tau B. 15
Figure 2.1.1 Gas temperature structure of a MMSN-like disk from thermo-chemical simulations. 22
Figure 2.2.1 Predictions of a collision model from micro-gravity experiments. 36
Figure 2.2.2 Vertically integrated dust density distribution after 1 Myr of evolution, as a function of the distance to the star, for a given disk model. 37
Figure 2.2.3 Absorption mass opacity at $\lambda = 1.3$ mm as a function of particle size, for a dust mixture comprised of 60% astrosilicates and 40% water ices. 39
Figure 2.3.1 Colatitudinal velocity v_θ field in cylindrical coordinates obtained for two 3D simulations performed with the FARGO3D code with different flaring indexes. 44
Figure 2.3.2 Development of the RWI in a disk, in the vicinity of the outer edge of a Saturn-mass planet's gap, at the RWI initiation and after vortices merging from a 2D gas+dust hydrodynamical simulation. 45
Figure 2.A.1 Effective temperature of the disk as a function of radius, for the viscous heating case and the stellar irradiation case. 48
Figure 2.A.2 Effective temperature at 10 au of the DSHARP disks as a function of the stellar mass obtained with a simple stellar irradiation model. 48
Figure 3.1.1 Mass separation diagram for exoplanets with known mass and eccentricity. 51
Figure 3.1.2 Histogram of the ratio of orbital periods between successive planets in multiplanetary systems observed with Kepler. 55
Figure 3.1.3 Observation of the PDS 70 system using a coronagraphic angular differential imaging method. The presence of two giant planets has been proposed to explain the blobs and structures detected in multi-wavelength observations. 56

Figure 3.1.4 Comparison of gap widths produced by a single 1.5 M_{Saturn} planet on a fixed circular orbit and the predictions in Lodato et al. (2019). . . . 57
Figure 3.2.1 Result of a 2D hydrodynamical simulation of a massive protoplanetary disk unstable against the GI and having a short cooling timescale ($\tau_{cool}\Omega \lesssim 3-5$), from Paardekooper et al. (2011b). . . . 59
Figure 3.3.1 Relative perturbation of the gas surface density $(\Sigma - \Sigma_0)/\Sigma_0$ in a protoplanetary disk, with a 1.5 Saturn-mass planet from a 2D hydrodynamical simulation. . . . 63
Figure 3.3.2 Type-I migration specific torque on planets with different masses as a function of their orbital position. . . . 67
Figure 3.3.3 Results of 2D hydrodynamical simulations: impact of planetary migration on the carving of a gap for different migration rates. 71
Figure 3.3.4 Representation of the three regimes of migration thanks to results of 2D hydrodynamical simulations. . . . 77
Figure 4.1.1 Disk area compared to beam area for the disk sample in Long et al. (2018, 2019). . . . 81
Figure 4.1.2 ALMA 1.3 mm continuum map of the protoplanetary disk HD 169142, adapted from Fedele et al. (2017) and Pérez et al. (2019). 83
Figure 4.1.3 Statistics of Disks with Annular Substructures. . . . 84
Figure 4.3.0 A gallery of disk observations. . . . 89
Figure 4.3.1 Scanning electron microscopy images of SiO_2 spheres before and after sintering. . . . 90
Figure 4.4.1 Sketch that shows the impact of a planet-related gap in the gas pressure profile and the corresponding $\delta V_{rot} = \delta v_\phi$ profile, from Teague et al. (2018a). . . . 94
Figure 4.4.2 Channel maps for an ideal 2D Keplerian disk, seen at an inclination $i = 30$ degrees. . . . 96
Figure 4.4.3 ALMA observations of the dust and gas disk surrounding HD 163296 and HD 97048 along side results of 3D numerical simulations for HD 97048, including the presence of a planet, post-processed with radiative transfer calculations in the dust and in the gas. The model shows similar substructures to the observations. . . . 98
Figure 4.5.1 Radial asymmetry of bright rings due to planet migration. . . . 100
Figure 4.5.2 Impact of planet migration on the dust distribution depending on the relative velocity between the planet and the dust. . . . 102
Figure 5.1.1 Example of 2D multifluid simulation with FARGO3D, using the size distribution methodology. . . . 115
Figure 5.1.2 Dust settling in a 3D multifluid simulation with FARGO3D, using the size distribution methodology. . . . 117
Figure 6.2.1 Overview of our results of hydrodynamical simulations: time evolution of the planet's orbital radius for three values of the gas surface density (Σ_0), two values of the alpha turbulent viscosity (α) and of the disk's aspect ratio (h_0). . . . 131

Figure 6.3.1 Numerical estimation of the coorbital vortensity deficit (δm) during the inward migration of $\mathcal{P}$ in the Uther simulation. . . . 134
Figure 6.3.2 Numerical estimation of the vorticity $\omega(r_p)$ of the material trapped in libration (red curve), during the inward migration of $\mathcal{P}$ in the Uther simulation. . . . 135
Figure 6.3.3 Results of the Uther simulation: time evolution of the planet's orbital radius, migration rate and screenshots of the inverse vortensity ($\mathcal{J}_V$) at seven times. . . . 136
Figure 6.3.4 Results of the Uther simulation: gas structure and dust spatial distribution . . . 139
Figure 6.3.5 Space-time diagram for the Uther simulation, illustrating the longevity of dust rings formed by multiple stages of runaway planet migration. . . . 141
Figure 6.3.6 Predicted continuum emission at 1.3 mm and optical depth for the Uther simulation at 12500 years . . . 143
Figure 6.4.1 Results of the Pendragon simulation : planet's orbital evolution, gas structure and dust spatial distribution. . . . 145
Figure 6.4.2 Same as Fig. 6.3.5 for the Pendragon simulation. . . . 147
Figure 6.4.3 Same as Fig. 6.3.6, but for the Pendragon simulation at 59900 years. . . . 148
Figure 6.4.4 Impact of dust anisotropic scattering in the dust radiative transfer calculations at 1.3 mm in the Pendragon case. . . . 149
Figure 6.5.1 Impact of the initial surface density profile of the gas on the planet's orbital evolution and the gas inverse vortensity in the Uther disk model. . . . 150
Figure 6.5.2 Impact of the initial surface density profile on the initial (non-perturbed) inverse vortensity profile and the coorbital vortensity deficit. . . . 151
Figure 6.5.3 Impact of the initial surface density profile on the continuum emission . . . 153
Figure 6.5.4 Same as Fig. 6.3.5 for the σ_0 run. . . . 154
Figure 6.5.5 Impact of including gas self-gravity on the planet's orbital evolution in the Pendragon simulation. . . . 155
Figure 6.5.6 Impact of the energy equation on the planet's orbital evolution and the continuum emission for the Pendragon run. . . . 158
Figure 6.5.7 Impact of increasing grid resolution on the planet's orbital evolution in the Uther and Pendragon simulations. . . . 159
Figure 6.5.8 Impact of dust torques and dust feedback on the planet's orbital evolution for the Pendragon run. . . . 161
Figure 6.5.9 Results of two 2D numerical simulations with FARGO3D, which models dust as pressure-less fluids and including dust back-reaction. . . . 162
Figure 6.5.10 Impact of an inner planet on the intermittent runaway migration of an outer planet. . . . 163
Figure 6.6.1 Same as in Fig. 6.3.5 for an extra run with the same setup as Pendragon but with a turbulent viscosity $\alpha = 10^{-5}$. . . . 165

Figure 6.7.1 Robustness of the intermittent runaway migration scenario and geometrical spacing . . . 167
Figure 6.A.1 Numerical estimation of the mass inside the Hill sphere during the inward migration of $\mathcal{P}$ in the Uther and Pendragon simulations. 169
Figure 6.B.1 Perturbed gas surface density relative to its initial profile, in two migration regimes: slow and fast. . . . 170
Figure 7.1.1 Predicted intensity and spectral index profiles as a function of the distance to the star in the Pendragon simulation. . . . 176
Figure 7.1.2 Dust spatial distribution between the edges of a bright ring and the center of a gap. . . . 178
Figure 7.1.3 Spectral index α_ν maps between 0.87 and 1.3 mm from the Pendragon simulation for a 0.″02 circular beam and a 0.″01 circular beam. . . . 179
Figure 7.2.1 Dust continuum emission images for three disks in the DSHARP sample compared to three different snapshots (at three evolution stages) of a single disk simulation. . . . 180
Figure 7.3.1 Synthetic dust continuum emission map, gas intensity map, gas velocity map and channel maps from 3D multifluid simulations post-processed with radiative transfer calculations. . . . 184
Figure 7.3.2 Synthetic velocity maps (1st moment) from ^{13}CO J $= 3 \rightarrow 2$ emission. Between the two maps, the beam has been rotated by 90 degrees. . . . 185
Figure 7.3.3 Collection of intensity maps (0th moment) and corresponding channel maps at $\Delta v = 1.00$ km/s testing different hypotheses. . . . 187
Figure 7.3.4 Numerical experiments on the origin of velocity kinks, and channel maps. . . . 189
Figure 7.4.1 Time evolution of the planet's semi-major axis for a second planet included initially beyond the outermost $\mathcal{I}_\nu$ maximum in the Pendragon simulation. Three values of planet mass are considered: (2 M_{Earth}, 8 M_{Earth} and 16 M_{Earth}. . . . 192
Figure 7.5.1 Impact of migration on the dust's azimuthal distribution and continuum emission near Lagrange points. . . . 196
Figure 7.5.2 Radial asymmetry between bright rings due to migration. . . . 197
Figure 7.5.3 Dust spatial distribution to illustrate the dust dynamics near Lagrange points. . . . 199
Figure 7.5.4 Temporal evolution of dust emission around Lagrange points. . . . 200
Figure 7.5.5 Emission kicks due to the planet wakes in two migration regimes: inward and outward. . . . 201
Figure 7.6.1 Intermittent runaway migration in 3D: time evolution of the planet's orbital radius for two values of the thickness smoothing. 203
Figure 7.6.2 Intermittent runaway migration in 3D: perturbed gas volume density relative to its initial profile. . . . 204
Figure 7.7.1 Tracking a group of particles: selection and space-time diagram. 207

LIST OF TABLES

Table 1 List of general constants and units used in this manuscript. . . . xiv
Table 3.3.1 Planet-to-primary mass ratio for typical planet masses in the Solar System. . . . 69
Table 6.1.1 Main parameters of the fiducial cases for our hydrodynamical simulations. . . . 127
Table 6.3.1 Parameters of simulation Uther (section 6.3) . . . 133
Table 6.3.2 Parameters of the dust radiative transfer calculations . . . 142
Table 6.4.1 Parameters of simulation Pendragon (section 6.4) . . . 144
Table 7.3.1 Main fiducial parameters for the 3D numerical simulations, dust and line radiative transfer calculations presented in section 7.3. 183
Table 7.6.1 Main fiducial parameters for the 3D numerical simulations presented in section 7.6. . . . 202

Quantity	Symbol	Value	Unit
Planck constant	h	6.626×10^{-34}	$m^2.kg.s^{-1}$
light speed	c	2.998×10^{8}	$m.s^{-1}$
Boltzmann constant	k_B	1.381×10^{-23}	$m^2.kg.s^{-2}.K^{-1}$
Stefan-Boltzmann constant	σ_{SB}	5.670×10^{-8}	$kg.s^{-3}.K^{-4}$
gravitational constant	G	6.674×10^{-11}	$m^3.kg^{-1}.s^{-2}$
mean molecular weight of the Sun	$\mu_\odot$	2.4	—
proton mass	m_p	1.673×10^{-27}	kg
mass of the Sun	$M_\odot$	1.989×10^{30}	kg
luminosity of the Sun	$L_\odot$	3.828×10^{26}	$kg.m^2.s^{-3}$
astronomical unit	au	1.496×10^{11}	m
parsec	pc	3.086×10^{16}	m

Table 1: List of general constants and units used in this manuscript.

AVANT-PROPOS

Les étoiles naissent de l'effondrement gravitationnel des nuages moléculaires en rotation. Une grande partie de la masse des nuages alimente la formation stellaire, et la matière restante se réorganise en un disque circumstellaire façonné par les forces impliqués dans l'effondrement. Enveloppés dans ce manteau de gaz et de poussière, des embryons de planètes, ou protoplanètes, émergent. Bien que les interactions de ce disque protoplanétaire avec son étoile hôte et ses planètes naissantes ne perdurent que quelques millions d'années, elles constituent une étape majeure dans l'évolution future du système planétaire. S'attarder sur les premières étapes de la vie d'une étoile et de son disque protoplanétaire permet donc d'appréhender la formation et l'évolution des systèmes stellaires.

Les disques protoplanétaires sont principalement composés de gaz (99% de leur masse), mais aussi de matériaux solides (~1% de leur masse) que nous appellerons poussières ou grains. Malgré la faible proportion qu'ils représentent dans la composition des disques, les grains de poussière sont essentiels car ils sont à la fois les briques fondamentales des systèmes planétaires, des régulateurs de la température des disques et des traceurs majeurs de leur dynamique. Il existe en fait trois principaux traceurs observationnels pour étudier les disques protoplanétaires :

- **L'émission thermique des poussières** rend compte de l'absorption/ré-émission des photons de l'étoile par les particules de poussière à toutes longueurs d'onde. En particulier, les grandes poussières (de taille $\sim$ 1 mm) dominent l'émission thermique (sub-)millimétrique depuis les régions froides des disques, principalement leur plan médian. Les petites poussières (de taille micrométrique), en suspension dans les couches superficielles de disques, dominent quant à elle l'émission en infrarouge proche.

- **La lumière diffusée** témoigne de la réflexion des photons de l'étoile par les petites particules distribués à toutes altitudes dans l'atmosphère des disques. Ce traceur optiquement épais dans le domaine infrarouge donne un aperçu de la géometrie 3D des disques protoplanétaires.

- **Les raies d'émission moléculaires** révèlent le comportement de molécules de gaz dans les disques. Plus l'émission est optiquement mince, plus les régions sondées se situent a priori proche du plan médian.

A partir de ces traceurs, il est possible d'accéder à quelques paramètres physiques essentiels à la compréhension des disques protoplanétaires. Leur masse, par exemple, peut être estimée à partir de l'émission radio supposée optiquement mince. Leur durée de vie peut être déduite de la fraction d'étoiles au sein d'une même region de formation stellaire présentant un excès d'émission proche-infrarouge.

Grâce à l'émission du gaz, on peut aussi remonter à la structure cinématique des disques. L'image classique de systèmes en rotation quasi-Keplerienne a été remise

en cause par ce type d'observations, avec par exemple la détection de vents et de jets évacués par les disques. Les vents magnétiques occupent d'ailleurs une place de choix dans l'avenir de la modélisation des disques protoplanétaires, de par leur connexion forte avec les phénomènes d'accrétion. D'autres phénomènes physiques sont souvent invoqués pour expliquer l'accrétion, notamment le transport turbulent résultant d'instabilités (magnéto-)hydrodynamiques, comme l'instabilité magnéto-rotationelle. Ces instabilités interviennent également dans la dynamique du gaz et des poussières, et ont fait l'objet de nombreuses études notamment via des simulations numériques (l'instabilité gravitationelle, l'instabilité de Rossby ou encore l'instabilité de cisillement vertical). Dans tous les cas, une question importante est de déterminer ce qui régit le transport efficace de masse des disques vers leur étoile, mesuré notamment en modélisant l'excès ultraviolet dans leur distribution spectrale d'énergie. Concilier les taux d'accrétion stellaire souvent élevés avec la finesse de certaines sous-structures observées dans l'émission de la poussière est en effet un enjeu important à la fois théorique et observationnel: il s'agit de comprendre les rouages de l'évolution des disques.

Des sous-structures dans la poussière ? Les observations montrent en effet que la poussière et le gaz ne se comportent pas de la même manière. Cette dissemblance est particulièrement saillante lorsque l'on estime l'extension radiale des disques. Définir une taille est compliquée, car elle dépend en réalité du traceur observationnel considéré. Le gaz des disques semble en effet s'étendre sur une distance typiquement ~ 2.5 fois plus grande que les larges poussières, ce qui traduit une dynamique et une évolution différentes de ces deux composantes des disques. Ces différences sont d'ailleurs en accord avec les prédictions des modèles d'interaction gaz-poussières. En particulier, la friction du gaz sur la poussière est à l'origine d'une dérive radiale vers l'étoile des poussières, d'autant plus rapide que celles-ci sont grandes. L'interaction gaz-poussières est également à l'origine de la sédimentation verticale des poussières dans le plan médian des disques.

Comprendre la dynamique des interactions gaz-poussières est également nécessaire pour interpréter les sous-structures observées dans l'émission des disques protoplanétaires. Ces structures, qui prennent souvent la forme d'anneaux brillants et sombres (en particulier dans le domaine radio) sont les témoins figés de mécanismes dynamiques à l'œuvre et ont suscité beaucoup d'activité de la part des modélisateurs des disques protoplanétaires. Ces structures observées ne sont d'ailleurs pas sans rappeler celles prédites par les modèles d'interactions disque-planète. En outre, selon un modèle répandu, chaque anneau sombre dans l'émission des disques correspondrait au sillon ouvert par une planète en orbite fixe autour de son étoile. D'une part, il n'y a pas encore de preuve observationnelle directe de la présence de telles planètes, et d'autre part, l'interaction entre une planète et le gaz du disque protoplanétaire peut rapidement modifier la distance de la planète à son étoile. Prendre en compte cette migration planétaire peut donc apporter des informations plus précises quant à l'impact d'une planète sur l'émission des poussières, en radio notamment. Les signatures de la présence de planètes et de leur migration sont multiples. Par exemple, une asymétrie dans la direction radiale de la position d'anneaux brillants proches peut indiquer la présence d'une planète, et contraindre la direction de sa migration. La position d'un anneau brillant par rapport à un anneau sombre peut aussi être

évocatrice de la vitesse de migration d'une planète par rapport à la vitesse de dérive des particules.

1

OBSERVATIONAL CONTEXT

The disks that rotate around young stars are an inevitable milestone of star and planet formation. Over the last few years, multi-wavelength observations have not only underlined that the gas and solids of these disks may have very different behaviors, but also provided a fertile ground for theoretical models to develop. The diversity of the observations, whether in the near infrared or in radio, has indeed shed some light on the dynamical and evolutionary processes behind the protoplanetary disks, these birthplaces of planets. We first introduce in section 1.1 the important observational tracers in order to study the structures of protoplanetary disks. We then briefly talk in section 1.2 about some disk properties that are derived from these observations, in particular their lifetime, size and mass.

CONTENT

1.1 Multi-wavelength observations 3
1.2 Important properties of protoplanetary disks 7
1.2.1 Disk lifetimes 7
1.2.2 Disk sizes 8
1.2.3 Disk masses 10
1.2.4 Disk temperatures 11
1.2.5 Other valuable observations 12

2 DYNAMICS OF PROTOPLANETARY DISKS 17

1.1 MULTI-WAVELENGTH OBSERVATIONS

Stars are born from the gravitational collapse of molecular clouds. Even though a large fraction of the cloud mass fuels the stellar birth, all the material does not entirely end up swallowed by the newly-formed star. Because of the forces involved in this collapse, the remaining material rearranges itself into a flattened circumstellar disk. Shrouded in this mantle of gas and dust, embryos of planets, called protoplanets, are expected to emerge. These early interactions between the protoplanetary disk, its host star and its potential planets may well last a few million years, they still constitute a key stone in the forthcoming evolution of the planetary system. Lingering over the first stages of a star's life gives therefore the opportunity to apprehend how stellar systems form and evolve.

Protoplanetary disks are mainly composed of gas (99% of their mass), but also of solid materials (~1% of their mass) that we will call dust or grains. Despite this little fraction in the disk composition, dust grains are essential as they are at once the building blocks of planetary systems, important cooling agents that regulate the disk temperature, and probably the most outstanding tracers of the disk behavior. There are actually three main observational tracers to study protoplanetary disks: dust thermal emission, scattered light and molecular line emission. Fig. 1.1.1 shows a rough idea of the radial and vertical structures of a protoplanetary disk and their contribution to the observational tracers.

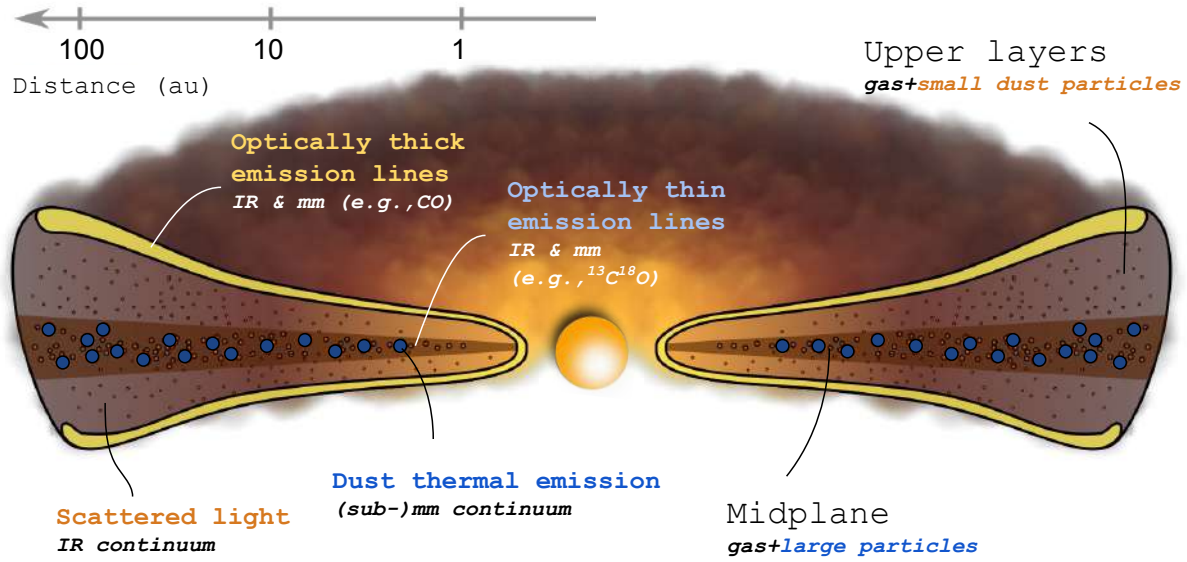

Figure 1.1.1: Pre-ALMA sketch of a disk structure seen edge-on, adapted from Testi et al. (2014) and Andrews (2020). The left side gives an idea of the link between the observational diagnostics and the regions they probe in the disk. The right side presents a schematic view of the vertical structure of a disk with the approximate location of gas and dust particles.

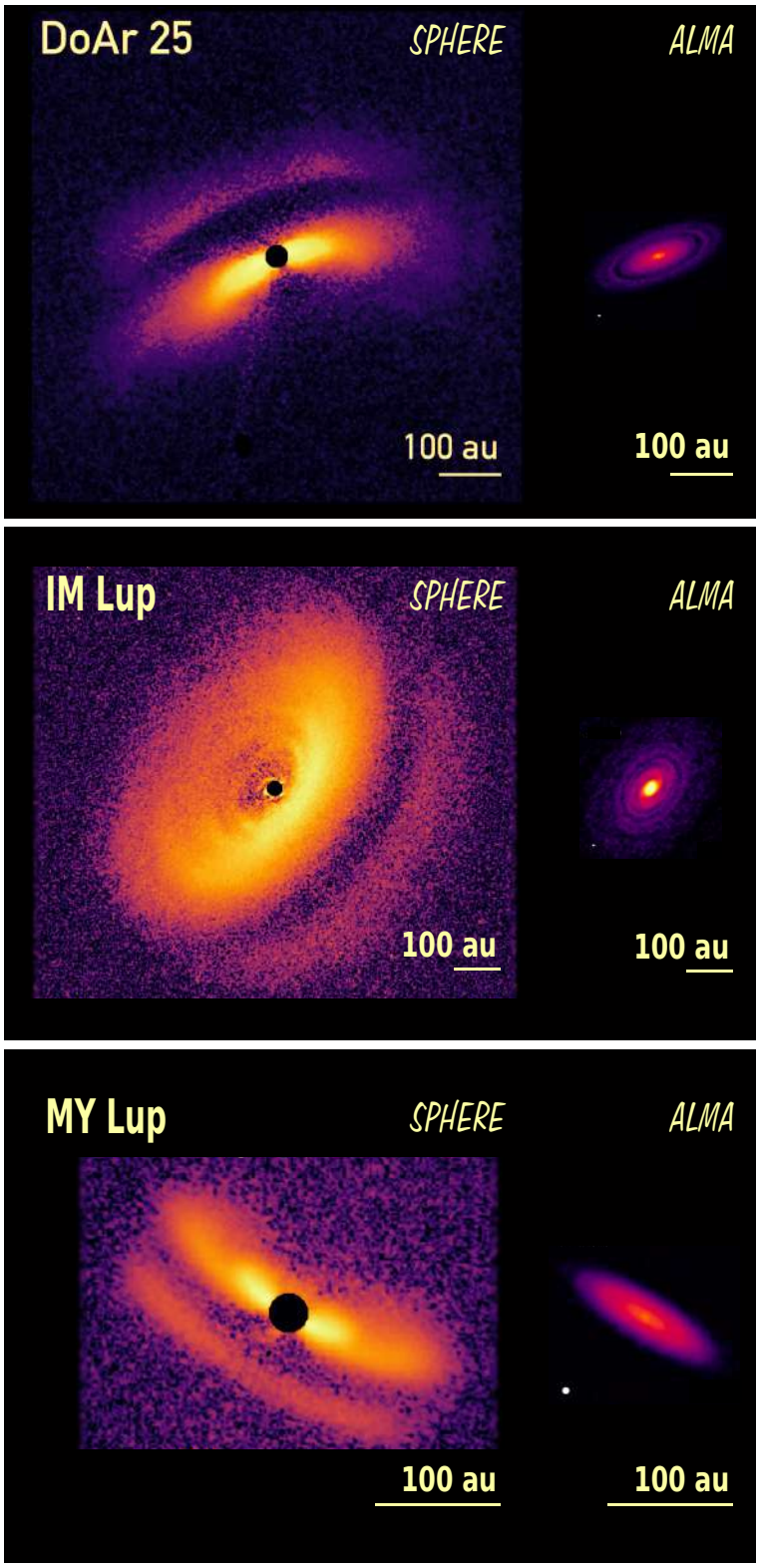

Figure 1.1.2: Three disks (DoAr25, IM Lup and MY Lup) observed with two dust tracers: the dust thermal emission of large particles observed with ALMA in radio at $\lambda = 1.25$ mm (right, from Andrews et al. (2018)) and the scattered light from smaller particles observed with SPHERE in the infrared (H band) at $\lambda = 1.65$ μm (left, from Avenhaus et al. (2018) and Garufi et al. (2020)). The beam is shown by the ellipse in the bottom-left corner of each dust thermal emission map.

- Dust thermal emission: stellar photons are absorbed by dust grains and re-emitted at all wavelengths (in the following, we will refer to this emission as thermal emission or continuum emission). In particular, in the sub-mm, dust thermal emission is most sensitive to large particles (around a mm in size) rather located in the disks midplane. In mid-IR, dust thermal emission is this time expected to trace smaller particles located in the superficial layers of protoplanetary disks. If the emission is optically thick, the emissivity will pinpoint the temperature of the observed layer. On the contrary, if the emission is optically thin, the intensity will also depend on the surface density of solids. Whether the emission is optically thin or thick depends, in particular, on the dust's size distribution and local density. For spherical and compact dust grains, dust thermal emission peaks at a wavelength λ comparable to the particles size s_d: $\lambda \sim 2\pi s_d$. Note that this is not the case for non-spherical non-compact dust grains (see Kataoka et al., 2014, and section 2.2.5).

- Scattered light boils down to the reflection of the star radiation by small dust grains (typically with size up to a μm) in the upper layers of the disk atmosphere. Because the population of small grains is distributed at all altitudes in the disk and constitutes a very optically thick medium at optical / near-IR wavelengths, scattered light probes the 3D geometry of the disk, and in particular how the vertical structure in the dust distribution varies radially.

- **Spectral lines** trace specific atomic or molecular transitions. Depending on if the emission is optically thin or optically thick, this tracer is sensitive to the gas distribution at different altitudes, respectively closer to the midplane or at larger scale heights. Whether the emission is optically thin or thick depends, in particular, on the gas-species-to-H_2 number density ratio, which is uncertain.

Because all these techniques shed light on various materials in protoplanetary disks, the resulting observations provide a wide heterogeneity in the appearance of these disks. Fig. 1.1.2 gives an example of three disks (DoAr 25, IM Lup, and MY Lup) observed with two tracers: scattered light in the near-IR (left) and dust thermal emission at $\lambda = 1.3$ mm (right), with approximately the same spatial scale. While the former shows clearly the vertical structures of the flared disks, the latter unveils radial substructures close to their midplane. We will come back to these substructures in a dedicated chapter (4). This diversity in how protoplanetary disks appear shows the necessity of conducting multi-wavelength and multi-tracer observations, in order to grasp all their complexity and their dynamics.

We have anticipated that for a given tracer, the optical depth of the medium has a strong influence on the interpretation of observed structures. Why exactly? Focusing on the dust thermal emission, the physical quantity that we actually measure in the telescope is the specific intensity I_ν at the frequency ν, and not the spatial distribution of dust in the disk (Eq. 1):

$$I_\nu = B_\nu(T_d) \times (1 - \exp(-\tau)), \tag{1}$$

with $B_\nu(T_d)$ the Planck function (see Eq. 2 below), T_d the dust temperature, and τ the optical depth (Eq. 3). Eq. (1) is the analytical solution to the radiative transfer equation

in two dimensions when dust scattering is discarded. We therefore only consider dust absorption and emission. In Eq. 1, the Planck function is given by

$$B_\nu(T_d) = \frac{2h\nu^3}{c^2}\frac{1}{\exp(\frac{h\nu}{k_B T_d}) - 1}, \tag{2}$$

where the various constants are given in Table 1 just before chapter 1. The optical depth

$$\tau = \int \kappa_\nu \Sigma_d ds \tag{3}$$

is a distinctive feature of the medium and measures how an electromagnetic radiation is transmitted throughout this medium. This quantity is defined as the dust density Σ_d times the dust absorption opacity κ_ν integrated over the line of sight s. From the optical depth, two regimes can be highlighted.

- $\tau \gg 1 \Longrightarrow I_\nu(\mathrm{thick}) \simeq B_\nu(T_d)$: A medium is *optically thick* if on average a photon cannot pass through the medium without absorption. The numerous interactions between photons and grains (absorption/emission) imply that the intensity or flux of emission mainly depends on the temperature of the dust T_d, according to the black body theory.

- $\tau \ll 1 \Longrightarrow I_\nu(\mathrm{thin}) \simeq \tau \times B_\nu(T_d)$: Conversely, an *optically thin* medium is nearly transparent at the observed wavelength. There are few interactions between the light from the star and the dust in the disk, therefore the photon we collect in the telescope is in a way a reliable witness of what happened during its journey. It gives some information about the temperature of the dust T_d, but also about the density of the dust Σ_d.

Note that the emission of the dust continuum at a given wavelength is never independent of the dust temperature. When interpreting structures in protoplanetary disks as an accumulation or deficit of dust particles, one should never forget the strong impact of dust temperature and opacities. For example, in an optically thin medium, does an absence of emission indicate an absence of particles ($\Sigma_d = 0$), a low dust temperature ($T_d \to 0$), or a low opacity ($\kappa_\nu = 0$)? Besides, the uncertainty between the optically thick and optically thin regimes can be approached through the study of the spectral index. If we have two maps of dust continuum emission at two wavelengths, say at $\lambda_0 = 0.87$ mm and $\lambda_1 = 1.3$ mm, it is possible to derive the spectral index:

$$\begin{aligned} \alpha_\nu &= \frac{d\log I_\nu}{d\log \nu}, \\ \alpha_\nu &= \frac{\log\left(I_{\lambda_1}/I_{\lambda_0}\right)}{\log\left(\lambda_0/\lambda_1\right)}, \end{aligned} \tag{4}$$

where we used $\nu = c/\lambda$. Because these maps are obtained in (sub-)mm (large) wavelengths, the Planck function can be approximated via the Rayleigh–Jeans law, and we can write $B_\nu(T_d) \propto \nu^2$. Then, two extreme cases can be highlighted, depending on the optical depth of the medium:

- **optically thick** $\tau \gg 1$: $\alpha_\nu = 2$, because of the dependence of $B_\nu(T_d)$ in ν^2,
- **optically thin** $\tau \ll 1$: $\alpha_\nu = 2 + \beta_\nu$, with $\beta_\nu = \dfrac{d \log \kappa_\nu}{d \log \nu}$ the absorption opacity spectral index.

When computing the spectral index for our maps at λ_0 and λ_1, two interpretations are therefore possible if $\alpha_\nu = 2$. Either the medium is optically thick, and the structures that we observe mainly depend on the dust temperature, or the medium is optically thin and $\beta_\nu = 0$. In practice, this latter case means that we have access to the dust opacities. For example, for a given dust composition and assuming that particles are spherical and compact, $\beta_\nu = 0$ also means that the continuum emission is dominated by very large particles (with a size larger than the wavelength of observation). We will make use of α_ν and β_ν in section 7.1.

1.2 IMPORTANT PROPERTIES OF PROTOPLANETARY DISKS

Constraining the physical properties of protoplanetary disks such as their mass, their size or their lifetime constitutes a sound investment to set up the initial conditions of theoretical models.

1.2.1 *Disk lifetimes*

It is possible to constrain the typical lifetime of protoplanetary disks by measuring the fraction of disks that show near-infrared excess emission, in a given star-forming region. This excess is a signature of the presence of small warm dust surrounding the star. Because it is hard to estimate individually the age of a star, a statistical approach is used. Instead of observing a single star, it is possible to consider a group of stars in the same star-forming region, assuming that all stars within it have more or less the same age. Fig. 1.2.1 shows that the fraction of stars in specific star-forming regions with infrared excess decreases with stellar age (Ribas et al., 2015). Different studies have come to a similar conclusion: disk lifetimes can typically vary from less than 1 Myr up to 10 Myr (e.g., Briceño et al., 2019; Fedele et al., 2010; Hernández et al., 2007b,a).

After this age, we can expect that there is nearly no more gas in the disk, which reveals that gas giant planets, mainly composed of hydrogen and helium, have to be formed during the protoplanetary disk phase. Put another way, the formation timescale from micrometer-sized dust grains to gas giants (about 14 orders of magnitude in size and 42 in mass) can be really short.

Biases:

- In this estimation, we have considered near-infrared excess emission as a proxy for the presence of a disk, while it only traces the presence of warm dust close to the star (which comprises only a small fraction of the total disk mass). Note that gas and dust do not necessarily follow the same dynamics, therefore this method

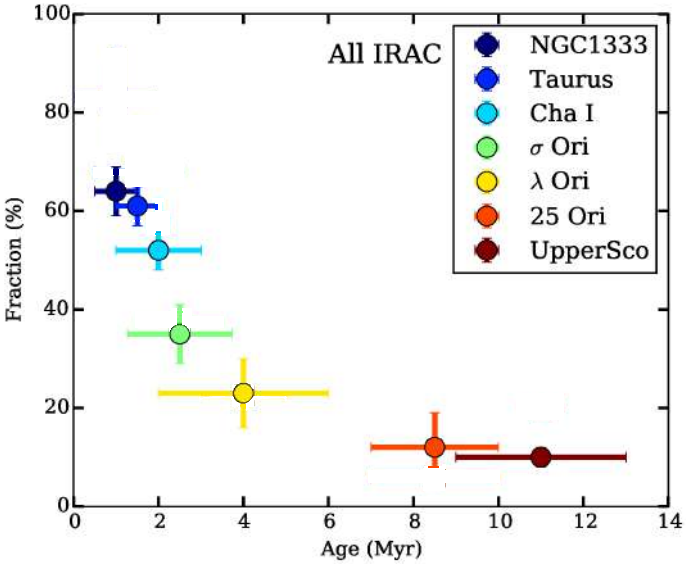

Figure 1.2.1: Disk fractions as a function of stellar age for different star-forming regions, adapted from Ribas et al. (2015).

only gives a constraint on the lifetime of the warm dust content in protoplanetary disks.

Note that it is also possible to estimate the disks lifetime from the emission of the disk gas, in H_α, due to accretion shocks onto the stellar surface. This H_α emission line is visible on top of the H_α absorption line due to the stellar photosphere.

1.2.2 *Disk sizes*

Let us now consider the observed size of protoplanetary disks. There is a clear discrepancy between the disk size given by dust thermal emission in radio, which preferentially probes large particles, and the disk size induced from scattered light, which is sensitive to smaller dust grains coupled with the gas. Such disparity indicates that dust particles and gas elements do not follow the same dynamics, for the largest grains are located much closer to the star and seem to settle down in the midplane of the disk (see the large diversity in the observations of the same objects in Fig. 1.1.2). Because of this, one needs a prescription to define the size of protoplanetary disks depending on the tracer, based on the luminosity of the objects. In practice, we choose the typical size of a disk such that it encompasses a large fraction ($\sim 90\%$) of its total luminosity. Note that the most luminous objects are also the largest ones. The dust continuum (at 0.9 mm) method suggests a range of sizes typically between $R_{0.9\ \mathrm{mm}} \sim 10 - 500$ au[1], whereas the CO line emission points toward larger disks (the order of $R_{CO} \sim 100 - 1000$ au). In practice, observations suggest that disk sizes inferred with (optically thick) CO line emission is about 2.5 times larger than disk sizes inferred with sub-mm (0.9 mm) dust thermal emission. Fig.1.2.2 shows this discrepancy between the two tracers, adapted from Andrews (2020), with the data from Öberg et al. (2011); Simon et al. (2017); Ansdell et al. (2018); Facchini et al. (2019). The one-to-one correspondence is shown with the gray dotted line. All the disks are smaller in sub-mm than in CO (red dashed line). Note that it is also possible, in

1 1 astronomical unit (au) represents the mean distance between the Sun and the Earth.

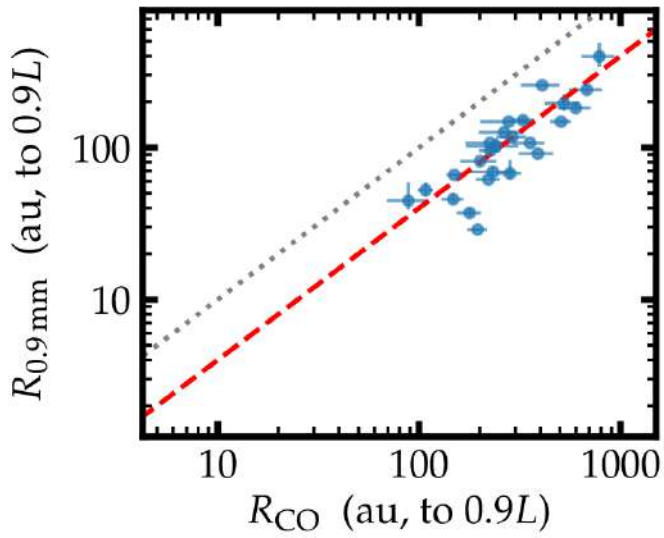

Figure 1.2.2: Comparison of disk sizes, with the 0.9 mm dust thermal emission tracer (y-axis) and the CO emission line tracer (x-axis). The red dashed line shows the $R_{CO} \simeq 2.5\ R_{0.9\ mm}$ relation; the dotted line corresponds to $R_{CO} \simeq R_{0.9\ mm}$ (Andrews, 2020).

principle, to constrain the vertical extent of protoplanetary disks, in particular the dust's pressure scale height (see section 2.2.3 for more details about this quantity). One can for example look at edge-on observations at different wavelengths and carry out dust radiative transfer calculations to have access to this quantity (see Fig. 1.1.2 and Villenave et al., 2020).

Besides the fact that gas and dust are decoupled in their dynamics, the characterization of disk sizes brings other valuable knowledge in the modeling of protoplanetary disks. In particular, the radial extent of the disk gas from spectral line emission gives a strong constraint on the minimal and maximal radii that we choose for numerical models. Furthermore, the fact that the dust thermal emission does not show much of a vertical structure can justify at first order the approximation of two-dimensional models, which is fundamental to have less time-consuming models.

Biases:

- The minimal sizes are probably constrained by resolution.
- Sub-samples of brighter sources induce biases towards larger objects.
- Concerning scattered light, radiation from the star will not necessarily reach the outer parts of disks, which potentially underestimates the real size of the object.
- The intensity does not only depend on the density distribution, and many other quantities play a role, in particular the temperature and the opacities. Therefore, the size that we measure is not simply the radius beyond which there is no disk material left.
- Finally, CO molecules tend to freeze-out onto dust grains when the gas temperature is smaller than $\simeq 19$ K. The radial extent of the gaseous disk could therefore be larger than expected.

1.2.3 *Disk masses*

Estimating the typical mass of protoplanetary disks is necessary, as part of this mass will be transferred to the future bodies that will constitute the planetary system. The diversity of disk appearance when observed through different tracers makes the estimation of the mass complicated: continuum emission of large particles is more compact compared to smaller grains or the line emission, which demonstrates the importance of measuring independently gas and dust properties.

Regarding dust thermal emission, it is possible to estimate the dust mass by integrating the measured intensity over the disk surface on the sky-plane, with the assumption that the emission is optically thin. Because in this regime the intensity I_ν depends on the temperature T_d, surface density Σ_d and opacities κ_ν of dust grains, all these quantities are involved in the expression of the total dust mass, as well as the disk distance (see, e.g., Eq. 3 in Williams & Cieza, 2011). Note that the flux of continuum emission at longer wavelengths λ (radio in particular) is a good probe of the disk's dust mass, because the emission is dominated by large particles ($s_d \sim \lambda/2\pi$ for spherical compact grains) located close to the midplane (where the mass volume density is highest).

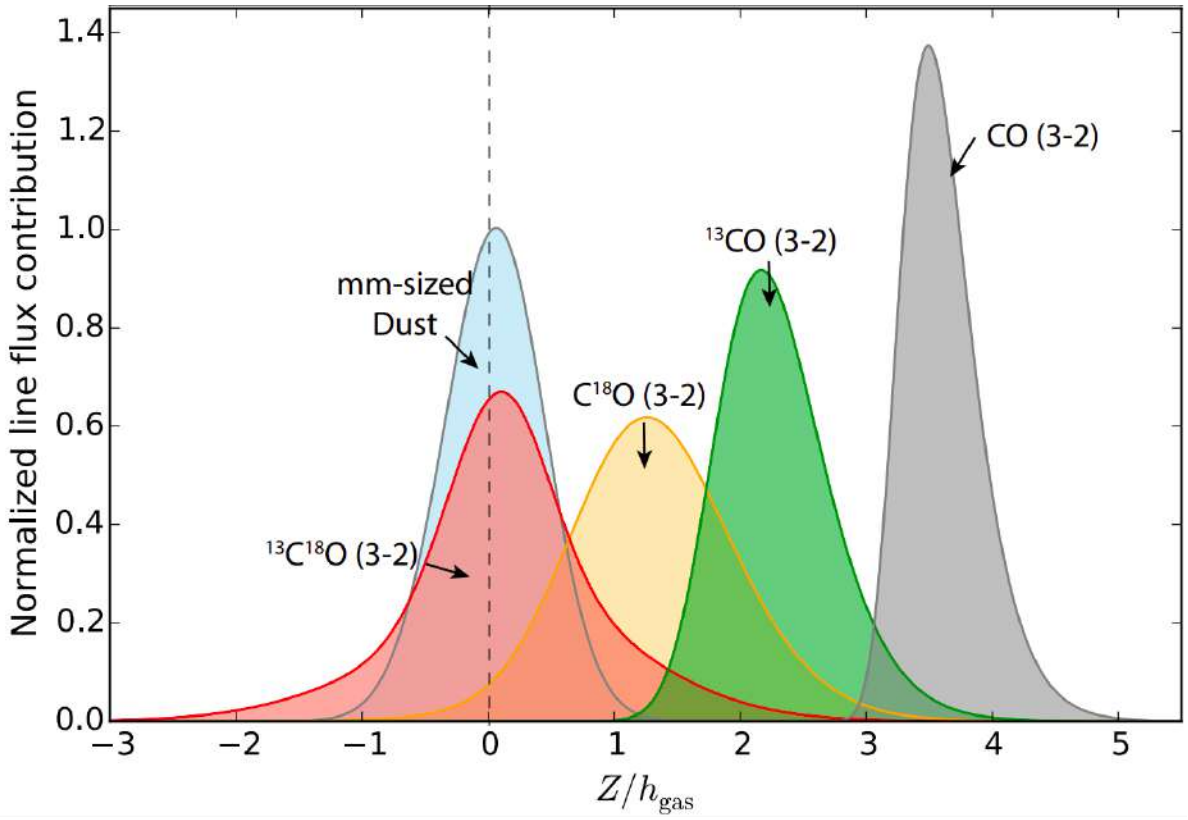

Figure 1.2.3: Vertical contributions of four CO isotopologues in the J=3-2 line and 0.93 mm dust continuum emission in the inner region of the TW Hya disk (Zhang et al., 2017). A rarer isotopologue probes closer regions to the midplane, through optically thin line emission.

In theory, spectral line emission allows to study the gas mass distribution in protoplanetary disks. The most abundant molecule that enables clear detection of lines emission is CO and its isotopologues. Depending on if the emission lines are optically thin or optically thick, this gas tracer of specific molecular transitions can probe the gas distribution at different altitudes, either close to the midplane (where most of the bulk mass is) or at larger altitudes. For example, Fig. 1.2.3 (Zhang et al., 2017) shows for the TW Hya disk that the $J = 3 \rightarrow 2$ optically thick line emission of CO is sensitive to the gas temperature in the uppermost layers of the disk. Likewise, the $J = 3 \rightarrow 2$ optically thin line emission of the rare isotopologue $^{13}C^{18}O$ this time mainly arises from the gas in the midplane. With a typical conversion factor from $^{13}C^{18}O$ to CO, and an abundance of the CO molecule relative to H_2, it is then possible to deduce a typical disk mass. Note that there is a wide range of possible rare isotopologues (HCN, C_2H, HD, ...) when it comes to spectral line emission, some of them being good candidates in the future to obtain a more precise estimate of the gas mass (see, e.g., Bergin et al., 2013).

Caveats:

- There are strong uncertainties on the properties of dust particles. In particular the fact that particles are not necessarily compact spheres, but are likely fluffy aggregates. In this case, Mie theory is not valid anymore and the opacities κ_ν used to derive the relationship between integrated intensity and disk mass may not be reliable.
- The hypothesis of optically thin emission is used, but some regions might be optically thick, making the measured intensity largely independent of the surface density Σ_d. An optically thick emission therefore underestimates the disk mass.
- Even in the optically thin regime, strong approximations are made in the integration of the intensity to derive the total dust mass, in particular the fact that the dust temperature is independent of the distance R from the star.
- Disk mass estimators almost always need a highly uncertain conversion factor: either a dust-to-gas mass ratio, or an abundance factor, from CO to H_2 for instance.

1.2.4 *Disk temperatures*

The disk temperature T is an essential quantity to grasp in order to appreciate the meaning of each observation. As we have seen already, the temperature intervenes in the expression of the intensity of thermal emission I_ν, and is even dominant when the observed region is optically thick. Temperature plays also a key role in the gas and dust dynamics of protoplanetary disks. For example, it intervenes in the sound speed c_s:

$$c_s = \sqrt{\frac{k_B T}{\mu_\star m_p}}, \tag{5}$$

and thus in the radial and vertical pressure gradients of the disk, which strongly impact the dust dynamics via a velocity difference between the gas and the dust (vertical settling, radial drift, see chapter 2). An important related quantity is the pressure scale height of the gas H_g:

$$H_g = \frac{c_s}{\Omega_K}, \tag{6}$$

where Ω_K is the Keplerian frequency, which corresponds to the orbital frequency of a test particle on a circular orbit at a distance R from the star:

$$\Omega_K(R) = \sqrt{\frac{GM_\star}{R^3}}, \tag{7}$$

with $M_\star$ the mass of the star. We will describe more in depth these quantities in chapter 2. Because H_g gives an idea of the vertical distance over which the density and pressure fall by a factor of $\exp(-1/2)$ (see chapter 2), the temperature is therefore a key quantity to describe the vertical distribution of gas and dust in the disk (see Fig. 1.1.2). There is **no direct method** to date to measure the temperature. One way to constrain the disk temperature profile is to suppose a dust density and opacity profile, perform radiative transfer calculations with these priors in order to reach a temperature of equilibrium for the dust, and compare the obtained synthetic intensity with real observations (see, e.g., Heese et al., 2017). However, this method can be costly and give degenerate results. It is also possible to estimate tomographically the temperature by considering several optically thick emission lines (see as an example the vertical structures and lines emission in TW Hya Fig.1.2.3).

1.2.5 *Other valuable observations*

Many other quantities can be derived from observations and play an important role in numerical models of protoplanetary disks. We sum up here some of these quantities. For a general review on observations of solids and gas in protoplanetary disk, see Andrews (2020); Williams & Cieza (2011).

- Using dust thermal emission and a touch of optimism, it is possible to estimate the dust surface density Σ_d, among several disk properties, by fitting spatially resolved disk observations with a disk model (see, e.g. Tazzari et al., 2017). That way, Σ_d is found to roughly scale as R^{-1} in the inner disk and to decrease more rapidly further away from the star. We then suppose a dust-to-gas density ratio to obtain the gas surface density Σ_g. The typical density profile used to fit disks observations and to model these systems is the following one (Lynden-Bell & Pringle, 1974, to see the theoretical origin of this self-similar solution to the equation governing the surface density in the viscous accretion disk model):

$$\Sigma_g(R) = \Sigma_g(R_c)\left(\frac{R}{R_c}\right)^{-\sigma} \exp\left(-\left(\frac{R}{R_c}\right)^{2-\sigma}\right), \tag{8}$$

  $\sigma \sim 1$ being the surface density slope.

- Our Solar System is approximately 4.6 billion years old, but scrutinizing it from the angle of its formation can unveil some generic processes lying behind the evolution of all protoplanetary disks. From observations of our current system, we are able to derive some constraints about the properties and features of its primordial phase. In particular, the Minimum Mass Solar Nebula (MMSN) is a model of protoplanetary disk that gives a minimum mass of solid material that must have been present to build the eight planets of the Solar System, assuming planets accreted all the solids and formed at their current position, with material having the same relative elemental abundances as those in the Solar photosphere. The latter assumption comes from the analysis of primeval meteorites which have a composition similar to the composition of the Sun, except for the most volatile chemical elements (H, He, O, C, N), not present in these meteorites. The mass distribution in the MMSN is obtained upon adding to the actual mass of the planets all the elements (solids and volatiles) present in the Sun so that the relative elemental abundances of the Sun and the planets be the same (Weidenschilling, 1977). Spreading out these augmented planet masses over annuli gives an insight of what the gas surface density of the disk should have been as a function of the distance to the Sun (Eq. 9), as well as the mass of the primordial disk compared to the mass of the Sun (Eq. 10):

$$\Sigma_{MMSN}(R) = 1700 g\,cm^{-2} \left(\frac{R}{1au}\right)^{-\frac{3}{2}}, \tag{9}$$

$$M_{MMSN} = 0.01 - 0.07 M_{\odot}. \tag{10}$$

- From spectral line emission, it is possible to probe the gas kinematics (via 1st moment maps, see section 7.3) if the disk is inclined compared to the line of sight. In practice, for a given energy transition, gas molecules emit at a specific wavelength. But because the gas in the disk rotates, the emission is Doppler-shifted: the emission line coming from disk material that moves towards the observer is blue-shifted, whereas the emission line coming from disk material that moves away from the observer is red-shifted (see the 1st moment map in the left panel of Fig. 1.2.4 for the disk HD 163296, from (Isella et al., 2018)). From this kinematics, it is then easy to detect the disk rotation axis and create a Position-Velocity diagram (right panel of Fig. 1.2.4) to estimate a typical Keplerian profile of the disk material, and eventually a measurement of the stellar mass. We will see in sections 4.4 and 7.3 that studying the gas kinematics can also bring valuable insights on non-Keplerian flows around protoplanetary disks.

- The evolution of protoplanetary disks is largely dominated by the dynamics of its constituents. In particular, it is possible to detect accretion phenomena onto the surface of the star. An ultraviolet (UV) excess in the spectral energy distribution gives through continuum fitting methods a quantitative estimate of the stellar accretion rate $\dot{M}$, with a typical value of 10^{-8} $M_{\odot}.yr^{-1}$. The classical picture proposes that the observed accretion points out a radial turbulent transport of

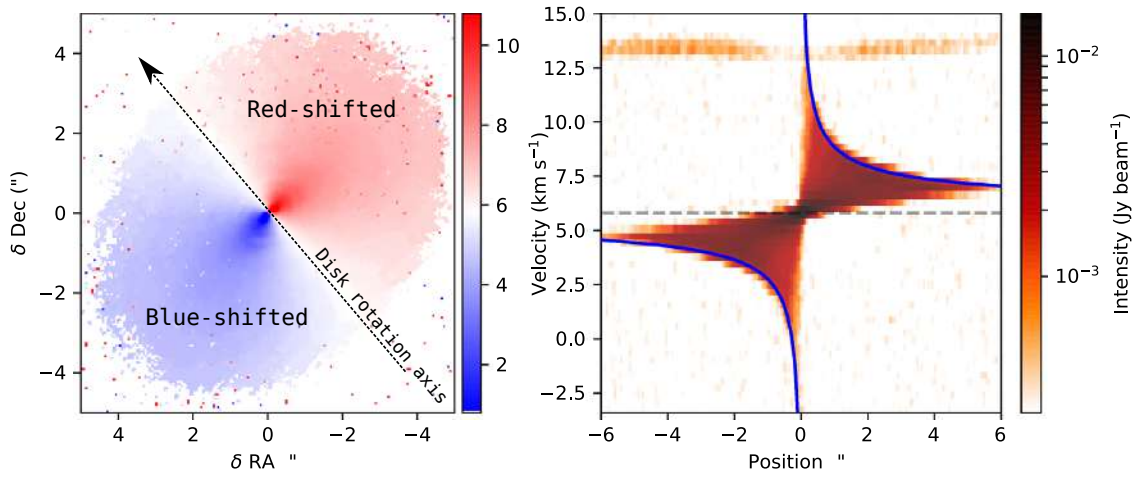

Figure 1.2.4: Gas kinematics of the HD 163296 disk, adapted from Isella et al. (2018). **Left panel**: intensity-weighted velocity map (1st moment) of the ^{12}CO J = 2 → 1 line emission. **Right panel**: position–velocity diagram obtained by averaging along the direction perpendicular to the disk rotation axis. Position= 0 corresponds to the location of the star. The horizontal gray dashed line marks the systemic velocity, whereas the blue curve shows the Keplerian rotation profile at large distance from the star. From this profile and for a disk inclination of ~ 47 deg, the stellar mass is expected to be 2 $M_\odot$. See Isella et al. (2018) for more details.

mass, modeled as an equivalent kinematic viscosity ν (see Chapter 2). We usually parametrize ν with a dimensionless quantity α (Shakura & Sunyaev, 1973) :

$$\alpha = \frac{\nu}{c_s H}. \tag{11}$$

Different types of observations aim to measure this α parameter. Firstly, measuring the spectral width of emission lines gives a hint of non-thermal broadening, in the case where we can safely model the thermal component of the broadening (Flaherty et al., 2015). Depending on the chosen line, we have access to upper limits in the values of α (typically a few $10^{-3} - 10^{-2}$) at different altitudes (higher altitudes for optically thick emission lines). Secondly, observations of radial substructures in the dust thermal emission is also a good proxy for α, because this parameter intervenes in the apparent sharpness of such dust structures (see Pinte et al., 2016, for the modelling of HL Tau). α controls the turbulent mixing, i.e. the ability for dust particles to efficiently accumulate in the disk midplane, or to be diffused at higher altitudes. It therefore defines a dust's vertical scale height. In order to infer α from the dust's vertical scale height, it is possible to carry out radiative transfer calculations on different models of disk with radial variations in the intensity. The main difference between these disk models is the dust's vertical scale height, and its impact on the contrast between bright and dark rings. The disk model that matches most closely with the observations is selected. Assuming a standard dust settling model, it is then possible to obtain an estimation of α (see also section 2.2.3). Such studies suggest $\alpha < 10^{-3}$ close to the midplane (see, e.g. Flaherty et al., 2015).

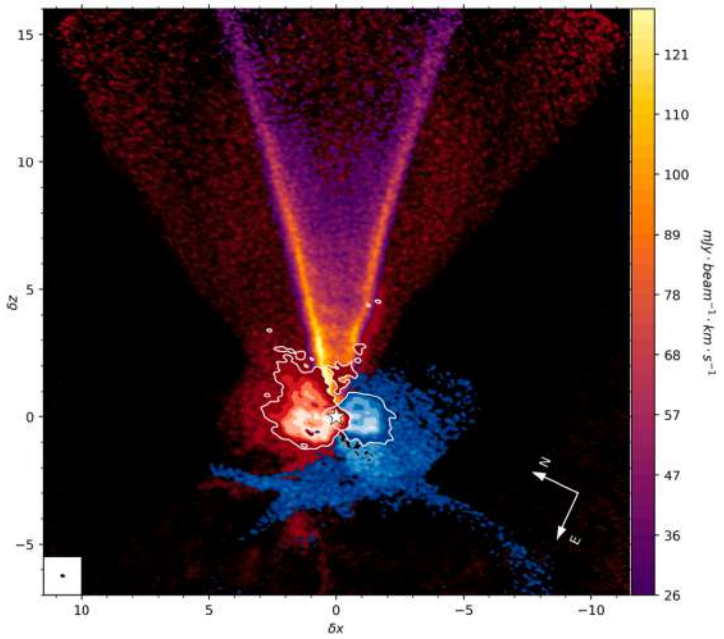

Figure 1.2.5: Detection with the J = 2 → 1 emission line of ^{12}CO of a slow-component wind (dark red wide structure, $\delta z \gtrsim 2''$) and a fast-component wind (purple-to-yellow V-shaped structure) in the disk DG Tau B. The Keplerian rotation is shown in red and blue (see $\delta z \lesssim 2''$). The blue material is rotating towards the observer, whereas the red material is moving away from the observer. Note that the outflows are redshifted, and thus are moving away from the observer (de Valon et al., 2020).

- Knowing that the gas mass should be efficiently transported from the outer parts of the disk towards the star and yet that the level of turbulence is (much) lower than expected has triggered the development of another paradigm of disk evolution, different from the viscous accretion model. In the wind-driven accretion model, angular momentum is evacuated from the surface of the disk by a magnetized wind, which induces a radial transport of the gas mass, laminar this time. This model reconciles at once the high stellar accretion rate and the *a priori* low turbulence in protoplanetary disks (Blandford & Payne, 1982; Bai & Stone, 2013; Lesur et al., 2014). Note that both models are not mutually exclusive, and come both from the equation of angular momentum conservation (see Section 2.1.3). Outflows coming from the inner parts of the disk are more and more frequently observed, as in de Valon et al. (2020) (see Fig.1.2.5).

My thesis project focuses on the substructures that are observed in protoplanetary disks, which will be presented in chapter 4. But first, it is necessary to introduce in chapter 2 the dynamics of gas, dust, and their interactions in planet-forming regions.

2

DYNAMICS OF PROTOPLANETARY DISKS

From collapse to dispersal, the life of a protoplanetary disk is constantly regulated by various and complex processes. However, the diversity of these phenomena is not inextricable: despite the richness of their manifestations, their origin remains generic. On the one hand, the prevailing forces related to gravity, pressure or differential rotation tend to structure and balance gas and solids. On the other hand, the dissipative processes inevitably lead to a rupture of this equilibrium. Whether by a variation in the gas angular momentum (at the origin of accretion), or by a variation in the dust angular momentum (at the origin of both radial drift and settling), the resulting dynamics offer an intricate canvas that modelers are gradually unraveling. The main stages in the disks life are presented in section 2.1. We then deal in section 2.2 with gas-dust interaction in protoplanetary disks, before briefly mentioning in section 2.3 some hydrodynamical/magneto-hydrodynamical instabilities that are relevant for the disks structure and evolution.

CONTENT

2.1 The life and death of protoplanetary disks . . . 19
2.1.1 Formation: from cloud to protoplanetary disk . . . 19
2.1.2 Equilibrium . . . 20
2.1.2.1 Centrifugal balance . . . 20
2.1.2.2 Vertical hydrostatic equilibrium . . . 21
2.1.2.3 Turbulent viscosity ν and α-parameter . . . 23
2.1.3 Accretion models . . . 24
2.1.4 Disk dispersal: from protoplanetary disk to stellar system . . . 27
2.2 Dust dynamics . . . 29
2.2.1 Aerodynamic drag force . . . 29
2.2.2 Radial drift . . . 30
2.2.3 Vertical settling . . . 33
2.2.4 Dust growth . . . 35
2.2.5 Dust properties . . . 38
2.3 Selected magneto-hydrodynamical instabilities . . . 40
2.3.1 Magneto-Rotational Instability . . . 41
2.3.2 Gravitational Instability . . . 41
2.3.3 Vertical Shear Instability . . . 43
2.3.4 Rossby Waves Instability and vortices . . . 44

Appendices 47
2.A Disk temperature . . . 47

3 PLANET FORMATION AND ORBITAL EVOLUTION 49

2.1 THE LIFE AND DEATH OF PROTOPLANETARY DISKS

2.1.1 *Formation: from cloud to protoplanetary disk*

Let us start with a collapsing spherical molecular cloud[1] in rotation, with radius R_{cl}, mass M_{cl} and angular frequency vector $\overrightarrow{\Omega_{cl}} = \Omega_{cl}\overrightarrow{e_z}$, in a cylindrical coordinate system (R,ϕ,z). If the cloud does not rotate, the collapse of its envelope will be due only to gravitational accelerations and pressure support, so that we would obtain a denser cloud, with a smaller radius R'_{cl}, but still spherical. Though, rotation changes what really happens. The conservation of specific[2] angular momentum $\overrightarrow{l_{cl}}$,

$$\overrightarrow{l_{cl}} = R_{cl}\overrightarrow{e_R} \times R_{cl}\Omega_{cl}\overrightarrow{e_\phi}, \tag{12}$$

gives a constant value for $l_{z,cl}$, the component of the specific angular momentum along the rotation axis:

$$l_{z,cl} = R_{cl}^2\Omega_{cl}. \tag{13}$$

Therefore if the cloud collapses, R_{cl} decreases and the angular frequency Ω_{cl} increases. This produces a centrifugal acceleration term $\overrightarrow{\Omega_{cl}} \times (\overrightarrow{\Omega_{cl}} \times \overrightarrow{R})$ whose magnitude depends on the radial distance (R) from the rotation axis. If we consider a particle on the cloud's envelope with a position vector described by spherical coordinates (r,θ,ϕ), the time evolution of its collapse velocity $\overrightarrow{v_r}$ satisfies

$$\frac{d\overrightarrow{v_r}}{dt} = \left(-\frac{GM_{cl}}{r^2} + r\Omega_{cl}^2 \sin^2\theta\right)\overrightarrow{e_r}, \tag{14}$$

where we have assumed for simplicity $\frac{d\phi}{dt} = \Omega_{cl}$, and $\frac{d\theta}{dt} \simeq 0$. For $\theta = 0$, i.e. at the poles, the centrifugal acceleration cannot stop the infall of the particle. On the contrary, an equilibrium is possible at $\theta = \pi/2$, i.e. at the equator, where the gravitational and centrifugal acceleration can balance each other. The infall of a rotating molecular cloud therefore produces a disk.

We have considered here the simple case of a Lagrangian test particle. In reality, for a gas particle, pressure support will slow down the infall of the particle by adding an additional acceleration outwards. It is the competition between these three accelerations (gravitational, centrifugal, pressure) that gives the object its shape: while a cloud shaped by pressure will be spherical, a cloud shaped by centrifugal acceleration will be flat, i.e. elongated perpendicularly to the rotation axis.

1 interstellar gas cloud whose density and temperature allow the formation of molecules, in particular molecular hydrogen H_2.

2 per unit mass.

2.1.2 *Equilibrium*

2.1.2.1 *Centrifugal balance*

First of all, what is a Keplerian disk ? Now that the particles coming from the molecular cloud are distributed throughout a flat disk, we choose to describe their motion in a polar coordinate system (R,ϕ) centered on the star, with R the cylindrical radius and ϕ the azimuthal angle. We neglect in this section the self-gravity of the disk gas. Let a dust particle be on circular orbits in the disk midplane, its motion follows Kepler laws caused by the central massive body. Centrifugal acceleration balances gravity (Eq. 15) and the azimuthal velocity around the star, called Keplerian velocity v_K, is given only by the mass $M_\star$ of the star and the distance R between the particle and the star (Eq. 16).

$$\frac{-GM\star}{R^2} + R\Omega_K^2 = 0. \tag{15}$$

$$v_K(R) = R\Omega_K = \sqrt{\frac{GM_\star}{R}}. \tag{16}$$

Eq. (16) shows that a more massive star leads to a larger Keplerian velocity. Likewise, a particle that is closer to the star will orbit faster. Concerning a gas element, pressure will act as an additional acceleration, and the centrifugal balance that governs the motion of the gas in the inertial frame centered on the star reads

$$\frac{-GM\star}{R^2} + R\Omega_g^2 - \frac{1}{\rho_g}\frac{\partial p_g}{\partial R} = 0. \tag{17}$$

Using the ideal gas law, the pressure of the gas p_g is linked to its density ρ_g and its temperature T_g:

$$p_g = \frac{\rho_g k_B T_g}{\mu m_p} = \rho_g c_s^2, \tag{18}$$

with c_s the isothermal[3] sound speed, as defined in Eq. (5). Using Eq. (17) and Eq. (18), we obtain the azimuthal velocity of the gas:

$$v_{\phi,g}(R) = v_K(R)\left(1 + \frac{c_s^2}{v_K^2}\frac{\partial \log p_g}{\partial \log R}\right)^{1/2}. \tag{19}$$

We define here an important quantity called *aspect ratio* and noted $h_g = \frac{c_s}{v_K}$. h_g is the pressure scale height to radius ratio, H_g/R, and is related at once to the gas temperature and the vertical structure of the disk (see section 1.2.4). Because c_s is a small fraction of the Keplerian speed (h_g is typically a few percent) the disk gas is a compressible fluid that is particularly sensitive to the effects of pressure, and therefore subject to the development of acoustic waves (like the planet wakes, see chapter 3).

3 in a locally isothermal equation of state, c_s is stationary: $\partial_t c_s = 0$.

The isothermal sound speed only depends on the square root of the gas temperature: $c_s \propto T_g^{1/2}$. We assume that T_g has a power-law dependence on R:

$$T_g(R) = T_{g,c}\left(\frac{R}{R_c}\right)^{-\beta}, \tag{20}$$

with $T_{g,c}$ the disk temperature at a given distance R_c. Therefore, because $v_K \propto R^{-1/2}$, the aspect ratio can also be written as a power-law of R:

$$h_g(R) = h_{g,c}\left(\frac{R}{R_c}\right)^{f}, \tag{21}$$

with $h_{g,c}$ the disk aspect ratio at R_c. The quantity f such that

$$f = \frac{1-\beta}{2} \tag{22}$$

is usually called the *flaring index*, and it depends on the temperature's power-law exponent β. For more details about the power-law dependence of the temperature, the typical values of f and some classical values of disk temperatures, see Appendix 2.A.

Eq. (21) indicates that the aspect ratio is higher further away from the star. In particular, a disk whose aspect ratio increases with R is flared, which seems to be in agreement with the observations of edge-on disks (see for example the disk DoAr 25 in the top-left panel of Fig. 1.1.2). By defining $\eta_g = \left(\frac{\partial \log p_g}{\partial \log R}\right)$ as the local gas pressure logarithmic gradient, we can rewrite Eq. (17) as

$$v_{\phi,g}(R) = v_K(R)\left(1 + h_g^2\eta_g\right)^{1/2}. \tag{23}$$

In Eqs. (17), (19) and (23), we highlight in red the terms linked to the gas pressure. Note that with no pressure, we find again the expression of the Keplerian velocity v_k for a dust particle. Because $|h_g^2\eta| \ll 1$ and usually $\eta < 0$ since the gas is warmer and denser close to the star, the gas azimuthal velocity at a given distance from the star is slightly lower that the Keplerian velocity. We talk about nearly Keplerian or sub-Keplerian disks. In such disks, the gas velocity deviates more from the Keplerian speed at larger radii.

2.1.2.2 *Vertical hydrostatic equilibrium*

Let us now consider an element of gas, this time at a certain altitude $z \neq 0$ from the midplane, in a cylindrical coordinate system (R,ϕ,z). The equation of motion in the vertical direction reveals the competition between gravity and pressure :

$$\frac{-GM\star}{(R^2+z^2)^{3/2}}z - \frac{1}{\rho_g}\frac{\partial p_g}{\partial z} = 0, \tag{24}$$

where we have projected the radial unit vector in spherical coordinates, $\overrightarrow{e_r} = \frac{R}{(R^2+z^2)^{1/2}}\overrightarrow{e_R} + \frac{z}{(R^2+z^2)^{1/2}}\overrightarrow{e_z}$, onto the vertical direction $\overrightarrow{e_z}$. Then, we suppose that the isothermal

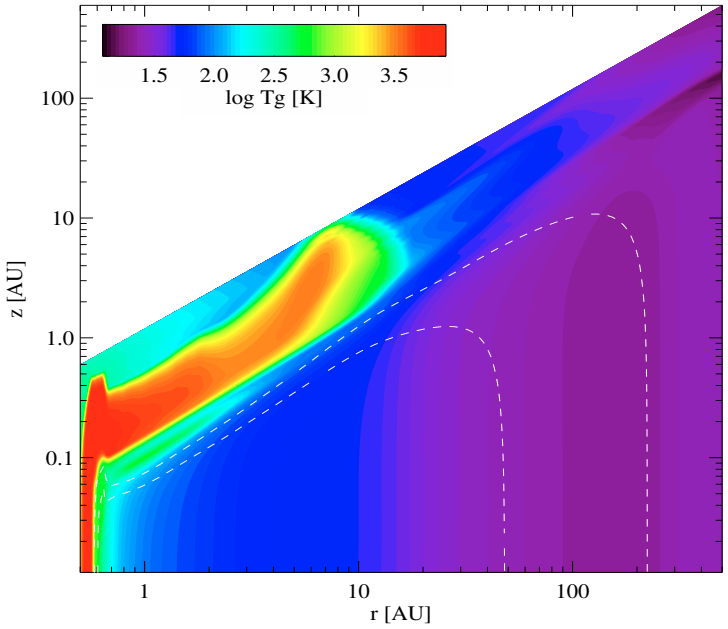

Figure 2.1.1: Gas temperature structure T_g in the (R-z) plane of a MMSN-like disk with $M_{disk} = 0.01\ M_\odot$, from thermo-chemical simulations (Woitke et al., 2009).

sound speed c_s is independent of z, which is a safe approximation beyond a few astronomical units from the star. This assumption has been validated in regions near the disk midplane by thermo-chemical radiative transfer models that account for various heating and cooling processes (Woitke et al., 2009). Fig. 2.1.1 shows the results of one such model in the (R-z) plane of a MMSN-like protoplanetary disk. The vertically isothermal hypothesis is particularly robust beyond 10 au.

From Eq. (24), we can then derive the expression of the gas density ρ_g with respect to the altitude z:

$$\begin{aligned} \frac{c_s^2}{\rho_g}\frac{\partial \rho_g}{\partial z} &= -\frac{-GM\star}{(R^2+z^2)^{3/2}}z, \\ \ln\left(\frac{\rho_g(R,z)}{\rho_g(R,z=0)}\right) &= \frac{1}{h_g^2}\left[\frac{1}{\left(1+\frac{z^2}{R^2}\right)^{1/2}}-1\right], \\ \rho_g(R,z) &= \rho_g(R,z=0)\exp\left(-\frac{z^2}{2H_g^2}\right), \end{aligned} \tag{25}$$

where we have used the ideal gas law $p_g = \rho_g c_s^2$ (Eq. 18) along with the expressions of the aspect ratio h_g (Eq 21) and of the pressure scale height H_g (Eq. 6), and the thin disk approximation $z/R \ll 1$. Then, we typically use a power-law to describe the evolution of the gas density in the midplane $\rho_g(R, z = 0)$ as a function of the distance from the star. It is relevant as this kind of radial profile is also used to fit observations

(see Section 1.2.5). Finally, if we consider 3D calculations, it is possible to link the gas density in the midplane $\rho_g(R, z = 0)$ and the gas surface density $\Sigma_g(R)$:

$$\begin{aligned}\Sigma_g(R) &= \int_{-\infty}^{+\infty} \rho_g(R, z)\,dz,\\ \Sigma_g(R) &= \rho_g(R, z = 0)\int_{-\infty}^{+\infty} \exp\left(-\frac{z^2}{2H_g^2}\right) dz,\\ \Sigma_g(R) &= \rho_g(R, z = 0)\sqrt{2\pi}H_g.\end{aligned} \tag{26}$$

We can rewrite $\rho_g(R, z)$ as a function of $\Sigma_g(R)$:

$$\rho_g(R, z) = \frac{\Sigma_g(R)}{\sqrt{2\pi}H_g}\exp\left(-\frac{z^2}{2H_g^2}\right). \tag{27}$$

Note that

$$\rho_{mid}(R) = \frac{\Sigma_g(R)}{\sqrt{2\pi}H_g} \tag{28}$$

is the gas volume density in the midplane. From Eq. (27), we find one of the important properties of H_g, related to the thickness of the disk. H_g corresponds to the vertical distance over which the gas pressure and gas density fall by a factor of $\exp(-1/2)$. With the vertical hydrostatic equilibrium, the gas density at an altitude $z = 3H$ is only 1% of the gas midplane density.

2.1.2.3 *Turbulent viscosity ν and α-parameter*

In the two previous sections, we have introduced some important quantities that are commonly used as initialization when it comes to modeling protoplanetary disks via hydrodynamical simulations. We will develop this aspect from a numerical point of view in chapter 5. What about the evolution of the gas in protoplanetary disks ? We have presented in Section 1.2.5 some observational constraints on stellar accretion rates $\dot{M}$. In order to explain such high values of $\dot{M}$, one needs to rely on mass and angular momentum transport models. Eq. (23) demonstrates that a ring A of gas elements closer to the star will orbit faster than a ring B of gas elements that is located further away. We will assume next that $v_{\phi,g} \simeq v_K$, which means that the pressure gradient is negligible compared to the gravitational potential. Said differently, we assume that the disk is Keplerian.

Because ring A moves faster than ring B, there is a friction between the two rings which tends to slow down A and speed up B. In terms of specific angular momentum (see Eq. 13),

$$l_{z,A} = \sqrt{GM_\star r_A}, \tag{29}$$

this friction between A and B means that $l_{z,A}$ decreases, therefore r_A decreases too (Eq. 29) and ring A moves inward. For the outer ring B, its specific angular momentum $l_{z,B}$ increases, and so does its orbital distance r_B. By virtually decomposing the disk as a series of many consecutive rings, we can show that shear-driven friction

tends to transport mass inward, which is responsible for the phenomenon of *accretion*. The friction between the rings depends on the *viscosity* of the fluid, and can result from different physical processes. However, molecular viscosity is much too small to account for the substantial stellar accretion rates ($\dot{M} \sim 10^{-8}$ $M_\odot.yr^{-1}$), and a different source of dissipation, of *turbulent* origin, is often invoked. Turbulence in disks is supposed to be the consequence of the non-linear saturation of the Magneto-Rotational Instability (MRI), and characterized by turbulent eddies and transport of matter. Although the MRI is the most promising instability to explain turbulence-driven accretion, recent global simulations of protoplanetary disks with non-ideal magneto-hydrodynamical (MHD) effects have shown that the MRI may not occur in most regions of protoplanetary disks (see, e.g. Lesur et al., 2014). We will see in Section 2.3 a wide range of instabilities that can be at the origin of turbulence. Some of these instabilities are also important to apprehend the substructures that we see in recent disk observations.

We recall here that the disk viscosity ν is commonly parametrized with an α-parameter (see Eq. 11 and Shakura & Sunyaev, 1973). ν then features H_g (the maximum length scale of turbulent eddies, roughly equal to the disk's pressure scale height), c_S (the maximum velocity of turbulent motions relative to the mean flow), and $\alpha < 1$ (a dimensionless parameter that needs to be in the range $\left[10^{-4} - 10^{-2}\right]$ to explain disk lifetimes and measured stellar accretion rates). We interpret Eq. (11) as unsteady turbulent eddies with a characteristic perturbed velocity $< c_S$ and a characteristic mean free path[4] $< H$ that generate the turbulent viscosity. For a temperature profile dominated by stellar irradiation (see Interlude in Section 2.1.2.1), i.e. for $\beta = 1/2$, we obtain a linear increase of the turbulent viscosity with stellar distance ($\nu(R) \propto R$).

2.1.3 *Accretion models*

We have seen in Section 1.2.5 the two paradigms that aim at explaining the origin of accretion, through a radial stress (viscous accretion model) or a vertical surface stress (wind accretion model). In this section, we give some clues on where these two approaches come from, by considering the Navier-Stokes equation, in the presence of a magnetic field, and in cylindrical coordinates (R,ϕ,z), with the hypothesis of axisymmetry ($\partial_\phi = 0$):

$$\rho_g \left(\frac{\partial \vec{u}}{\partial t} + (\vec{u}.\vec{\nabla})\vec{u} \right) = \vec{J} \times \vec{B} - \vec{\nabla} p_g - \rho_g \vec{\nabla} \Phi, \tag{30}$$

with $\vec{u}$ the velocity flow, ρ_g and p_g the gas density and pressure, $\Phi = -\frac{GM_\star}{\sqrt{R^2+z^2}}$ the gravitational potential, $\vec{J}$ the electric current density and $\vec{B}$ the magnetic field. To simplify Eq. (30), we assume hydrostatic equilibrium, $\vec{\nabla} p_g - \rho_g \vec{\nabla} \Phi = 0$, and a

4 average distance traveled by a turbulent eddy before its disappearance.

steady-state evolution ($\partial_t = 0$). We project Eq. (30) on the azimuthal direction $\overrightarrow{e_\phi}$, which is the same as considering the equation of angular momentum conservation:

$$\left[\rho_g(\overrightarrow{u}.\overrightarrow{\nabla})\overrightarrow{u} - \overrightarrow{J} \times \overrightarrow{B}\right].\overrightarrow{e_\phi} = 0. \tag{31}$$

In Eq. (31), we have taken into account the advection term $\overrightarrow{F_A} = \rho_g(\overrightarrow{u}.\overrightarrow{\nabla})\overrightarrow{u}$ and the volume Lorentz acceleration term $\overrightarrow{F_B} = \overrightarrow{J} \times \overrightarrow{B}$. Let us consider independently $\overrightarrow{F_A}$ and $\overrightarrow{F_B}$.

- Lorentz acceleration term $\overrightarrow{F_B}$: using the Maxwell-Ampère equation, we can write $\overrightarrow{J} = \dfrac{\overrightarrow{\nabla} \times \overrightarrow{B}}{\mu_0}$. We then have:

$$\begin{aligned}
\overrightarrow{F_B}.\overrightarrow{e_\phi} &= \left[\overrightarrow{J} \times \overrightarrow{B}\right].\overrightarrow{e_\phi}, \\
&= \left[-\frac{\overrightarrow{B} \times (\overrightarrow{\nabla} \times \overrightarrow{B})}{\mu_0}\right].\overrightarrow{e_\phi}, \\
&= \frac{1}{\mu_0}\left(B_z\partial_z B_\phi + B_R\partial_R B_\phi + \frac{B_R B_\phi}{R}\right).
\end{aligned} \tag{32}$$

To simplify Eq. (32), we first make use of the Gauss's law for magnetism, in the axisymmetric case:

$$\begin{aligned}
\overrightarrow{\nabla}.\overrightarrow{B} &= 0, \\
\frac{B_R B_\phi}{R} &= -\left(B_\phi\partial_z B_z + B_\phi\partial_R B_R\right).
\end{aligned} \tag{33}$$

In addition, we use the following relation:

$$\frac{1}{R^2}\partial_R(R^2 B_R B_\phi) = \partial_R(B_R B_\phi) + 2\frac{B_R B_\phi}{R}. \tag{34}$$

We can now combine Eq. (33) and Eq. (34) in Eq. (32):

$$\begin{aligned}\overrightarrow{F_B}.\overrightarrow{e_\phi} &= \frac{1}{\mu_0}\left(\partial_z(B_\phi B_z)+\partial_R(B_\phi B_R)\underbrace{-B_\phi(\partial_R B_R+\partial_z B_z)}_{=\frac{B_R B_\phi}{R}(33)}+\frac{B_R B_\phi}{R}\right),\\ &= \frac{1}{\mu_0}\left(\partial_z(B_\phi B_z)+\partial_R(B_\phi B_R)+\underbrace{2\frac{B_R B_\phi}{R}}_{\frac{1}{R^2}\partial_R(R^2 B_R B_\phi)-\partial_R(B_R B_\phi)(34)}\right),\\ &= \frac{1}{\mu_0}\left(\frac{1}{R^2}\partial_R(R^2 B_R B_\phi)+\partial_z(B_z B_\phi)\right).\end{aligned} \tag{35}$$

- Advection term $\overrightarrow{F_A}$:

$$\begin{aligned}\overrightarrow{F_A}.\overrightarrow{e_\phi} &= \left[\rho_g(\overrightarrow{u}.\overrightarrow{\nabla})\overrightarrow{u}\right].\overrightarrow{e_\phi},\\ &= \rho_g\left(v_z\partial_z v_\phi+v_R\partial_R v_\phi+\frac{v_R v_\phi}{R}\right).\end{aligned} \tag{36}$$

Note that Eq. (32) and Eq. (36) have the exact same structure. Instead of using the Gauss's law for magnetism, we consider the continuity equation in the steady-state case:

$$\begin{aligned}\overrightarrow{\nabla}.(\rho_g\overrightarrow{u}) &= 0,\\ \frac{1}{R}\partial_R(R\rho_g v_R)+\partial_z(\rho_g v_z) &= 0.\\ \frac{\rho_g v_R v_\phi}{R} &= -\left(v_\phi\partial_z(\rho_g v_z)+v_\phi\partial_R(\rho_g v_R)\right).\end{aligned} \tag{37}$$

We then obtain a similar expression for $\overrightarrow{F_A}.\overrightarrow{e_\phi}$:

$$\overrightarrow{F_A}.\overrightarrow{e_\phi} = \frac{1}{R^2}\partial_R(R^2\rho_g v_R v_\phi)+\partial_z(\rho_g v_z v_\phi). \tag{38}$$

Let us now separate $\overrightarrow{v} = (v_R, v_\phi, v_z)^T$ into a mean flow $\overrightarrow{v_K} = (0, R\Omega_K, 0)^T$ and a perturbation $\overrightarrow{u} = (u_R, u_\phi, u_z)^T$. These deviations are small compared to the Keplerian flow $u_R, u_\phi, u_z \ll R\Omega_K$. We can rewrite Eq. (38), using Eq. (37):

$$\overrightarrow{F_A}.\overrightarrow{e_\phi} = \frac{\rho_g u_R}{R}\partial_R(R^2\Omega_K)+\frac{1}{R^2}\partial_R(R^2\rho_g u_R u_\phi)+\partial_z(\rho_g u_z u_\phi)+\rho_g u_z\partial_z(R\Omega_K). \tag{39}$$

Combining Eq. (35) and Eq. (39), and integrating over the whole vertical extension of the disk, the vertically and azimuthally averaged equation of angular momentum conservation reads:

$$\int_{-z_S}^{z_S} \left(\overrightarrow{F_A} - \overrightarrow{F_B}\right).\overrightarrow{e_\phi} dz = 0,$$

$$\frac{\overline{\rho_g u_R}}{R}\partial_R(R^2\Omega_K) + \frac{1}{R^2}\partial_R\left[R^2\left(\overline{\rho_g u_R u_\phi} - \frac{\overline{B_R B_\phi}}{\mu_0}\right)\right] + \left[\rho_g u_z u_\phi - \frac{B_z B_\phi}{\mu_0}\right]_{-z_S}^{z_S} = 0. \quad (40)$$

In Eq. (40), z_S corresponds to the altitude of the disk surface, which is basically the disk scale height. The overlined quantities are vertically and azimuthally averaged. Note that Eq. (40) is identical to Eq. (4.10) in Lesur (2020). The second term on the l.h.s of Eq. (40) is linked to a radial stress that makes the angular momentum transported outward radially. From this term comes the viscous accretion model, with the α-parametrization. As for the third term on the l.h.s of Eq. (40), it is linked to a surface stress that makes the angular momentum evacuated vertically from the disk surface. This evacuation of angular momentum is used in the wind accretion model, where for example a magnetized wind is present. This term is important as it evacuates the angular momentum and it triggers as well a radial laminar transport of mass (Lesur et al., 2014). It is a promising mechanism to explain on the one hand the strong stellar accretion rates, on the other hand the thinness of some dust structures in the dust thermal emission, but also part of the disk dispersal in the latest stages of protoplanetary disks evolution.

2.1.4 *Disk dispersal: from protoplanetary disk to stellar system*

Now that we have covered the first stages of disk formation and relevant models for the gas evolution and transport, we introduce here briefly the late phases of a disk life. In chapter 1, we have seen that the disk emission in the IR is used as a tracer of the presence of circumstellar material close to the central star. This IR excess, almost systematically detected in the youngest clusters ($\lesssim$ 1 Myr), is a lot rarer in older clusters ($\gtrsim$ 5 Myr) (Fedele et al., 2010; Ribas et al., 2015). This measurement is not the only hint that suggests a rapid evolution of the constituent material in protoplanetary disks, after a few million years. If we adopt a statistical point of view, that is if we make the assumption that all the observed disks are screenshots of different periods of their life, relatively few objects show evidence of partial disk-clearing (called transitional disks) (Alexander et al., 2014). Thus, transition between gas-rich objects and disk-less stars is very rapid. Statistical estimates suggest that dispersing the disk takes around ten times shorter that the typical disk lifetime (Koepferl et al., 2013). This implies a strong efficiency of the mechanism(s) that removes gas and dust from protoplanetary disks after a few Myrs. Several phenomena take part in this disk dispersal, with various contribution:

- As we saw earlier, turbulent accretion removes mass mainly from the inner edge of the disk, which is not sufficient to explain the large scale dispersal of

protoplanetary disks, but is essential to realize that there is an evolution of the gas in protoplanetary disks.

- In addition to their strong influence in the laminar transport of mass and evacuation of angular momentum, high-density magnetic winds might play a role in the disk dispersal in the outer parts of disks for low accretion rates disks (Matsuyama et al., 2009). Some models suggest that disk winds could also have an impact closer to the star by (i) helping the gas removal in the inner disk and (ii) generating a large positive slope of the surface density that could reverse the inward drift of dust grains and the inward migration of protoplanets (Suzuki et al., 2016). Besides, depending on the magnetization of the disk, magnetic winds could outperform other wind-launching mechanisms, like photoevaporative winds (Rodenkirch et al., 2020).

- The picture of a gaseous and dusty disk rotating around a central body might well be classical, there is still various systems that do not fit this simple model. The presence of a binary companion can have a strong impact in the early development of circumstellar material. In particular, sub-millimeter thermal continuum emission surveys have shown that the observed luminosity from a pair of stars is much lower when such stars are closer to one another (Harris et al., 2012). Besides, the radiation from massive stars in the neighborhood can also dramatically change the disk evolution. Such radiation can ablate protoplanetary disks and chip away at their constituent material (Scally & Clarke, 2001). However, this mechanism does not occur in all systems, and disk dispersal still arises in protoplanetary disks that are not located in hostile environments. A generic mechanism is thus needed to drive disk dispersal in a general way.

- Note that even though some massive gaseous planets can form in such systems, it corresponds in reality to a small fraction of the initial gas content, typically $\lesssim 1\%$, and therefore not enough to fully explain disk dispersal.

- Finally, photoevaporation is probably the most promising mechanism, along with magnetic winds, to explain disk dispersal. Photons from the central star with high energy (typically X-ray and UV) contribute to increase the temperature of the medium. As it is being heated, the gas acquires a thermal velocity sufficient to reach the escape velocity and to escape the gravity of the star. This mechanism is likely to dominate the final dispersal of the disk gas, from the inner edge to the outer edge of the disk, progressively. This inside-out clearing is also an interesting model to interpret some of the large cavities observed in transitional disks. Note that some models suggest that transitional disks can roughly be separated in two distinct populations: non-accreting low-mass systems whose inner holes are mostly due to photoevaporation, and more massive disks with high accretion rates whose large cavities could be generated by giant planets (see, e.g., Owen, 2016).

For a general review on the dispersal of protoplanetary disks, see Alexander et al. (2014).

2.2 DUST DYNAMICS

2.2.1 *Aerodynamic drag force*

We saw in subsection 2.1.2.1 that an element of gas in the disk usually moves at a slightly sub-Keplerian velocity $v_{\phi,g}$ (Eq. 23), whereas a solid particle (like a dust grain) moves at the Keplerian speed $v_K \gtrsim v_{\phi,g}$ (Eq. 16). This velocity difference $\overrightarrow{\Delta v}$ between gas and dust particles causes an aerodynamic drag acceleration $\overrightarrow{a_d}$ (Eq. 41) acting by the gas on the dust particles. With the law of action and reaction, dust particles also drag the gas (called dust backreaction or feedback), with an aerodynamic drag acceleration $\overrightarrow{a_g}$ (Eq. 42). A classical analogy for the drag force is to say that dust particles feel a headwind (tailwind) due to a slower (faster) gas motion. Thus, particles lose (gain) energy and angular momentum and therefore drift towards the star (outwards) (Eq. 29), with a speed depending on the size s_d of the grains among other things, as will be detailed below.

$$\overrightarrow{a_d} = -\frac{\overrightarrow{\Delta v}}{\tau_{stop}}, \tag{41}$$

$$\overrightarrow{a_g} = \epsilon\frac{\overrightarrow{\Delta v}}{\tau_{stop}}, \tag{42}$$

with $\epsilon = \rho_d/\rho_g$ the dust-to-gas density ratio, and τ_{stop} the stopping time, that is to say the time after which gas and dust follow the same motion. With the drag force, dust particles adjust their velocity as a function of the gas elements, and vice versa. Usually, one considers $\epsilon \ll 1$ since the gas mass volume density is usually much larger than that of the solids. This usually implies $|\overrightarrow{a_g}| \ll |\overrightarrow{a_d}|$. However, we will consider in this section both the impact of the gas onto the dust and the dust backreaction. Let us now consider the expression of τ_{stop}.

Under the assumption that the relative motion between the gas and dust particles is subsonic, $|\overrightarrow{\Delta v}| < c_s$, we can separate two regimes, depending on how the particle size s_d compares with the mean-free path λ of the molecular gas. λ is the average distance traveled by a gas element before interacting with another gas element. It gives a rough idea of the typical distance after which any perturbation in the gas element motion will be passed on to the neighboring gas elements. Its expression is:

$$\lambda = (n_g \sigma_{cs})^{-1}, \tag{43}$$

with $n_g = \rho_g/\mu m_p$ the gas number density and $\sigma_{cs} \sim \pi d^2$ the collisional cross section between gas molecules. d is a typical diameter of gas molecules (around one Angström $\sim 10^{-8}$ cm). For a MMSN disk model, at 1 au, $\lambda \simeq 10$ cm, and is even higher at larger radii for typical density and temperature profiles in the midplane ($\sigma + f > 1$, using Eq. 8 for Σ_g with no exponential cutoff and Eq. 28 for ρ_{mid}). Note that we assume that dust particles are compact spheres, which is consistent with chapter 1 where we already used this assumption to interpret the dust thermal emission observations. The two regimes of gas/dust interactions are:

- **Epstein regime**, $s_d \ll \lambda$: let us consider a dust particle that constitutes an obstacle to the gas motion. Gas molecules that hit this particle will impart the presence of this particle to other molecules via molecular collisions, after having traveled the distance λ. Because λ is much greater than the size s_d of the particle, the information of the presence of the particle in the gas will be communicated far away from the particle. This implies that the ram pressure exerted by molecules upstream is larger than the ram pressure exerted by molecules downstream. This differential ram pressure force leads to an effective drag force between the gas and the dust particle.
- **Stokes** regime, $s_d \gg \lambda$: dust particles larger than the mean-free path instead interact with the gas as a fluid. Any perturbation due to the presence of the particle will be quickly taken into account by molecules surrounding the dust grain. More specifically, a boundary layer appears around the particle. A drag force is then generated through a viscous force due to the gas molecular viscosity.

Given the typical particle sizes and the disks that we consider in this work, we will mainly use the Epstein regime. In this regime, we can express the stopping time as a function of the particle size s_d, its internal density ρ_{int}, the sound speed c_s and the gas density ρ_g:

$$\tau_{stop} = \frac{s\rho_{int}}{c_s \rho_g}. \tag{44}$$

Eq. (44) can be recast in terms of the dimensionless *Stokes number* S_t (Eq. 45):

$$S_t = \tau_{stop}\Omega, \tag{45}$$

with $\Omega = \sqrt{\frac{GM_\star}{R^3}}$ the angular frequency that sets a typical evolution timescale of the particle, called dynamical timescale $\frac{2\pi}{\Omega}$. If $S_t \ll 1$, that is for a short τ_{stop}, the aerodynamic drag acceleration a_d is high enough that gas and dust adjust to one another very quickly (see Eq. 41). We say that dust particles are well coupled to the gas flow. On the contrary, when $S_t \gtrsim 1$, dust grains do not adjust to the gas motion. Particles are decoupled from the gas flow ($a_d \simeq 0$).

To simplify the notations, we will use $D = \frac{1+\epsilon}{\tau_{stop}} = D_g + D_d$, with $D_g = 1/\tau_{stop}$ the typical frequency at which the dust adjusts to the gas, and $D_d = \epsilon D_g$. See Nakagawa et al. (1986) for more details. Note that with this notation, we can write:

$$D = (1+\epsilon)D_g. \tag{46}$$

2.2.2 *Radial drift*

We can write the equations of motion of a two-phase flow composed of dust particles and the gas:

$$\left(\frac{\partial}{\partial t} + \overrightarrow{u_d}.\overrightarrow{\nabla}\right)\overrightarrow{u_d} = -\overrightarrow{\nabla}\Phi + \overrightarrow{a_d}, \tag{47}$$

$$\left(\frac{\partial}{\partial t}+\vec{u_g}.\vec{\nabla}\right)\vec{u_g}=-\frac{\vec{\nabla}p_g}{\rho_g}-\vec{\nabla}\Phi+\vec{a_g}, \tag{48}$$

with $\vec{u_d}$ and $\vec{u_g}$ the velocities of the dust and the gas respectively, in the inertial frame of reference. Φ is the gravitational potential as defined in Section 2.1.3, such that $\vec{\nabla}\Phi \simeq \Omega_K^2(R\vec{e_R}+z\vec{e_z})$. We neglect here the terms of self-gravity, for both the gas and the dust, and use the thin disk approximation $z/R \ll 1$. For small particles, the motion of the two-phase fluid becomes steady within a timescale $1/D$, as we have seen earlier. We can thus consider steady-state equations ($\partial_t = 0$), and rewrite Eq. (47) and Eq. (48) as:

$$\left(\vec{u_d}.\vec{\nabla}\right)\vec{u_d}=-\Omega_K^2(R\vec{e_R}+z\vec{e_z})-D_g\vec{\Delta v}, \tag{49}$$

$$\left(\vec{u_g}.\vec{\nabla}\right)\vec{u_g}=-\Omega_K^2(R\vec{e_R}+z\vec{e_z})-\frac{\vec{\nabla}p_g}{\rho_g}+D_d\vec{\Delta v}, \tag{50}$$

with $\vec{\Delta v}=\vec{u_d}-\vec{u_g}$ the velocity difference between dust and gas. We first focus on the projection of Eq. (49) and Eq. (50) onto the radial and azimuthal directions. Moreover, because gas and dust move azimuthally at a velocity close to the Keplerian speed v_K, we can define the deviations from the Keplerian speed: $\vec{v_d}=\vec{u_d}-\vec{v_K}$ and $\vec{v_g}=\vec{u_g}-\vec{v_K}$, with $\vec{v_K}=(0,R\Omega_K,0)^T$. These deviations are small compared to the Keplerian speed $|\vec{v_d}| \ll |\vec{v_K}|$ and $|\vec{v_g}| \ll |\vec{v_K}|$. We suppose axisymmetry ($\partial_\phi = 0$), and we leave only the first-order terms in $|\vec{v_d}|$ and $|\vec{v_g}|$:

$$\frac{u_{d,\phi}^2}{R}-\frac{v_K^2}{R}-D_g(u_{d,R}-u_{g,R})=0, \tag{51}$$

$$-u_{d,R}\partial_R(v_K)-\frac{u_{d,R}u_{d,\phi}}{R}-D_g(u_{d,\phi}-u_{g,\phi})=0, \tag{52}$$

$$\frac{u_{g,\phi}^2}{R}-\frac{v_K^2}{R}+D_d(u_{d,R}-u_{g,R})+2\Omega_K v_K\bar{\eta}=0, \tag{53}$$

$$-u_{g,R}\partial_R(v_K)-\frac{u_{g,R}u_{g,\phi}}{R}+D_d(u_{d,\phi}-u_{g,\phi})=0, \tag{54}$$

where $\bar{\eta}=-\frac{h_g^2\eta}{2}=-\frac{1}{2}h_g^2\frac{\partial \log p_g}{\partial \log R}$ is linked to the local gas pressure gradient. Now, we use two relations for the gas and the dust:

$$\frac{u_\phi^2}{R}-\frac{v_K^2}{R}=2\Omega_K v_\phi+\mathcal{O}(\frac{v_\phi^2}{R}), \tag{55}$$

$$-u_R\partial_R(v_K)-\frac{u_R u_\phi}{R}=-\frac{\Omega_K v_R}{2}+\mathcal{O}(\frac{v_R v_\phi}{R}). \tag{56}$$

We can rewrite Eq. (51), (52), (53) and (54) as:

$$2\Omega_K v_{d,\phi}-D_g(v_{d,R}-v_{g,R})=0, \tag{57}$$

$$-\frac{\Omega_K v_{d,R}}{2} - D_g(v_{d,\phi} - v_{g,\phi}) = 0, \tag{58}$$

$$2\Omega_K v_{g,\phi} + D_d(v_{d,R} - v_{g,R}) + 2\Omega_K v_K \bar{\eta} = 0, \tag{59}$$

$$-\frac{\Omega_K v_{g,R}}{2} + D_d(v_{d,\phi} - v_{g,\phi}) = 0. \tag{60}$$

This system of four equations with four unknowns finally gives:

$$\begin{aligned}
v_{d,R} &= -\frac{1}{1+\epsilon}\frac{2D\Omega_K}{\Omega_K^2 + D^2} v_K \bar{\eta}, \\
v_{d,\phi} &= -\frac{1}{1+\epsilon}\frac{D^2}{\Omega_K^2 + D^2} v_K \bar{\eta}, \\
v_{g,R} &= \frac{\epsilon}{1+\epsilon}\frac{2D\Omega_K}{\Omega_K^2 + D^2} v_K \bar{\eta}, \\
v_{g,\phi} &= \left(\frac{\epsilon}{1+\epsilon}\frac{D^2}{\Omega_K^2 + D^2} - 1\right) v_K \bar{\eta},
\end{aligned} \tag{61}$$

which correspond to Eqs. (2.11) to (2.14) in Nakagawa et al. (1986). At first order in ϵ and Ω_K/D, supposing $\epsilon \ll 1$ (gas-dominant phase) and $\Omega_K/D \ll 1$ (particles rapidly adjusting to gas motion), the radial and azimuthal velocities become:

$$\begin{aligned}
v_{g,R} &\simeq 0, \\
v_{g,\phi} &\simeq -v_K \bar{\eta}, \\
v_{d,R} &\simeq -2\frac{\Omega_K}{D} v_K \bar{\eta}, \\
v_{d,\phi} &\simeq -v_K \bar{\eta}.
\end{aligned} \tag{62}$$

We find here at first order that particles are dragged by the gas at the same sub-Keplerian speed $u_\phi = v_K(1 - \bar{\eta})$, in accordance with Eq. (23), and that this gas drag generates a radial drift of the dust particles at a velocity close to $-2\frac{\Omega_K}{D} v_K \bar{\eta}$. For typical profiles of gas pressure, $\bar{\eta} > 0$ (monotonously decreasing pressure profile), thus particles drift towards the star as $v_{d,R} < 0$.

Two important points should be noticed here. First, we can write a more general expression for the radial drift of particles as a function of ϵ and the Stokes number S_t, from Eq. (61):

$$v_{d,R} = \frac{1}{S_t + \frac{(1+\epsilon)^2}{S_t}} v_K h_g^2 \frac{\partial \log p_g}{\partial \log R}, \tag{63}$$

which shows that the radial drift is maximum when $S_t = 1 + \epsilon \simeq 1$ in a gas-dominant fluid. For a MMSN disk model, this corresponds to particles a few meters in size. For a less dense model, the maximal radial drift is reached for centimeter-sized particles. Such particles are expected to rapidly drift towards the star; this is known as the radial drift barrier, and has to be overcome by dust grains in order to reach the size

of planetesimals (~km) (see Section 2.2.4). Secondly, from Eq. (63), we can notice that $v_{d,R} \propto \frac{\partial \log p_g}{\partial \log R}$, which highlights the absence of dust's radial drift at pressure maxima, that is when $\overline{\eta} = 0$. In this case, particles no longer feel the 'headwind' from the gas. This trapping of dust particles at pressure maxima is largely used to explain the accumulation of particles in optically thin regions in recent disks observations, in particular the disks with bright and dark rings (see chapter 4 and Andrews et al., 2018; Huang et al., 2018a). Interestingly, the presence of a massive planet could trigger a local pressure maximum (see chapter 3) which traps dust particles, and the resulting over-densities of dust could be a signature of a planet caught in formation. Note finally that when the dust-to-gas density ratio ϵ increases, $v_{d,R}$ decreases, which means that dust grains drift less quickly in a dustier environment. For high values of ϵ, the gas starts to strongly feel the dust feedback and tends to drift outwards. If ϵ is high enough, the gas adjusts to the dust azimuthal velocity $v_{d,\phi} \simeq v_{g,\phi} \simeq -\frac{v_K \overline{\eta}}{\epsilon} > 0$.

In this section, we have chosen to study the interaction between a gas fluid and a single dust fluid, but the calculations can be generalized to several dust fluids coupled to the gas. In practice, the expressions of $\overrightarrow{a_d}$ and $\overrightarrow{a_g}$ presented in Eq. (41) and Eq. (42) are modified: the aerodynamical drag acceleration acting by the gas onto each dust fluid i is now $\overrightarrow{a_d^{multi}} = -\frac{\overrightarrow{\Delta v_i}}{\tau_{stop,i}}$, and the aerodynamical drag acceleration acting by the dust species onto the gas in now $\overrightarrow{a_g^{multi}} = \sum_i \epsilon_i \frac{\overrightarrow{\Delta v_i}}{\tau_{stop,i}}$. ϵ_i is the dust-to-gas density ratio of the dust fluid i, with velocity $\overrightarrow{u_{d,i}} = \overrightarrow{u_g} + \overrightarrow{\Delta v_i}$ and a stopping time $\tau_{stop,i}$. Dipierro et al. (2018) use these expressions to derive new steady-state solutions for the radial and azimuthal velocities of a viscously evolving gas fluid and the populations of dust particles. In particular, they found that the backreaction of multiple dust species onto the gas decreases the amplitude of the gas radial velocity compared to the single dust fluid case. They also found that dust feedback leads to an outward gas drift in the outer regions of protoplanetary disks at low viscosity ($\alpha = 10^{-3}$) due to a strong dust settling, even at low dust-to-gas density ratio. Another important result indicates that the inward drift of particles can be slowed down in the inner disk, and even directed outward at high dust-to-gas density ratio in intermediate regions of protoplanetary disks. In a more general way, dust backreaction is found to slow down the radial drift of dust grains, which increases the lifetime of such grains in protoplanetary disks. This challenges the typical picture of large grains quickly drifting and disappearing towards the star. For more details on multiple dust fluids and their backreaction onto the gas, see Dipierro et al. (2018); Benítez-Llambay et al. (2019).

To know more about dust dynamics and the dust/gas interaction, see for example Birnstiel et al. (2016).

2.2.3 *Vertical settling*

In the previous section, we focused on the azimuthal and radial motions of dust particles, and emphasized their radial drift due to the aerodynamic drag with the gas. We focus here on the vertical motion of a dust particle suspended in the disk, by

considering this time the projection at first order in $|\overrightarrow{v_d}|$ of Eq. (49) onto the vertical axis $\overrightarrow{e_z}$. We keep the time-dependence ($\partial_t \neq 0$), write $\dot{z} = v_{d,z}$ and suppose that the vertical component of the gas velocity is negligible compared to the dust's vertical velocity, $v_{g,z} \ll v_{d,z}$. Said differently, the motion of dust particles does not affect the hydrostatic equilibrium in the vertical direction (Nakagawa et al., 1986). Further assuming $z \ll R$, and that Ω_K is thus independent of z, we find:

$$\ddot{z} + \frac{\Omega_K}{S_t}\dot{z} + \Omega_K^2 z = 0. \tag{64}$$

Depending on the Stokes number, there are two possibilities concerning the vertical evolution of the dust.

- If $S_t > 1/2$, that is for larger particles, the particles' altitude $z(t)$ reads:

$$z(t) = z_0 \exp\left(-\frac{\Omega_K t}{2S_t}\right) \exp\left(\pm i\Omega_K t\sqrt{1 - \frac{1}{4S_t^2}}\right). \tag{65}$$

  This solution is made of an oscillating term and an exponential damping. From an altitude z_0, particles will oscillate around the disk midplane until they settle down at $z = 0$, in the case without turbulent diffusivity. We talk about dust's vertical settling. This phenomenon depends on the radial location in the disk and on the Stokes number S_t, which is linked to the particle size s_d for a given disk model. For a given particle size, the accumulation in the midplane is more efficient closer to the star because the stopping time is shorter, hence the settling time is shorter as well. Similarly, at a given radial location, particles drift quickly towards the midplane when S_t is low enough, but still superior to 1/2. When $S_t \to \infty$, the damping term has no influence and particles are only oscillating around the midplane, with a frequency equal to the Keplerian frequency Ω_K.

- For $S_t \ll 1$, particles quickly adjust to the gas and can thus easily reach an equilibrium settling velocity. Under this assumption, we use $\ddot{z} = 0$ in Eq. (64), and the solution is now:

$$z(t) = z_0 \exp\left(-\Omega_K S_t t\right). \tag{66}$$

  Like the other case, the settling is here less efficient further away from the star. For small particles, the vertical position evolves slowly as a function of time. On the contrary, for larger particles with still $S_t < 1/2$, the dust efficiently settles down in the midplane, as the characteristic settling timescale in this case is $\sim (S_t\Omega_K)^{-1}$.

Combining these two cases, the typical timescale τ_{sett} over which dust settling occurs is $\sim \Omega_K^{-1} \times (S_t + S_t^{-1})$, which is minimum for a Stokes number of unity. As stated earlier, turbulent viscosity changes the settling behavior of particles by counteracting the accumulation of particles towards the midplane. Although the exact nature and level of turbulence in protoplanetary disks is not well constrained, we assume it acts like a diffusive process. This is known as vertical stirring, and has a typical

timescale τ_{stir} of z^2/ν_d, with ν_d a turbulent diffusion coefficient for dust particles in the vertical direction. ν_d is related to the turbulent viscosity ν defined in Section 1.2.5 as $\nu_d = \nu/(1 + S_t^2)$. Note that $\nu_d < \nu$, that is to say the diffusion of particles is always weaker than the diffusion of gas elements. More specifically, smaller particles (i.e. for smaller S_t) will be more affected by diffusion than larger particles for which inertia restrains more easily their turbulent motion. Equating τ_{sett} and τ_{stir} sets a typical dust's vertical scale height:

$$H_d \sim H_g \sqrt{\frac{\alpha}{S_t}}, \tag{67}$$

where we clearly see the competition between turbulence (α-parameter) and settling (Stokes number). By developing Eq. (39) of Dubrulle et al. (1995), one can find a slightly more appropriate expression for H_d:

$$H_d \sim H_g \sqrt{\frac{\alpha}{\alpha + S_t}}, \tag{68}$$

which is the same as Eq. (67) for large particles $S_t/\alpha \gg 1$ but gives $H_d = H_g$ for small particles well-coupled to the gas ($S_t/\alpha \ll 1$). We stress here that any vertical dependence of S_t is discarded. See Dubrulle et al. (1995); Youdin & Lithwick (2007) for more rigorous calculations of vertical settling and stirring.

2.2.4 *Dust growth*

In the models and simulations presented in this work, we do not include any change in the size of dust particles, as we use a stationary size distribution. In particular, dust growth is not taken into account. In reality, interactions between dust particles make their size change. Taking into account particles collisions is necessary to apprehend, for example, the size distribution that we choose in our models.

We have seen that various velocities intervene in the dust evolution, in particular due to the gas drag. Besides, because these velocities depend on the particle size through the Stokes number (see Eqs. 61 and 64), collisions between particles of different sizes should happen. Numerical and experimental studies aim to determine the outcome of particles collisions, as a function of their relative velocity (Blum, 2018). More specifically, numerical simulations are used to model the collision between two dust aggregates that are composed of a number of small compact monomers about a micron in size (see, e.g., Seizinger et al., 2013). Regarding laboratory experiments, collisions between silicate grains are performed under micro-gravity in order to recreate conditions close to those of the interstellar medium.

In Fig. 2.2.1, Blum (2018) display the typical relative velocity (dashed curves) for solid particles in a MMSN disk model (see Section 1.2.5), at 3 au, assuming a turbulent viscosity $\alpha = 10^{-3}$. The typical collision outcomes are represented in color. The green color means that dust growth occurs, orange corresponds to particle sizes that decrease after the interaction, and the red color is for particles that fragmented or got destroyed after the collision. The dominance of orange and red for particles with size superior to 1 cm means that the formation of aggregates is precluded at high relative velocity. This is called the centimeter barrier. Note that the radial drift is also

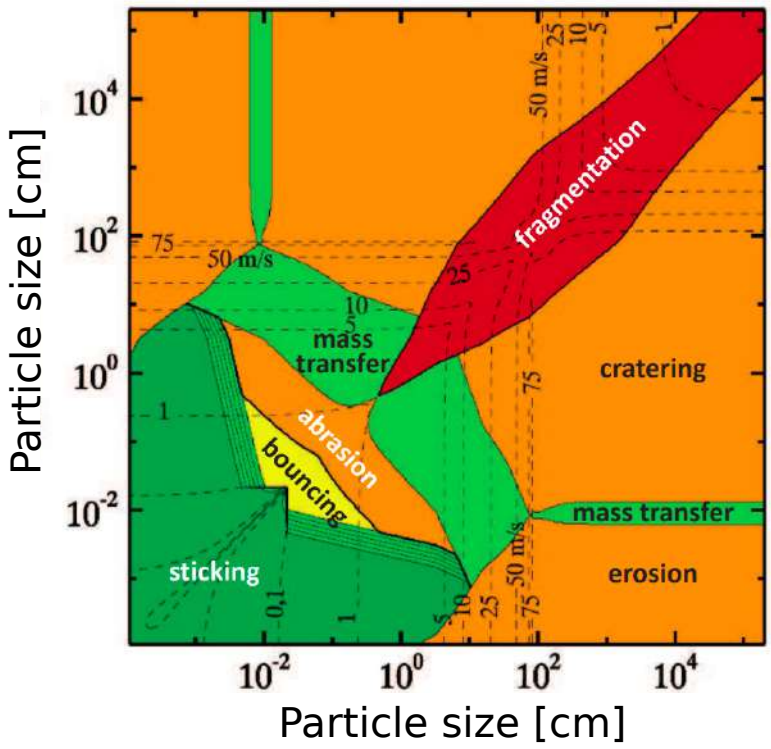

Figure 2.2.1: Predictions of a collision model from micro-gravity experiments, with a MMSN model at 1 au in the midplane and a turbulent α parameter of 10^{-3}. The dashed lines correspond to isovelocity contour in $\mathrm{m.s^{-1}}$, and the collisional outcomes are shown in color (see description in the text). Figure extracted from Blum (2018).

very efficient for centimeter-sized particles, as we have seen in Section 2.2.2, which makes the formation of large pebbles even or equally harder. Note that Fig. 2.2.1 was obtained by extrapolating the results of micro-gravity laboratory experiments, which in reality focus on a small range of target sizes, projectile sizes and relative velocities.

We sum up here more specifically the possible outcomes of the collision between two particles.

- **Sticking**: so long as both particles have a size smaller than about a centimeter, they collide into a more massive dust aggregate. For a small relative velocity (~ 0.1 $\mathrm{m.s^{-1}}$), the aggregate has a fluffy morphology. On the contrary, a slightly higher relative velocity leads to a more compact aggregate.
- **Bouncing**: if the relative velocity is close to 1 $\mathrm{m.s^{-1}}$, dust growth does not occur and particles carom with no change in size.
- **Abrasion**: centimeter-sized particles are subjected to gradual mass loss, with a relatively weak efficiency. Around 1000 collisions are necessary in order to completely destroy the aggregates.
- **Fragmentation**: two particles similar in size that collide at high speeds ($\gtrsim 10$ $\mathrm{m.s^{-1}}$) tend to be completely shattered. This phenomenon prevents dust growth from occurring.

- **Mass transfer**: at quite high velocity, for particles that are different in size (typically a millimeter-sized projectile onto a meter-sized target and beyond), the projectile is destroyed during the collision but transfers part of its mass to the target. This is a possible way to bypass the centimeter barrier, even if the range of sizes for which mass transfer occurs is particularly narrow (see the light green band in Fig. 2.2.1).

- **Cratering**: for larger projectiles, but still outside the fragmentation regime, a phenomenon similar to mass transfer occurs. However, instead of bringing part of its mass to the target, the colliding projectile extracts some mass from the target, thereby stopping dust growth.

- **Erosion**: for projectiles smaller than mass transfer projectiles, experiments and simulations have shown that the target is once again subjected to mass loss.

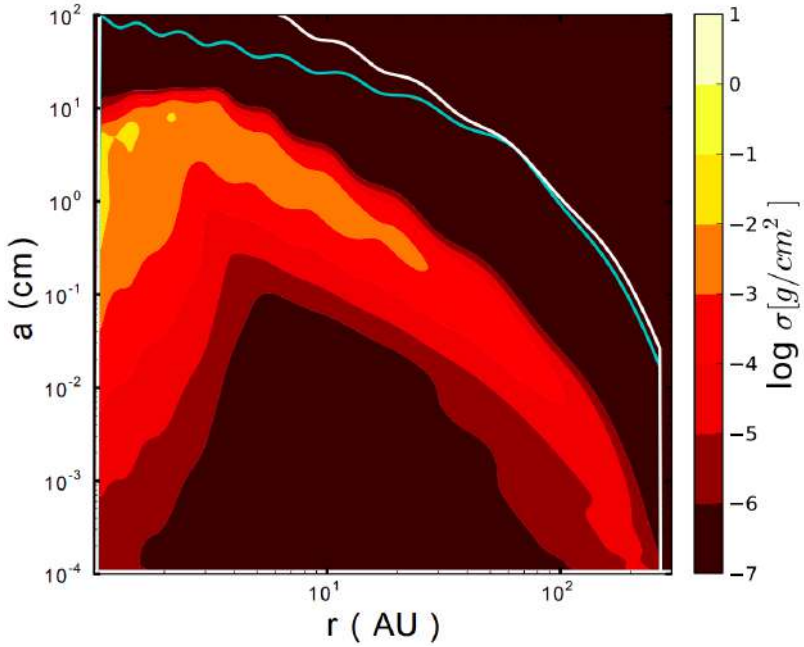

Figure 2.2.2: Vertically integrated dust density distribution after 1 Myr of evolution, as a function of the distance to the star, for a given disk model (see (Pinilla et al., 2012)). The solid white line shows the particle size corresponding to a Stokes number of unity. The blue line represents the fragmentation barrier beyond which particles are shattered.

Along with laboratory experiments, simulations of dust growth are useful tools to constrain the dust size distribution. In particular, the 1D models presented for example in (Pinilla et al., 2012) aim to resolve the so-called Smoluchowski coagulation equation in order to determine the time evolution of the number density of particles as they collide. Fig. 2.2.2 shows the vertically integrated dust density distribution in a protoplanetary disk for a given gas surface density profile, after 1 Myr of evolution,

taking into account coagulation, radial turbulent mixing[5], radial drift, or fragmentation. Note in particular for their disk model the blue line which represents the maximum size of the particles before they reach fragmentation velocities. Beyond this fragmentation barrier (set here to 10 $m.s^{-1}$), particles fragment into smaller grains.

The maximum grain size given by fragmentation can be estimated by the following relation in Pinilla et al. (2012):

$$s_{max} \simeq \frac{4\Sigma_g}{3\pi\alpha\rho_{int}} \left(\frac{v_f}{c_s}\right)^2. \tag{69}$$

For a protoplanetary disk large of a few tens of au, with power-laws to describe its gas surface density Σ_g (Eq. 8) and its aspect ratio (Eq. 21) such that $\Sigma_0 \simeq 89 g.cm^{-2}$ at 1 au, $\sigma = 1$, $h_0 = 0.05$ at 1 au, $f = 0.15$, and further assuming a dust's internal density of $\rho_{int} = 2$ $g.cm^{-3}$, a turbulent parameter $\alpha = 10^{-3}$ and a fragmentation threshold velocity $v_f = 10$ $m.s^{-1}$, the maximum value of the grain size $s_{d,max}$ is a few centimeters. This estimation of $s_{d,max}$ is used to set the maximum size of the dust particles in the hydrodynamical simulations and/or radiative transfer calculations presented in chapters 6 and 7.

2.2.5 *Dust properties*

We continue to describe in this section some important properties of dust particles, like their size distribution and their composition. Disk models usually assume a power-law **dust size distribution** scaling as $s_d^{-3.5}$ (Mathis et al., 1977). However, such distribution was obtained for the interstellar medium (ISM), and there is no obvious reason why the size distribution in the ISM should be the same as in protoplanetary disks. We choose the value of the **maximum particles size** ($s_{d,max}$) to suit the results of 1D models of dust growth, drift and fragmentation in planet-less disks having similar physical properties as the background disk in our simulations (Birnstiel et al., 2012, see also previous subsection). The **minimum particles size** ($s_{d,min}$) is chosen such that the associated Stokes number, for a given disk model, is small enough that even smaller particles would be particularly well-coupled with the gas and thus follow its dynamics. For example, 10 µm-sized particles with a typical disk model presented in chapter 6 have $S_t \lesssim 10^{-6}$. Moreover, sub-µm grains are expected to grow efficiently in particular in the midplane (Laibe et al., 2008; Gonzalez et al., 2017), which ensures a deficit in such small particles. The **dust-to-gas density ratio** is chosen such that the medium is gas-dominant ($\epsilon \ll 1$). We also have to be aware that dust particles feel a **turbulent motion** imparted by the gas, which depends mainly on the gas turbulent viscosity ν defined in Section 1.2.5 and Section 2.1.2.3. Additionally, we will see in the following paragraph that classical models suppose **spherical compact particles** with an **internal mass volume density** of a few g cm^{-3}, and a **mixed composition** (like silicates, amorphous carbons, or water ices). In particular, in this PhD thesis, we will mainly assume a dust mixture comprised of astrosilicates and water ices, with a mean internal density of ~2 g cm^{-3} or less.

5 equivalent of the vertical stirring in the radial direction, which tends to counteract any dust accumulation.

An important caveat of the dust modelling is related to the shape of dust grains. Whether it be numerical simulations or radiative transfer calculations, we assume that particles are compact spheres. Relaxing this assumption makes the radiative transfer calculations more complicated to interpret[6], and could lead to huge discrepancies in the results. Particles are actually expected to take the form of fractal fluffy aggregates, which we can model as chains of spherical monomers. In particular, the fact that dust particles consist of porous irregular aggregates has been revealed by cometary dust observations with the Rosetta mission. About half of the particles observed in the coma of comet 67P/TG have quite low densities, typically less than 0.1 g cm^{-3} (Bentley et al., 2016; Langevin et al., 2016). When it comes to numerical simulations, such assumption on the particles shape has a strong influence in the dust dynamics. In particular, the aerodynamic gas drag onto a compact sphere has no reason to imprint the same behavior as the aerodynamic gas drag onto a fluffy aggregate. A possible model that would allow a slightly more realistic approach would be to increase the porosity of spherical particles by decreasing their internal density. Said differently, this model would not consider compact spheres but porous spheres. This kind of model is however unable to account for the asymmetry of the particle, as well as its fractality.

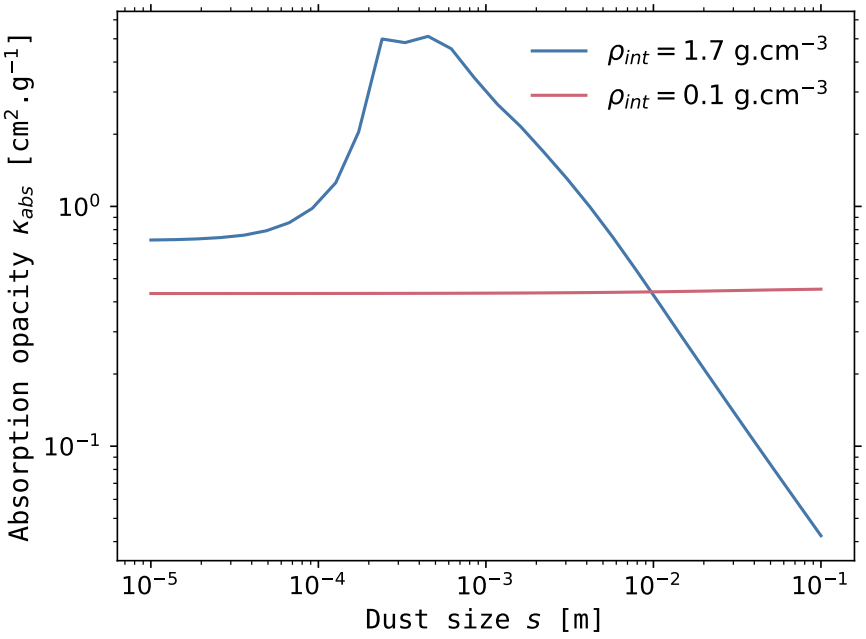

Figure 2.2.3: Absorption mass opacity at $\lambda = 1.3$ mm as a function of the particle size, for a dust mixture of 60% astrosilicates and 40% water ices. The blue line illustrates the most compact case, whereas the red line takes into account a volume filling factor smaller than 1 (porous case).

The dust velocity and the gas-dust interaction are not the only things that are modified by considering non-spherical and non-compact particles. When carrying out radiative transfer computations, the "compact sphere" assumption allows to use Mie

6 because Mie theory does not apply anymore.

theory, which largely simplifies the calculations of the interaction between photons and dust grains. In particular, optical properties of fluffy dust aggregates like the opacities are deeply changed, because their effective cross section of interaction with gas or radiation can be quite different from the surface area of a sphere. In particular, Fig. 2.2.3 shows the evolution of the absorption opacity as a function of the size of spherical particles, at $\lambda_{obs} = 1.3$ mm, for a dust mixture comprised of 60% astrosilicates and 40% water ices. To compute the dust opacities, we use the public code presented in Bohren & Huffman (1983), which is based on Mie theory. To do so we need to specify a dust composition as well as a vacuum inclusion when porosity is taken into account. We then apply the Bruggeman rules to obtain the optical constants of the mixture. The optical constants of water ices are obtained from the Jena database, those of astrosilicates are from Draine & Lee (1984). The code from Bohren & Huffman (1983) then derives the absorption and scattering opacities for anisotropic scattering, as well as the mean scattering angle (see Baruteau et al., 2019, for more details about the methodology, and section 5.2.1 to know how these opacity calculations are used to carry out dust radiative transfer calculations). The blue line in Fig. 2.2.3 represents the absorption opacity of compact spheres ($\rho_{int} = 1.7$ g.cm^{-3}), whereas the red line shows how the absorption opacity is modified in the case of porous spheres ($\rho_{int} = 0.1$ g.cm^{-3}). The presence of a peak at size $s_d \sim \lambda/\pi$ in the compact case suggests that the flux of continuum emission is expected to peak at a certain size for a given wavelength (as presented in Section 1.1). In particular, this phenomenon is commonly used to argue that the millimeter dust thermal emission is mostly sensitive to millimeter particles. Because this peak is not present in the porous case, one should be aware that dust continuum observations can actually be harder to interpret, as a large range of particle sizes contributes equally to the absorption opacity (see also Kataoka et al., 2014).

2.3 SELECTED MAGNETO-HYDRODYNAMICAL INSTABILITIES

Under the assumption that protoplanetary disks evolution is the result of a turbulent transport of angular momentum, many studies have tried to explain the origin of turbulence with hydrodynamical or MHD instabilities. There is a wide range of instabilities that can take place in protoplanetary disks, but few of them can generate a sufficient level of turbulence to explain the observed stellar accretion rates. Let us dwell a little bit on some important instabilities predicted by theoretical models. The aim here is not to present an extensive review on instabilities, but rather to give the reader some introductory remarks on the relevance of some instabilities that emerge in our simulations. The principle behind magneto-hydrodynamical instabilities is actually most often the same: a tiny perturbation in the fluid quantities grows exponentially (*linear growth stage*) until it saturates (because of a finite energy reservoir) and reaches a maximum amplitude (*saturation stage*). It is the dissipation of energy and / or angular momentum associated to the fluid perturbations in the saturated stage which is suspected to be the origin of turbulent transport.

2.3.1 *Magneto-Rotational Instability*

The Magneto-Rotational Instability (MRI) can occur in protoplanetary disks that possess a weak magnetic field. Any perturbation in the position of a fluid element is amplified as the magnetic tension force tries to oppose the perturbation. Let us consider a Keplerian disk for which gas is dynamically coupled to a weak toroidal magnetic field. For this topology, the magnetic field lines are directed along the azimuthal direction. If the perturbation makes a fluid element move inward (R decreases), the gas element will move faster due to the Keplerian speed $\propto R^{-1/2}$. Said differently, not only the fluid element is closer to the star, but it has also an increased position angle ϕ_{pert} compared to its initial azimuthal position ϕ_0: $\overrightarrow{\Delta\phi} = (\phi_{pert} - \phi_0)\overrightarrow{e_\phi} > \overrightarrow{0}$. Thus, the magnetic field line attached to the fluid element is elongated and exerts a restoring force whose aim is to bring the element back to its initial radial and azimuthal position. Because the direction of the restoring force F_ϕ opposes the initial perturbation, $F_\phi < 0$ and the corresponding torque $R\overrightarrow{e_R} \times (-|F_\phi|\overrightarrow{e_\phi})$ is negative. The gas elements then loses angular momentum, which makes it move further in. In order for the instability to operate, the magnetic field needs to be weak, for a stronger field would generate stable oscillations of fluid elements around their initial position. As we have tried to point out with our illustrative example, differential rotation does play a key role in setting in the MRI (Balbus & Hawley, 1991).

Recent numerical simulations have shown that MRI is actually not as efficient as expected in the whole protoplanetary disk (Bai & Stone, 2013). Non-ideal MHD effects, namely Ohmic resistivity, Hall effect, and ambipolar diffusion, can quell the MRI in specific regions of weakly ionized disks. In particular, Ohmic resistivity dominates in the midplane (dense region with weak magnetic field) whereas ambipolar diffusion dominates in the superficial layers and the outermost parts of protoplanetary disks. The former restrains the growth of MRI modes in the inner region (about 0.5 to 5 au in the midplane) and is behind the notion of "dead zone". The latter is found to suppress MRI activity in the disk surface layers. Due to these non-ideal MHD effects, the disk accretion rates obtained in such simulations are extremely low compared to observations (by two to three orders of magnitude). We remind here that these non-ideal MHD effects take part in the development of MHD winds that cause laminar transport of mass and angular momentum. Note that below ~ 0.5 au, the disk ionization through thermal collisions should be sufficient for the MRI to develop, leading to a high turbulent stellar accretion rate, comparable to observations (see, e.g., Bai, 2013; Simon et al., 2013; Lesur et al., 2014).

2.3.2 *Gravitational Instability*

The Gravitational Instability (GI) can occur in the outer parts of young, still massive protoplanetary disks as a result of the competition between gas self-gravity, differential rotation and pressure support. Gas self-gravity tends to collapse the gas, whereas differential rotation and pressure support tend to oppose the collapse. This instability may occur during the first stages of the disk evolution (when the disk is still massive) and, depending on the disk's cooling timescale, may create clumps that fragment the

disk. In order to be a little more quantitative, let us present the dispersion relation, in 2D, associated to the linearized governing equations. For this we need:

- The radial and azimuthal projections of the Navier-Stokes equation with self-gravity.
- The continuity equation.
- The Poisson equation

It is possible to obtain an asymptotic solution to the Poisson equation (see, e.g., the appendix of Lin & Shu, 1964) in order to link the self-gravitating potential in the disk midplane Φ_D and the surface density Σ_g:

$$\Phi_D = -\frac{2\pi G\Sigma_g}{|k|}, \tag{70}$$

with k the radial component of the wave vector. By assuming that all perturbations can be described as plane waves ($\propto \exp[i(\omega t - kR)]$, ω being the wave frequency), we can write the dispersion relation:

$$\omega^2 = \Omega^2 - 2\pi G\Sigma_g|k| + k^2c_s^2, \tag{71}$$

where we see that Ω^2 (term linked to differential rotation) and $k^2c_s^2$ (linked to the pressure gradient through the ideal gas law) are stabilizing terms (they are positive), whereas the second term (linked to self-gravity) is negative, thus destabilizing. For a sufficiently high gas surface density, self-gravity is dominant and the gravitational instability can develop. This can also be seen through the Toomre parameter Q:

$$Q = \frac{c_s\Omega}{\pi G\Sigma_g}, \tag{72}$$

where we clearly see the competition between pressure, differential rotation (numerator term) and self-gravity (denominator term). If at least one value of ω^2 is negative, perturbations of the fluid quantities will be amplified (because ω contains a complex term which will make the exponential $\exp(i\omega t)$ diverge) and the GI will develop. Because the minimum value of ω^2 is negative if $Q < 1$, comparing the Toomre parameter to unity is a first good guess to assess if self-gravity must be included in models or not. We will talk a little bit more about the GI in a planet formation context (section 3.2).

Note that we can describe the angular momentum transport due to GI-induced turbulence with an effective α: we talk about gravito-turbulent disks. Though self-gravity can lead to an effective transport of mass inward (and angular momentum outward), it is not expected to last long enough to explain the high stellar accretion rates commonly observed. If the disk fragments into gas clumps, the conditions for which GI occurs are indeed not satisfied anymore (Klahr et al., 2018), in particular due to a decreased Σ_g.

Non-linear evolution of the GI: the disk's cooling timescale determines the non-linear outcome of GI (Gammie, 2001). Is the gas able to efficiently radiate away the heating provided by its gravitational collapse? The answer will determine whether or not the

pressure support is able to withstand self-gravity. In particular, if the cooling timescale τ_{cool} is shorter than a few dynamical timescales $1/\Omega$, typically $\tau_{cool}\Omega \lesssim 3-5$, the thermal pressure is not sufficient to resist the gravitational instability. In this case, the disk fragments and breaks up into bound clumps. This phenomenon is behind one of the two main models to generate giant planets (see section 3.2). On the contrary, if $\tau_{cool}\Omega \gtrsim 3-5$, that is if the gas is able to retain the internal energy it gained during the phase of collapse, the system reaches a quasi steady-state. In that case, the disk creates large spiral density waves at the origin of a gravito-turbulent mass accretion.

2.3.3 *Vertical Shear Instability*

The Vertical Shear Instability (VSI) is similar to another well-known instability thought to occur in stars: the Goldreich-Schubert-Fricke Instability (GSF) (Goldreich & Schubert, 1967; Fricke, 1968). The VSI is expected to develop if the disk's angular frequency Ω has a vertical dependence (Urpin & Brandenburg, 1998; Urpin, 2003; Arlt & Urpin, 2004; Nelson et al., 2013; Lyra & Umurhan, 2019). According to studies about the VSI, the resulting unstable modes are expected to be vertically elongated. We can write the radial and vertical projections of the Navier-Stokes equation in cylindrical coordinates:

$$R\Omega^2 - R\Omega_K^2 - \frac{1}{\rho_g}\frac{\partial p_g}{\partial R} = 0, \tag{73}$$

$$-z\Omega_K^2 - \frac{1}{\rho_g}\frac{\partial p_g}{\partial z} = 0. \tag{74}$$

From Eq. (74), it is possible to derive the expression for $\rho_g(R,z)$ (with a methodology similar to the calculations in Section 2.1.2.2). As for Eq. (73), we can obtain the expression of Ω, supposing that the midplane gas density ρ_{mid} and the gas temperature T_g are power-laws of the stellar distance R, with power-law exponents of p and $-\beta$ respectively:

$$\Omega(R,z) = \Omega_K(R)\left((p-\beta)h_g^2 + (1-\beta) + \frac{\beta R}{\sqrt{R^2+z^2}}\right)^{1/2}. \tag{75}$$

We remind here that h_g is the disk's aspect ratio. To obtain this result, we used the hypothesis that the temperature is vertically isothermal (i.e. does not depend on z), which is usually a good approximation (see Woitke et al., 2009, and Fig. 2.1.1). The vertical dependence of Ω arises in the last term of Eq. (75). Note that for $z = 0$, we find again the expression of the azimuthal (sub-Keplerian) velocity obtained for the gas in the midplane (Eq. 23).

Now that we have the expression of Ω, let us have a closer look at the VSI itself. Three quantities and their radial and vertical dependences play a crucial role to understand how the VSI works: the angular frequency $\Omega(R,z) \propto R^{-3/2}$, the specific kinetic energy $\varepsilon_k = R^2\Omega^2 \propto R^{-1}$ and the specific angular momentum $l = R^2\Omega \propto R^{1/2}$. What is important to notice is that Ω and ε_k decrease when R increases, unlike l which increases. If a fluid element with angular momentum l_0 is displaced vertically via a small perturbation, it will find itself in a region with smaller angular momentum $l_z < l_0$, due to $\Omega(R,z)$ decreasing away from the midplane for positive (commonly

expected) values of β. By conservation of the angular momentum, this fluid element will perform a radial outward displacement. Its angular momentum is once again l_0, but it has now a lower energy state since ε_k decreases with R, which means that the instability is favored and will develop.

The destabilizing effect of the centrifugal force is actually countered by buoyancy, which acts as a restoring force. Buoyancy appears if the disk has a vertical temperature profile (in fact, a vertical entropy profile) and is stabilizing so long as the vertically displaced fluid element cannot efficiently adjust its temperature to that of the surrounding gas (non-adiabatic displacement). In other words, buoyancy cannot be stabilizing for short thermal diffusion or cooling timescales (short in comparison to the dynamical timescale; see, e.g., Barker & Latter, 2015; Fromang & Lesur, 2019). It is possible to quantify more precisely the impact of buoyancy by deriving the so-called Solberg-Høiland criteria with a finite cooling time (see, e.g., Nelson et al., 2013).

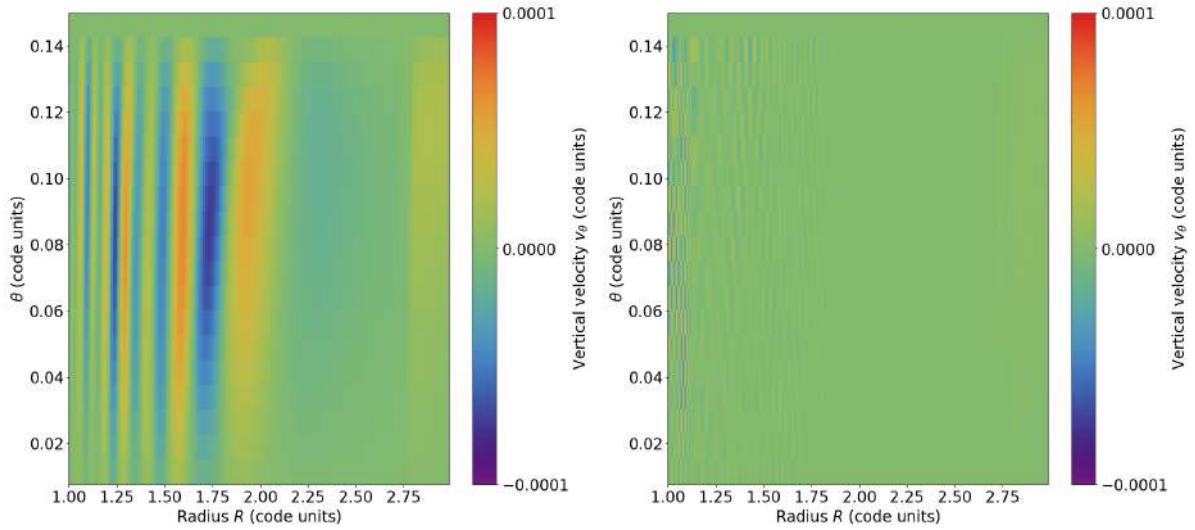

Figure 2.3.1: Results of 3D simulations performed with the FARGO3D code: colatitudinal velocity v_θ shown in the (R-θ) plane at an arbitrary azimuth ϕ. **Left:** flaring index $f = 0.2$, the VSI develops through vertical modes. Note that the perturbations are a few 10^{-4} compared to the initial profile. **Right:** flaring index $f = 0.5$, absence of significant perturbations in the v_θ field.

Note that if Ω does not depend on z, the disk is stable to the VSI, which is verified when $\beta = 0$, i.e. for globally isothermal disks (T_g is uniform). Typically, this is expected for a flaring index $f = 1/2$ (using the relation between f and β given by Eq. 22). This is something that we noticed in our 3D simulations, as shown in Fig.2.3.1.

Simulations show that the VSI produces waves that transport angular momentum radially outward in protoplanetary disks. This transport can be modeled via an α parameter of the order of 10^{-4} (Stoll & Kley, 2014).

2.3.4 *Rossby Waves Instability and vortices*

The Rossby Wave Instability (RWI) is an instability described in the context of protoplanetary disks by Lovelace et al. (1999); Li et al. (2000, 2001) and for which inertial

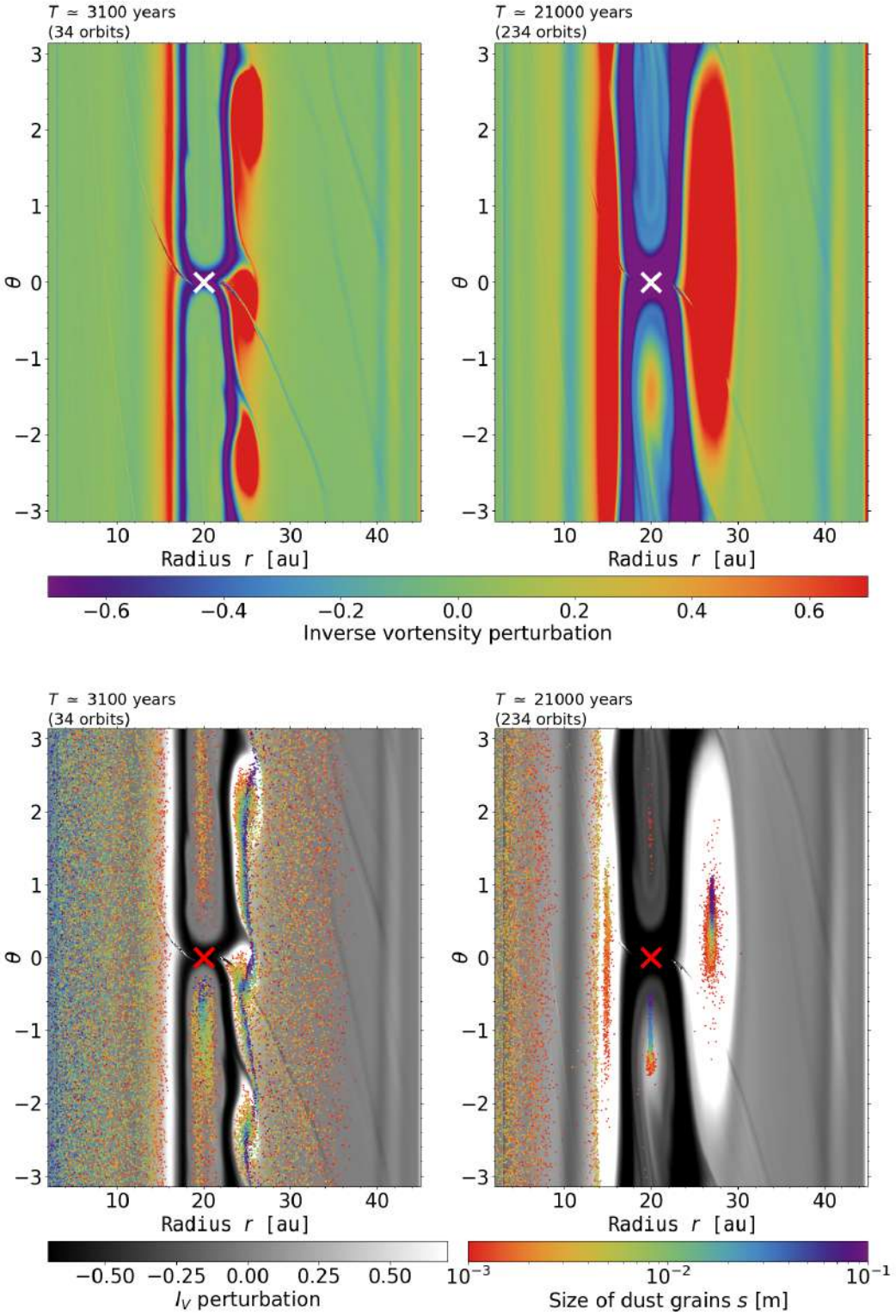

Figure 2.3.2: Results of a 2D gas+dust hydrodynamical simulation: development of the RWI in a disk, in the vicinity of the outer edge of a Saturn-mass planet's gap (at around 25 au), at the RWI initiation (left) and after vortices have merged (right). **Top:** perturbed inverse vortensity $\mathcal{I}_\mathcal{V}$ field. Note that $\mathcal{I}_\mathcal{V}$ is maximum in vortices (red spots), where the RWI develops the most. **Bottom:** dust particles (color dots) superimposed on the perturbed inverse vortensity $\mathcal{I}_\mathcal{V}$ field, in black and white. Note that particles accumulate more in the center of the vortices.

(Rossby) waves are partly trapped in specific regions of the disk. We here present some important aspects about the RWI, not for that it can play an important role in the transport of mass and angular momentum, but rather because we commonly observed its consequence in our simulations, and because it constitutes a strong bond between hydrodynamical processes, dust dynamics and planet formation. The RWI can develop if the quantity $\mathcal{L} = \mathcal{I}_\mathcal{V} S^{2/\gamma}$ has an extremum, with $S \propto c_v \log(P_g/\Sigma_g^\gamma)$ the specific entropy of the disk matter, c_v the heat capacity at constant volume, γ the adiabatic index, and $\mathcal{I}_\mathcal{V}$ the inverse vortensity, that is the ratio of the gas surface density Σ_g over the vertical component of the gas vorticity $((\vec{\nabla} \times \vec{v_g}).\vec{e_z})$. We will come back to this important hydrodynamical quantity in section 3.3.1.2 in the context of disk-planet interactions and planetary migration. In practice, such instability can develop at a given radius if an axisymmetric bump in the pressure profile is present. It gives rise to exponentially growing non-axisymmetric modes that result in anticyclonic vortices. A process similar to RWI is expected to be at the origin of the formation of the long-lived Great Red Spot on Jupiter. Note that RWI vortices can not emerge in an unperturbed laminar disk, but need a mechanism able to generate a pressure maximum linked to an inverse vortensity maximum. We will talk a little bit more about this pressure maximum generation in chapter 6.

Several mechanisms can create the necessary conditions for the RWI to develop, through the generation of pressure maxima. This is for example the case around the boundary between a dead zone and a magnetically active zone (Lyra et al., 2009). We saw earlier in this section that the MRI can be suppressed due to non-ideal MHD effects (here the Ohmic resistivity), and a pressure maximum can emerge in this transition region. Pressure maxima can also form at the edges of a massive planet's gap and generate multiple vortices (see, e.g., de Val-Borro et al., 2007). Fig. 2.3.2 shows the perturbed gas surface density in the vicinity of a massive planet (red cross), at different times. The formation of multiple vortices is strongly connected to the accumulation of dust particles within them, as shown by the colored dots that follow the vortices dynamics. Red dots represent mm-sized particles and blue dots represent 10 cm-sized particles. This dust accumulation is due to the fact that vortices create local non-axisymmetric pressure maxima that can trap particles. Remember that pressure is the only quantity that allows the presence of an aerodynamic drag acceleration between gas and dust. Thus, for a low dust-to-gas density ratio, a pressure maximum is a position of equilibrium for dust grains which follow the gas motion and do not drift. After a few hundred local orbital periods, simulations show that multiple vortices (with an azimuthal wavenumber $m \in [3-5]$) then evolve by merging into a larger unique vortex (m=1) (Meheut et al., 2012), also visible in the different panels of Fig. 2.3.2.

Finally, because of the trapping ability of anticyclonic vortices, RWI is also a promising candidate to trigger the first stages of planet formation. See Lovelace & Romanova (2014) for a detailed review about the RWI.

APPENDIX

2.A DISK TEMPERATURE

Depending on which physical processes heat and cool down the gas in protoplanetary disks, we expect different values for β:

- If T_g is dominated by viscous heating: the total heating is equal to $\frac{9}{4}\Sigma_g \nu \Omega_K^2$, with Σ_g and ν respectively the gas surface density and viscosity. If we suppose that the disk is in a steady state ($\partial_t \Sigma_g = 0$), then the accretion rate is uniform, equal to $\dot{M} = 3\pi\Sigma_g\nu$, and the heating is proportional to $\Omega_K^2 \propto R^{-3}$ (see, e.g., Eq. 50 in Lodato, 2007). If the disk efficiently radiates away this heating as a black body, the use of the Stefan-Boltzmann law gives $T_g^4 \propto \Omega_K^2$, and therefore $T_g \propto R^{-3/4}$:

$$\beta = \frac{3}{4} \Longrightarrow f = \frac{1}{8}. \tag{76}$$

- If T_g is dominated by stellar irradiation: the total heating is proportional to the flux of stellar radiation $\frac{L_\star}{4\pi R^2}$ with $L_\star$ the luminosity of the star. Using similarly the Stefan-Boltzmann law, we have $T_g^4 \propto \frac{L_\star}{R^2}$, and therefore $T_g \propto R^{-1/2}$:

$$\beta = \frac{1}{2} \Longrightarrow f = \frac{1}{4}. \tag{77}$$

We display in Fig. 2.A.1 the temperature profile for the two aforementioned regimes (viscous heating and stellar irradiation). We chose a typical value for the stellar accretion rate $\dot{M} = 10^{-8}\ M_\odot.yr^{-1}$ (blue solid line). The star luminosity $L_\star \simeq 0.8 L_\odot$ and mass $M_\star \simeq 1.7 M_\odot$ are typical of the objects observed in the DSHARP disks sample (Disk Substructures at High Angular Resolution Project) presented in Andrews et al. (2018). The figure shows that stellar irradiation generally dominates over viscous heating. For larger values of $\dot{M}$, viscous heating can prevail at small radii (see upper limit of the blue-shaded area in Fig. 2.A.1). At 10 au, the disk temperature is largely dominated by stellar irradiation by almost an order of magnitude. With the stellar irradiation model, we can therefore plot in Fig. 2.A.2 the typical values of the temperature at 10 au as a function of the stellar mass for example, for each of the famous disks in the DSHARP sample (Andrews et al., 2018). We find that the typical temperature of these objects at 10 au corresponds to a few tens of Kelvins ($T_g(10\ au) \simeq 70$ K for a Solar-mass star). Note that Fig. 2.A.2 suggests a linear relation between the gas temperature T_g and the stellar mass $M_\star$. Because in this temperature model $T_g \propto L_\star^{1/4}$, $T_g \propto M_\star$ is equivalent to $L_\star \propto M_\star^4$, which is the classical Mass-Luminosity relation (Kuiper, 1938; Wang & Zhong, 2018). Note that this relation is obtained for main sequence stars whereas here we consider pre-main sequence stars.

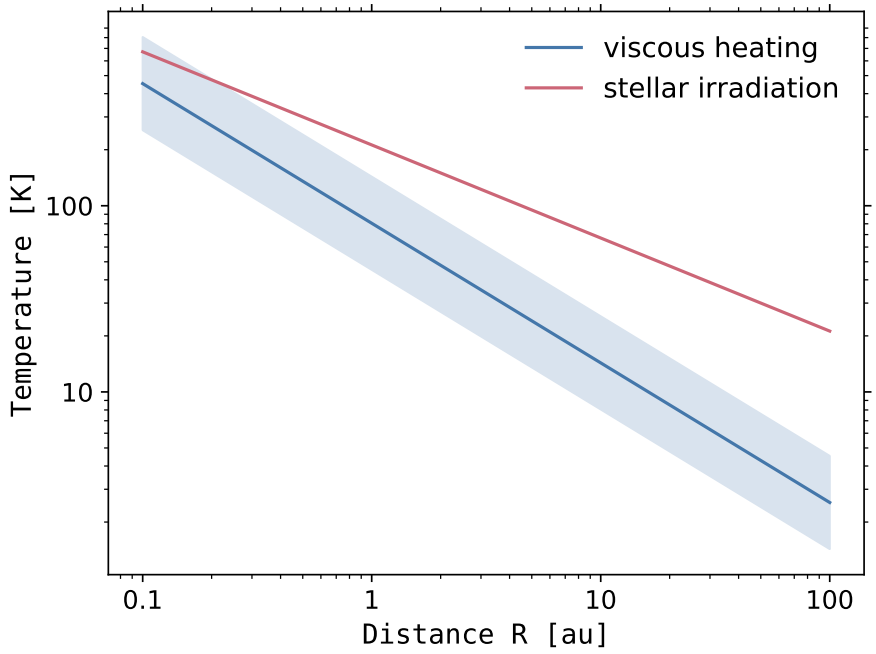

Figure 2.A.1: Effective temperature of the disk as a function of radius, for the viscous heating case ($\dot{M} = 10^{-8}$ $M_\odot.yr^{-1}$, blue solid line) and the stellar irradiation case (red line). The blue-shaded area shows the possible values of the temperature, for typical values of $\dot{M}$ between 10^{-7} and 10^{-9} $M_\odot.yr^{-1}$.

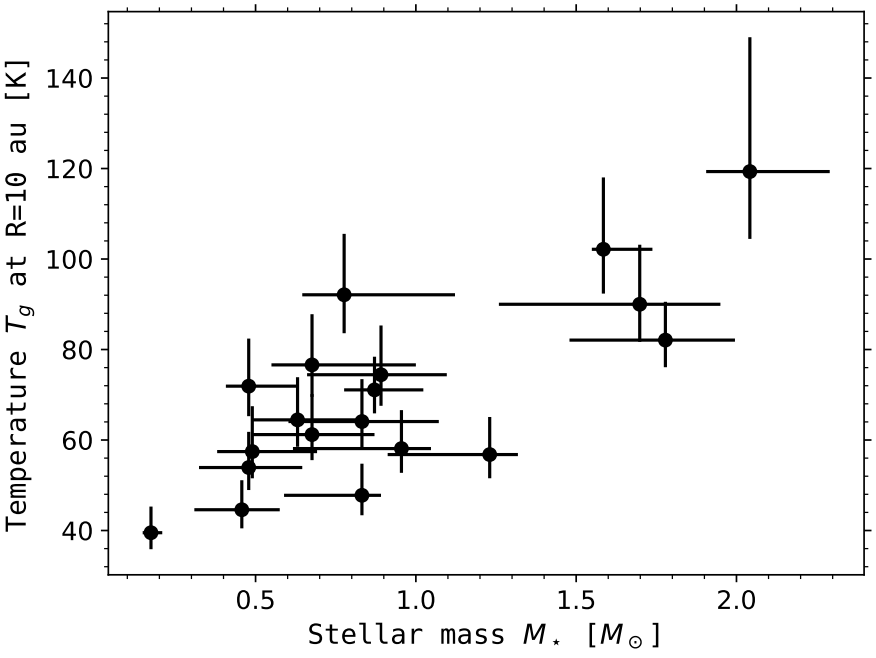

Figure 2.A.2: Effective temperature at 10 au of the DSHARP disks as a function of the stellar mass obtained with a simple stellar irradiation model.

3

PLANET FORMATION AND ORBITAL EVOLUTION

The age of protoplanetary disks does not last indefinitely. When they eventually fade away, they leave behind the seeds of a new epoch: the age of planets. A closer look at the properties of these planets raises the question of their birth. How are such massive bodies produced from gas and dust alone? The question of planetary formation immediately raises the question of planetary evolution. The powerful interaction between the disk, the gas and the solids at the origin of planets does not end once they are formed. Just as the newly born planets are gravitationally bound to the central star, they are also bound to the protoplanetary disk that surrounds them. Models indeed predict an orbital evolution of planets, called planet migration, whose consequences are to be reconciled with the current distribution of the exoplanets. In section 3.1, we make a link between the exosystems discovered so far and protoplanetary disks, before briefly introducing in section 3.2 the main scenarios for planet formation. Finally in section 3.3, we dive into the main processes behind planet migration.

CONTENT

3.1 Linking protoplanetary disks to stellar systems . . . 51
3.2 Planet formation . . . 58
3.3 Planet migration . . . 61
3.3.1 Type-I migration . . . 62
3.3.1.1 The wake torque Γ_L . . . 64
3.3.1.2 The static corotation torque Γ_C . . . 65
3.3.1.3 Impact of self-gravity on the Lindblad torque . . . 68
3.3.2 Gap opening and the onset of type-II migration . . . 68
3.3.3 Type-III migration . . . 73
3.3.3.1 Dynamical corotation torque . . . 73
3.3.3.2 A coorbital deficit . . . 73
3.3.4 A short recap on planet migration . . . 76

4 DISK SUBSTRUCTURES AND HOW TO CREATE THEM 79

3.1 LINKING PROTOPLANETARY DISKS TO STELLAR SYSTEMS

Over these last twenty years, observational progress has been made in detecting and characterizing both extrasolar planets and protoplanetary disks. As of august 2020, more than 4000 extrasolar planets have been confirmed (http://exoplanet.eu), with a wide diversity of their characteristics (semi-major axis, mass, radius, eccentricity, ...). Significant improvements have also been brought to theoretical formation and evolution models. Using all these models and observational constraints, some studies aim at comparing the actual planet population with statistical synthesis of planet population (Mordasini et al., 2009a,b; Alibert et al., 2011). At first glance, the degeneracy of the evolutionary path from a collapsing molecular cloud to a fully grown planetary system seems boundless, as it involves sizable scales, whether it be length scales, time scales or mass scales. Over billions of years, the challenge is indeed to go from small dust grains to massive gaseous giants, in a disk of gas and dust about a hundred astronomical units wide. However, studying statistically the properties of exoplanets and finding patterns in the current planet population distribution can help constrain the physical processes behind it.

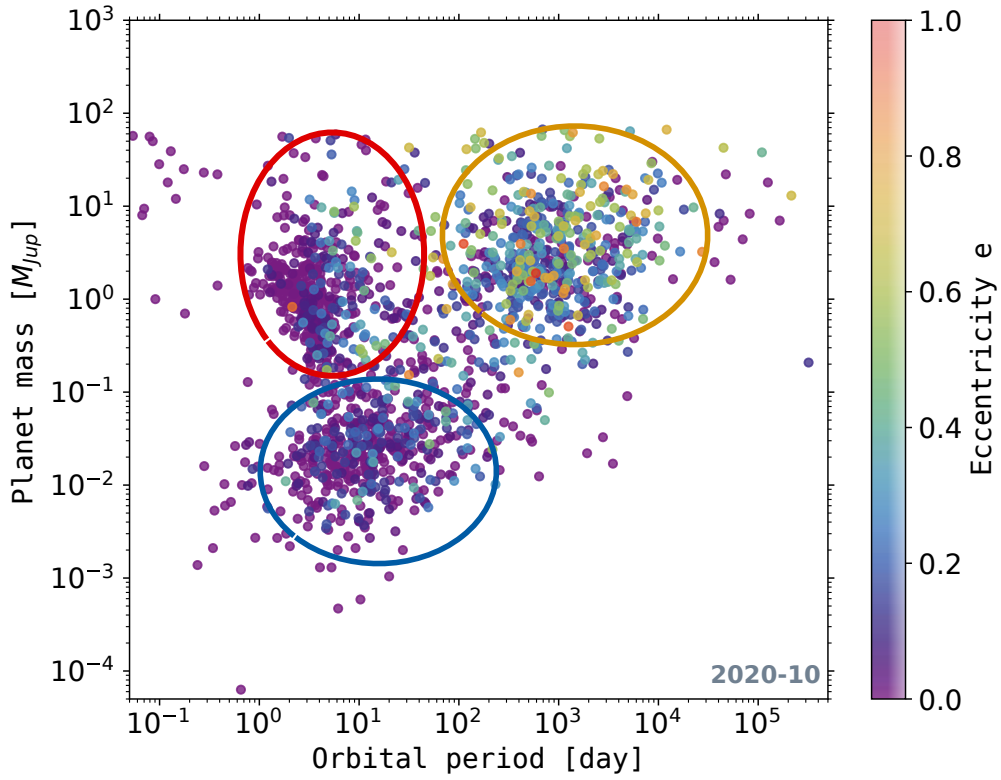

Figure 3.1.1: Planetary mass as a function of orbital period (median values), for a subset of exoplanets extracted from http://exoplanet.eu. This subset corresponds to planets for which measurements of the mass (or the minimum mass) and the eccentricity are available. The colorbar shows the eccentricity e, with small e in purple and large e in red. Three planet populations are highlighted with the colored circles: the hot Jupiters in red, the warm Jupiters in orange and the mini-Neptunes (or super-Earths) in blue.

There is a huge diversity in the orbital periods P_p, the planetary masses M_p and the eccentricities e of exoplanets, among other things. Some planets can orbit their star in a few hours, others in hundreds of years. A legitimate question is to ask what role the interactions between planets and their protoplanetary disks can play in this diversity. Fig. 3.1.1 shows the planetary mass as a function of the orbital period, for a subset[1] of extrasolar planets detected as of October 2020. The colorbar represents the eccentricity of these planets. Note that the eccentricity is an interesting parameter, as different interaction processes result in different eccentricities for the planets. In particular, planet-disk interactions most generally tend to damp the eccentricity, whereas planet-planet interactions tend to amplify it. In this diagram, three major populations of planets can be identified:

- **Hot Jupiters** ($M_p > M_{Saturn}$, $P_p < 10$ days): Such planets have a mass comparable to that of Jupiter (around 300 M_{Earth}), but orbit around their star in a few days typically (P_p=1 to 10 days), i.e. closer than Mercury is to the Sun ($P_{Mercury} \sim 88$ days). Most of these planets have been discovered with the transit photometry, by studying the changes in the stellar luminosity due to the passing of a planet in front of its parent star's disk. It thus makes sense that the larger a planet is, the easier it is to detect changes in stellar luminosity. This creates a bias towards the detection of more massive planets. It has been shown that this kind of planet around solar-type stars is actually quite rare, with a probability of about 1% (Mayor et al., 2011; Wright et al., 2012). Despite this scarcity, their existence rises a question about the dynamics during the early phase of their formation. How can such massive planets end up so close to their host star? During the protoplanetary disk phase, the gas reservoir at the current location of hot Jupiters is way too small to give rise to giant planets (typically much lower than 1 M_{Earth} versus the necessary 300 M_{Earth}), and dynamical processes are expected to occur to transport a massive planet away from its place of birth. It may be possible to maintain this *in situ* formation model by taking into account the radial drift of large dust particles, in addition to an efficient turbulent gas transport during the young phase, which can both help the development of giant planets *in situ* (see for example Batygin et al., 2016). Beside this *in situ* formation model for hot Jupiters, two main models have been proposed to explain their presence close to the star: disk migration and high-eccentricity migration. The former results from planet-disk interactions (see Section 3.3). The latter results from the circularization by star-planet tidal interactions of an eccentric planet orbit, with the initial eccentricity resulting from (i) the gravitational scattering by a vigorous, close interaction with another planet or a (sub-)stellar companion (see, e.g., Jurić & Tremaine, 2008; Chatterjee et al., 2008), or (ii) Kozai cycles with a nearby inclined[2] star (see, e.g., Fabrycky & Tremaine, 2007). Note that in Fig. 3.1.1, the eccentricity of hot Jupiters is most of the time close to 0, so eccentricity alone cannot easily help distinguish between the disk migration and the high-eccentricity migration scenarios. However, the projected orbital

1 for which the planet mass and eccentricity are estimated.

2 the angle between the line connecting the two stars and the equatorial plane of the planetary system must be $\gtrsim 40$ degrees.

obliquity of hot Jupiters could do so. It corresponds to a spin-orbit misalignment, that is the sky-projected angle between the stellar spin axis and the direction perpendicular to the planetary orbit. Two categories of hot Jupiters stand out, depending on whether the projected orbital obliquity is high or not.

- A low (< 30 deg) projected obliquity ($\lesssim 2/3$ of hot Jupiters) suggests that their evolution is dominated by disk-planet interactions, although gravitational scattering followed by efficient orbital realignment due to star-planet tidal interactions could also explain it.
- A high (> 30 deg) projected obliquity ($\sim 1/3$ of hot Jupiters) rather points towards a gravitational scattering model (planet-planet interaction). In practice, a planet is scattered towards the star on an inclined and eccentric orbit. This orbit is then progressively circularized by tidal star-planet interactions each time the planet reaches the periastron. This circularization makes the eccentricity decrease, but not necessarily the inclination, hence the high projected obliquity in that model. Note that such a high value for the projected obliquity might also be due to a disk-planet interaction followed by an instability (called elliptic instability) resulting from the star-planet interaction and which modifies the axis of rotation of the star (see Cébron et al., 2013, their section 5.4).

The detection of two hot Jupiters around young stars a few million years old favors disk migration over high-eccentricity migration for these planets (Donati et al., 2016; Yu et al., 2017). The eccentricity of these giant planets is indeed compatible with 0, and the circularization timescale of the orbit of a hot Jupiter by tidal effects is expected to be much longer than the current age of these stellar systems. It is therefore unlikely that the eccentricity and semi-major axis of such young planets have been damped by tidal effects.

- **Warm Jupiters** ($M_p > M_{Saturn}$, $P_p > 100$ days): These giant planets that orbit in more than 100 days are present in approximately 10% of solar-type stars (Mayor et al., 2011), and have a mean eccentricity of about 0.25. For comparison, Jupiter's eccentricity is close to 0.05. This value of 0.25 is on average higher than the eccentricity measured for hot Jupiters. It suggests that dynamical processes occurred after the disk dispersal, in particular planet-planet interactions or close encounters with stellar companions that amplified the eccentricity. However, observations of such systems do not show a strong correlation between eccentricity and the presence of companions (Knutson et al., 2014; Ngo et al., 2015). Thus, several mechanisms can be at the origin of the large eccentricities of warm Jupiters, like resonances between planets or hydrodynamical processes. In particular, when a Jupiter-like planet orbits in the cavity of a protoplanetary disk, it can acquire an eccentricity (Papaloizou, 2011) that can be excited through the exchange of angular momentum between disk and planet at eccentric Lindblad resonances. This disk-planet interaction in a sparse medium can make the gas giant even more eccentric, with values that can easily reach 0.4. This generic mechanism in a disk cavity proposed in a work recently submitted by Debras, Baruteau and Donati can potentially

explain the relatively high eccentricities observed for warm Jupiters. Note that cavities are expected to appear in protoplanetary disks as the result of photoevaporation (see section 2.1.4) or magnetic effects, and that observations frequently highlight the presence of cavities in disks called transition disks. In such disks, cavities observed in the dust thermal emission are **also** cavities in the gas content (Carmona et al., 2017; van der Marel et al., 2018).

- **Mini-Neptunes** ($M_p < M_{Neptune}$, $P_p < 100$ days): Mini-Neptunes (or super-Earths) are the most common extrasolar planets discovered around solar-type stars, with an occurrence rate of $\sim$ 50% (Mayor et al., 2011). As their name suggests, they are exoplanets whose radius is between that of the Earth and that of Neptune. Because they are the most common ones, it is possible to give some statistics. In particular, half of them are part of multiple systems, which suggests that forming several planets in a same system should be quite common. These planetary systems can be quite compact, with a ratio of orbital periods between successive planets smaller than $\sim$ 2-3, and the eccentricities of their planets remain fairly small (see the purple dots in Fig. 3.1.1). Note that the mini-Neptunes currently discovered are not all represented in this diagram, as the mass of a large fraction of them is still unknown, or poorly constrained. The compactness of these systems is also reflected in their small size, with for example the eight planets orbiting around the solar-type Kepler-90 (all having a radius of between 1.3 R_{Earth} and 11.3 R_{Earth}) that are all located inside 1 au, i.e. inside the distance Sun-Earth in the Solar System (Shallue & Vanderburg, 2018). These observational constraints are consistent with a system where the planets have evolved under the influence of planet-disk interactions and migration. However, this model of planetary migration is challenged by other observational constraints. In particular, it is generally expected that the ratio of orbital periods between adjacent planets of the same system are close to those of mean-motion resonances (commonly defined when the orbital periods of two planets are related by the ratio of small integers). This is not the case, as shown by the histogram in Fig. 3.1.2, with a wide diversity of the ratios, although some peaks are detected near the resonances 3:2 or 2:1 (Baruteau & Papaloizou, 2013).

  This wide diversity suggests that the orbital architecture of some of these systems cannot be explained by simple planet-disk interactions during the protoplanetary disk phase. Some models try to account for this diversity via mechanisms occurring before the disk dispersal, like for example the departure from mean-motion resonance due to planet wakes / planet gap interaction (Baruteau & Papaloizou, 2013); other models use an argument of *in situ* formation after the disk dispersal (see for example Hansen & Murray, 2013). Some other models try to explain this diversity with both *in situ* formation and planet migration (Ogihara et al., 2015).

  Finally, if these planets are formed very early in the star's life, the protoplanetary disks commonly observed in the dust continuum emission should carry within them multiple planetary embryos in formation. Under the assumption that compact systems could be resolved with ALMA, scrutinizing the impact of such

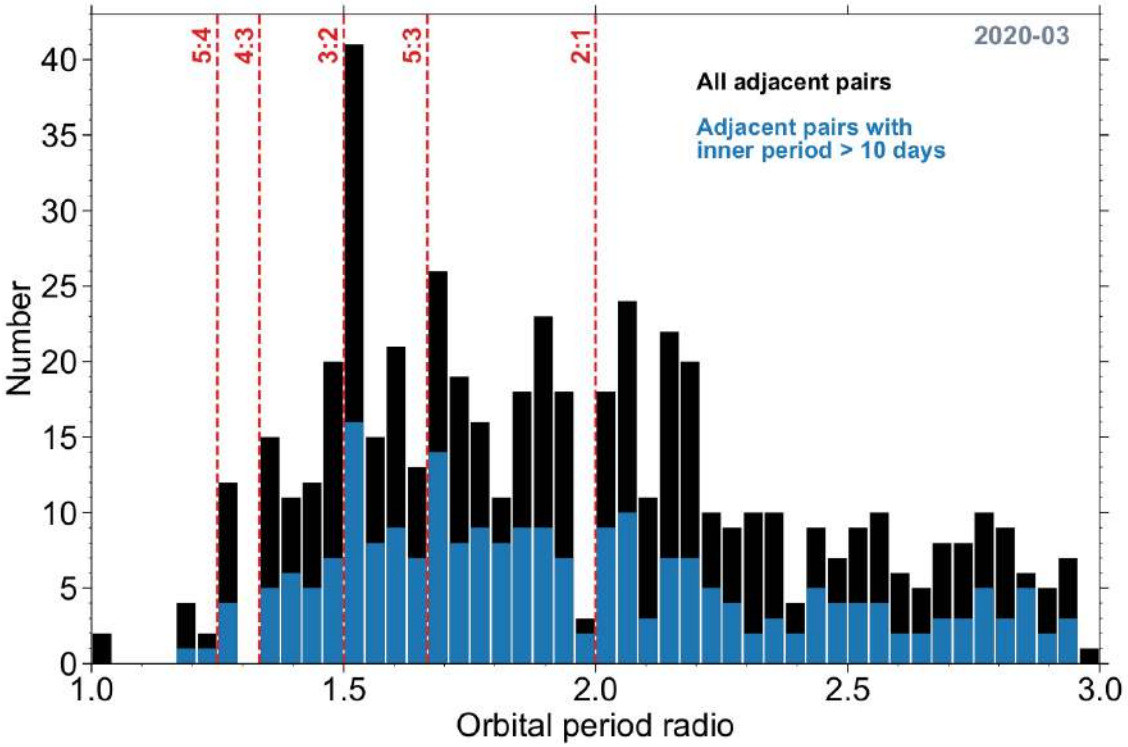

Figure 3.1.2: Histogram of the ratio of orbital periods between successive planets in multi-planetary systems observed with Kepler, adapted from (Baruteau & Papaloizou, 2013) and the Habilitation Thesis of Clément Baruteau. The black bars are for all planets, whereas the blue bars correspond to planets with $P_p > 10$ days.

embryos on the dust grains, in particular via the substructures, could therefore shed light on the formation, but also the evolution of super-Earths.

Concerning the detection of planets in young stellar systems, still in the protoplanetary disk phase, there is only one example of direct planet detection around the 5-million-year-old K7 star PDS 70 with the SPHERE instrument (Müller et al., 2018) and the MUSE instrument (Haffert et al., 2019). The protoplanetary disk in this system has a cavity where two bright structures have been detected: PDS 70b in the IR (see Fig. 3.1.3) and PDS 70c with H_α emission near the outer edge of the cavity. If these structures are due to giant planets in formation, and not to the dynamics of gas and dust, they have an estimated mass of a few $M_{Jupiter}$ and are essential to constrain the early phase of planetary formation.

Most other claims of planet detections in young systems are indirect or derived from numerical simulations, whose aim is to model the numerous substructures observed in protoplanetary disks (see chapter 4). In particular, an interesting work has been proposed by Lodato et al. (2019), which deals with an interpretation of gaps in protoplanetary disks as by-products of giant planets formation. This study analyses the largest gap sample to date (48 gaps), assuming that the observed gaps are due to planets (see chapter 4 for other interpretations of the observed substructures). They used a simple scaling relation between the observed gap width and the corresponding planet mass. These putative planets occupy a unique region in the mass-semi-major axis diagram (similar to the one presented in Fig. 3.1.1), from a few Earth masses to

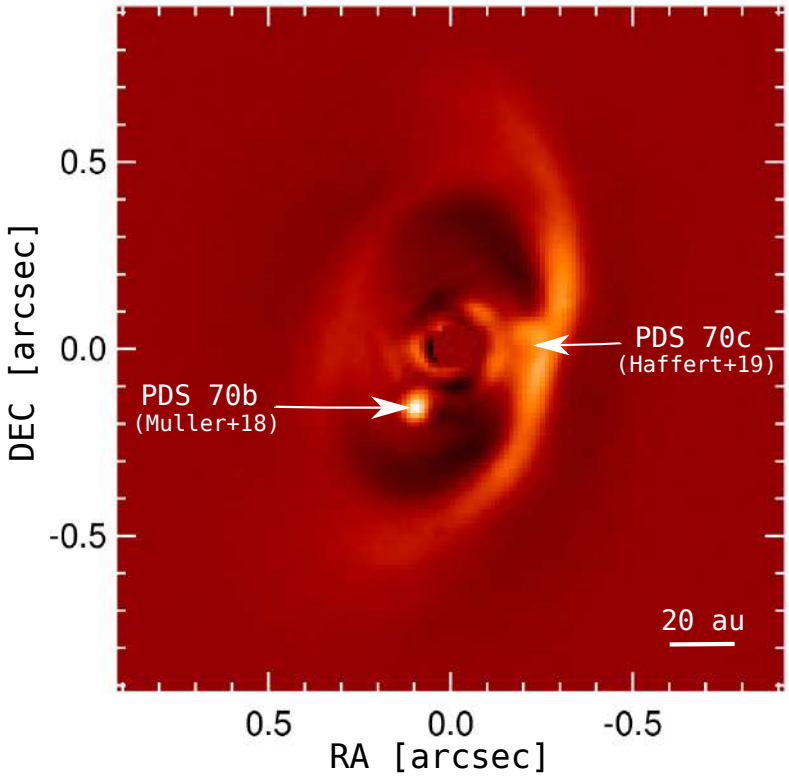

Figure 3.1.3: Observation from Müller et al. (2018) of the PDS 70 system with SPHERE at 2.1 μm using a coronagraphic angular differential imaging method. The presence of two giant planets has been proposed to explain the blobs and structures detected in multi-wavelength observations (Müller et al., 2018; Haffert et al., 2019).

a few Jupiter masses, but orbiting further away from their star than warm Jupiters (typically between 10-100 au; see Zhang et al., 2018; Lodato et al., 2019, respectively their Fig. 21 and Fig. 1). Such cold planets are hardly accessible through current planet detection methods, but Lodato et al. (2019) have shown that taking into account a simple prescription for planet migration and planet accretion makes these hypothetical planets to populate the warm Jupiter and hot Jupiter regimes in the mass-separation diagram, after 3-5 Myr of planetary evolution. Because of this motion in the parameter space, there is no inconsistency in suggesting that young massive planets carve gaps without being visible later on at this same position. Note that there are huge uncertainties in the methodology used in Lodato et al. (2019) in many ways. For example, the estimated planet masses are obtained from the emission of dust substructures, and not directly from the gas content. The gap carved in the dust by a massive planet is indeed not expected to have the same width as the gap carved in the gas (Fouchet et al., 2010). Besides, they use prescriptions of migration in order to compare the final position of their putative planets in the mass-separation diagram, and choose between two migration regimes depending on their ability to carve a gap (see section 3.3.2). This ability depends among other things on the value of the α parameter that has been here chosen fixed ($\alpha = 5 \times 10^{-3}$) for all the protoplanetary disks, which strongly impacts the migration regimes of the planets during their orbital

evolution. Note also that the gas and dust substructures (bright and dark rings) in the disk may also have an influence on the planets migration. Finally, the biggest hypothesis here is to consider that each observed gap has been carved by a giant planet orbiting within it on a fixed orbit. We will later call such assumption the *N Gaps N Planets* model (NGNP). However, many works have shown that one gap can be created by multiple planets (see Zhu et al., 2011; Baruteau & Papaloizou, 2013, their Fig. 3), and alternatively multiple gaps can be created by one planet only (Zhang et al., 2018; Wafflard-Fernandez & Baruteau, 2020). Such substructures can moreover be obtained without ever invoking the presence of planets (see for example Lyra et al., 2015a; Riols & Lesur, 2019, and chapter 4).

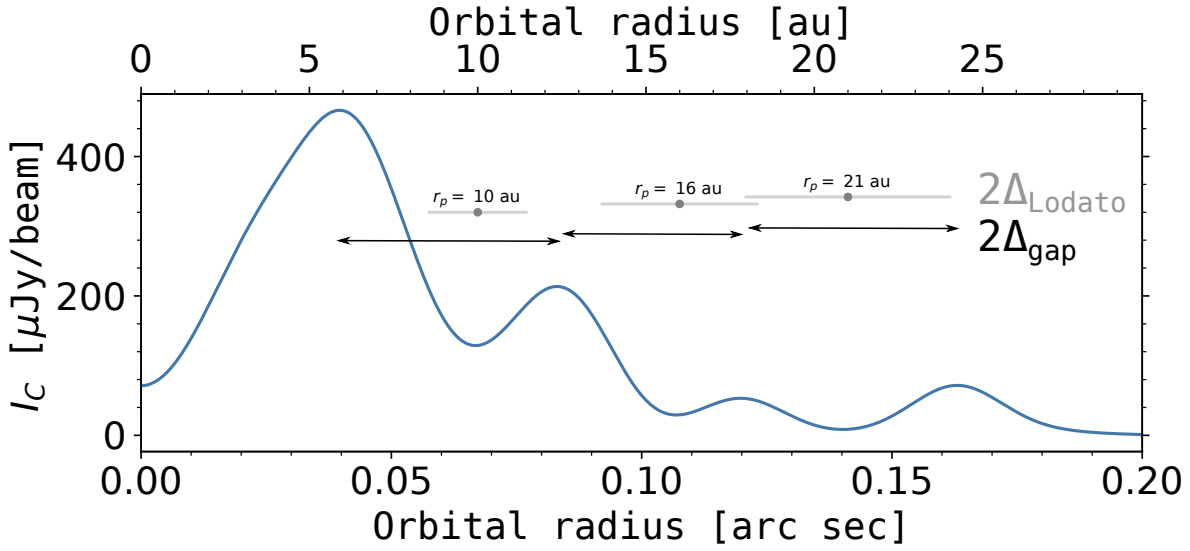

Figure 3.1.4: Predicted continuum emission at 1.3 mm for a single 1.5 M_{Saturn} planet on a fixed circular orbit, producing a sequence of bright and dark rings (similar to the phenomenon highlighted in Zhang et al., 2018). The blue curve is the azimuthally-averaged convolved intensity as a function of the distance to the star. The gray segments show the estimated gap width using the simple scaling relation in Lodato et al. (2019) for three putative 1.5 M_{Saturn} planets in the center of the three gaps. The black arrows mark the real gaps width.

As an example, Fig. 3.1.4 shows the result of a dust radiative transfer calculation for a model with a single planet on a fixed circular orbit (at $r_p = 20$ au) that creates multiple gaps. The y-axis corresponds to the azimuthally-averaged intensity of the dust continuum emission at 1.3 mm, convolved with a 0.″02 circular beam (see chapter 5 for the methodology, and chapters 6 and 7 for more details about the parameters of the simulation). The x-axis is the distance from the star, in au and arcsec. The variations in the intensity feature actually four bright rings / crescents and three gaps. Lodato et al. (2019) define a gap width as the distance between the location of the brightness minimum in the center of the gap and the neighboring bright ring. The gray segments in Fig. 3.1.4 correspond to twice the gaps width according to their simple scaling relation for three 1.5 M_{Saturn} planet, and the black arrows show twice the real gaps width in the synthetic continuum map. The scaling relation chosen by

Lodato et al. (2019) works fairly well at the location of the planet ($r_p \sim 21$ au), but it would suggest the presence of another 1.5 M_{Saturn} planet at $r_p \sim 16$ au, and an even more massive one in the center of the large gap at $r_p \sim 10$ au. There are other uncertainties important to notice here. On the one hand, regarding the scaling relation used by Lodato et al. (2019), they propose that the gap width mainly depends on the planet mass. The dependence on α and h_g (see section 3.3.2) is hidden behind a constant $k = 5.5$ that relates the gap width with the planet's Hill radius (see the definition of the Hill radius in Eq. 78). On the other hand, the median mass of the planets obtained with their scaling relation is that of Neptune. One can thus wonder about the ability of a Neptune-like planet to generate an inner pressure maximum able to trap particles efficiently in an inner bright ring. And if an inner pressure bump is present, it is not guaranteed that it can prevent large particles to drift radially. The gap width for such planets strongly depends on the particles Stokes number, and is therefore possibly larger than expected taking into account the gas/dust interaction. A lot of free parameters are thus added to their model, leading to strong uncertainties in the results. Finally, the planet mass estimate is obtained at a given resolution, and higher resolutions can unveil thinner structures that a massive planet cannot always reproduce alone (see Fig. 4.1.2 for the substructures in the disk HD 169142).

3.2 PLANET FORMATION

We briefly describe in this section general aspects of planet formation theory. Planets are expected to form early in a protoplanetary disk, consisting mainly of gas and a small fraction of dust (with typically a dust-to-gas mass ratio of a few percents). This two-phase fluid is the reservoir of the planetary formation. Two mainstream scenarios are commonly used to describe how planets form and grow:

- **Top-Down** scenario, through the **gravitational instability**: let us consider a massive primordial disk, which verifies the condition $Q < 1$ for the GI to set in (see Section 2.3.2 for an overview of the GI). In the outer parts of the disk (typically beyond 50 to 100 au from the star), the cooling of the disk is expected to be quite fast. In the case where the disk's cooling time is less than a few dynamical times (typically 3-5), the non-linear evolution of the GI leads to the fragmentation of the disk (Gammie, 2001). The disk eventually breaks up into massive bound clumps of a few $M_{Jupiter}$ (Paardekooper et al., 2011b). Although the transition from a gas clump to a giant planet is uncertain, this mechanism makes it possible to create massive planet embryos at large distance from the star, which is more difficult with the more conventional core accretion scenario described below (see the gas clumps in Fig. 3.2.1 from Paardekooper et al. (2011b)). The fate of these embryos is then unclear, as it is subject to an inward fast migration due to disk-clump interactions (Boley et al., 2010; Baruteau et al., 2011). It may be difficult for giant planets to exist far from the star, but any mechanism that slows down the migration can help to overcome this problem. Furthermore, this GI mechanism can also contribute to the formation of mini-Neptunes or super-Earths. Let us consider the typical distance R_H from

the protoplanet below which its gravity dominates over the star's gravitational potential, called Hill radius and expressed as:

$$R_H = a \left(\frac{M_p}{3M_\star} \right)^{1/3}, \tag{78}$$

with M_p the mass of the planetary embryo, $M_\star$ the stellar mass and a the semi-major axis, that is the distance between the center of gravity and the embryo[3]. We supposed in Eq. (78) an eccentricity $e = 0$. R_H defines the sphere of influence of the embryo, and any test particle closer to the protoplanet may be trapped inside its potential well. R_H depends roughly on the distance between the star and the protoplanet. Thus, if the protoplanet gets closer to the star via inward migration, its Hill radius will also decrease. The protoplanet can therefore lose material during its migration, depending on the cooling time of the gas, and thus become either a super-Earth or a giant planet. This mechanism that goes along with the gravitational instability is called tidal downsizing scenario and is thoroughly developed in the review by Nayakshin (2017).

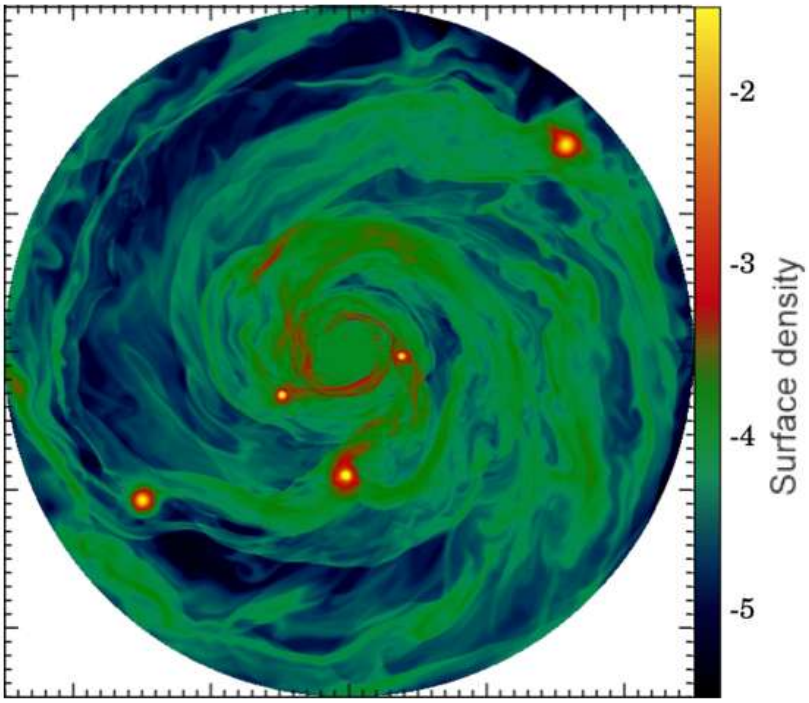

Figure 3.2.1: Result of a 2D hydrodynamical simulation of a massive protoplanetary disk unstable against the GI and having a short cooling timescale ($\tau_{cool}\Omega \lesssim 3-5$), from Paardekooper et al. (2011b).

- **Bottom-Up** scenario, with the **core accretion** theory: we know that the Earth is a terrestrial planet, mostly composed of rocks (silicates,...), and giant planets are mainly made of gas (hydrogen, helium,...) with a supposed rocky core. In the

3 the major axis is the longest diameter of the planet's elliptical orbit. The semi-major axis is therefore half this quantity and gives an insight about the distance between the central star and the planet.

early phases of planetary systems, the only solid component is the dust content of protoplanetary disks. One possible planet formation theory is thus to consider the growth of solids all the way from micrometer-sized grains to massive cores through various physical processes. Such processes occur in huge size ($\sim 10^{14}$) and mass ($\sim 10^{42}$) scales, and face several barriers. Growing dust grains from µm to cm (called pebbles) is quite easy, with the help of surface forces that make the grains stick together. Beyond this critical size, two physical processes prevent the pebbles from getting even bigger, namely the radial drift barrier (section 2.2.2) and bouncing (at small velocity difference) or fragmentation (at large velocity difference) (section 2.2.4). Note that mass transfer from small projectiles to large targets (see section 2.2.4) may help bypass this fragmentation issue. Besides, the most promising mechanism to go from pebbles to planetesimals is related to an instability resulting from a strong dust-gas interaction and the prevalence of the dust's self-gravity (Youdin & Goodman, 2005). In essence, how does the so-called *streaming instability* work? Let us consider a set of radially drifting pebbles in a disk. If there is a slight accumulation of pebbles somewhere in the disk, that is if the dust-to-gas density ratio ϵ increases, their drift velocity $v_{d,R}$ tends to decrease (see Eq. 63). Due to this reduced velocity drift, other particles further away easily reach this dust accumulation, increasing ϵ even more until the dust's self-gravity ends up dominating the dynamics. When $\epsilon \sim 100 - 1000$, the dust filaments start indeed to collapse into clumps. Local shearing-box simulations that use a simplified growth model for solids show that it is possible to form $\sim$ 100 km-sized planetesimals with the solid fragmentation of a disk subject to the streaming instability (see the review by Johansen et al., 2014). Beyond this size, solids mainly interact through gravity and gas drag becomes a minor (though non-negligible) actor of their dynamics. There are two main scenarios to form planetary cores from planetesimals:

- **planetesimal accretion:** planetesimals grow by accreting other planetesimals, and the dynamics is dominated by collisions. See for example Armitage (2007); Baruteau et al. (2016) for a pedagogical introduction about planetesimal accretion. Classical models of planetesimal accretion have investigated *in situ* growth of protoplanetary cores, and find that it is difficult to explain the formation of giant planets at large orbital separations. Although the mass reservoir at large distances is sufficient to create giant planets, the core growth timescale to reach enough mass to trigger rapid gas accretion is way too long (longer than the disk's lifetime) to explain the formation of distant massive planets (see table 1 from Kokubo & Ida, 2000; Bitsch et al., 2015). Taking into account protoplanet migration can help decrease this growth timescale, because the reservoir of planetesimals is constantly being replenished during the phase of migration. The growth timescale typically becomes of the order of 1 Myrs (Alibert et al., 2005).
- **pebble accretion:** In addition to the impact of orbital migration, it has been shown that pebbles turn out to be much more efficient in the growth of a protoplanetary core. These mm- to cm-sized grains are strongly coupled to the gas ($S_t \sim 1$) which damps their eccentricity and inclination during

gravitational encounters, via aerodynamic gas drag. The probability of accretion onto big planetesimals (or protoplanetary cores) is thus enhanced, leading to an efficient and fast core growth (typically more than 10^4 faster than the planetesimal accretion's timescale at 30 au (Kokubo & Ida, 2000; Baruteau et al., 2016)). See (Baruteau et al., 2016) for an overview of the pebble accretion scenario, and (Bitsch et al., 2015) for a numerical study about pebble accretion with planet migration.

Finally, in this core accretion model, once the protoplanetary cores are formed through planetesimal/pebble accretion, they start to progressively accrete a gaseous envelope. This accretion process is subject to a runaway phase when the envelope's mass becomes comparable to the core mass, which is typically the case when the planet's core mass reaches about 10 Earth masses (Bodenheimer et al., 2000; Lissauer & Stevenson, 2007). A giant planet is born.

We have seen gas-dust interactions in section 2.2, dust-dust and dust-planet interactions through planet formation in section 3.2. In the next section, we will examine the gas-planet interaction responsible for planet migration.

3.3 PLANET MIGRATION

On the one hand, Alibert et al. (2005) highlighted in their global formation and evolution models that the planetary formation timescale is of the same order of magnitude as the migration timescale for giant planets. This is an excellent reason to consider migration issues in formation models. On the other hand, the presence of hot Jupiters extremely close to their host stars (see section 3.1 and Fig. 3.1.1), that is with very short orbital periods (typically a few days), is very difficult to explain via *in situ* formation. Planetary migration theory is a plausible scenario to understand how such massive planets can be detected in regions of the disk where the available mass was insufficient and the temperature too high for *in situ* formation of protoplanets. A high temperature can be problematic for different reasons. On the one hand, because of the vicinity of the star, stellar irradiation can be sufficient to allow the MRI to develop in an ionized medium. It can therefore lead to a strong turbulence that does not favor locally solids growth (see for example in section 2.2.3 its impact on dust settling). On the other hand, silicates sublimate beyond ~ 1500 K. In a MMSN disk model, such a high temperature is reached at a location corresponding to an orbital period of a few days, which is typical of hot Jupiters. Without solids to trigger the core accretion scenario, *in situ* giant planet formation is complicated in regions close to the star. With a planetary migration theory at hand, a giant planet can form in the outer parts of the disk and then migrates towards the star through planet-disk interactions, to finally stop when there is no gas anymore to affect its orbital radius. In this and the following sections, it is assumed that the orbital evolution of the planets is essentially governed by the gas dynamics, and little by the dust dynamics, given the low dust-to-gas density ratio expected to be found in the young phases of the protoplanetary disks. Note however that some studies have considered the impact of dust particles on planet migration (Chen & Lin, 2018; Hsieh & Lin, 2020).

3.3.1 *Type-I migration*

We already insisted on the significance of angular momentum to study the evolution of protoplanetary disks (Eq. 13 for the collapse of a molecular cloud into a protoplanetary disk, Eq. 29 for the turbulent transport of mass and angular momentum). This quantity is also important to model the interaction between a disk $\mathcal{D}$ and a planet $\mathcal{P}$. $\mathcal{D}$ acts here on $\mathcal{P}$ through a *torque* Γ_p. A torque is a physical quantity that usually models how the rotational motion of a body is modified. Put another way, we can say that torque is to rotation and angular momentum as force is to translation and linear momentum[4]. To begin with, we assume a planet on a circular (*eccentricity* $e = 0$) and coplanar (*inclination* $i = 0$) orbit. We also assume that the planet mass is stationary ($dM_p/dt = 0$), that is to say the timescale of gas and pebble accretion onto the planet is long compared to the timescale of planet's orbital evolution. Thus, the projection of the torque along the normal to the orbital plane reveals how the (vertical component of the) angular momentum $L_{z,p} = M_p\sqrt{GM_\star a}$ of a planet of mass M_p and semi-major axis a evolves as a function of time (Eq. 79, Eq. 80):

$$\begin{aligned}\Gamma_p &= \frac{dL_{z,p}}{dt}\\ &= M_p\sqrt{GM_\star}\frac{d\sqrt{a}}{dt}\\ &= \frac{L_{z,p}}{2a}\frac{da}{dt}\end{aligned} \tag{79}$$

which gives for the migration rate :

$$\frac{da}{dt} = \Gamma_p \underbrace{\frac{2a}{L_{z,p}}}_{>0}. \tag{80}$$

The direction and speed of migration are directly given by the sign and amplitude of Γ_p. If the torque is positive, the migration rate is also positive, which means that the semi-major axis a increases under the action of the disk. It corresponds to an outward migration. On the contrary, a negative torque makes the migration rate negative, that is the semi-major axis decreases. It is an inward migration. We neglected eccentricity and inclination in this simplified approach, but note that disk-planet interactions generally damp these quantities, whereas planet-planet interactions can also trigger an orbital evolution while amplifying e and i.

Because the disk acts on the planet through Γ_p, the planet also perturbs the disk in return. Fig. 3.3.1 shows the relative perturbation of the gas surface density, where a 1.5 Saturn-mass planet is forming. This is a result from a 2D simulation performed with the hydrodynamical code `FARGO-ADSG` (see Chapter 5). Basically, the Navier-Stokes equations are solved on a 2D polar mesh, for a vertically-averaged disk.

4 hence the two fundamental theorems in physics that connect these quantities : the Angular Momentum Theorem and Newton's Second Law.

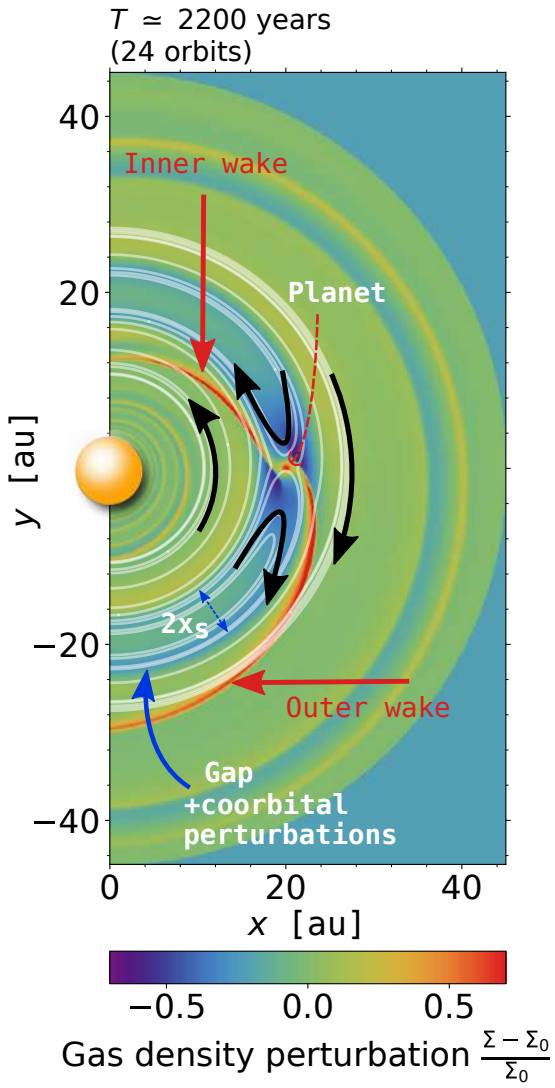

Figure 3.3.1: Result of a 2D hydrodynamical simulation: relative perturbation of the gas surface density $(\Sigma - \Sigma_0)/\Sigma_0$ in a protoplanetary disk, with a 1.5 Saturn-mass planet with orbital radius $R_p = 20$ au. Regions in blue depict gas under-densities, whereas regions in red represent gas over-densities. The orange sphere marks the position of the star.

Here are some structures visible in Fig. 3.3.1:

- A **planet** at the radial location $R = R_p$ perturbs the disk, with stronger perturbations as the planet is more massive and the disk is more receptive to these perturbations (i.e. rather cold and not too turbulent, see section 3.3.2).
- White streamlines show the **gas trajectories** in the frame of reference in corotation with the planet. Fluid elements at $R < R_p$ move counterclockwise, while fluid elements at $R > R_p$ move clockwise. A good analogy would be to consider a car in the middle of a three-lane road, overtaken by cars in the left lane and overtaking vehicles in the right lane. The radial region close to the planet where fluid elements make U-turns but remain trapped at $R \sim R_p$ on average is called the **horseshoe region** (see the U-turning black arrows). x_s is the half-width of this region.
- **Inner and outer wakes** are spiral density waves launched by the planet, and propagate on both sides of the planet's orbit throughout the disk.
- An **annular gap** in the gas surface density is created by the wakes that progressively expel the gas out of the planet's horseshoe region. We clearly see that the under-density in the gas is more pronounced close to the planet (dark blue region near the planet), and will eventually propagate all over the planet's horseshoe region.
- The gap is one example of **coorbital perturbations** that are located around the orbital radius of the planet. They are confined to the horseshoe region of the planet. The Lagrange points are another example of coorbital structures (see section 7.5).

Most studies that deal with migration seek to determine the sign and amplitude of the total torque exerted on the planet, in order to assess the direction and speed of migration respectively. For example, the torque measured in the simulation shown in Fig. 3.3.1 at time $t = 2200$ years is negative. It is therefore expected that the migration will be inward in this case. Although studying the total torque gives a general idea of the orbital evolution of planets, it is important to decompose this torque in order to isolate the physical mechanisms behind planetary migration. The total torque on the planet can essentially be split into two components: the wake torque (or Lindblad torque, see section 3.3.1.1) and the static corotation torque (section 3.3.1.2).

3.3.1.1 *The wake torque* Γ_L

We have seen in Fig. 3.3.1 that the planet creates spiral density waves, or wakes, that will act retroactively onto the planet's semi-major axis, via a gravitational torque. This wake torque can be divided in two parts. The gas over-densities (upstream of the planet) linked to the inner wake exert a gravitational force whose azimuthal component is positive ($F_{\phi,i} > 0$). The corresponding torque is therefore positive: $\Gamma_{w,i} \simeq R_p F_{\phi,i} > 0$. It means that $\Gamma_{w,i}$ tends to increase the planet's semi-major axis via an outward migration. On the contrary, the azimuthal component of the force exerted by the gas over-densities linked to the outer wake onto the planet is negative ($F_{\phi,o} < 0$). The corresponding torque $\Gamma_{w,o} \simeq -R_p F_{\phi,o}$ is negative, leading to an inward migration. Because the inner wake and the outer wake act in an opposite way, we talk about differential wake torque. The goal of the game is to determine who the winner is of this gravitational arm wrestling match. To do so, it is possible to solve analytically the linear equations of the perturbations of a planet in a disk, whether in 2D or 3D (see, e.g., Tanaka et al., 2002; Paardekooper et al., 2010). Linearized equations mean small perturbations analysis, which is valid for small masses of planets (typically up to a few tens of Earth masses). The formalism shows that spiral density waves are propagating away from the radial location of Lindblad resonances (hence the name 'Lindblad torque'), which correspond to the locations where the gas azimuthal velocity relative to the planet is equal to the phase velocity of acoustic waves in the azimuthal direction. Note that the wakes are in corotation with the planet. These results are obtained thanks to the dispersion relation arising from the linearized equations. This analysis, in good agreement with numerical simulations, shows that the total Lindblad torque is **negative** for typical decreasing density and temperature radial profiles. This domination of the outer wake over the inner wake leads to a fast inward migration (around 3×10^5 years for an Earth-mass planet at 1 au in a MMSN disk model, see Baruteau et al. (2014)), difficult to blend with the observations of distant planets. How to keep planets in a protoplanetary disk if they quickly end up on the edge of the star? One of the many possible answers can be found in the analysis of the coorbital perturbations visible in Fig. 3.3.1, which are at the origin of another famous torque called 'static corotation torque'.

3.3.1.2 *The static corotation torque* Γ_C

Let us look at the gas elements that interact with the planet within the horseshoe region. These elements are located in an annular region around the orbital radius R_p of the planet. Any gas element outside this region circulates freely without directly interacting with $\mathcal{P}$: they only interact with the planet's inner/outer wake. On the contrary, gas elements located on the same lane as $\mathcal{P}$ will perform a set of half-turns according to a horseshoe pattern, hence the name of this region. Let us follow a gas element $\mathcal{G}$ located at $R_g = R_p - \epsilon_R$, with $\epsilon_R/R_p \ll 1$. Being closer to the star than $\mathcal{P}$, $\mathcal{G}$ moves at a larger azimuthal speed $v_K(R_p - \epsilon_R) > v_K(R_p)$, and will eventually get closer to $\mathcal{P}$'s Hill radius. At this point, $\mathcal{P}$ transfers some angular momentum to $\mathcal{G}$. The orbital radius of $\mathcal{G}$ then increases, and it passes behind the orbital radius of P, at $R_g = R_p + \epsilon_R$. The gas element now rotates more slowly than $\mathcal{P}$ around the star, at $v_K(R_p + \epsilon_R) < v_K(R_p)$. It is said to have made an outward U-turn. The torque exerted by $\mathcal{G}$ on $\mathcal{P}$ during the U-turn is negative, by the law of action and reaction. After some time, actually the time it takes for the planet to catch up with $\mathcal{G}$, a new interaction between $\mathcal{P}$ and $\mathcal{G}$ occurs. This time, the planet drains angular momentum from $\mathcal{G}$, which makes it get closer to the star, at $R_g = R_p - \epsilon_R$. This inward U-turn is the orbital representation of a positive torque exerted by $\mathcal{G}$ on $\mathcal{P}$. This back-and-forth motion defines a horseshoe-shaped orbit. Note that $\mathcal{G}$ alternates between the azimuthal velocities $v_K(R_p - \epsilon_R)$ and $v_K(R_p + \epsilon_R)$, so it moves on average at the speed of the planet $v_K(R_p)$, thus in corotation with it. That is why the horseshoe region is often called the 'corotation region'.

At any moment, the planet undergoes both a positive torque related to the flow of gas elements performing inward U-turns at a position angle $\phi_g \gtrsim \phi_p$, and a negative torque related to the flow of gas elements performing outward U-turns at a position angle $\phi_g \lesssim \phi_p$. As for the Lindblad torque, the corotation torque is thus the result of two contributions of opposite sign.

Studies about the corotation torque have shown that it depends in a complex way on the physical properties of the gas, in particular on the advection-diffusion of some important hydrodynamical quantities. The first one that I will describe here is related to the **potential vorticity**, called **vortensity** in the field of protoplanetary disks. We have already talked a little bit about it in section 2.3.4 when mentioning the Rossby Wave Instability; we will talk about it again throughout this manuscript, because it constitutes a fundamental quantity that links the gas dynamics to the planets' dynamics in a protoplanetary disk. The vortensity in 2D is written as the ratio between the vertical component of the vorticity, i.e. the curl of the gas velocity v_g, and the gas surface density Σ_g:

$$\mathcal{V} = \frac{(\vec{\nabla} \times \vec{v_g}).\vec{e_z}}{\Sigma_g}. \tag{81}$$

In 3D, the expression of the vortensity is given by $\mathcal{V}^{3D} = \left[\int_{-\infty}^{+\infty} \left(\frac{(\vec{\nabla} \times \vec{v_g}).\vec{e_z}}{\rho_g}\right)^{-1} dz\right]^{-1}$ in (Masset & Benítez-Llambay, 2016, their Eq. 50). Note that the corotation torque

actually depends on the radial gradient of the inverse vortensity $\mathcal{I}_\mathcal{V} = 1/\mathcal{V}$ and not on the vortensity itself.

- **Advection** of $\mathcal{I}_\mathcal{V}$: the sign and amplitude of the corotation torque depend directly on the radial gradient of the inverse vortensity in the horseshoe region, and thus indirectly on the gas density along the streamlines. Gas elements will advect their initial inverse vortensity as they perform inward and outward horseshoe U-turns. Without $\mathcal{I}_\mathcal{V}$ diffusion, the total Lindblad + corotation torque therefore oscillates around the value set by the Lindblad torque. In practice, gas elements do not advect their initial $\mathcal{I}_\mathcal{V}$ indefinitely as they perform U-turns. The $\mathcal{I}_\mathcal{V}$ actually ends up homogenizing throughout the horseshoe region. Without a radial gradient of $\mathcal{I}_\mathcal{V}$, the static corotation torque is eventually cancelled: it saturates.

- **Diffusion** of $\mathcal{I}_\mathcal{V}$: In reality, the $\mathcal{I}_\mathcal{V}$ is subject to an advection-diffusion equation, and not just an advection equation, i.e. the corotation torque depends on the efficiency of the radial angular momentum transport in the horseshoe region. Assuming that angular momentum transport can be modeled as a viscous diffusion process, the corotation torque will then depend on α.

The second quantity that determines the evolution of the corotation torque is the **specific entropy** ζ, linked for a 2D model to the gas pressure P_g, the gas surface density Σ_g, the adiabatic index γ and c_v the specific heat at constant volume:

$$\zeta = c_v \log\left(P_g \Sigma_g^{-\gamma}\right). \tag{82}$$

Note that, just like the vortensity, the specific entropy is involved in the setting of the RWI (section 2.3.4). Advection of specific entropy within the planet's horseshoe region implies that the sign and amplitude of the corotation torque also depend directly on the radial gradient of the specific entropy across the horseshoe region, and thus indirectly on the gas temperature and the gas surface density along the streamlines (P_g depends on the gas temperature T_g via the ideal gas law). Similarly to the vortensity, gas elements do not advect their initial specific entropy indefinitely as they perform U-turns. ζ actually ends up homogenizing throughout the horseshoe region, cancelling eventually the entropy-related corotation torque. The diffusion of ζ depends on how efficient the radial transport of temperature is in the horseshoe region. The impact of the advection-diffusion of specific entropy is obtained by taking into account the radiative properties of protoplanetary disks. In order to study the entropy-related corotation torque, one needs a non-zero thermal diffusion, and therefore a finite cooling timescale. In that case, the entropy-related corotation torque does not saturate (see, e.g., the 3D radiative simulations in Kley et al., 2009). In practice, this is done by solving numerically an energy equation in addition to the continuity and Navier-Stokes equations (see section 5.1.1.3). The energy equation includes in particular a cooling source term, which can be quantified by vertically integrating the divergence of the radiative flux. Two components emerge from this integration: a term which accounts for the radiation transport in the disk midplane, and a term which models the vertical evacuation of temperature from the disk surfaces (Müller & Kley, 2013). Note the structural analogy with Eq. (40) about the vertically averaged equation of

angular momentum conservation, which did not deal with thermal diffusion, but with viscous diffusion. Similarly, Eq. (40) for the angular momentum was split into a term of radial transport in the midplane and a term of vertical evacuation from the disk surfaces.

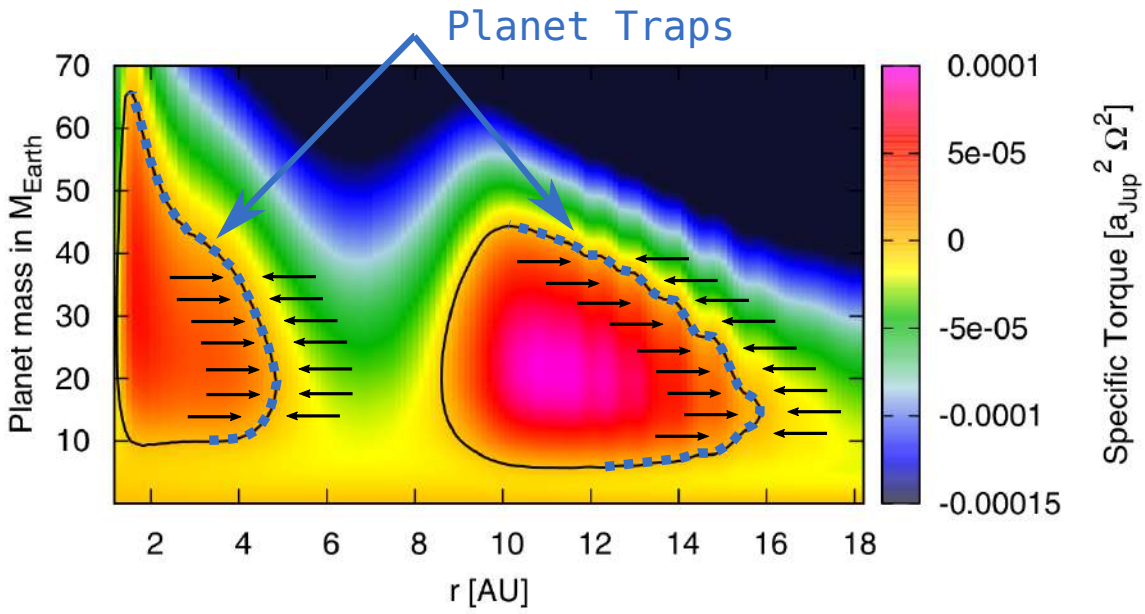

Figure 3.3.2: Type-I migration specific torque on planets with different masses ($< 70 M_{Earth}$) as a function of their orbital position, using torque prescriptions from (Paardekooper et al., 2011a). Figure from (Bitsch et al., 2013), with a stellar irradiated and viscous heated disk model. Black arrows show the direction of migration.

Typically, the total corotation torque is found to be **positive**, slowing down - or even reversing - the inward migration of low-mass planets. The sum of the Lindblad torque Γ_L and the corotation torque Γ_C in the case of small planet masses define what is called the type-I migration. Bitsch et al. (2013) performed 2D axisymmetric numerical simulations of a simple evolving disk model with constant viscosity ν to predict the outcome of type I migration in a non self-gravitating disk. They solved an energy equation described by viscous heating, radiative cooling, and stellar irradiation, and used prescriptions for the direction and speed of type I planet migration derived in (Paardekooper et al., 2011a). In such disk model, they find that stellar irradiation dominates in the outer regions, while the viscous heating dominates close to the star (see Appendix 2.A). Due to a positive total torque, they find for their model that type-I migration can be directed outwards, in a range of radial locations and for a range of planet masses, which makes the survival of planetary embryos in a disk possible. Fig. 3.3.2 shows the total specific torque (torque per unit planet mass) acting on planets with different masses as a function of their distance to the star. The red region encompassed by black lines are regions of outward migration. Outside these regions, planets are subject to inward migration. For instance, planets less massive than ~ 10 Earth masses irremediably migrate towards the star. The blue dashed lines, on the right-hand side of the black circles, are stable equilibrium positions for planets as any

perturbation in their orbital position will be countered by an episode of migration in the opposite direction (see the black arrows). Such regions are called "planet traps". Note that these regions are obtained for models with non-migrating planets and can be different when taking planet migration into account.

3.3.1.3 *Impact of self-gravity on the Lindblad torque*

As we will see in Chapter 6, the disk's self-gravity has an impact on planet migration in our simulations. Baruteau & Masset (2008b) have shown that self-gravity modifies the Lindblad torque without changing the corotation torque. More specifically, the migration rate of a planet migrating in a non self-gravitating disk is overestimated compared to the migration rate of the same planet when self-gravity is taken into account. This is due to a spurious inward shift of the Lindblad resonances when the planet feels the gravitational potential of the disk but the disk does not feel its own potential (Pierens & Huré, 2005; Baruteau & Masset, 2008b). The increase in the magnitude of the net Lindblad torque (faster migration) becomes significant when $Qh \lesssim 1$, with Q the Toomre parameter and h the disk's aspect ratio.

In general, not considering self-gravity can have an impact on many physical processes, whether it be on the Lindblad torque, but also on the setting of the gravitational instability for a Toomre parameter $Q < 1$, or on the damping of large-scale vortices. Concerning the latter, the non-axisymmetric part of the gas self-gravity significantly damps large-scale vortices induced by the Rossby-Wave Instability (with azimuthal wavenumber $m = 1$) when $Qh \lesssim 1$ (e.g., Lovelace & Hohlfeld, 2013; Zhu & Baruteau, 2016). When carrying out numerical simulations, it is therefore important to verify if self-gravity significantly modifies the results, for example by calculating the Toomre parameter beforehand. Basically, if $Qh \lesssim 1$, self-gravity has to be included in our numerical simulations of disk-planet interactions.

3.3.2 *Gap opening and the onset of type-II migration*

In the previous section (3.3.1), we have only considered the dynamical interaction between the gas of a protoplanetary disk and a low-mass planet, for which a perturbation theory is valid. However, if the perturbations are too large, that is if the perturbing planet is too massive, such linear analysis is not possible anymore.

For a planet mass typically larger than the mass of Saturn, the wakes evolve nonlinearly into shocks at a certain distance from the planet (Goodman & Rafikov, 2001; Rafikov, 2002). The wakes of a more massive planet will become shocks closer to the planet and deposit their angular momentum there. These shocks transfer angular momentum to the gas that eventually escapes from the coorbital region, leaving instead an annular gap (see Fig.3.3.1). How does this gap opening work? The inner wake conveys a negative flux of angular moment (the torque of the planet onto the gas through the inner wake is negative by the law of action and reaction, as $\Gamma_{w,i} > 0$), which tends to push the gas inward. Conversely, the outer wake conveys a positive flux of angular moment (the torque of the planet onto the gas through the outer wake is positive by the law of action and reaction, as $\Gamma_{w,e} < 0$) that pushes the gas outward. The size of the gap is mainly dominated by the competition between the **gravitational**

Planet	q_p
Earth	$\sim 3 \times 10^{-6}$
Saturn	$\sim 3 \times 10^{-4}$
Jupiter	$\sim 1 \times 10^{-3}$

Table 3.3.1: Planet-to-primary mass ratio for typical planet masses in the Solar System.

impact of the planet onto the gas and the turbulent **diffusion processes** that tend to fill with gas the gap that the planet carves. It also depends on the **pressure support** of the gas which determines the response of the disk to the imposed perturbations. This response depends on the sound speed. Thus, the ability of a planet to carve a gap depends logically on three parameters: the planet-to-primary mass ratio $q_p = M_p/M_\star$, the parametrization of angular momentum transport α (see sections 1.2.5, 2.1.2.3 and 2.1.3) and the disk's aspect ratio h_p in the vicinity of the planet's orbital radius. There is a widely used criterion to determine if a gap is carved around fixed circular planets, i.e. if the disk-planet interaction becomes non-linear. This **gap-opening criterion** (Crida et al., 2006) defines gap opening when the coorbital surface density drops to 10% of its unperturbed value. It reads:

$$\frac{h_p}{q_p^{1/3}} + \frac{50\alpha h_p^2}{q_p} \lesssim 1. \tag{83}$$

We give in Table 3.3.1 some typical values of q_p for planets in the Solar System ($M_\star = M_\odot$). Along with the formation of a gap, note that a massive enough planet also acquires a circumplanetary disk, which is an accretion disk around the planet that is fueled with material from the protoplanetary disk. Numerical studies seek to determine the global evolution of a protoplanetary disk a few tens of astronomical units wide as well as the gravitational influence of this smaller but closer structure. This contrast in scales is a challenge for such numerical simulations as it is costly to resolve the entire system.

We saw earlier that fluid elements circulating just outside the co-orbital region receive a kick of angular momentum every time they cross the wake (Masset, 2008, paragraph 4.2.1). The timescale over which a fluid element inside the horseshoe region performs a horseshoe orbit is called the libration timescale. One half of a libration timescale corresponds roughly to the time it takes for a gas element circulating just outside the horseshoe region to travel a complete orbit relative to the planet. Every time the fluid elements circulating just outside the co-orbital region cross the wake, they receive a kick of angular momentum. Therefore, planet wakes cede **cumulatively** some angular momentum to the background flow. What if the planet migrates in the disk? Numerical simulations have shown that the ability of a planet to carve a gap through the shocks of its wakes does not depend only on on q_p, h_p and α, but also on the planet's migration speed. The timescale for emptying the co-orbital region is linked to the libration timescale at the separatrices of the planet's horseshoe region[5], and is even shorter as the the migration timescale is longer. More specifically, for a

5 these separatrices separate the regions where fluid elements are in libration with the planet from regions outside the horseshoe region.

small migration rate (long migration timescale), the planet wakes shock repetitively the same gas elements as they circulate outside the horseshoe region. By doing so, the wakes deposit their angular momentum at that location and efficiently clear the coorbital region. On the contrary, for a large migration rate (short migration timescale), this slow-burning deposit of angular momentum cannot occur, and the planet wakes are unable to clear efficiently the horseshoe region.

The impact of planet migration on the gap formation is shown in Fig. 3.3.3. We force a 1.5 Saturn-mass planet to move radially inward in a disk at different migration rates: $\dot{a} = 0, -0.4, -1.7, -5.8, -17.6, -50$ m.s^{-1} (which approximately corresponds to $0, 0.1, 0.4, 1.3, 4, 11.3$ percents of the local sound speed at the initial location of the planet). In these 2D hydrodynamical simulations, the planet does not migrate freely given the disk-planet interactions, i.e. we do not consider the impact of the total torque on its orbital position. The six top panels show the gas density perturbation for these six values of the migration rate, and the bottom panel illustrates the corresponding axisymmetric gas density perturbations.

Several things can be noted in the bottom panel of Fig. 3.3.3, in particular on the properties of the gap. In the case without migration (dark blue line), the gap is roughly symmetric, with:

- a **local density maximum** at the radial position of the planet $R \sim R_p$, and which corresponds to the surviving fluid elements that perform horseshoe U-turns in corotation with the planet. In that region, some fluid elements are trapped in the gravitational equilibrium points of the planet, namely the L4 (in front of the planet in azimuth) and L5 (behind the planet in azimuth) Lagrange points (one can guess the L5 Lagrange point in the upper-left panel (no migration case) between $\phi = -1$ rad and $\phi = -2$ rad).

- two approximately symmetrical **density minima** that are present on each side of the planet, at $|R - R_p| \lesssim x_s$, with x_s the radial half-width of the horseshoe region (see Fig. 3.3.1). We denote by $\Delta^{\pm}_{r,gap}$ the radial distance between R_p and the local density minimum outside R_p, and between R_p and the local minimum inside R_p (see annotation in Fig. 3.3.3).

- two approximately symmetrical **density maxima** at both edges of the gap (at $|R - R_p| \gtrsim x_s$). Because gas density and gas pressure are linked via the expression $P_g \propto \Sigma_g T_g$, density maxima are related to pressure maxima for typical decreasing temperature profiles and sufficiently massive planets. At the radial location of these pressure maxima, the RWI develops, and consequently vortices form.

- the presence of **secondary gaps**, just inside the internal pressure maximum, closer to the star (at $R \sim 10$ au). These secondary gaps have been reported and studied in particular by Zhang et al. (2018).

Note that without migration, the gap is roughly symmetrical on both sides of the planet, i.e. the planet will empty its coorbital region approximately the same way internally and externally, and create pressure maxima at the origin of the vortices visible in the top-middle and top-right panels of Fig. 3.3.3. Several gap properties are

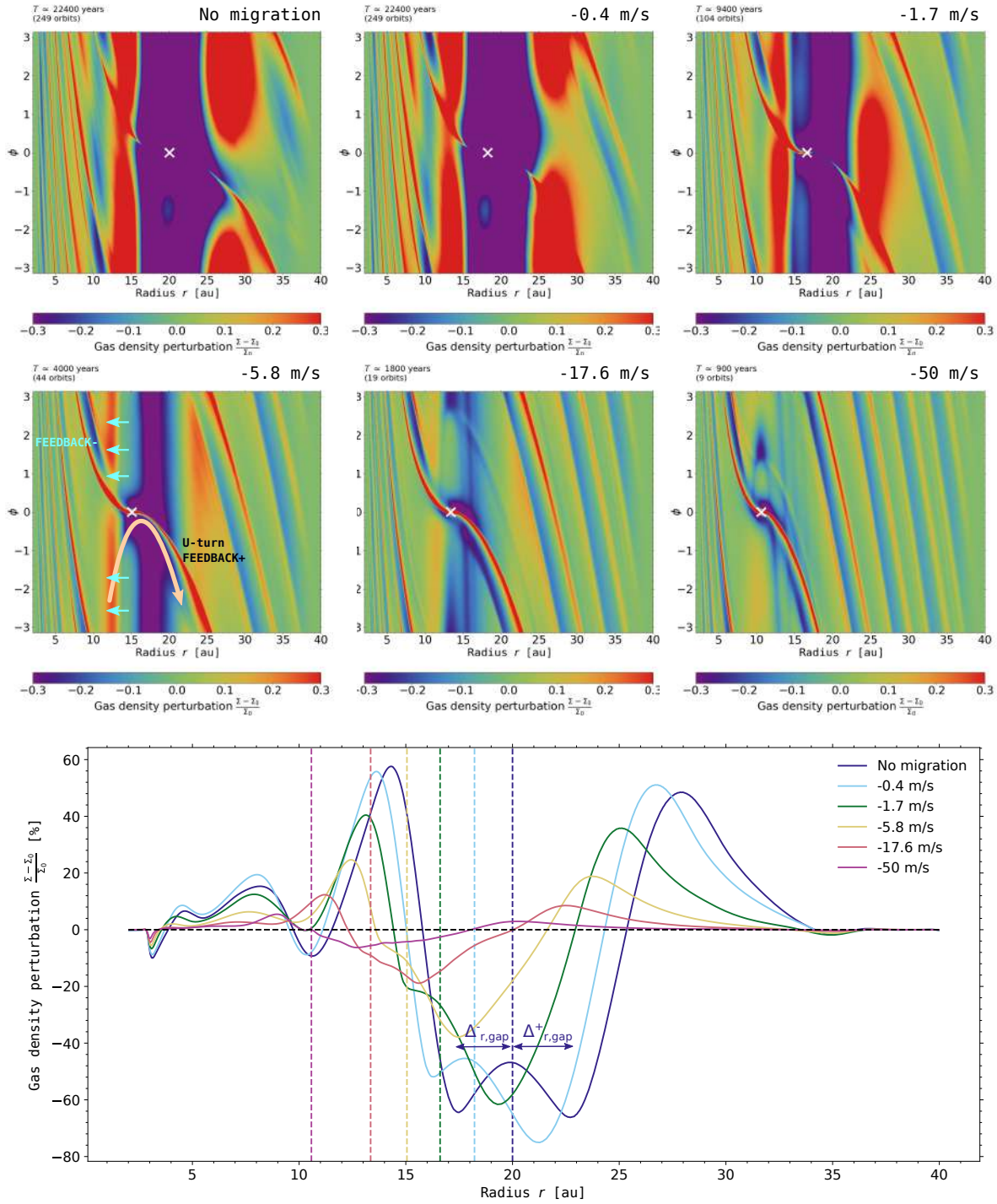

Figure 3.3.3: Results of 2D hydrodynamical simulations: impact of planetary migration on the carving of a gap. The planet-to-primary mass ratio $q_p = 4.3 \times 10^{-4}$ corresponds to a 1.5 Saturn-mass planet around a Solar-mass star. The six top panels show the relative perturbation of the gas surface density of the disk, with a migration rate fixed at $\dot{a} = 0, -0.4, -1.7, -5.8, -17.6, -50$ m.s^{-1}. The slower the planet, the deeper the gap. The bottom panel shows the axisymmetric gas surface density perturbation as a function of the distance to the star for these different $\dot{a}$. Vertical dashed lines show the position of the planet. The curves above and below the horizontal dashed line are over-densities and under-densities, respectively.

affected by planet migration, especially as the migration is fast (see also Malik et al., 2015).

- **Depth of the gap**: in this disk model, planets that migrate inward faster than ~ 5 m.s^{-1} (yellow curve) carve a gap half as deep as planets on a fixed orbit (dark blue curve). A non-migrating planet that follows the gap-opening criterion from Crida et al. (2006) will not necessarily do so if it migrates, even at low speed. It shows that migration reduces the ability of a planet to carve a gap.

- **Radial asymmetry of the gap**: the planet carves a (i) deeper and (ii) wider gap outside its orbital radius than inside it, even for a slow (inward) migration. For example, the light blue curve, for a speed $\dot{a} = -0.4$ m.s^{-1}, shows a deeper gap (75% density drop at $R > R_p$ instead of 50% at $R < R_p$) and wider gap ($\Delta^{+}_{r,gap} \sim 3.5$ au at $R > R_p$ instead of $\Delta^{-}_{r,gap} \sim 1.5$ au at $R < R_p$) than without migration.

- **Pressure maxima**: akin to the depth of the gap, the pressure bumps (linked to the density bumps) on each side of the planet's radial position are less pronounced. For instance, the pressure maximum outside R_p for $\dot{a} = -50$ m.s^{-1} is twelve times fainter than the pressure maximum outside R_p without migration. A fast migrating planet is therefore less efficient at carving a gap and creating pressure maxima.

- Note the asymmetrical structure visible inside the horseshoe region in the density panels corresponding to $\dot{a} = -17.6$ and -50 m/s, in front of the planet in azimuth for an inward migrating planet. This structure, sometimes called 'tadpole region', is in corotation with the planet and is related to the planet's fast migration. We will come back to this structure in chapter 6.

Generally speaking, the faster the planet migrates, the shorter the time it can interact with the disk gas near its orbit and the less visible its perturbations in the gas density (very few visible structures in the panel with $\dot{a} = -50$ m/s compared to the panel with no migration, apart from the wakes). It is therefore essential to consider the feedback of these perturbations on the migration itself.

As for low-mass planets, the migration of massive planets opening a gap around their orbit results from the Lindblad and static corotation torques. On the one hand, for planets which carve a deep gap ($> M_{Jupiter}$ planets), the corotation torque is largely weakened. The Lindblad torque thus becomes the main source of migration (usually directed inwards). This is called type-II migration. On the other hand, for intermediate-mass planets that open a partial gap around their orbit (typically around $1 M_{Saturn}$), the planet migration can have a strong feedback effect on the corotation torque in particular, which can lead to the triggering of episodes of runaway migration. This is called type-III migration. We consider in the following section the impact of planet migration onto the corotation torque, which gives rise to a new component of the corotation torque called dynamical corotation torque.

3.3.3 *Type-III migration*

3.3.3.1 *Dynamical corotation torque*

When an intermediate-mass planet ($\sim M_{Saturn}$) partially carves a gap, the remaining material in the corotation region can have a strong impact on the planet dynamics. In a few words, this dynamical corotation torque is, again, the result of two opposite phenomena:

- **Negative feedback**: the planet drags the trapped coorbital fluid elements like Sisyphus drags its boulder. It creates a torque that tends to slow down the migration. For instance, when the planet moves inwards, it needs to exert a negative torque on its corotation region so that both the planet and its corotation region migrate jointly. By the law of action / reaction, the gas in the migrating corotation region thus exerts a positive torque on the planet that slows down the joint inward migration, hence the negative feedback.

- **Positive feedback**: due to its migration, the planet progressively interacts with disk regions where the gas, which was initially on circular orbits relative to the planet before the planet coming through, ends up making single U-turns relative to the planet. This orbit-crossing new material creates a torque that tends to speed up the migration. For instance, when the planet moves inward, the material from the inner disk is forced to perform outward horseshoe U-turns. This flow thus exerts a negative torque on the planet that speeds up the inward migration, hence the positive feedback.

In massive protoplanetary disks, for gaps sufficiently cleared out, the negative feedback can be reduced while the positive feedback is enhanced. We will find again this positive feedback enhancement in the next section. See an illustration of this enhancement with the arrows in the panel with $\dot{a} = -5.8$ m/s in Fig. 3.3.3. Without anything to restrain the positive feedback on migration, the planet can undergo an episode of runaway migration, called type-III migration (Masset & Papaloizou, 2003). Note that the effect of the dynamical corotation torque may also be important for type-I migration, i.e. for planets that do not open a significant partial gap (Paardekooper, 2014; Pierens, 2015). For the disk models in Paardekooper (2014), depending on the radial gradient of vortensity and the initial direction of migration, inward migration can be slowed down and outward migration can run away. We describe in the next section a useful criterion to constrain the runaway regime: the coorbital vorticity-weighted deficit.

3.3.3.2 *A coorbital deficit*

We derive here for convenience simple calculations that lead to the criterion for migration to run away. More details can be found in the works of Masset & Papaloizou (2003); Masset (2008). Remember that x_s is the radial half-width of the horseshoe region (see Fig. 3.3.1). Fluid elements that are located at $R \in [R_p - x_s, R_p + x_s]$ perform at least one horseshoe U-turn from the inner/outer disk to the outer/inner disk. On

the contrary, fluid elements located at $R < R_p - x_s$ and $R > R_p + x_s$ freely circulate around the star. The radial locations $R_p - x_s$ and $R_p + x_s$ therefore define the inner separatrix and the outer separatrix respectively. In this section we suppose that the planet migrates inward. We therefore consider the torque due to fluid elements that cross the orbit from the inner to the outer disk.

- **1st step**: we calculate the gain of specific angular moment Δl (total angular momentum ΔL per unit of mass ΔM) of a fluid element switching from the inner separatrix to the outer separatrix, to the detriment of the planet:

$$\begin{aligned} \Delta l &= \frac{\Delta L}{\Delta M}, \\ &= l(R_p + x_s) - l(R_p - x_s), \\ &= \sqrt{GM_\star}\left[\sqrt{(R_p + x_s)} - \sqrt{(R_p - x_s)}\right], \\ &= \sqrt{GM_\star R_p}\frac{x_s}{R_p} + \mathcal{O}\left[\left(\frac{x_s}{R_p}\right)^2\right], \\ &= \Omega_p R_p x_s, \end{aligned} \tag{84}$$

at first order in x_s/R_p, with Ω_p the Keplerian angular frequency at the planet location. The dynamical corotation torque Γ_C exerted on the planet during this passage of the fluid elements from $R_p - x_s$ to $R_p + x_s$ is therefore, using the conservation of angular momentum:

$$\begin{aligned} \Gamma_C &= \frac{\Delta L}{\Delta t}, \\ &= \frac{\Delta L}{\Delta M}\frac{\Delta M}{\Delta t}, \\ &= \Delta l \dot{M}. \end{aligned} \tag{85}$$

In order to determine the expression of Γ_C, we thus look for the mass flow $\dot{M}$ crossing the coorbital region, for a planet in steady migration at the migration rate $\dot{a} = \Delta a/\Delta t$. The mass of the ring of fluid elements of radial width Δa next to the inner separatrix is, assuming a uniform gas surface density Σ_S:

$$\Delta M = 2\pi\Sigma_S R_p(1 - \frac{x_s}{R_p})\Delta a, \tag{86}$$

which gives for the mass flux:

$$\dot{M} = 2\pi\Sigma_S R_p \dot{a} + \mathcal{O}\left(\frac{x_s}{R_p}\right). \tag{87}$$

Finally, the dynamical corotation torque on the planet from Eq. (85) becomes, at first order in x_s/R_p:

$$\Gamma_C = (2\pi\Sigma_S R_p \dot{a}).(\Omega_p R_p x_s). \tag{88}$$

The expression in Eq. (88) does not depend on the hypothesis of an inward migrating planet. Note that Γ_C has the sign of $\dot{a}$, which leads to a **positive** feedback.

- **2nd step**: we apply the equation of conservation of angular momentum $\frac{dL}{dt} = \Gamma_L + \Gamma_C$, to the whole system (with mass M_{tot}) in corotation with the planet, namely the planet itself (with mass M_p), its circumplanetary disk (with mass M_{CPD}) and the horseshoe region (with mass M_{HS}). We define the total mass of the circumplanetary system $\overline{m_p} = M_p + M_{CPD}$, assuming that the circumplanetary disk dynamically belongs to the planet. We have thus $M_{tot} = \overline{m_p} + M_{HS}$ and

$$\frac{dL}{dt} = \frac{\Omega_p}{2} R_p \dot{a} M_{tot}, \tag{89}$$

where we used $L = \sqrt{GM_\star R_p} M_{tot}$ and $\dot{a} = \frac{dR_p}{dt}$.

- **3d step**: we can combine Eq. (88) and Eq. (89):

$$\begin{aligned} \frac{\Omega_p}{2} R_p \dot{a} M_{tot} &= \Gamma_L + (2\pi\Sigma_S R_p \dot{a}).(\Omega_p R_p x_s), \\ \frac{\Omega_p}{2} R_p \dot{a} (\overline{m_p} + M_{HS}) &= \Gamma_L + \frac{\Omega_p}{2} R_p \dot{a} (4\pi\Sigma_S R_p x_s), \\ \frac{\Omega_p}{2} R_p \dot{a} \overline{m_p} &= \Gamma_L + \frac{\Omega_p}{2} R_p \dot{a} \delta m. \end{aligned} \tag{90}$$

$\delta m = 4\pi\Sigma_S R_p x_s - M_{HS}$ is called the *coorbital mass deficit*, as it corresponds to the difference between the mass that the horseshoe region would have if its surface density was uniform and on average equal to Σ_S (the gas surface density in the inner separatrix) and the mass that this region actually has. In reality, fluid elements **about** to make U-turns at the inner separatrix do not instantaneously impact the angular momentum of the circumplanetary system. There is a delay (denoted by τ), a latency between the moment when fluid elements engage a horseshoe U-turn at $R_p - x_s$ and the moment when they actually modify the angular momentum of the circumplanetary system through the corotation torque Γ_C. By including the time dependence of Γ_C, Eq. (90) reads:

$$\frac{\Omega_p}{2} R_p \dot{a}(t) \overline{m_p} = \Gamma_L(t) + \frac{\Omega_p}{2} R_p \dot{a}(t-\tau) \delta m, \tag{91}$$

which becomes, using a first order Taylor expansion in time $\dot{a}(t-\tau) = \dot{a}(t) - \tau\ddot{a}(t)$:

$$\left(1 - \frac{\delta m}{\overline{m_p}}\right) \dot{a}(t) + \tau \frac{\delta m}{\overline{m_p}} \ddot{a}(t) = \frac{2\Gamma_L(t)}{\Omega_p R_p \overline{m_p}}. \tag{92}$$

This first-order differential equation takes the form $\dot{X} + KX = b$, with $X = \dot{a}$ and

$$K = \frac{1}{\tau}\left(\frac{\overline{m_p}}{\delta m} - 1\right), \tag{93}$$

and its solution can be written as:

$$X(t) = X_0 + X_1 \exp(-Kt), \tag{94}$$

with X_0 and X_1 two constants. Depending on the value of K, one can distinguish between two migration regimes:

- if $K > 0$, that is if $\delta m < \overline{m_p}$: the exponential term in Eq. (94) decreases with time. It means that the migration rate quickly reaches the constant value X_0, which mostly depends on the Lindblad torque Γ_L.
- if $K < 0$, that is if $\delta m > \overline{m_p}$: the migration rate increases exponentially, and the planet enters a regime of fast runaway migration, also referred to as type-III migration. For δm to be high enough, there must be a significant density difference between the separatrix location and the coorbital region, which is the case when the planet is able to carve a significant gap in its coorbital region. Moreover, as δm increases with Σ_S, a more massive protoplanetary disk favours type-III migration. Note however that if the planet is too massive, the gap is larger. It implies a lower value of Σ_S, which decreases δm and the dynamical corotation torque. The planet then enters a regime of type-II migration.

Note that δm is actually a bit more involved, as it features a gradient of vortensity (Masset & Papaloizou, 2003). We saw indeed in section 3.3.1.2 that the static corotation torque strongly depends on the radial gradient of the inverse vortensity $\mathcal{I}_\mathcal{V}$, and not directly on the gas surface density. A more complete approach taking into account $\mathcal{I}_\mathcal{V}$ gives a "coorbital vorticity-weighted deficit". We will use this more accurate definition in chapter 6.

3.3.4 *A short recap on planet migration*

In this PhD thesis (in particular in chapter 6), we will largely use the q/h^3 parameter. This dimensionless parameter is present in the gap-opening criterion (Eq. 83) and is a good quantity to discriminate between the different regimes of migration:

- $\frac{q}{h^3} \ll 1 \implies$ This condition defines the type-I migration regime. More applicable to low-mass planets ($\lesssim 10$ Earth masses), this regime strongly depends on the disk's properties (gas surface density, gas temperature, turbulent viscosity,...). See section 3.3.1 for more details.
- $\frac{q}{h^3} \gg 1 \implies$ Massive planets (Jupiter-like planets) deplete their horseshoe region which becomes a deep annular gap because of shocks that push matter away

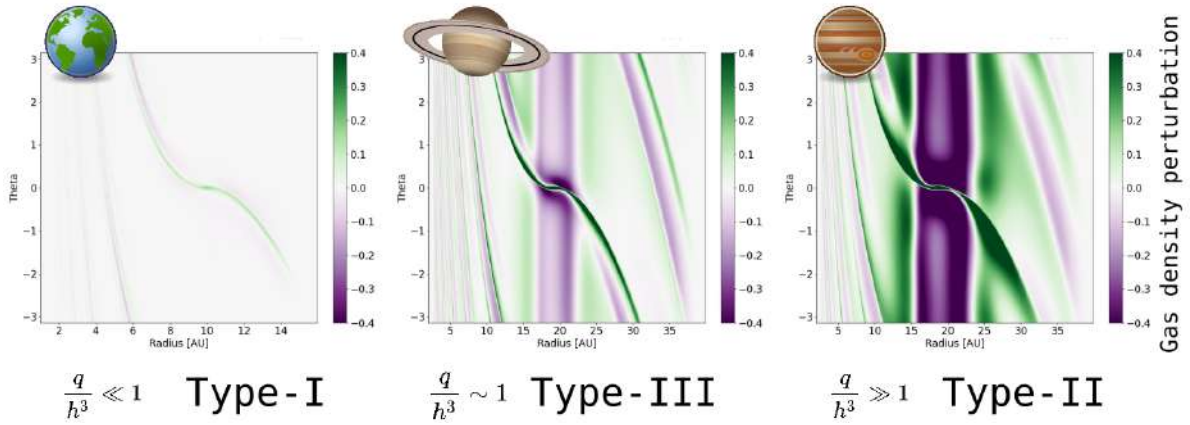

Figure 3.3.4: Representation of the three regimes of migration thanks to results of 2D hydrodynamical simulations. Low-mass planets in type-I migration induce small perturbations in the gas (less than ~ 10%, see left panel). More massive planets generate strong shocks via spiral density waves, and can open a partial gap (middle panel) or a deep gap (right panel) depending on their mass and on the disk's physical properties (mainly its temperature and its turbulent viscosity), leading to type-III or type-II migration respectively.

from the planet. In 2D simulations, gap-opening planets usually migrate inwards, and are subject to type-II migration. See section 3.3.2 for more details.

- $\frac{q}{h^3} \sim 1 \Longrightarrow$ Planets with intermediate masses (Saturn-like planets) can be subject to a fast runaway migration when the disk is massive enough. This phenomenon is due to a backreaction of the planet dynamics onto the disk torques, creating an additional torque: the dynamical corotation torque (see section 3.3.3). This regime is called type-III migration (see section 3.3.3.2 for more details).

We show in Fig. 3.3.4 a polar representation of the three migration regimes, with the relative perturbations of the gas surface density induced by planets. For a general review on formation, orbital and internal evolutions of young planetary systems, see Baruteau et al. (2016). In this work, we mainly assess the impact of the gas on planet migration, but other works have shown that the planet orbital evolution can be different in a dusty environment. In particular, some studies have proposed that low-mass planets can be subject to torque oscillations whose amplitude increases with the dust-to-gas density ratio. These oscillations arise from small-scale vortices that develop in the planet's corotation region due to a Rossby-Wave-like instability setting in the dust fluid and which generate spiral density waves in the gas. They induce fluctuations in the corotation torque that add up to the background Lindblad and corotation torques. This phenomenon is found to be amplified for increasing Stokes numbers and dust-to-gas mass ratios, and can even lead to a stochastic migration. More generally, such studies suggest that the inward migration of low-mass planets can be slowed down and even reversed in a dusty environement. For more details you can see the works of Chen & Lin (2018); Benítez-Llambay & Pessah (2018); Hsieh & Lin (2020).

4

DISK SUBSTRUCTURES AND HOW TO CREATE THEM

Over the last few years, spatially resolved observations have revealed many diverse substructures in protoplanetary disks, which have challenged the classical picture of disks being smooth continuous sub-Keplerian objects. A fair fraction of spatially resolved disks show indeed substructures, including spirals, axisymmetric and asymmetric rings when observed from the near-IR to the (sub-)mm. In particular, sequences of dark rings (gaps) and bright rings are the most frequent substructures revealed by radio interferometry with ALMA. Spectral line emission also provides a variety of substructures, with in particular the promise of velocity kinks. Either way, all the observations that are now able to resolve the outer parts of protoplanetary disks have stimulated theoretical studies about the physical processes at work in these young systems. In section 4.1, we present some statistics about disks with annular substructures. We then describe the diversity of substructures in the dust of protoplanetary disks in section 4.2 and their possible origin in section 4.3. Some substructures in the gas are introduced in section 4.4. Finally, we focus more specifically in section 4.5 on the predicted signatures of planet migration in the dust continuum emission.

CONTENT

4.1 Statistics and biases . . . 81
4.1.1 General mechanisms... . . . 81
4.1.2 ... able to generate multiple rings . . . 82
4.2 Substructures in the dust . . . 83
4.3 How to create rings and crescent-like structures? . . . 87
4.3.1 Snowlines-related mechanisms . . . 90
4.3.2 The pressure maxima, these dust traps . . . 91
4.4 Substructures in the gas . . . 93
4.4.1 Global diagnostics . . . 94
4.4.2 Channel maps . . . 95
4.4.3 Velocity kinks . . . 97
4.5 What about the predicted signposts of planetary migration ? . . . 99

5 NUMERICAL METHODS 105

4.1 STATISTICS AND BIASES

4.1.1 *General mechanisms...*

One of the least biased samples of substructures in disks has been studied by Long et al. (2018, 2019). This ALMA 1.33 mm survey gathers observations of 32 disks in the Taurus star-forming region. These disks have been divided in three sub-samples: Disks with Annular Substructures (DAS), smooth disks in single stars and smooth disks around the primary of multiple-star systems. These disks are represented in the three parts of Fig. 4.1.1 delimited by black vertical dashed lines. In Long et al. (2018, 2019), ~ 40% (12/32) of their sample features axisymmetric rings and gaps. In order to explain such a large fraction of DAS, we thus need one or several general mechanisms. Note that this fraction of DAS is actually a lower boundary, as explained below.

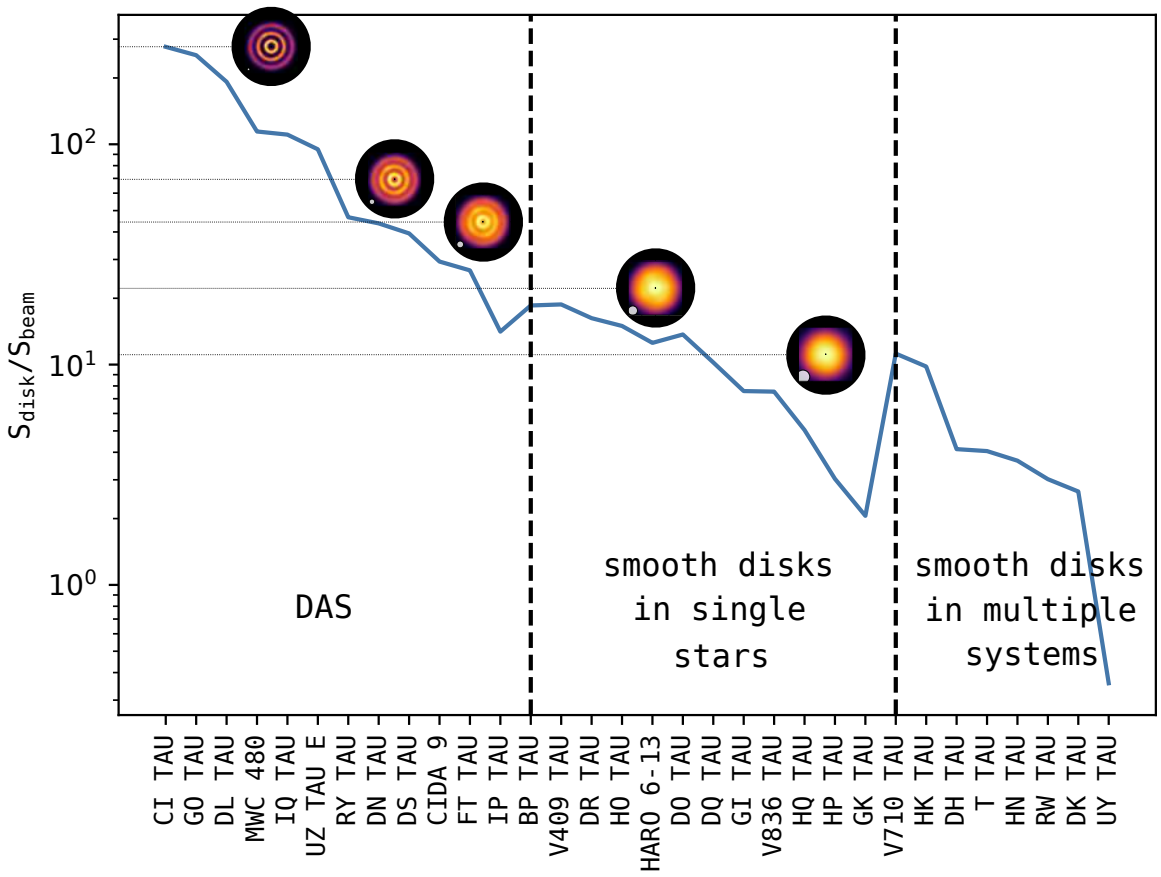

Figure 4.1.1: Disk area compared to beam area for the disk sample in Long et al. (2018, 2019). The first twelve disks are DAS, the others are smooth disks, whether they be in single-star or in multiple-star systems. These three sub-samples are delimited by vertical black dashed lines. Each inset image shows the results of dust radiative transfer calculations performed with `RADMC3D` (see text and chapter 5).

Long et al. (2018) highlighted that multiple-ring systems tend to be more extended than single-ring ones. But in general, DAS tend to be more extended than smooth

disks. This is shown in Fig. 4.1.1, where we display the disk-to-beam surface ratio S_{disk}/S_{beam} of all the disks in their sample. Recall that $S_{beam} = \frac{\pi b_{min} b_{max}}{4 \ln 2}$, with b_{min} and b_{max} respectively the beam minor-axis and major-axis. Since all the disks in the aforementioned sample have about the same beam area, S_{disk}/S_{beam} gives an idea of the disk sizes $R_{1.3\ mm}$. The size $R_{1.3\ mm}$ of a disk encircles here 95% of this disk's total intensity at 1.3 mm wavelength (see section 1.2.2). Most of the DAS (left part in Fig. 4.1.1) are larger than the smooth disks, with the exception of IP TAU, which has a deep cavity in the sub-mm. The quantity S_{disk}/S_{beam} gives also an idea of the resolution. For example, if $S_{disk}/S_{beam} = 100$, then the disk is well-resolved, depending on the typical width of the radial substructures. The impact of the beam size on the visibility of substructures when decreasing resolution is illustrated in Fig. 4.1.1 by the horizontal dotted lines terminated by synthetic disk images. They show the evolution of the dust continuum emission at 1.3 mm for a single simulation that features multiple bright and dark rings, by just varying the disk-to-beam surface ratio ($S_{disk}/S_{beam} \simeq 277, 69, 44, 22, 11$). While the multiple rings are clearly visible in the top patches ($S_{disk}/S_{beam} \gtrsim 30$), they cannot be discerned for $S_{disk}/S_{beam} \lesssim 25$. For this disk model, the beam size is thus essential in the detection or non-detection of bright rings. One may therefore wonder whether the non-detection of substructures in small smooth disks ($S_{disk}/S_{beam} \lesssim 20$) really reflects the absence of bright rings, or whether it is only a matter of beam resolution. For a smaller beam size, the fraction of DAS could potentially increase. We will come back to this question of resolution in the next section.

4.1.2 *... able to generate multiple rings*

Not only the mechanisms behind DAS need to be general, but they have to be able to generate multiple rings in a given system. If we focus on DAS in the (sub-)mm continuum from the Disk Substructures at High Angular Resolution Project (DSHARP) in addition to HL Tau, TW Hya, the sample of Long et al. (2018) and other DAS listed in Table 5 of Huang et al. (2018a), we see that around $\sim$ 35% (16/45) of DAS are single-ring systems and $\sim$ 65% (29/45) are multiple-ring systems. As stated in section 4.1.1, this classification is based on the current resolution at which disks are observed. A better resolution could possibly reveal more rings. This is the case for example of the disk around HD 169142, for which the outer bright ring observed with a $\sim 0''.2 \times 0''.2$ beam ($S_{disk}/S_{beam} \lesssim 25$) by Fedele et al. (2017) (right part of Fig. 4.1.2) turns out to be comprised of three narrow rings when observed with an angular resolution about ten times better ($S_{disk}/S_{beam} \lesssim 2800$) (Pérez et al., 2019, and left part of Fig. 4.1.2). Another bias is the choice of the targets: if, as suggested by Long et al. (2018), multiple-ring disks are truly more massive and larger, targets were deliberately composed of massive and extended disks in the DSHARP sample. This argument could explain the seemingly large current fraction of multiple-rings disks. In any case, the mechanisms behind the presence of annular substructures should be sufficiently general to occur in a significant fraction of protoplanetary disks and should be able to generate multiple rings.

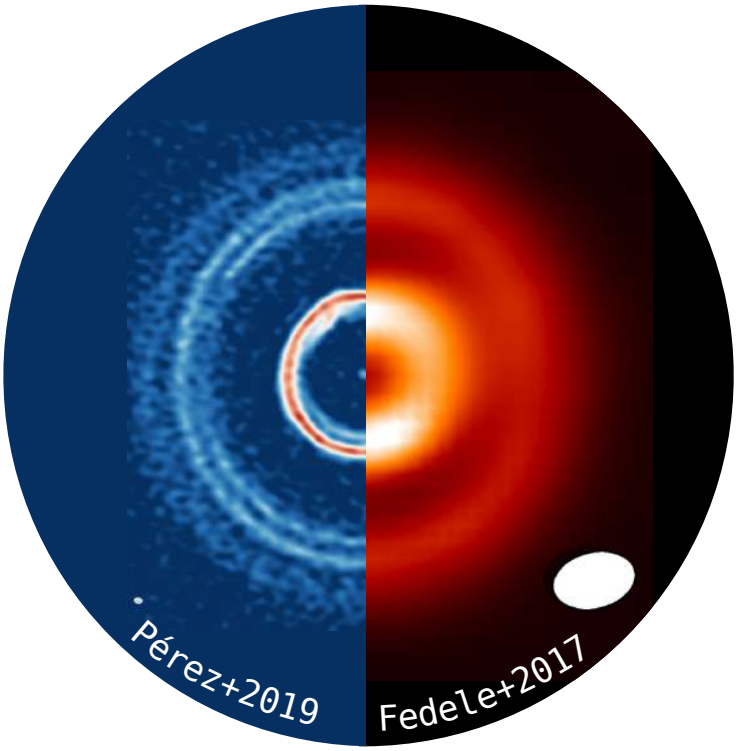

Figure 4.1.2: ALMA 1.3 mm continuum map of the protoplanetary disk HD 169142, adapted from Fedele et al. (2017) and Pérez et al. (2019).

Fig. 4.1.3 summarizes the statistics presented in the previous two sections. Please note that not every annular substructure is commonly referred to as a ring. In some cases, what we call here 'annular substructure' may be the result of a cavity carved in the inner regions of the disks. The DAS listed in the statistics here have one or more bumps/rings/crescents in the radial intensity profile of the dust continuum emission, regardless of the origin (radial bump, ring or cavity).

In order to illustrate the following sections, we largely make use of Fig. 4.3.0, which displays a gallery of sixteen disks with substructures at different wavelengths, obtained with various observational tracers (dust thermal emission, scattered light and CO emission). Several observations of the same disk are sometimes displayed. Note that we focus in Fig. 4.3.0 on recent observations which highlight clear substructures in the specific intensity. Some observations with less clear detection of substructures are not considered here.

4.2 SUBSTRUCTURES IN THE DUST

Substructures in protoplanetary disks are now commonly detected thanks to the rapid improvements of the facilities and instrumentation. A few years ago, disks were typically observed at a $\sim 0''.5 - 1''.0$ angular resolution so that it was not possible indeed to resolve such structures. You can see again in Fig. 4.1.2 the outstanding evolution of the beam resolution in the space of two years. Many types of substructures are

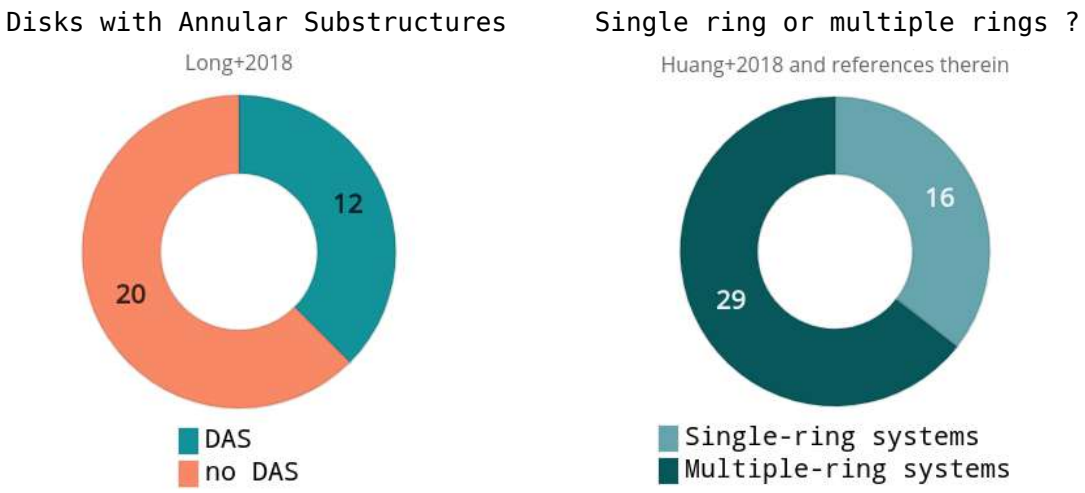

Figure 4.1.3: Left: number of disks with annular substructures (DAS) in the sample of Long et al. (2018). 40% (12/32) of their sample show at least one ring. Right: among the DAS listed in Huang et al. (2018a), including the 12 DAS in the left panel, a large fraction of them shows multiple bright rings.

detected in the dust content of protoplanetary disks, with a current resolution limit of a few au. Dealing with high resolution observations is necessary in order to constrain the plausible models at the origin of dust substructures. In particular, the first step when faced with the multitude of observations available, whether via scattered light or thermal dust emission, is to try to determine similarities and differences. This is a classification step, where different categories of substructures emerge.

- **Spirals**: large-scale spirals are frequently observed, mainly in scattered light (see, for example, Benisty et al., 2015; Stolker et al., 2016; Benisty et al., 2017), but sometimes also in the dust thermal emission (Huang et al., 2018b). Whether at the surface of protoplanetary disks or deep in the midplane, this type of substructure seems to be fairly common. Spirals in disks are a generic response of a compressible fluid in differential rotation subject to perturbations, and are thus an indirect consequence of many mechanisms at work in protoplanetary disks. These mechanisms can be divided into several categories. First of all there are the disk responses to a **gravitational** perturbation, such as the impact of a planet or a substellar companion (see for example Bae & Zhu, 2018a,b; Baruteau et al., 2019; Calcino et al., 2020, and Fig. 3.3.1), of a stellar flyby (Cuello et al., 2019, 2020), or of localized massive structures like vortices (Zhu & Baruteau, 2016). Then there are the responses of the disk to a **hydrodynamical** perturbation, for example related to the nonlinear evolution of the gravitational instability (see Gammie, 2001, and section 2.3.2), to the accretion shock between a disk and an infalling envelope (Lesur et al., 2015; Hennebelle et al., 2016, 2017) or to the action of MRI turbulence (Heinemann & Papaloizou, 2009a,b). Given the multiplicity of possible models at the origin of the spirals, we can expect to find these structures at all scales in protoplanetary disks. See for example Meru et al. (2017); Forgan et al. (2018) for three different models of the spirals morphology

in the Elias 2-27 disk: due to an internal companion, an external companion or gravitational instability. Elias 2-27, WaOph 6, MWC 758 and HD 135344 B, which are displayed in Fig.4.3.0, are examples of disks that exhibit a spiral pattern.

- **Cavities**: Cavities are observed in the disks also at all wavelengths, in the dust thermal emission (see for example in Long et al., 2018; Keppler et al., 2019), but also in scattered light (see, e.g., in Follette et al., 2017; Avenhaus et al., 2017; Pinilla et al., 2018) and in the gas emission, in particular in CO lines (Carmona et al., 2017; van der Marel et al., 2018). However, a cavity in the dust emission is not always a cavity in the gas (Carmona, 2010). A disk with a cavity is generally characterized by a ring of emission inside which the emission dramatically drops off down to the star. Such disks are often called 'transitional disks' (see section 2.1.4). Note that the sub-mm observation of a cavity in a disk corresponds to a drastic decrease in the continuum emission intensity in the disk's central parts, and not directly a decrease in the dust density, since the intensity also depends on the dust temperature and opacity (see Eq. 1 for an analytical expression in 2D without scattering). If such cavities are related to a dust depletion in the disks' inner regions, they can be due to an inside-out clearing photoevaporation process, or by one or several giant planets lurking in the inner disk (see section 2.1.4 and Owen, 2016). In addition, the difference between ring/cavity and other types of substructures such as ring/gap can be subtle and arbitrary, as such observations also depend on how well the inner parts of the disks are resolved. You can see some examples of disks with a cavity in Fig.4.3.0, with HD 142527, Oph IRS 48, CIDA 9, RX J1604-2130 and PDS 70.

- **Crescents**: These arc features are mainly observed in radio (van der Marel et al., 2013; Boehler et al., 2017; Dong et al., 2018; Cazzoletti et al., 2018) and in the spectral line emission (see for example MWC 758, HD 142527 in Fig.4.3.0 respectively from Boehler et al., 2018, 2017). They are sometimes isolated (for example HD 142527 or Oph IRS 48 in Fig.4.3.0) or alongside other substructures, either rings (e.g., HD 135344 B in Fig.4.3.0) or other arcs features (e.g., MWC 758 also in Fig.4.3.0). If this kind of non-axisymmetric emission is indicative of an azimuthal accumulation of dust, it is generally associated with vortices created by the RWI (see section 2.3.4), or with the trapping of particles in the Lagrange points of a massive planet (see, e.g., Montesinos et al., 2020, and section 7.5 on the impact of migration on Lagrange points). But it can also be the consequence of inclined structures (warps) close to the star, like a tilted inner disk (Marino et al., 2015) or tilted binaries (Facchini et al., 2013). Note that we have noticed in some of our radiative transfer calculations that a dust clump in the inner part of a disk can create a 'wall' that partly blocks the star radiation. The dust temperature just behind this wall can decrease sharply, which also strongly decreases the intensity of the continuum emission. This shadow from inner structures could also create asymmetries in the dust thermal emission. Be aware that the shape of the beam can also be at the origin of some artificial non-axisymmetric structures in the dust thermal emission. See for instance the inner ring of HD 169142 in Fig. 4.1.2, which shows an increased emission along the beam's minor axis (right panel),

but this asymmetric emission is not recovered at higher angular resolution (left panel).

- **Bright and dark rings**: The observation of axisymmetric annular sub-structures, sometimes multiple, has aroused a lot of interest in the field of protoplanetary disks. Since the groundbreaking observation of HL Tau in 2015 (ALMA Partnership et al., 2015), sequences of bright rings and dark rings (or gaps) have been observed in many disks (see the statistics presented in Fig. 4.1.3), notably using ALMA in radio (see for example Huang et al., 2018a; Isella et al., 2018; Guzmán et al., 2018; Long et al., 2018) and SPHERE in near-IR (see, e.g., Avenhaus et al., 2018). A few examples in mm (HD 163296, HD 169142, AS 209) and in near-IR (RX J1615-3255, V4046) are presented in Fig. 4.3.0. We will dedicate the next subsection 4.3 to discuss the possible origins of bright and dark rings in the dust emission of protoplanetary disks.

- Many other substructures have been observed, less frequently, in protoplanetary disks. For instance, **large-scale filaments** are detected in the scattered light of WW Cha or DoAr 21 (see Garufi et al., 2020, and Fig. 4.3.0). It could be material falling into, or else ejected from the disk. In some of our simulations with a planet and a large disk, we noticed that eccentric modes could sometimes wipe the disk out after the formation of a bright ring outside the planet location, creating some eccentric and extended material. A close encounter during a stellar flyby could also generate such large-scale filaments (Cuello et al., 2020). **Blobs** or apparent point sources observed in near-IR are often presented as planetary or substellar companion candidates. The most striking example is given by Müller et al. (2018) with PDS 70 (see Fig. 4.3.0 and section 3.1). However, the transition from observing a blob to declaring a planetary companion can sometimes be challenging. Is a blob the bright counterpart of a circumplanetary environment, or a localized emission feature from the disk ? Depending on the beam resolution, it can be difficult to judge if such substructure is a forming planet or a disk feature that is not well resolved (see Quanz et al., 2015; Currie et al., 2014, for the disk HD 100546). Other small-scale structures have been detected, like the **'coma-shaped' structures** (see Fig. 4.3.0) in HD 169142 (Pérez et al., 2019) and in HD 163296 (Isella et al., 2018). In this latter case, Isella et al. (2018) have suggested that such localized structures can be due to the emission of dust particles trapped in the vicinity of a Lagrange point of a massive planet. For a gap-opening planet on a fixed circular orbit, it is however expected that Lagrange points are located in the center of the gap. In the HD 163296 disk, the coma-shaped emission is located in the outer half of the gap in the radial direction (i.e. closer to the gap's outer edge), and one can thus wonder if an outward migrating planet could generate such coma-shaped features. We will briefly present a project about the dust emission at the Lagrange points of a migrating planet in section 7.5. Filaments, blobs or coma-shaped structures, which are less frequently observed than rings and gaps for example, could be related to fast or transient phenomena. Perhaps they will become more and more visible as observation techniques and facilities improve.

The above classification is not only important to refine models, but also to guide future observations. However, several pitfalls are to be avoided. First of all, it is necessary to fight against the idea that substructures within the same category have to be the consequence of a same phenomenon. Finding a single mechanism responsible for a collection of substructures may be attractive, but by doing so one neglects the possibility of a complex dynamics where several mechanisms are mixed and blended. On the other hand, one must keep in mind that a given mechanism can evolve over time and create different types of substructures. Let us take the example of the RWI which generates vortices at the location of pressure maxima. Over time, vortices tend to merge and form axisymmetric rings. What was originally a crescent of dust eventually becomes a symmetrical ring of dust. This temporal dimension is thus not to be neglected in the interpretation of substructures. We will come back to this point in sections 4.5 and 7.2. Finally, multi-wavelength observations can unveil several substructures within the same disk (see Fig. 1.1.2, and each row in Fig. 4.3.0). The same mechanism can therefore, for example, generate several types of features that only make sense once observed in several wavelengths. This is the classical picture of several people watching the same animal from different angles, and who understand that it is actually an elephant only by sharing each of their isolated observations.

We present in the next section some mechanisms able to generate rings, gaps and crescent-like structures in protoplanetary disks.

4.3 HOW TO CREATE RINGS AND CRESCENT-LIKE STRUCTURES?

Bright and dark rings observed in the (sub-)mm are often interpreted as dust over-densities and under-densities in the midplane of protoplanetary disks. However, generally, radial variations of the observed intensity are not necessarily related to radial variations of the dust density. When scattering is negligible, the specific intensity at frequency ν (I_ν) is linked to the dust temperature T_d, the dust's surface density Σ_d, and the dust's absorption opacity κ_ν (see, e.g., the review by Andrews, 2015, his Eq. 2, or Eq. 1). Thus, radial variations of I_ν can be due to radial variations of T_d, Σ_d and/or κ_ν. Any mechanism able to induce radial variations of these quantities could in principle explain bright and dark rings of emission.

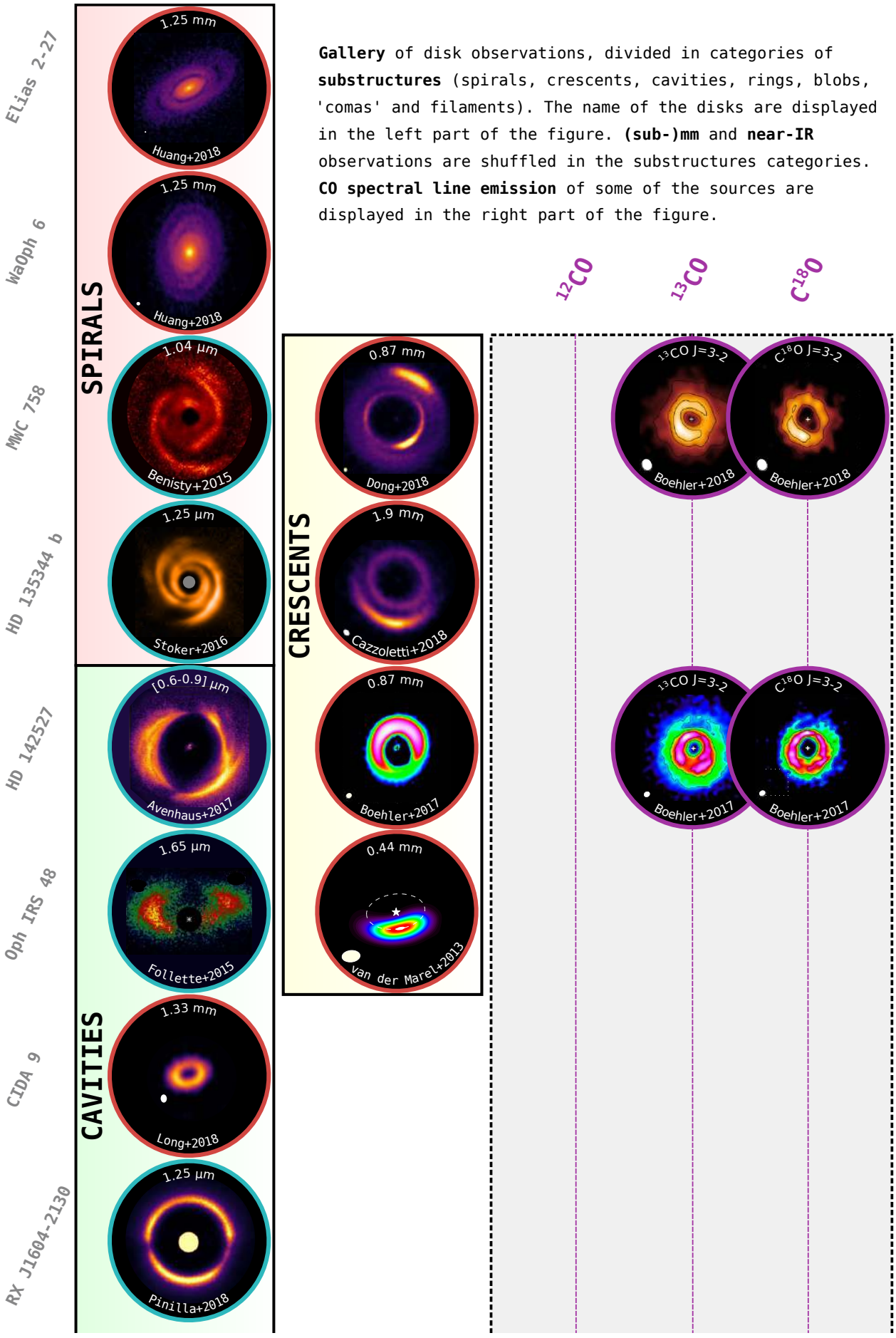

Gallery of disk observations, divided in categories of **substructures** (spirals, crescents, cavities, rings, blobs, 'comas' and filaments). The name of the disks are displayed in the left part of the figure. **(sub-)mm** and **near-IR** observations are shuffled in the substructures categories. **CO spectral line emission** of some of the sources are displayed in the right part of the figure.

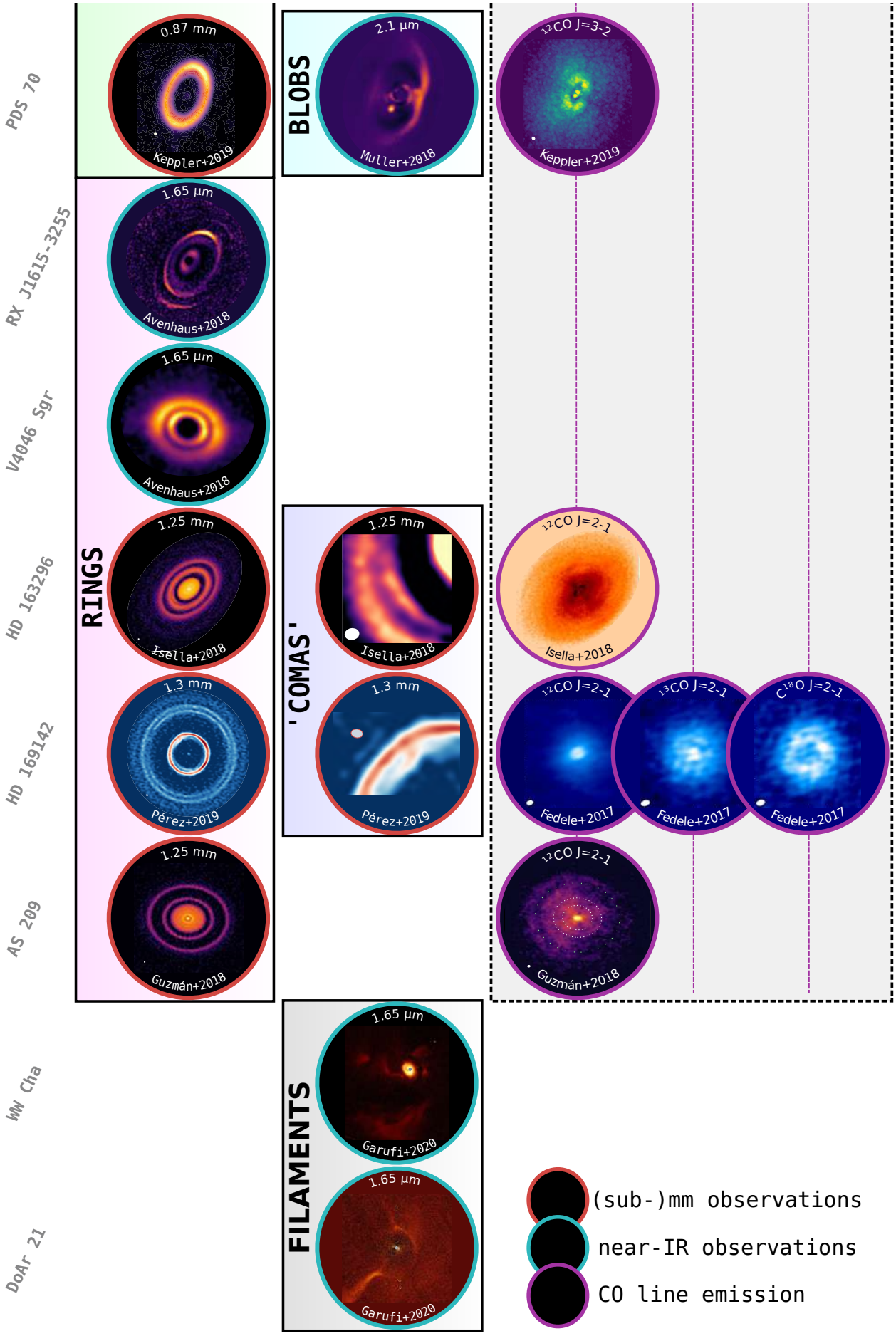

Figure 4.3.0: A gallery of disk observations, see text and legends for more details.

4.3.1 *Snowlines-related mechanisms*

- **Pebble growth near condensation fronts** (Zhang et al., 2015): if the temperature in the disk is sufficiently low, gas molecules like H_2O or CO tend to be accreted onto dust grains, forming icy aggregates. It is a freeze-out of the gas phase molecules onto dust grains. On the contrary, if the temperature is high enough, volatile compounds tend to evaporate easily. This phenomenon is called thermal desorption. The competition between these two opposite processes defines for given gas species a region in the disk called condensation front line, or snow line for H_2O. Numerical simulations and laboratory experiments (see, e.g., Blum & Wurm, 2000; Musiolik et al., 2016) show that icy aggregates have a growth efficiency larger than silicate non-icy aggregates, even if more recent studies seem to challenge this general behavior (see, e.g., Musiolik & Wurm, 2019). Zhang et al. (2015) thus proposed in the case of HL Tau a bimodal size distribution in the disk, considered as optically thin. Particles near the condensation front lines of abundant gas species are assumed to grow efficiently up to ~ 10 cm, whereas particles are smaller elsewhere (~ 1 mm). Since large (spherical) particles do not emit much in the sub-mm, a dark ring is expected at the locations of condensation lines, surrounded by bright rings in which the emission of smaller dust is predominant. They are thus able to reproduce a sequence of dark and bright rings, via variations in the dust opacities κ_ν. This study is possible by analyzing the radial variations of the spectral index α_ν in an optically thin medium (see the definition of α_ν in section 1.1, and an example of application in section 7.1). One question that can be asked concerns the choice of the chemical species whose condensation lines are able to impact the dust growth. A slippery slope would be to choose chemical species, and thus condensation lines only according to the position of dark rings and a profile of gas temperature in the disk. In addition, the assumption of an optically thin disk may be not verified everywhere in the disk.

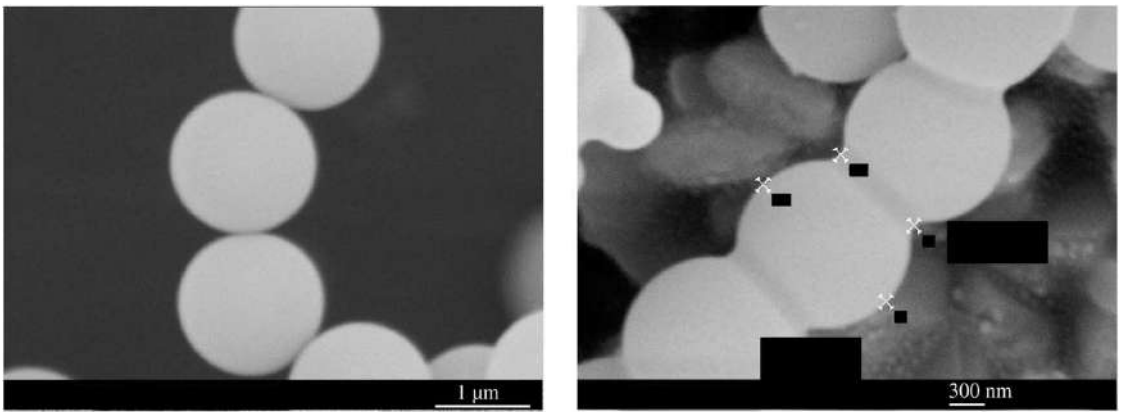

Figure 4.3.1: Scanning electron microscopy images from Poppe (2003) of SiO_2 spheres before (left panel) and after (right panel) sintering. Sintering bounds particles together via a partial fusion between the spheres called sinter necks.

- **Sintering** (Okuzumi et al., 2016): this mechanism is different from the previous one, but also involves condensation front lines. Sintering, which bonds dust particles together, occurs efficiently for micro-metric dust monomers slightly outside the snow lines of volatile species (see Fig. 4.3.1 for a visual representation of sintering). When sintered aggregates collide, they are prone to bouncing, fragmentation and erosion because the collision energy cannot be dissipated, which decreases their sticking efficiency. Sintering thus decreases the size of dust aggregates and therefore their drift velocity, thereby causing a dust pile-up slightly beyond the snow lines. This dust pile-up gives rise to an accumulation of particles, which increases locally the dust density Σ_d, and thus the specific intensity. This mechanism is therefore able to produce one or several bright rings in the dust thermal emission.

We mainly concentrate in the following section on mechanisms that cause radial variations of Σ_d, due to the formation of one or several pressure maxima.

4.3.2 *The pressure maxima, these dust traps*

Several disks show very thin bright rings intercalated between dark rings in the continuum emission, such as HD 163296 or AS 209 (see Huang et al., 2018a, and Fig. 4.3.0). Assuming these bright rings are dust over-densities, their thinness suggests that they are located at positions of equilibrium for the dust, where radial drift is stalled. These so-called dust traps can be naturally obtained at pressure maxima in a disk. We indeed saw in section 2.2.2 that when the gas drag on particles is maximum, that is for $S_t \simeq 1$, the dust radial drift $v_{d,R}$ is also maximum (Eq. 63). However, $v_{d,R}$ can still be equal to zero if the gas pressure gradient is null, which is the case at a pressure maximum. From Eq. 63, we directly see that just outside a pressure maximum, $\frac{d \log p_g}{d \log R} < 0$ implies $v_{d,R} < 0$, that is an inward drift of particles. Conversely, just inside a pressure maximum, $\frac{d \log p_g}{d \log R} > 0$ implies $v_{d,R} > 0$, that is an outward drift of particles. This dependence of the direction of radial drift on the sign of the radial pressure gradient explains that pressure maxima are equilibrium positions for the dust. Before mentioning several ways to form pressure bumps in a disk, we recall that a pressure maximum is susceptible to the RWI (section 2.3.4), which may trigger the formation of one or several vortices that also trap dust in the azimuthal direction (Li et al., 2001; Barge & Sommeria, 1995). Dust trapping in vortices is often invoked to explain the asymmetric crescent-shaped structures in the disks continuum emission at radio wavelengths (e.g., Lyra & Lin, 2013; Baruteau et al., 2019).

- **Self-induced dust traps** (Gonzalez et al., 2017): when backreaction from the dust on to the gas is taken into account, as well as grain growth and fragmentation, particles can be trapped in pressure maxima. They are generated by the competition between these three phenomena alone, hence the name of this mechanism: self-induced dust traps. It has been shown in global disk simulations that, for regular values of the fragmentation threshold (a few $m.s^{-1}$), grains start to grow from the outer disk while they drift inward. This drift slows down

as the dust-to-gas density ratio ϵ increases (see Eq. 63) and as large particles progressively decouple from the gas. Dust grains eventually pile up and start to strongly impact the gas distribution around their location. If ϵ is high enough, dust backreaction can reverse the natural inward viscous drift of the gas and create an accumulation of gas outside the particles location. It produces a gas pressure maximum that traps every particle coming from the outer disk, and therefore a bright ring of emission in the (sub-)mm.

- **Magnetically active and dead zones**: a pressure bump can be generated at the sharp transition between magnetically active regions in disks (where the MRI sets in) and magnetically dead zones (where the MRI is quenched due to non-ideal magneto-hydrodynamic effects), via radial changes in the accretion efficiency (see, e.g., Varnière & Tagger, 2006; Flock et al., 2015; Lyra et al., 2015b).

- **Zonal flows**: when the disk is threaded by a large-scale poloidal magnetic field, a linear instability driven by magneto-hydrodynamic winds can induce zonal flows which take the form of axisymmetric rings with alternating minima and maxima in the magnetic pressure, which are associated with maxima and minima in the thermal pressure, and thus in the gas density (Béthune et al., 2017). This mechanism relies on a radial transport of mass and magnetic field and a vertical ejection of mass along magnetic field lines. If there is a slight depletion of gas somewhere in the disk, turbulent diffusion processes tend to fill with gas the newly-formed gap. The larger α, the stronger this response of the disk to the perturbation. This radial transport of mass is associated with a corresponding radial transport of the magnetic field lines. It leads to an accumulation of magnetic field lines in the gap, and thus an increase in the magnetization[1] in that depleted region. With the hypothesis that an increase of magnetization induces an excess of ejected mass, magnetic winds in the gap efficiently evacuate the gas previously carried via viscous drift. The gas density in the gap becomes therefore even lower, hence a 'local wind instability' (Riols & Lesur, 2019). The MHD wind-related mechanism presented here produces pressure maxima that trap dust particles and create multiple rings of emission after post-processing with radiative transfer calculations at mm wavelengths. With this mechanism, many thin (with a radial width of $\sim 0.3 - 0.4$ H_g, H_g being the gas pressure scale height) bright rings can be produced (Riols et al., 2020).

- **Planets**: Another popular scenario that can account for bright and dark rings is related to planets. A planet that is sufficiently massive to carve an annular gap around its orbit will form pressure maxima at both edges of its gap due to the deposition of the angular momentum flux carried away by the wakes of the planet (see, e.g., Baruteau et al., 2014; Bae et al., 2016, and section 3.3). From there, a myriad of models have been developed to report observations of bright and dark rings, depending on the ability of one or more planets to generate one or more gaps. We present here some of these planet-related mechanisms.

1 defined as the magnetic-to-thermal pressure ratio.

- NGNP model: Models that invoke planets to explain annular substructures in disks observations almost always assume a planet on a fixed circular orbit at the middle of each dark ring (see, e.g., Dipierro et al., 2015, for the HL Tau disk). Put another way, N gaps would correspond to N planets in a disk (hereafter, NGNP model). Some models have actually proposed to use the radial width of a dark ring to estimate the mass of the planet which created that ring (e.g., Dipierro & Laibe, 2017; Zhang et al., 2018; Lodato et al., 2019). The presence of planets in dark rings still eludes direct detection, with the notable exception of the massive planet companion PDS 70b in the large gap of the PDS 70 transition disk (Keppler et al., 2018).
- Secondary gaps: Other studies have also explored the idea that, in low-viscosity disks, a planet on a fixed circular orbit may form a secondary gap inside its orbit, and even a tertiary gap in some cases (Bae et al., 2017; Dong et al., 2017; Zhang et al., 2018). Bae & Zhu (2018a) have demonstrated that a single planet can generate a primary spiral arm, but also secondary and tertiary spiral arms if the viscosity is low enough. While the primary wakes contribute to create a primary gap around the orbital position of the planet, the secondary wakes carve a secondary gap inward of the primary gap, where they turn into shocks and deposit angular momentum. The same goes for tertiary wakes, even closer to the star and with less efficient gas depletion. This phenomenon generates multiple gaps that lead to the formation of multiple rings of emission alternating with dark rings.
- Intermittent runaway migration: in Wafflard-Fernandez & Baruteau (2020), we have considered a mechanism related to the intermittent runaway migration of a Saturn-mass planet in a young massive protoplanetary disk. As we will see in chapter 6, the alternation of phases of slow migration and runaway migration modifies the ability of this planet to build pressure maxima on each side of its orbit, which leads to the formation of multiple dust rings. Radiative transfer calculations subsequently show a sequence of dark and bright rings. More generally, a migrating planet and a fixed planet impact their surroundings in different ways (see section 4.5).

In any case, the presence of such radial substructures in protoplanetary disks has a significant advantage. Because dust particles in such structures no longer drift, it makes more material in the disk that can potentially serve as a reservoir for planetary formation. Moreover, if the grains accumulate efficiently in very localized regions, the dust-to-gas density ratio can increase and be sufficient for streaming instability (Johansen et al., 2014) or self-induced dust trap mechanism (Gonzalez et al., 2017) to operate.

4.4 SUBSTRUCTURES IN THE GAS

Observations of the emission lines of abundant gas molecules has enabled observers to glimpse substructures in the gas content of protoplanetary disks. The right part of Fig. 4.3.0 shows some integrated intensity maps of different isotopologues of the CO

molecule (^{12}CO,^{13}CO and C^{18}O), for the disks presented in section 4.2. These disks have also substructures in the dust thermal emission and/or in the scattered light. We mainly detect annular substructures in the spectral line emission, although the intensity contrast is in general not sufficient to be clearly detected. Because of the high spectral resolution, the spatial resolution may not yet be decisive to observe substructures as distinctly in the gas as in the dust, but its future improvement will undoubtedly allow to complement the information given by the dust continuum emission. The high spectral resolution in the spectral line emission is useful to constrain the gas kinematics, as we will see in the following sections.

4.4.1 *Global diagnostics*

Substructures in the gas can be revealed via the search for deviations from Keplerian motions. The strategy is basically to detect perturbations in the radial profile of the gas azimuthal velocity $\delta v_\phi = \frac{v_{\phi,g} - v_K}{v_K}$. Such perturbations can provide valuable insights on the radial gas pressure profile, as we have seen with Eq. 19 in section 2.1.2.1. For example, $\delta v_\phi = 0$ can be the sign of the presence of a pressure maximum. Besides, the sign of δv_ϕ can indicate if the radial pressure gradient is positive or negative. This method is another way to detect pressure maxima, complementary to the maps of dust continuum emission. Using this technique, deviations of a few percents have been detected (Teague et al., 2018a,b; Pérez et al., 2018) with optically thin emission lines (for example with the C^{18}O, expected to probe regions close to the disk midplane). We show in Fig. 4.4.1 an illustration from (Teague et al., 2018a) of the δv_ϕ radial profile and the corresponding radial pressure profile. Note that the sensitivity and the radial resolution needed to account for these small δv_ϕ perturbations can be quite challenging. Other studies have used the good spectral resolution of spectral line emission in order to generate channel maps. The aim is to detect localized variations of δv_ϕ due to the presence of a nearby massive planet (a few Jupiter masses). In the following, we first introduce the channel maps, then we talk about the velocity kinks detected in these channel maps.

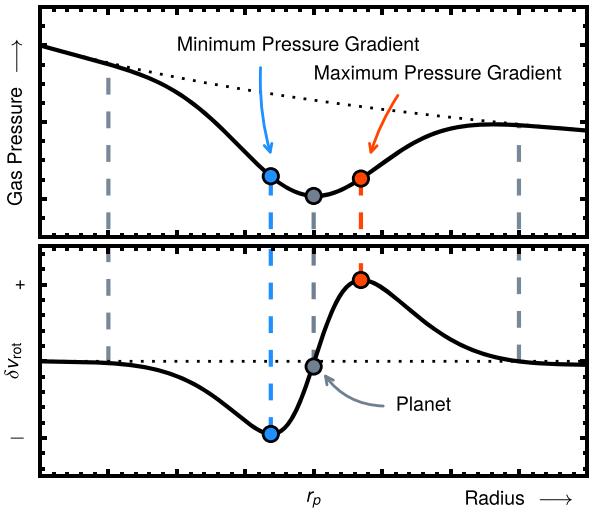

Figure 4.4.1: Sketch that shows the impact of a planet-related gap in the gas pressure profile and the corresponding $\delta V_{rot} = \delta v_\phi$ profile, from Teague et al. (2018a).

4.4.2 *Channel maps*

A channel map is a spatial image that displays only the emission of a given range of velocities along the line of sight, i.e. a certain velocity "channel". Integrating these channel maps over a large interval of velocities gives the intensity maps presented in the right part of Fig 4.3.0, also called 0th moment maps.

When an electromagnetic wave interacts with a non-symmetrical diatomic molecule (CO for example), this molecule is excited. It goes from an initial state of energy E_1 to a final state of higher energy $E_2 > E_1$. Due to the rotation of this molecule, it will be able to evacuate this excess of energy, via a de-excitation which makes it go from the energy state E_2 to a lower energy state $E_1' < E_2$. Different rotational transitions are possible, and the CO molecule will therefore emit a set of molecular lines (emission lines) depending on the transition level. The simple case presented above is valid for the emission of molecules at rest. If the molecules emit from a moving system, in rotation for example, the spectrum of the emission lines that an observer is able to measure is different from the spectrum of the emission lines that they can measure in the laboratory. The emission lines can thus be Doppler-shifted, depending on the speed of the fluid whose molecules experience the rotational energy transition. For example, the emission line of the CO molecule associated with the $J = 2 \rightarrow 1$ rotational transition peaks at $\lambda_0 \simeq 1300$ mm. For a cloud of CO at rest, the observation of this fluid at $\lambda = \lambda_0$ shows the zones of emission of the CO $J = 2 \rightarrow 1$ rotational transition. However, if the whole cloud moves away from the observer at a certain speed, the observation at $\lambda = \lambda_0$ does not show any emission for this specific rotational transition. Because of the global motion of the cloud, the emission line is redshifted, and it is necessary to observe at a longer wavelength in order to detect any emission: according to the expression of the redshift, $(\nu - \nu_0)/c = (\lambda - \lambda_0)/\lambda_0 > 0$ implies $\lambda > \lambda_0$, with $(\nu - \nu_0)$ the deviation from the systemic velocity ν_0 associated with λ_0. An interesting question, which largely motivates some observations of protoplanetary disks, is related to the emission lines of the ^{12}CO molecule for example, or its isotopologues: what is the structure of the CO emission in a given protoplanetary disk?

It is possible to design an oversimple toy model to get an idea of the emission of an ideal 2D Keplerian disk ($\nu_r, \nu_\theta \ll \nu_\phi \simeq \nu_K$), in the absence of a perturber. This toy model simply considers the dynamical impact of a fluid in Keplerian rotation on the zones of emission of this fluid, assuming that if the disk was at rest, it would emit everywhere uniformly at the rest-frame wavelength of the emission line. This model gives an idea of the possible zones of emission of all the molecules moving at Keplerian speed **relative** to the observer. It is thus a **projected** Keplerian speed, taking into account the inclination of the disk with respect to the line of sight. Fig. 4.4.2 shows the projected deviation from Keplerian speed (projected $\delta\nu_\phi$) of an ideal 2D Keplerian disk, seen at an inclination $i = 30$ degrees. Note that if $i = 0°$ (face-on disk), the projected $\delta\nu_\phi$ is of course equal to zero everywhere in the disk. The red color represents a projected super-Keplerian motion ($\delta\nu_\phi > 0$), which means that the corresponding material is moving away from the observer. Reciprocally, the blue color represents a projected sub-Keplerian motion ($\delta\nu_\phi < 0$), which means that the corresponding material is moving towards the observer. Over the projected velocity field are superimposed iso-velocity contours that follow a dipole-like morphology. We

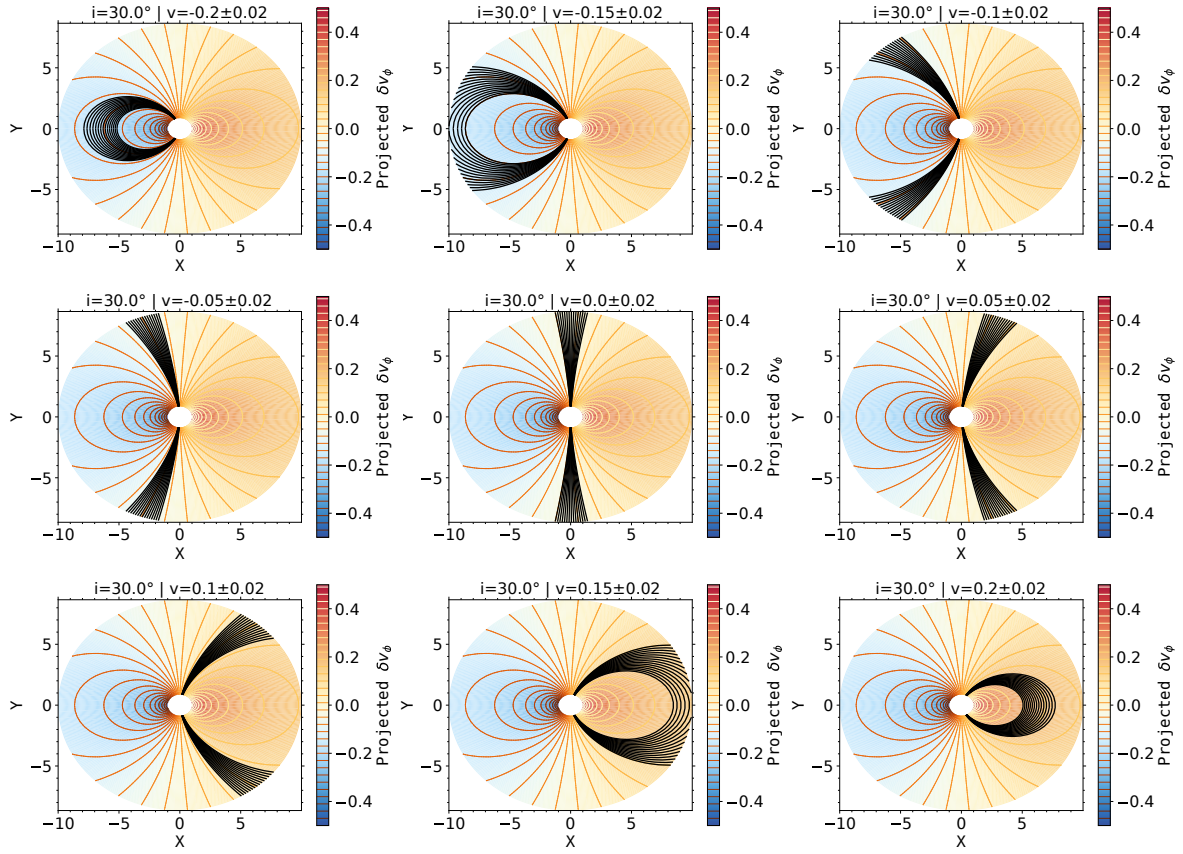

Figure 4.4.2: Channel maps for an ideal 2D Keplerian disk, seen at an inclination $i = 30$ degrees. The colormap shows the projected deviation from Keplerian speed δv_ϕ, and the red-to-yellow lines are iso-velocity contours. In all panels, the black patterns show the possible zones of emission for molecules in the disk, depending on the departure from the systemic velocity. The departure from the systemic velocity (noted here v) for the channel maps is indicated in km/s in the caption at the top of each panel.

typically use this symmetry in real disks observations to determine their direction of rotation.

- For this disk inclination and at systemic velocity $v = 0$ (center panel), i.e. when we observe in a band of wavelength around the centroid of a spectral line $\lambda = \lambda_0$, the possible zones of emission follow a 'bow tie' pattern (black region in the panel). It means that in a 2D Keplerian disk without a perturber, molecules are expected to emit in this specific region.

- Starting from the middle and going to the left and then in the upper panels, the departure from the systemic velocity (i.e. from the rest-frame centroid of the spectral line) gets larger and larger. We observe the emission of molecules moving towards the observer. In that case, the possible zones of emission follow a 'parachute' pattern (black region in the top-left panel for example).

- Due to the symmetry of the Keplerian disk, the pattern of possible emission is similar for molecules moving away from the observer ('parachute' pattern, see bottom-right panel for instance).

I have written this toy model as a pedagogical tool to present simply the physics behind channel maps in protoplanetary disks. It has therefore to be taken with a grain of salt as, to date, it does not take into account the 3D shape of the disk emission among other things. For now, we see in the next section how channel maps can be useful to infer the presence of massive planets in protoplanetary disks.

4.4.3 *Velocity kinks*

The use of channel maps for the detection of gas substructures has become possible thanks to the combination of a good spectral resolution ($\lesssim 0.5$ km/s) and an excellent spatial resolution ($\lesssim 15$ au). Recently, several studies have detected localized perturbations in channel maps compared to the shape expected for a velocity profile of sub-Keplerian 3D disks without perturbation (see, e.g., Pérez et al. (2018), HD 100546 in Pérez et al. (2020), HD 97048 in Pinte et al. (2019) or nine DSHARP targets in Pinte et al. (2020)). These perturbations in the channel maps are called 'velocity kinks'. From the shape of a velocity kink, one can try to constrain the mass of the planet responsible for this perturbation in the Keplerian flow. In all these works, the methodology is as follows:

- 3D numerical simulations with `FARGO3D` (Pérez et al., 2018) or with the `PHANTOM SPH` code (Pinte et al., 2019, 2020) are carried out in the presence of a planet. The mass of the planet in the disk is modified in various simulations.
- Results from these hydrodynamical simulations are post-processed with line radiative transfer calculations, for CO isotopologues in particular. The methodology can be quite similar to the one presented in chapter 5.
- With the help of channel maps, it is possible to compare the gravitational impact of the simulated planet with the velocity kinks observed in real observations.

Using this methodology, velocity kinks have been associated with the perturbation on the gas kinematics by planets of a few Jupiter masses.

Fig. 4.4.3, from (Pinte et al., 2019, 2020), shows some examples of velocity kinks detected in the channel maps of HD 163296 (top panels), HD 97048 (middle panels), and a 3D disk model for HD 97048 with a 2 M_{Jup} planet and the corresponding velocity kink (bottom panels). The blue dots pinpoint the possible position of the planet. Note the impact of the 3D structure of the disks, in particular for HD 163296, on the shape of the spectral line emission in the channel maps. Because the emission of CO molecules does not come from the disk midplane but from upper layers[2] on both sides of a flared disk (see Fig. 1.2.3), it is possible to detect line emission arising from the front side and the rear side of the disk at once. We do not see for now this kind of kinematics in the toy model presented in section 4.4.2. An important but as

2 a few H_g away from the midplane.

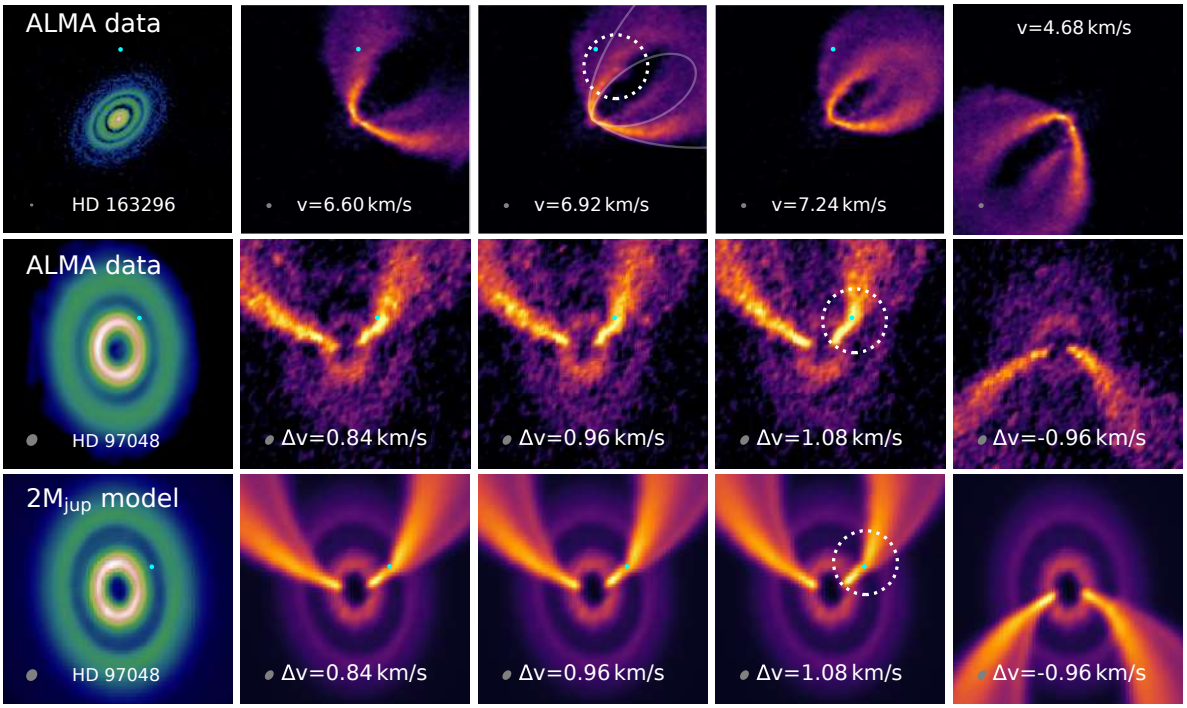

Figure 4.4.3: **First row**: ALMA observations of the dust and gas disk surrounding HD 163296. The top-left panel corresponds to the 1.3 mm continuum emission. The other panels in the first row show the ^{13}CO J = 2 → 1 emission in several channel maps. **Middle row**: ALMA observations of the dust and gas disk surrounding this time HD 97048. The first panel corresponds to the 0.89 mm continuum emission. The other panels show the ^{13}CO J = 3 → 2 emission in channel maps at different departures from systemic velocity. **Bottom row**: results of 3D numerical simulations for HD 97048 post-processed with radiative transfer calculations in the dust (first panel) and in the gas (channel maps panels). The sub-mm dust thermal emission is also visible under the channel maps. **In all panels**, blue dots indicate the location of the planet, and dashed circles highlight velocity kinks in the channel maps. Note that the candidate planets are located within continuum dust gaps. This figure is adapted from Pinte et al. (2019, 2020).

yet unsolved question concerns the origin of velocity kinks. If they are due to massive planets, is it because of gravitational perturbations of the circumplanetary disk around the planet or is it because of planet wakes that transfer angular momentum to nearby fluid elements? We will come back to this point in chapter 7.

Whether it be in the dust thermal emission, in the scattered light or in the channel maps from spectral line emission, the presence of planets is regularly invoked in the models in order to explain the substructures observed everywhere (chapter 4), but also to make the link between protoplanetary disks and the numerous exoplanetary systems commonly observed nowadays (section 3.1). In any case, the possible presence of planets in protoplanetary disks rises the question of the impact of planetary migration, which is an inevitable outcome of disk-planet interactions (see chapter 3). We discuss in the following section some observational predictions related to planetary migration, when the latter is taken into account in the models.

4.5 WHAT ABOUT THE PREDICTED SIGNPOSTS OF PLANETARY MIGRATION ?

In the last couple years, studies have started to consider the impact of planet migration, mainly on the dust thermal emission of protoplanetary disks. These studies were at the origin of my PhD subject, and motivated my early thesis research. The aim in particular is to detect signatures of planet migration in the substructures commonly observed with ALMA in radio for example, hence the title of this manuscript: *observational signatures of planetary migration in the cold dust emission of protoplanetary disks*. Planet migration impacts gas and dust in many ways. For example, we saw in section 3.3.2 with in particular Fig. 3.3.3 that planetary migration has a strong impact on the formation of a gap in the gas of a disk. We will use again these specific simulations in chapter 7 to study the impact of planet migration on the dust, especially on the Lagrange points of a Saturn-type planet. As we will see in this section, Meru et al. (2019); Nazari et al. (2019); Pérez et al. (2019); Weber et al. (2019) have recently assessed the effect of planetary migration on the dust dynamics, in particular the presence and location of dust rings on both sides of the planet, the dependence on the dust's size distribution, and how the position of a dust ring relative to the planet can be an indicator of the planet's migration speed. In most of these studies, a migrating planet can typically produce up to three bright rings surrounding two dark rings: a bright coorbital ring, a bright inner ring and a bright outer ring. In principle, a similar result is obtained for a stationary planet. But migration adds complexity to this result. The main predictions from these studies are two-fold.

- **Bright rings can be radially asymmetric.** Without migration, dust particles will accumulate roughly symmetrically on both sides of the planet. Said differently, the planet is expected to be equidistant from the inner ring and the outer ring. However, depending on the migration speed and the direction of migration, a migrating planet will tend to get closer to the inner ring or to the outer ring. This asymmetry is in principle distinguishable in dust continuum emission maps from ALMA (Weber et al., 2019). Fig. 4.5.1 shows an example of results of their 2D numerical simulations from Weber et al. (2019), for a 10 $M_{\texttt{Earth}}$ planet located at 30 au from the star. The yellow color corresponds to a high optical depth, typically where dust particles accumulate to form bright optically thick rings. Seven different migration rates are displayed in the `y`-axis of this graph. In the `fixed` scenario, the three bright rings are clearly symmetrically distributed around the planet location. Above this stationary scenario in this graph, the planet migrates inward and gets closer to the inner ring. The larger the migration rate, the stronger the radial asymmetry (top scenario `in-a`). Conversely, in the bottom part of Fig. 4.5.1, the planet migrates outward and gets closer to the outer ring, leading to a stronger radial asymmetry for a faster outward migration (bottom scenario `out-c`).

  Pérez et al. (2019) showed that the radial asymmetry detected in the dust thermal emission of HD 169142, between the three fine rings at $\sim 60-80$ from the star, could be due to a mini-Neptune that migrates inward in a poorly viscous disk. This structure is visible in Fig. 4.1.2.

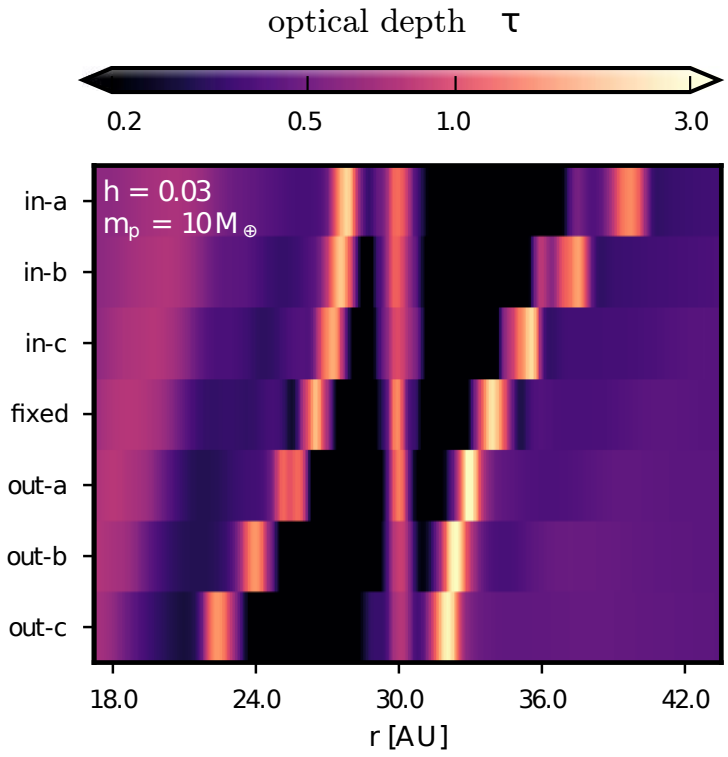

Figure 4.5.1: Radial asymmetry of bright rings due to planet migration. From Weber et al. (2019), the azimuthal average of optical depth is displayed for a 10 M_{Earth} planet at 30 au and a disk model such that $h_g = 0.03$, $\Sigma_g \propto r^{-0.5}$ and $\alpha = 10^{-5}$. Seven migration rates $\dot{a}$ are spread out on the y-axis. From top to bottom: three inward migrating planets ($|\dot{a}_{in-a}| > |\dot{a}_{in-b}| > |\dot{a}_{in-c}|$), a fixed planet ($\dot{a}_{fixed} = 0$) and three outward migrating planets ($|\dot{a}_{out-c}| > |\dot{a}_{out-b}| > |\dot{a}_{out-a}|$). See Weber et al. (2019) for more details.

- **The location of a ring with respect to a gap gives an idea of the migration velocity compared to the drift velocity of dust grains.** Planet perturbations on the pressure profile depend on the particle size... Meru et al. (2019) found in their 2D numerical simulations that large particles are preferentially trapped in an outer ring, whereas small particles are preferentially trapped in an inner ring. The main phenomenon at work is the radial drift of particles, which is faster for larger particles (as long as $S_t < 1$, see Eq. 63). The bottom panel of Fig. 4.5.2, labeled 'SLOW', helps understand the distribution of large particles in the outer ring and smaller particles in the inner ring. The position of the planet is marked with a purple sphere and the vertical dashed line, the star is in the left part of the scheme, and particles can be trapped in the pressure maxima represented with the dark blue curve. Black arrows give an idea of the migration speed of the planet compared to the large particles drift velocity. When the migration rate is small compared to the dust drift of large particles, the latter drift swiftly towards the star as the pressure bump inside the planet orbit in not sufficient to trap these large fast grains. Only small particles with slow radial drift are located near the inner pressure bump. However, when large particles initially

beyond the planet location start to drift inward, their motion is abruptly stopped when they eventually end up trapped in the outer pressure bump. At the end of the day, large particles are trapped in an outer ring whereas smaller particles are trapped in an inner ring. Actually, one can rather expect a gradient of dust sizes from the inner ring to the star. This process is one of the main results presented in Meru et al. (2019), and Nazari et al. (2019) used it in order to derive an observational prediction for planet migration. They have shown that in order to understand the perturbation of dust dynamics by the planet, it is actually important to compare the dust drift timescale with the migration timescale.

- When $v_{migr} < v_{drift}$, i.e. in the 'SLOW' regime presented just above, the dust thermal emission at a given wavelength $\lambda = \lambda_{mm}$ is expected to be dominated by a bright outer ring beside a gap, due to the emission of large millimeter particles at this location.
- In the other extreme case, if $v_{migr} > v_{drift}$, the planet is in a 'FAST' regime compared to the dust dynamics (see top panel of Fig. 4.5.2). The planet pushes the dust forward, like a snowplow. The dust drift is actually too slow: whereas particles in the inner disk are constantly caught up by the planet, particles in the outer disk cannot step up the pace and scatter, away from the planet. Inner particles eventually end up in the inner pressure bump generated by the planet. When observed at λ_{mm}, the dust configuration resulting from this 'FAST' regime gives rise to a bright inner ring beside a gap. This is the exact opposite of what happens in the 'SLOW' regime. Note that if the relative velocity between the planet and particles is too large, this snowplow mechanism no longer operates anymore, and large particles start to perform outward horseshoe U-turns from the inner to the outer disk (see chapter 6).
- Finally, when $v_{migr} \simeq v_{drift}$, the planet enters an 'INTERMEDIATE' regime, where two bright rings are visible in the dust thermal emission at λ_{mm}, due to a competition between the two processes presented in the 'SLOW' and 'FAST' regimes. Large particles can at once be trapped in the outer pressure bump due to their radial drift and be pushed inward in the inner pressure bump (see middle panel of Fig. 4.5.2).

Note that if we increase λ_{mm}, the dust thermal emission is a priori dominated by larger spherical particles, with a faster radial drift (as long as $St < 1$). Because v_{drift} increases and v_{migr} stays the same upon increasing particles size, the possible regimes presented in Fig. 4.5.2 are shifted downwards, i.e. the previous 'FAST' regime is now an 'INTERMEDIATE' regime, and the previous 'INTERMEDIATE' regime is now a 'SLOW' regime. Said differently, larger particles escape more easily the inner pressure bump and are more easily trapped in the outer pressure bump. Nazari et al. (2019) have found as well that, in an optically thin observation, the spectral index $\alpha_\nu = 2 + \beta_\nu$ (see section 1.1) in this outer bright ring (with large particles, $\beta_\nu \simeq 0$) is expected to be lower than the spectral index in the inner bright ring (with smaller particles $\beta_\nu > 0$). This gives an interesting prediction of planet migration for multi-wavelength observations.

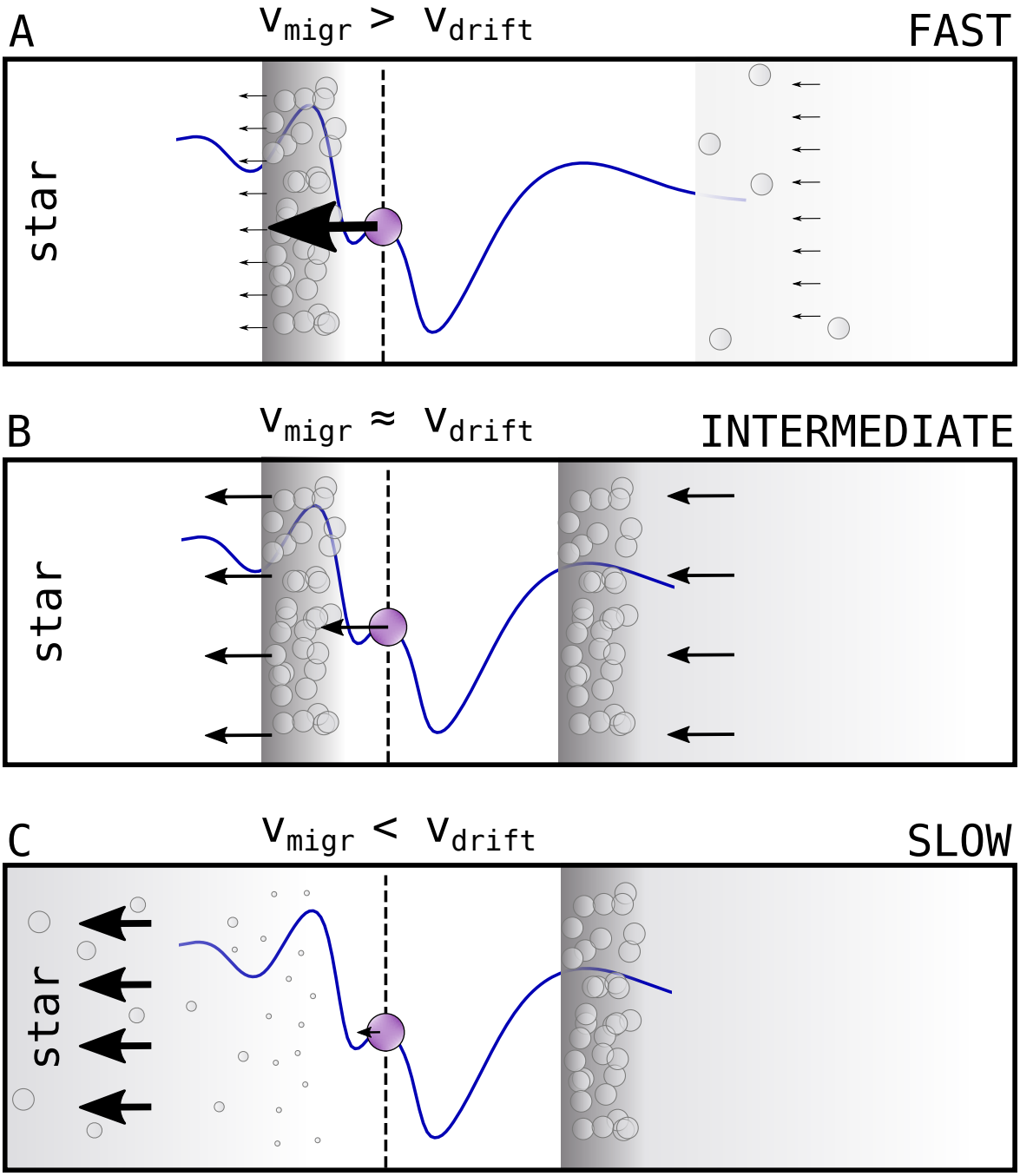

Figure 4.5.2: Impact of planet migration on the dust distribution depending on the relative velocity between the planet and the dust. Scheme adapted from Meru et al. (2017); Nazari et al. (2019). **bottom/top panel**: the planet migration is slow/fast compared to the dust drift ('SLOW'/'FAST' regime). It gives rise to an outer/inner ring in the dust spatial distribution, and then a outer/inner bright ring in the dust thermal emission. **Middle panel**: the 'INTERMEDIATE' regime is in between the 'SLOW' and 'FAST' regimes; it gives rise at once to an inner ring and an outer ring of emission. See body of the text for more details.

Note that in most of these studies, the migration rate is fixed by theoretical predictions of Type-I migration (i.e. for low-mass planets). In other words, the planet impacts the gas, but the reverse is not true.

The parameter space in order to study the planet-dust interaction is wide, as it involves a range of planet masses, disk's physical properties (density, temperature profiles etc.) and dust sizes. In the work presented in Chapter 6, we examine the migration of moderately massive planets (typically around a Saturn mass) in fairly massive disks, which are subject to rapid runaway migration (Masset & Papaloizou, 2003). Such planets can undergo multiple stages of intermittent runaway migration (Lin & Papaloizou, 2010; McNally et al., 2019). We find that these multiple stages of intermittent runaway migration lead to the formation of several dust rings and therefore sequences of dark and bright rings in the (sub-)mm continuum. We then extend these findings in chapter 7, with a series of ongoing works whose underlying backdrop is the link between planetary migration and substructures in protoplanetary disks.

5

NUMERICAL METHODS

Emission maps, regardless of the observational tracer, are snapshots in the life of protoplanetary disks and do not directly inform us on their evolution. Numerical simulations are therefore an essential tool to study the interactions between the main characters that are expected to prevail in the disk evolution. Place a young star at the center of a sturdy disk. Fill the disk almost to the top with gas. Add a pinch of dust to the mixture. Garnish with one or several planets, and let the system evolve. You will then need to retrieve dust and gas spatial distributions and use it as an input for radiative transfer calculations to generate synthetic emission maps. In this chapter, we first present in section 5.1 the hydrodynamical codes `Dusty FARGO-ADSG` *and* `FARGO3D`*, we then introduce in section 5.2 the dust and line radiative transfer calculations performed by* `RADMC3D`*. Finally, some python analysis tools are outlined in section 5.3.*

CONTENT

5.1 Hydrodynamical simulations: Dusty FARGO-ADSG and FARGO3D 107
5.1.1 Dusty FARGO-ADSG 107
5.1.1.1 Presentation of the code 107
5.1.1.2 The grid 110
5.1.1.3 The gas 111
5.1.2 multifluid FARGO3D 112
5.1.2.1 Initialization of the gas quantities 112
5.1.2.2 A fiducial setup 113
5.2 Radiative Transfer calculations: RADMC3D 116
5.2.1 Dust radiative transfer 116
5.2.2 Lines radiative transfer 119
5.3 Python analysis tools 121

Appendices 123
5.A Output step in FARGO-ADSG/FARGO3D 123

6 INTERMITTENT PLANET MIGRATION AND FORMATION OF MULTIPLE DUST RINGS AND GAPS IN PROTOPLANETARY DISKS 125

5.1 HYDRODYNAMICAL SIMULATIONS: DUSTY FARGO-ADSG AND FARGO3D

In section 5.1.1 we introduce the 2D hydrodynamical gas+dust code FARGO-ADSG, then we take a look in section 5.1.2 at the 3D multifluid code FARGO3D.

5.1.1 *Dusty FARGO-ADSG*

5.1.1.1 *Presentation of the code*

In order to study the dynamical evolution of the gas and dust of protoplanetary disks in the presence of one or multiple planets, we need to do realistic global simulations. Part of the simulations presented in this work were carried out with the freely-distributed public code Dusty FARGO-ADSG, which is an extension of the grid-based code FARGO-ADSG (Masset, 2000; Baruteau & Masset, 2008a,b) with dust modeled as Lagrangian test particles (Baruteau & Zhu, 2016; Fuente et al., 2017). This parallelized hydrodynamical code allows to carry out astrophysical fluid dynamics calculations by solving a system of partial differential fluid equations. It integrates the Navier-Stokes and continuity equations in a two-dimensional polar mesh for a nearly Keplerian disk subject to the gravity of the central object and that of an arbitrary number of embedded protoplanets, as well as self-gravity of the disk. In this version of FARGO, the energy equation can be added. We adopt a polar coordinate system (R, ϕ), with R the radial cylindrical coordinate measured from the central star and ϕ the azimuthal angle. All names written with `this police` are related to the variable names or outputs of the code.

The structure of the code is as follows.

- **Initialization**: First, the properties of the planet(s), the disk and dust particles are initialized. For the planet, it corresponds to its initial position and velocity, such that the planet's angular frequency Ω takes its Keplerian value, Ω_K, in a non self-gravitating disk. For the gas-related scalar quantities, it corresponds mainly to the initial surface density $\Sigma_{i,g}$ (see sections 1.2.5, 2.1.2.1 and 2.1.2.2), and the initial aspect ratio $h_{i,g}$ (see section 2.1.2.1 and Appendix 2.A), the latter being particularly important in the case without energy equation. The disk is initially axisymmetric, and both aforementioned quantities are assumed to be power-laws of R:

$$\Sigma_{g,i}(R) = \Sigma_0 \times \left(\frac{R}{R_0}\right)^{-\sigma} \tag{95}$$

$$h_{g,i}(R) = h_0 \times \left(\frac{R}{R_0}\right)^{f}, \tag{96}$$

  where $\Sigma_0 =$ `Sigma0` and $h_0 =$ `AspectRatio` are respectively the initial gas surface density and aspect ratio at the code's unit of length $R_0 =$ `FactorUnitLength`. $-\sigma = -$`SigmaSlope` and $f =$ `FlaringIndex` are the power-law exponents for these quantities. Concerning the vector quantities, the azimuthal velocity of the

gas $v_{\phi,g}$ is initially assumed to be sub-Keplerian. Without the disk's self-gravity, we actually use the expression obtained in Eq. 23. If the disk is self-gravitating, things are a little bit different as the radial self-gravitating acceleration $g_R(R)$ (see its expression in Appendix A of Baruteau & Masset (2008b)) has to be taken into account when expressing the initial centrifugal balance. In that case, $v^{SG}_{\phi,g}$ becomes:

$$v^{SG}_{\phi,g}(R) = v_K(R)\left(1 + h_g^2\eta_g - \frac{g_R}{R\Omega_K^2}\right)^{1/2}. \tag{97}$$

Note that g_R can be positive or negative, making the disk more or less sub-Keplerian compared to the case without disk's self-gravity. Furthermore, the planet's initial angular frequency Ω^{SG} with self-gravity depends also on g_R. More specifically, the planet is initially much like a pressure-less self-gravitating fluid element. Finally, for the radial velocity of the gas $v_{R,g}$, we typically set it to $v_{r,g} = -\frac{3\nu}{2R}$[1], which is the steady state gas radial velocity in the viscous accretion disk model, assuming a uniform kinematic viscosity ν (Lynden-Bell & Pringle, 1974, and section 2.1.3). Finally for the dust, `NbPart` Lagrangian super-particles are radially distributed between radius `RMinDust` and `RMaxDust`, given a power-law probability distribution set by the exponent `DustSlope`. Particles are subject to the same accelerations as fluid elements but the pressure gradient (see Eq. 47 and Eq. 48 for the corresponding equations). Their initial azimuthal velocity is thus Keplerian, except when gas self-gravity is included, in which case the dust's azimuthal velocity accounts for the gas self-gravitating acceleration. Particles are assumed to have an internal density ρ_{int} = `Rhopart` in g.cm^{-3}, independently of their size. Note that studying the evolution of dust particles defined by their size and internal density in physical units implies that the code's unit of length and the code's unit of mass have to be specified in the input parameter file. They have a size distribution such that $n(s)ds$, which corresponds to the number of super-particles in the size interval $[s, s+ds]$, is a power-law function of the particle size s, going from s_{min} = `SizeMinPart` to s_{max} = `SizeMaxPart`. The power-law exponent $q = -$ `SizePartSlope` is in general set to -1 in our simulations in order to have approximately the same number of particles per decade of size. Even though we need a (more) realistic size distribution exponent to compute the dust emission through radiative transfer calculations, the choice of the power-law exponent has no impact on the hydrodynamical simulations since dust feedback on the gas is discarded. We choose the value of the minimum and maximum particles sizes (s_{min} and s_{max}) to suit the results of 1D models of dust growth, drift and fragmentation (see section 2.2.4, in particular Fig. 2.2.2) in planet-less disks having similar physical properties as the background disk in our simulations (Birnstiel et al., 2012).

1 it results from the continuity equation (conservation of mass) and the azimuthal component of the Navier-Stokes equation (conservation of angular momentum).

- **Timestep evaluation**: Any hydrodynamical quantity cannot propagate over a distance larger than the size of a grid cell during an hydrodynamical timestep. This limitation defines the so-called CFL (Courant-Friedrichs-Levy) condition. The FARGO code calculates all hydrodynamical velocities involved in the disk evolution, like the sound speed c_s, the gas radial velocity $v_{R,g}$ or the gas azimuthal velocity $v_{\phi,g}$. The aim is then to determine the corresponding timesteps, fixed by the radial size (δR) and azimuthal size ($R\delta\phi$) of the cells. In practice, in most hydrodynamical codes that simulate astrophysical disks, the timestep δt_{tot} associated with the largest velocity is dominated by $v_{\phi,g}$, therefore $\delta t_{tot} = \delta t_\phi = R\delta\phi/v_{g,\phi}$. In general, the hydrodynamical timestep is mostly constrained by the minimum value of δt_ϕ at the inner edge of the grid. Note that the FARGO code corrects the azimuthal transport of material by an average azimuthal velocity $\widetilde{v}_{g,\phi}$, which reduces the limit related to δt_ϕ, now equal to $R\delta\phi/(v_{g,\phi} - \widetilde{v}_{g,\phi})$. With this trick, δt_{tot} is then dominated by the second largest velocity, which can be the sound speed for simulations with low-mass planets, or the velocity of the circumplanetary flow for simulations with high-mass planets. See more details in (Masset, 2000; Baruteau, 2008, section 3.1.2).

- **Planet update**: Using a fifth-order Runge-Kutta integrator, the planet(s) velocities (radial and azimuthal) are first updated, given the gravitational potential of the disk. Then, the planet(s) positions and velocities are updated, given the gravitational potentials of the star and the other eventual planets. In FARGO-ADSG, note that accretion is implemented following the prescription developed in Kley (1999). At each hydrodynamical timestep, a fraction of the mass contained in the planet's Hill radius is removed via a user-defined free parameter. The mass and the linear momentum lost by the gas are then transferred to the planet in such a way that the mass and the linear momentum of the total system planet + Hill sphere are conserved. For more details, see Kley (1999).

- **Dust update**: Particles positions and velocities are then updated, via the gravitational potential of the star (direct and indirect terms), of the planet(s), and of the disk gas (if self-gravity is included). The gas drag acceleration, as presented in section. 2.2.1, is taken into account, by interpolating the gas quantities at the particles location. Various interpolation schemes can be used: Nearest-Grid Point, Cloud-In-Cell or Triangular-Shaped Cloud. When the particles friction time is much shorter than the hydrodynamical timestep, which is typically the case for very small particles, the computation time to follow at once gas elements and dust particles can become unreasonably long. In that case, we use the Short-Friction Time approximation (Johansen & Klahr, 2005), which is actually a semi-analytical expression for the small particles velocity, keeping only the friction, gravity and pressure gradient terms. However, because we do not take into account dust self-gravity, collisions, dust growth nor fragmentation, particles do not feel each other. Moreover there is no dust back-reaction onto the gas. Finally in this step, stochastic kicks are applied to the position (R_d, ϕ_d) of the dust particles at each hydrodynamical timestep of the simulation, in order to model the effects of gas turbulence, via a dust's turbulent diffusion close to the one used at the end of section. 2.2.3 (see Ataiee et al., 2018 for more details).

- **Gas update**: The time derivative of Σ_g, $v_{R,g}$ and $v_{\phi,g}$ can be obtained by splitting in two parts the continuity equation, as well as the radial and azimuthal projections of the Navier-Stokes equations. The first part gathers the source terms, which include the gravitational potentials, the pressure gradient, the physical and artificial viscous accelerations and the centrifugal acceleration. Note that an artificial viscous pressure is indeed required in a staggered-mesh code in order to smooth eventual shocks between grid cells. The first part related to source terms only affects $v_{R,g}$ and $v_{\phi,g}$, as there is no source term for Σ_g in the continuity equation. Regarding the second part, it gathers the advection terms, which constitute three conservation equations for the mass, and the radial and angular momenta. The gas update is therefore two-fold. First the source terms are updated, then the advection terms, all this according to the boundary conditions that are applied in the grid. For the boundary conditions, we use in our numerical simulations wave-killing zones near the inner and outer radial edges of the grid to avoid reflections of the planet wakes. In these zones, $v_{\phi,g}$ is damped towards its axisymmetric instantaneous profile. Regarding Σ_g and $v_{R,g}$, there are two possibilities that we usually make use, labeled as `DampToAxi` and `DampToViscous` in the parameter file. For the former, we damp Σ_g and $v_{R,g}$ towards their instantaneous axisymmetric profiles. For the latter, Σ_g and $v_{R,g}$ are damped towards the radial profiles obtained by calculating the pure viscous evolution of the disk on a 1D grid simultaneously to the gas equations solved on the polar grid. This `DampToViscous` method corresponds basically to the same boundary condition as that implemented in `FARGO3D` by Benítez-Llambay et al. (2016). It is a very simplified way to model the viscous evolution of a global disk in the absence of planets. See section 5.1.1.3 for some details about the disk gas, with some insights on the energy equation and the disk self-gravity.

- **Output step**: Just before reevaluating the new timestep for the next iteration, outputs are produced by `FARGO` in several files. These files save the important properties of the gas, the dust and the planet(s), and are largely used in post-processing. See Appendix 5.A for a list of the main files and their content.

The values of the parameters chosen for our simulations are specified in the relevant chapters. (chapter 6 and chapter 7). We detail below the numerical setup and main hypotheses for the grid and the gas in our fiducial large-scale 2D simulations.

5.1.1.2 *The grid*

In the radial direction, the grid stretches from `Rmin` to `Rmax`. In the azimuthal direction, the grid extends from 0 to 2π and is paved by $N_\phi =$ `Nsec` cells that are evenly spaced. In the radial direction, we use $N_R =$ `Nrad` radial cells. If the disk's self-gravity is included, radial cells are logarithmically spaced, which is necessary for the self-gravitating acceleration to read as a convolution product and be computed via Fast Fourier Transforms (Baruteau & Masset, 2008b). As stated earlier, we use wave-killing zones for the boundary conditions. These zones extend from `Rmin` to `WKZRmin`, and from `WKZRmax` to `Rmax`. Concerning the flow quantities, they are discretized on a static grid encompassed by what we call "ghost cells" which can take on boundary

conditions. It is possible to study the evolution of these quantities in the reference frame in corotation with the planet (Frame = C) as well as in the frame centered on the primary (Frame = F).

5.1.1.3 *The gas*

FARGO is a staggered-mesh code. On the one hand, hydrodynamical scalar quantities (gas surface density Σ_g, gas pressure P_g, gas temperature T_g,...) are defined at the center of the grid cells. On the other hand, hydrodynamical vector quantities (gas radial velocity $v_{R,g}$ and gas azimuthal velocity $v_{\phi,g}$) are defined at the cell interfaces. In such codes, calculations of fluxes (mass, momentum and energy) between cells are convenient, and only scalar quantities (mainly Σ_g) need to be interpolated at the interfaces. Spatial gradients that intervene in the fluid dynamics equations (continuity, Navier-Stokes and energy equations) are therefore quite easy to compute. When the energy equation in not considered, only Σ_g, $v_{R,g}$ and $v_{\phi,g}$ are computed on the polar mesh at a given time, as the other quantities are either fixed initially, or related to these three fundamental variables.

- **Without energy equation**: T_g does not evolve with time, but is stationary. Its initial profile is given by a sound speed radial profile. The sound speed c_s is linked to the aspect ratio $h_g(R,t) = h_{g,i}(R)$ (see section 2.1.2.1 and its power-law profile in Eq. 21, recalled in Eq. 96). Remember in particular that the power-law exponent β of the gas temperature and the flaring index f are linked to each other: $\beta = 1 - 2f$. Using Σ_g and h_g, the gas pressure $P_g = \Sigma_g h_g^2 v_K^2$ is then computed. It defines a *locally isothermal equation of state*.

- **With energy equation**: the time evolution of the gas thermal energy density e_g is computed. e_g is linked to T_g and Σ_g, via $e_g = P_g/(\gamma - 1)$, with γ the adiabatic index. The gas temperature profile can therefore be modified by heating and cooling source terms. In particular, it is possible to include various physical processes like viscous heating, stellar irradiation, or radiative cooling.
  - Viscous heating depends on the viscous stress tensor, the velocity divergence, Σ_g and the viscosity ν, and is due to the shear exerted on adjacent cells in the fluid (see the 1D expression of the viscous heating for a Keplerian disk in Appendix 2.A, see the 2D expression in D'Angelo et al. (2003)).
  - Stellar irradiation on a given region of the disk mainly depends on the luminosity of the star (see Appendix 2.A).
  - Radiative cooling describes how the disk surfaces lose heat by thermal radiation, and can be written $2\sigma_{SB} T_{eff}^4$, with σ_{SB} the Stefan-Boltzmann constant (Table 1) and T_{eff} the effective temperature emitted from the disk surfaces. T_{eff} depends on the stellar irradiation, but also on the gas temperature and the Rosseland mean opacity (Pierens, 2015, see, e.g.,).

  See, e.g., Menou & Goodman (2004); Pierens (2015) for more complete expressions of the stellar irradiation and radiative cooling.

In the FARGO-ADSG code, gas self-gravity is implemented. Because we perform 2D simulations, a softening length ϵ_{SG} = SgThicknessSmoothing is used in the calculation of the self-gravitating acceleration to mimic the vertical extent of the disk (Baruteau & Masset, 2008b; Müller et al., 2012). The disk's gravitational potential can be written as a convolution product (if $\epsilon_{SG} \propto R$), which makes it possible to calculate it in Fourier space. This method helps to reduce the computational cost of the gas self-gravity. It is used in FARGO-ADSG via the paralleled version of the FFTW library.

Finally for the gas, the radial turbulent transport of the disk's angular momentum is modeled by an equivalent kinematic viscosity, as presented in section 2.1.3. The FARGO code parametrizes this viscosity as $\nu = \alpha c_S H_g$ (Shakura & Sunyaev, 1973), with α = AlphaViscosity a dimensionless constant, c_s the sound speed, and $H_g = h_g(R) \times R$ the disk pressure's scale height (defined in Eq. 6). We introduce in the next section the FARGO3D code, which I have started to use during the final year of my PhD thesis.

5.1.2 *multifluid FARGO3D*

FARGO3D is a hydrodynamical and magneto-hydrodynamical parallel multifluid code. FARGO3D is the successor of the FARGO code, and conserves the main features of the 2D code presented in section 5.1.1.

5.1.2.1 *Initialization of the gas quantities*

The calculations presented in Section 2.1.2.1 and Section 2.1.2.2 were done in two dimensions. We can extend the expressions given in Eq. 23 and Eq. 27 in three dimensions in a spherical coordinate system (r,θ,ϕ). The disk is initially axisymmetric $\partial_\phi = 0$. The gas azimuthal velocity v_ϕ^{3D} and the gas volume density ρ_g^{3D} have initially the following expression in 3D (see Masset & Benítez-Llambay, 2016, their Appendix A):

$$v_\phi^{3D}(r,\theta) = v_K(r)\left[(\sin\theta)^{-2f} + h_g^2\eta^{3D}\right]^{1/2}, \tag{98}$$

$$\rho_g^{3D}(r,\theta) = \rho_{mid}(r)\,(\sin\theta)^{\eta^{3D}} \exp\left[\frac{1}{h_g^2}\frac{1-(\sin\theta)^{-2f}}{2f}\right]. \tag{99}$$

v_K is the Keplerian speed, h_g the aspect ratio, and f the flaring index. $\rho_{mid}(r)$ is the gas volume density in the midplane (see Eq. 28), and is assumed to be a power-law of the distance r. η is the local gas pressure logarithmic gradient. More specifically, for a smooth disk whose gas surface density is a power-law of r (as in Eq. 8 but without exponential cutoff), η corresponds to the exponent of the gas pressure profile and is different in 2D and in 3D:

$$\begin{aligned} \eta^{3D} &= f - \sigma - 2, \\ \eta^{2D} &= 2f - \sigma - 1, \end{aligned} \tag{100}$$

with σ the power-law exponent of the gas surface density Σ_g. Concerning the radial and colatitudinal velocities, they are chosen initially null.

5.1.2.2 *A fiducial setup*

The important parameters defined in section 5.1.1 for the grid in FARGO-ADSG are similar in FARGO3D, with a third dimension for the colatitude θ. One of the main differences we are interested in is the treatment of dust. In FARGO3D, multiple dust species are modeled as multiple pressureless fluids, and not as Lagrangian test particles. Note that FARGO-ADSG allows to study the evolution of one single dust fluid, along with the gas and dust particles. The implementation of the dust fluids in FARGO3D is attractive as it automatically includes the dust feedback onto the gas, presented in sections 2.2.1 and 2.2.2. The user only needs to define an initial uniform dust-to-gas density ratio $\epsilon_d =$ `Epsilon` for a given dust fluid. FARGO3D is therefore able to describe the self-consistent dynamics of a mixture of gas and multiple pressureless dust species (Benítez-Llambay et al., 2019).

What is also particularly convenient about FARGO3D is its versatility. It is possible to easily develop new routines based on existing setups. In order to extend in 3D our work presented in chapter 6, I have modified the 3D setup `p3diso`. This setup `p3diso` models the evolution of one half of a protoplanetary disk (the upper one) in 3D spherical coordinates, in presence of one or several planets.

We wanted to describe the dust fluids as a function of their size s_d in physical units and not as a function of the dimensionless Stokes number S_t, as implemented in the code's public release. The aim was to treat dust fluids with FARGO3D in a similar way to Lagrangian particles with FARGO-ADSG, setting initially three parameters:

- the minimum dust size $s_{min} =$ `DustSizeMin`.
- the maximum dust size $s_{max} =$ `DustSizeMax`.
- the size distribution, given by a power-law exponent $q = -$ `DustSizeSlope`. Note that the choice of this power-law is much easier with FARGO3D than with FARGO-ADSG, because it does not involve a resolution issue in terms of number of Lagrangian particles. In FARGO3D, we can for example easily choose `DustSizeSlope`$= 3.5$, close to the size distribution in the ISM.

Thus, with an arbitrary number $N_d =$ `NFLUIDS-1` of dust fluids[2], it is possible to automatically set the size of each dust population, following the dust size distribution that we want. The initialization of the dust quantities is then straightforward. On the one hand, for the initial velocities of the dust fluid number k, $v_{r,k} = 0$, $v_{\theta,k} = 0$ and $v_{\phi,k} = v_K$. It means that dust fluids move initially on a Keplerian orbit, and there is no radial nor vertical motions. On the other hand, the density of the dust fluid number k is proportional to the gas density ($\rho_{d,k} = \epsilon_k \rho_g$). Thanks to the "size distribution" methodology that we used, it is possible to automatically determine the

2 the total number of fluids (gas fluid and dust populations) is set by `NFLUIDS`.

dust-to-gas density ratio ϵ_k for the dust population k, given its size s_k and the total initial dust-to-gas mass ratio μ_d:

$$\epsilon_k = \mu_d \frac{s_k^{4-q}}{\sum_{k=1}^{N_d} s_k^{4-q}}. \tag{101}$$

Finally, with this initialization, it is possible to compute for each dust fluid the Stokes number at every timestep, given the evolution of the gas and the dust-gas interactions, in order to determine the aerodynamic drag acceleration in the Epstein regime.

Note that the size distribution methodology is subsequently useful to carry out radiative transfer calculations with the RADMC3D code (section 5.2): for example, one can calculate the absorption opacities for each dust population with size s_k, and then directly perform radiative transfer calculations. The next paragraph is dedicated to some selected remarks and issues that we dealt with implementing this setup.

- Depending on the flaring index ($f \neq 0.5$), the VSI can develop (section 2.3.3) in addition to the perturbations generated by the planet. It is something that we noticed in our simulations (see Fig. 2.3.1). We did not specifically study the impact of the VSI perturbations on the planet migration nor on the dust dynamics, but it is possibly something to consider, and which would be a natural outcome of our gas+dust simulations in 3D.

- We noticed an unexpected and very significant increase in the duration of the simulations, depending on the initial position of the planet $r_{p,0}$. In particular, a test run on 4 cpus for $r_{p,0} = 1.0$ took ~ 15 times longer than the same test run for $r_{p,0} = 1.2$, that is a few hours instead of a few minutes for the disk model that we chose. We realized that it is due to the use of the `pow(`$r_{p,0}$`,f)` function in the code, for which $r_{p,0} = 1$ and $f \neq 0$ increases significantly the computation time.

- In Fig. 5.1.1, we show an example of results of 2D simulations with the multifluid version of FARGO3D. We specified the minimum and maximum population size of 7 dust fluids, with a realistic ($q = -3.5$) value for the dust size distribution, added a Jupiter-like planet at $r_{p,0} = 1$ on a fixed circular orbit, and computed the perturbed surface density after 30 orbits for all these fluids (as well as for the gas). We recognize many classical features in the gas and dust density perturbations: the opening of a gap by the planet wakes, a deeper gap for larger dust sizes, the appearance of dust-trapping vortices at both edges of the planet gap due to the Rossby Wave Instability, the accumulation of large solids in the vortices and around the Lagrange points of the planet,...

- The last remark to conclude this section about 3D hydrodynamical simulations is related to the dust settling. We saw in section 2.2.3 that the competition between dust settling (due to the vertical aerodynamic drag between gas and dust) parametrized by S_t and dust stirring (due to the vertical diffusion of particles because of turbulent viscosity) parametrized by α leads to the definition

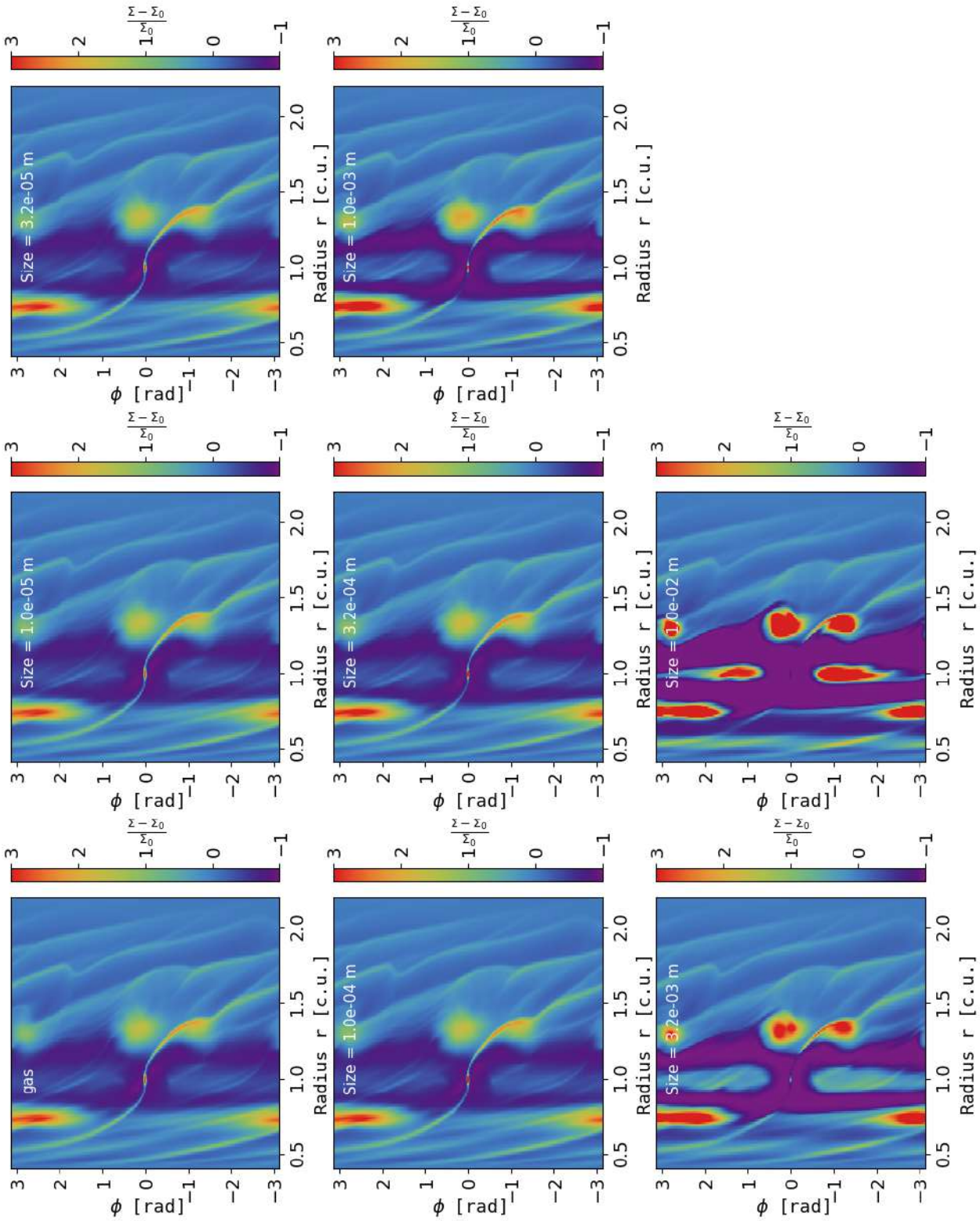

Figure 5.1.1: Example of 2D multifluid simulation with FARGO3D: perturbed surface density in the midplane for NFLUIDS=8 (one gas fluid and 7 dust fluids) and a Jupiter-mass planet, using the size distribution methodology ($s_{min} = 10$ μm, $s_{max} = 1$ cm, $q = -3.5$). The cylindrical radius r is in code units [c.u.]. The dust size increases from bottom to top, and from left to right.

of a dust aspect ratio $h_d = h_g \sqrt{\frac{\alpha}{\alpha + S_t}}$ (Eq. 68), different from but related to the gas aspect ratio h_g. In order to be initially closer to a vertical equilibrium state, we decided to initialize the dust density using h_d instead of h_g. This initialization anticipates the accumulation of particles towards the midplane, with an initial settling that occurs faster as the dust size is large. This initial settling is clearly visible in Fig.5.1.2, which shows the initial volume density profile in the (r-θ) plane (cross section of the disk) for 4 dust fluids (from 1 μm to 1 mm in size) and the gas. We wanted to be initially closer to a state of equilibrium in the gas/dust interaction and avoid the initial transient stage of settling, which can induce rapid vertical motions for the largest particles. However, the expression of h_d assumes for each fluid that dust feedback is neglected. The initial state may therefore be not so close to a numerical equilibrium state in the presence of dust backreaction and with a substantial dust-to-gas mass ratio. The relevance of this use of h_d for the dust density initialization is thus still to be addressed. Some FARGO3D multi-fluid simulations of disk-planet interactions will be presented in chapter 7, sections 7.3 and 7.6.

5.2 RADIATIVE TRANSFER CALCULATIONS: RADMC3D

To produce synthetic maps of the dust and/or gas emission, we post-process our results of hydrodynamical simulations with radiative transfer calculations, with the code RADMC3D (version 0.41, Dullemond et al., 2015). We use this code in 3D and in spherical coordinates. Depending on if the simulations were carried out in 2D or 3D, we either extend the FARGO's 2D polar grid in colatitude around the midplane or we directly use the code's 3D spherical grid in RADMC3D. Given the dust and/or gas density distributions, the important properties of a star (its radius and effective temperature) and the disk geometry (in particular its inclination compared to the line of sight), RADMC3D gives as an output a spectrum or a raw image. The raw intensity can then be convolved with a synthetic beam, given the disk distance and possibly a realistic level of noise. This procedure produces emission maps or spectra that can directly be compared with observations. We detail below the main steps for dust and line radiative transfer calculations. See RADMC3D manual for more details.

5.2.1 *Dust radiative transfer*

The majority of our simulations have been performed in 2D. Furthermore, we wanted to study the continuum emission associated with the dust substructures formed in our simulations. It is thus naturally that RADMC3D was first used to create maps of the dust thermal emission, in radio. Why in radio? At long wavelengths, the dust thermal emission is expected to be dominated by the emission of large grains (typically sub-mm grains, see section 1.1). Moreover, large particles are expected to accumulate efficiently around the midplane (see section 2.2.3), as shown in the bottom panel of Fig. 5.1.2. In this panel, the mass volume density of particles with size $s_d = 1$ mm is close to zero if $\theta \neq 0$, because particles are settled in the midplane. Therefore, because

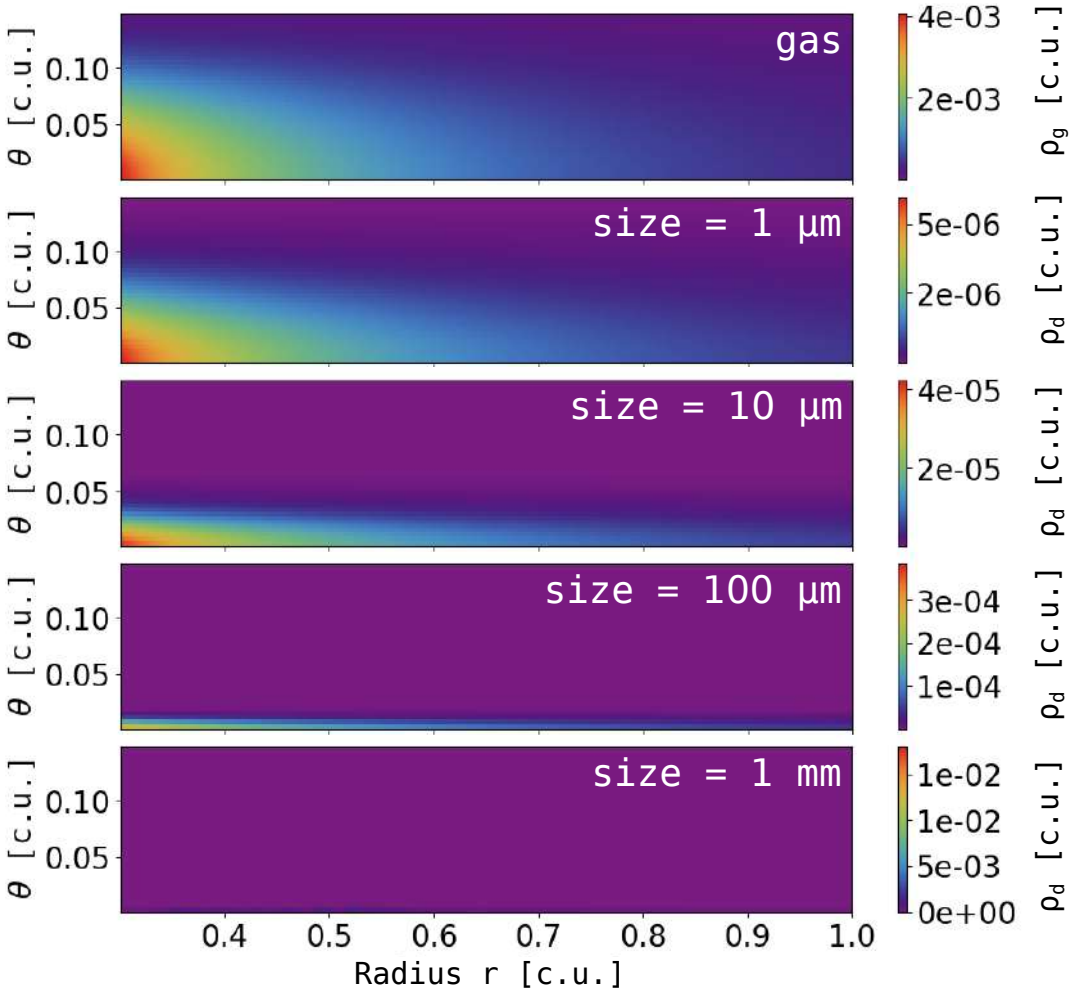

Figure 5.1.2: Example of 3D multifluid simulation with FARGO3D: initial volume density in the (r-θ) plane for NFLUIDS=5 (one gas fluid and 4 dust fluids), using the size distribution methodology ($s_{min} = 1$ µm, $s_{max} = 1$ mm, $q = -3.5$). We used h_d from Eq. 68. r, θ, ρ_g and ρ_d are all in code units [c.u.] here. Concerning the viscosity, $\alpha = 10^{-3}$.

the dust thermal emission in radio comes mainly from the midplane, carrying out 2D simulations can be considered as a good approximation. We present in the following paragraph how to adapt outputs from FARGO-ADSG to RADMC3D. See chapter 6 for the values chosen in the different simulations.

The three important quantities to perform radiative transfer calculations are the dust mass volume density ρ_d, the dust opacities κ_ν and the dust temperature T_d (see section 1.1).

- **Dust mass volume density**: FARGO-ADSG outputs the spatial distribution of particles of different sizes, after each timestep. We first derive the surface density of dust in a sufficiently large number of size bins logarithmically spaced between s_{min} and s_{max}, constrained by the minimum and maximum particle sizes in the hydrodynamical simulations. This is done by assuming a size distribution

$n(s) \propto s^{-q}$ and a total dust mass $M_{dust} = \mu_d M_{gas}$, where M_{gas} is the mass of the disk gas in the simulations. We then obtain the dust's volume density $\rho_{d,bin}$ in each size bin and in each grid cell of the 3D spherical grid used by RADMC3D. This 3D grid is actually the 2D polar grid of the simulations extended in colatitude around the midplane (a logarithmic spacing is used in colatitude with finer grid cells near the midplane). For this, we assume that the vertical distribution of $\rho_{d,bin}$ is Gaussian for each size bin, with a characteristic scale height equal to $H_g \times (1 + S_{t,bin}/\alpha)^{-1/2}$ (Eq.68), where $S_{t,bin}$ is the average Stokes number of dust particles in each size bin. Note that adapting 3D outputs from FARGO3D to RADMC3D is almost straightforward, by just reading the dust's volume density files for each dust fluid directly.

- **Dust opacities**: opacities are calculated using Mie theory, for a given dust composition (water ices, silicates, amorphous carbons, ...). The optical constants of each component of the mixture is obtained from databases, like the Jena database for water ices. We then make use of the Bruggeman formula to obtain the optical constants of the mixture. Finally, the code from Bohren & Huffman (1983) gives the absorption and scattering opacities, as well as the mean scattering angle for anisotropic scattering calculations (see section 2.2.5 and Baruteau et al., 2019, for more details on the methodology).

- **Dust temperature and specific intensity**: armed with the dust's volume density and opacities, the radiative transfer calculations then proceed in two steps: first, the dust temperature T_d is computed via a thermal Monte-Carlo calculation, next the specific intensity of continuum emission is calculated by solving the equation of radiative transfer via photon ray-tracing. This two-stage procedure is described in more details below.

  - **Thermal Monte-Carlo calculation**: The method used here is based on the work of Bjorkman & Wood (2001). First of all, all energy sources are identified, whether it be the star(s) and/or viscous heating. Note that in our radiative transfer calculations, we have only considered irradiation heating from the central star and no internal (viscous) heating. The total luminosity set by the source is then divided into photon packages emitted from the star. We clearly see in this step the importance of the star's properties, in particular its luminosity and its radius. Each photon package brings with itself part of the total energy available, and propagates throughout the grid. Each time it enters a grid cell, the package increases the energy of this cell and heats the dust it contains. Dust grains do not remain inactive in the process, for they have the ability to cool down in order to evacuate the heat brought by the stellar photons. Photon packages thus roam the grid, subject to absorption/re-emission/scattering by the dust, and finally escape once they reach the outer radius of the spherical grid. At the end of the Monte Carlo simulation, since many photon packages have been generated, a thermal structure for the disk is obtained. This thermal structure results from the competition in each cell between the heating by photons irradiation and the dust radiative cooling. It is a steady-state temperature structure for

the dust that is computed, which however discards other plausible heating sources like viscous turbulent heating.

– **Photon ray-tracing**: From the equilibrium dust temperature, but also the dust volume density and dust opacities, it is possible to compute maps of the dust continuum emission. We consider that photon rays are launched by the star. The equation of radiative transfer is thus solved on the spherical grid, given ρ_d, κ_ν and T_d. The specific intensity is calculated along photon rays, by taking into account dust absorption, re-emission and scattering. Note that photons change their direction when scattered, and are re-emitted at a different wavelength when absorbed. We are now able to render an image for the dust continuum emission at a specific wavelength. Other parameters are also important at this stage, in particular the disk inclination.

Finally, knowing the disk distance, the specific intensity is convolved with a beam in order to obtain a realistic synthetic flux map of continuum emission. In some of the synthetic maps presented in Chapter 6, white noise is included by adding at each pixel of the synthetic map of the raw intensity (that prior to beam convolution) a random number following a Gaussian distribution with zero mean and a standard deviation set to 50 μJy/beam. This standard deviation is similar to the rms noise level obtained in recent ALMA observations at 1.3 mm and at similar resolution than that adopted in our synthetic maps (see, e.g., Pérez et al., 2019).

5.2.2 *Lines radiative transfer*

In addition to dust radiative transfer, `RADMC3D` can also perform radiative transfer calculations in molecular or atomic lines. These calculations are particularly useful because molecular spectral line emission is an essential observational tracer to study disk structures. In particular, the emission from (sub-)mm rotational transitions of rare molecules can provide complementary and different information from the dust thermal emission. The radiative transfer calculations developed in chapter 7 were carried out for CO and its isotopologues. The methodology for line radiative transfer is somehow similar to the one used for dust radiative transfer.

- **Molecular properties**: first of all, we need to know the important spectroscopic properties of the chosen molecule (CO in our case), in particular the rotational energy levels of the possible radiative transitions, with the corresponding rest-frame wavelengths of emission.

- **Molecular number density**: then, we need to estimate the number density n_{CO} of that molecule (in cm^{-3}) in the spherical grid of `RADMC3D`. There are two options. Either we use the results from 2D simulations with `FARGO-ADSG`, or we read the gas volume density files directly from 3D simulations with `FARGO3D`. In the former case, we extend in colatitude the gas surface density field by assuming a vertical hydrostatic equilibrium. It leads to a Gaussian vertical profile of the gas volume density, similar to the one presented in Eq. 27 or in Eq. 99. However, we can wonder if a 2D disk model extended in 3D can efficiently mimic the

structures resulting from a complex 3D gas dynamics. Finally in this step, the goal is to translate a gas mass volume density ρ_g into a number density n_{CO} for the CO molecule. For this purpose, we assume a constant molecular abundance $\chi_{CO} = \rho_{CO}/\rho_{H_2}$, with $\rho_{H_2} = \rho_g$ the mass volume density of the most dominant species H_2 outputted by `FARGO-ADSG/FARGO3D`. n_{CO} reads:

$$n_{CO} = \frac{\chi_{CO}}{\mu_\star m_p}\rho_g, \tag{102}$$

with $\mu_\star$ the stellar mean molecular weight and m_p the proton mass (Table 1).

- **Gas temperature**: T_g is another essential quantity for `RADMC3D` to carry out line radiative transfer calculations. To quantify T_g, it may be useful to build on thermal Monte-Carlo calculations (see section 5.2.1) previously performed in a dust radiative transfer simulation, assuming $T_g = T_d$. It is also possible to choose the gas temperature directly from the hydrodynamical simulations.

- **LTE ray tracing**: in the gas radiative transfer calculations presented in this PhD thesis, we assume that molecules are in "Local Thermodynamic Equilibrium" (LTE), which means that the rotational energy levels of CO are populated given a thermal structure at equilibrium. Note that it may not be always the case, in particular for high transition levels that can be triggered by photons out of a state of thermal equilibrium. Before describing the LTE ray-tracing, let us take a closer look at this LTE hypothesis. The balance between heating sources and cooling sources in protoplanetary disks defines a steady-state temperature for the disk. Gas molecules, such as CO, thus acquire a thermal velocity related to this disk temperature, and are subject to collisions with the surrounding H_2 molecules (which is the dominant chemical species in disks). These collisions locally excite the CO molecules which then switch from an energy state J to an energy state J+1. This description is valid in the LTE hypothesis. In reality, the de-excitation (spontaneous or stimulated) of a molecule is also a local source of temperature that can lead to the excitation of neighboring CO molecules. If this local radiative heating process dominates the energy transitions of CO molecules over the local collisional heating process, then the LTE hypothesis is no longer valid. In practice, one can derive a criterion to determine whether or not the LTE hypothesis is relevant for a disk model (see, e.g., Weaver et al., 2018, their section 2.1). For a given chemical species (e.g. CO) in a given environment (e.g. dominated by H_2) and for a given energy transition (e.g. $J = 3 \rightarrow 2$), one can define a critical density n_{crit} of CO below which collisions are no longer sufficient to dominate the energy transition. Above n_{crit}, on the contrary, the medium is dense enough for the collisions, i.e. the kinetic temperature of the gas, to dominate the energy transition. It is possible to consider non-LTE prescriptions with `RADMC3D` and this is a possible extension of the work presented here. Under the LTE hypothesis, photon rays are launched by the star. The methodology to determine CO line emission is actually the same as the ray-tracing presented in section 5.2.1. This time, in order to determine the specific intensity, the source terms in the radiative transfer equations are different (spontaneous emission,

stimulated emission and absorption). Note that the thermal broadening of the lines is determined by T_g, and it is optionally possible to consider a non-thermal microturbulent line broadening. Finally, RADMC3D produces a multi-color image from which we can make channel maps (sections 4.4.2 and 7.3).

5.3 PYTHON ANALYSIS TOOLS

Apart from hydrodynamical simulations and radiative transfer calculations, I have dedicated a significant amount of time during my PhD thesis work on the use, modification, elaboration and/or development of python codes for post-processing my calculations results. To give a few examples, the publicly available python program fargo2radmc3d has been widely used as a coupler between FARGO-ADSG and RADMC3D. In particular, it processes and adapts FARGO-ADSG outputs to produce input parameter files that can be read by RADMC3D (see section 5.2.1). With my PhD supervisor, we have extended and automated the functionalities of fargo2radmc3d in order to make possible on the one hand the line radiative transfer calculations, and on the other hand to be able to adapt the outputs of FARGO3D to RADMC3D. I provide below a a further, non-exhaustive list of some python programs that I elaborated and/or developed.

- In all this manuscript, as well as the paper published earlier this year in February 2020 (Wafflard-Fernandez & Baruteau, 2020), we largely use the module colorblind, notably created for color-blind people. For the choice of color associations and colormaps, this module has been written based on the work of Paul Tol (2012) - "Colour Schemes" SRON Technical Note, SRON/EPS/TN/09-002. Color-bind readers (non-color-blind people as well) are by the way more than welcome to share their remarks on the visibility of the different plots and images presented here.

- A lot of visualization tools have been developed, with various goals, in particular to be able to display the numerous hydrodynamical quantities that FARGO-ADSG and FARGO3D produce (surface densities, velocities, inverse vortensities, ...). Some programs have been dedicated to the outputs regarding the planet, like the evolution of its orbital properties or the coorbital deficit (see its definition in section 3.3.3.2 and its use in chapter 6). For example, a simplified 2D toy model has also been developed to understand channel maps and the impact of a perturbed azimuthal velocity field onto these channel maps. Other programs have been used to study the dust dynamics and its evolution, with for example the possibility to track individually discernible groups of particles (see section 7.7 for an example of particles tracking).

APPENDIX

5.A OUTPUT STEP IN FARGO-ADSG/FARGO3D

The main files produced by FARGO and used in post-processing are listed below.

- **For the fluid(s)**: in FARGO-ADSG, the gas surface density, radial velocity and azimuthal velocity fields are respectively in the gasdensX.dat, gasvradX.dat and gasvthetaX.dat binary files, with X the output number. When the energy equation is taken into account, a new output is produced, the TemperatureX.dat file for the output number X, which describes the temporal evolution of the gas temperature T_g. In FARGO3D, if F is a gaseous fluid or a dusty fluid (F=gas,dust1,...), the FdensX.dat, FvxX.dat, FvyX.dat and FvzX.dat binary files contain respectively the volume density, 3D radial velocity, 3D azimuthal velocity and 3D colatitudinal velocity fields.

- **For the dust**: in FARGO-ADSG, the dustsystatX.dat are ascii files that contain the main quantities for dust particles at a given output number X: the particles orbital radius R_d, azimuth ϕ_d, radial velocity, azimuthal velocity, Stokes number St and physical size s_d in meters.

- **For the planet(s)**: in FARGO-ADSG and FARGO3D, four main files are produced. planeti.dat and bigplaneti.dat are ascii files that contain important quantities for the planet number i: the current output number, the planet x-coordinate, the planet y-coordinate, the x-component of the velocity v_x, the y-component of the velocity v_y, the planet mass, the mass lost in the inner edge of the grid, the date and the frame angular velocity. orbiti.dat are ascii files containing orbital parameters concerning the planet number i: the date, the planet eccentricity, the planet semi-major axis, the planet mean anomaly, the planet true anomaly and the periastron position angle. Lastly, tqwki.dat are ascii files that contain the quantities related to the torques Γ and the powers Π exerted onto the planet number i: the current output number, the full torque Γ_{in}^{tot} exerted by the inner disk onto the planet, the full torque exerted Γ_{out}^{tot} by the outer disk onto the planet, Γ_{in} without taking the Roche lobe into account, Γ_{out} without taking the Roche lobe into account, the full power Π_{in}^{tot}, the full power Π_{out}^{tot}, Π_{in} without the Roche lobe, Π_{out} without the Roche lobe and the date.

6

INTERMITTENT PLANET MIGRATION AND FORMATION OF MULTIPLE DUST RINGS AND GAPS IN PROTOPLANETARY DISKS

Part of this chapter is taken from Wafflard-Fernandez & Baruteau (2020), Intermittent planet migration and formation of multiple dust rings and gaps in protoplanetary disks, published in MNRAS. We investigate in this chapter how the large-scale inward migration of a single planet can structure the dust content of a massive disk. In many circumstances, the migration of a partial gap-opening planet with a mass comparable to Saturn is found to run away intermittently. By means of 2D gas and dust hydrodynamical simulations, we show that intermittent runaway migration can form multiple dust rings and gaps across the disk. Each time migration slows down, a pressure maximum forms beyond the planet gap that traps the large dust. Post-processing of our simulations results with 3D dust radiative transfer calculations confirms that intermittent runaway migration can lead to the formation of multiple sets of bright and dark rings of continuum emission in the (sub)millimeter beyond the planet location. The plan of this chapter is the following. In section 6.1, we briefly describe the physical model and numerical methods of the hydrodynamical simulations and the radiative transfer calculations. Primary results are presented in section 6.2, before focusing on two fiducial cases in sections 6.3 and 6.4. In section 6.5, we analyze the impact of several parameters and hypotheses on our numerical model. The longevity of the structures is discussed in section 6.6, and an opening to this work is proposed in section 6.7.

CONTENT

6.1 Physical model and numerical methods . . . 127
6.2 Overview . . . 130
6.3 Uther simulation ($h_0 = 0.05$, $\alpha = 10^{-3}$) . . . 132
6.3.1 Coorbital vorticity-weighted deficit . . . 133
6.3.2 Dust spatial distribution . . . 138
6.3.3 Continuum emission . . . 142
6.4 Pendragon simulation ($h_0 = 0.06$, $\alpha = 10^{-4}$) . . . 144
6.4.1 Dust spatial distribution . . . 145
6.4.2 Continuum emission . . . 147
6.5 Parameter space and beyond the fiducial cases . . . 149
6.5.1 Initial gas surface density profile . . . 149
6.5.2 Self-Gravity . . . 155
6.5.3 Energy equation . . . 156
6.5.4 Resolution . . . 159
6.5.5 Dust backreaction . . . 160
6.5.6 Inner planet and resonance . . . 163
6.6 Longevity of the dust rings . . . 164
6.7 Geometrical spacing . . . 165

Appendices 169
6.A Mass of the circumplanetary disk . . . 169
6.B Additional results for fast and slow migration . . . 169
6.C A simple modification to the expression of the coorbital vortensity deficit for fast migration . . . 171

7 FURTHER OBSERVATIONAL DIAGNOSTICS OF PLANET FORMATION AND MIGRATION: ONGOING PROJECTS 173

6.1 PHYSICAL MODEL AND NUMERICAL METHODS

In this chapter, we present results of 2D hydrodynamical simulations of the gas and dust of a protoplanetary disk with an embedded planet. Simulations are carried out with the code `Dusty FARGO-ADSG`, for which we detail the important parameters, structure and hypotheses in section 5.1.1. We then post-process our results of simulations with dust radiative transfer calculations to infer the continuum emission that results from the dust's annular substructures obtained in our simulations. Concerning the radiative transfer calculations, they are carried out with the code `RADMC3D`. Synthetic maps of continuum emission are computed for a face-on disk at $\lambda = 1.3$ mm, which is the same wavelength as in the ALMA survey of disks undertaken by DSHARP (Huang et al., 2018a). See section 5.2.1 for more details about dust radiative transfer calculations. Specifically for the study presented here, we adopt a polar coordinate system (r, θ), with r the radial cylindrical coordinate measured from the central star and θ the **azimuthal** angle. Some specific details about the physical model and numerical setup are presented in this section. A short summary of the general parameters of the simulations is given in Table 6.1.1.

Parameter	Symbol	Value
Code's unit of length	r_0	10 au
Code's unit of mass	$M_\star$	1 $M_\odot$
Initial Toomre parameter at r_0	Q	$\in [5.3 - 64]$
Self-Gravity	—	Yes
Energy equation	—	No
Gas surface density slope	σ	1.0
Flaring index	f	0.15
Planet's initial location	$r_{p,o}$	$2r_0 = 20$ au
—	$q/h^3(r_{p,o})$	~ 1.46
Dust's size range	$\in [s_{min} - s_{max}]$	$\in [10\ \mu m - 10$ cm$]$
Dust's internal density	ρ_{int}	2 g.cm^{-3}
Number of radial cells	N_R	600
Number of azimuthal cells	N_θ	900
Minimum disk radius	r_{min}	2 au
Maximum disk radius	r_{max}	40 au

Table 6.1.1: Main parameters of the fiducial cases for our hydrodynamical simulations.

We present here a summary of the important parameters, hypotheses and models for this study. For more details on the numerical methods, see chapter 5.

- Unless indicated, we assume for simplicity a locally isothermal equation of state for the gas. This means that the gas temperature, or equivalently the sound speed, is fixed in time but varies with r. This assumption is generally more appropriate to the outer parts of protoplanetary disks, where the radiative cooling and/or diffusion timescales are short compared to the orbital timescale. However, we will see in section 6.5.3 that allowing the gas temperature to vary with time by solving the energy equation does not qualitatively change our results. In our

simulations with a locally isothermal equation of state, the aspect ratio $h(r)$, which we recall is the ratio between the sound speed and the Keplerian speed, is chosen as $h(r) = h_0 \times (r/r_0)^{0.15}$, with $r_0 = 10$ au the code's units of length. Two values for the aspect ratio at r_0 are adopted : $h_0 = 0.05$ and 0.06, which respectively correspond to a temperature of 63 K and 91 K for a Sun mass star and a solar composition (mean molecular weight $\mu_\odot = 2.4$).

- For the radial turbulent transport of the disk's angular momentum, we use a constant α. The alpha turbulent viscosity at a few to a few tens of au in the disks midplane is highly uncertain. Non-ideal magneto-hydrodynamic simulations show that it may vary from a few $\times 10^{-5}$ to as high as a few percent, depending on the amplitude and sign of the vertical magnetic field that threads the disk (Simon et al., 2015; Béthune et al., 2017). Modeling of the ring-like structures in the (sub)millimeter continuum emission of some protoplanetary disks suggests that the midplane alpha at few tens of au should be $\lesssim 10^{-4}$ in order to reproduce the rings sharpness (e.g., Pinte et al., 2016; Pérez et al., 2019). These rather low values are overall consistent with observations of the non-thermal broadening in protoplanetary disks (Flaherty et al., 2015). To reflect this uncertainty, we will adopt two values of α in this study: 10^{-4} and 10^{-3}. We will see that, independently of its effect on planetary migration, the value of α has a clear impact on the dust structures that form because of disk-planet interactions, such as their lifetime, their radial width, or their degree of axisymmetry.

- The initial gas surface density profile is $\Sigma_0(r) = \Sigma_0 \times (r/r_0)^{-1}$, with Σ_0 the gas surface density at r_0. We adopt in this work three values for Σ_0: 3×10^{-4}, 10^{-3} and 3×10^{-3} in code units, which, by choosing a code's unit of mass of 1 $M_\odot$, correspond to about 27, 89 and 267 g.cm^{-2} at $r_0 = 10$ au, respectively. For these three values of Σ_0, the disk-to-star mass ratio amounts to 0.007, 0.02 or 0.07, respectively, while the Toomre Q-parameter at r_0, which is proportional to h_0, initially equals 53, 16 and 5.3, respectively, for $h_0 = 0.05$. Gas self-gravity is included in our simulations, and the disk gas is stable against the gravitational instability throughout the computational domain. Because we perform 2D simulations, a softening length of $0.3H(r)$ is used in the calculation of the self-gravitating acceleration to mimic the vertical extent of the disk (Baruteau & Masset, 2008b; Müller et al., 2012). We take into account the indirect terms due to the acceleration of the star by the planet and the disk.

- The important parameters for the grid are given in Table 6.1.1. In particular, the grid stretches from 2 au to 40 au, with 600 radial cells with a logarithmic spacing and 900 evenly spaced cells in the azimuthal direction. For the boundary conditions, we use wave-killing zones that extend from 2 to 3 au, and from 35 to 40 au. In these wave-killing zones, we use the `DampToViscous` parameter, in order to damp the gas density and gas radial velocity towards the radial profiles obtained by the 1D purely viscous evolution model (see section 5.1.1.1). Given the viscosity adopted in our disk models ($\alpha \leqslant 10^{-3}$) and the duration of our runs (a few thousand planet orbits, at most), this boundary condition is, in practice, nearly identical to damping the gas density and radial velocity towards their

initial radial profile. Our 1D grid has 1000 cells logarithmically spaced between 0.4 and 300 au, and the gas surface density is set to zero at the edges of the 1D grid. The choice of boundary conditions does not change significantly the results as long as the planet remains further than ~ 4.5 au.

- r_d and θ_d represent the radial and azimuthal position of a dust particle. There is no dust back-reaction onto the gas. We will discuss this assumption in the simulations results in sections 6.3 and 6.4. The important parameters concerning dust particles are presented in Table 6.1.1. In particular, they have an internal density of $\rho_{int} = 2$ g.cm^{-3}, and their sizes range from $s_{min} = 10$ µm to $s_{max} = 10$ cm, and they have a size distribution such that $q = -1$. The number of particles and their initial location will be specified in sections 6.3 and 6.4.

- The planet, which we will refer to as $\mathcal{P}$ in this chapter, is set initially at $r_{p,o} = 2r_0 = 20$ au from the star. This work focuses on how the migration of $\mathcal{P}$ due to its interactions with the disk gas impacts the formation of dust rings by the spiral wakes of $\mathcal{P}$. The mass of $\mathcal{P}$ is therefore chosen such that its wakes can form pressure maxima on either side of the planet's orbit, where dust particles can be trapped. We have chosen to study planets that carve a partial gap in the gas around their orbit, and which can be subject to fast runaway type III migration if the disk is sufficiently massive (Masset & Papaloizou, 2003). Accretion on the planet is discarded in this study.

- The range of planet-to-primary mass ratios (q_p) for which partial gap opening occurs depends on the disk's aspect ratio and turbulent viscosity near the planet's location. Throughout this work, unless otherwise stated, results are obtained for $q_p \approx 1.46h^3(r_{p,o})$. More specifically, the simulations with $h_0 = 0.05$ have $q_p = 2.5 \times 10^{-4}$, those with $h_0 = 0.06$ have $q_p = 4.3 \times 10^{-4}$. These correspond to planets of ~ 0.9 and ~ 1.5 the mass of Saturn orbiting Solar-mass stars. The mass of the planet is gradually increased over its first 5 orbits, yet it is allowed to migrate from the beginning of the simulations. A softening length of $0.6H(r_p)$ is used to calculate the planet acceleration on the gas, where r_p denotes the (time varying) orbital radius of the planet.

- For the dust radiative transfer calculations, we assume a size distribution $n(s) \propto s^{-3.5}$ and a total dust mass $M_{dust} = 10^{-2}M_{gas}$. The 3D spherical grid used by `RADMC3D` corresponds to the 2D polar grid of the simulations extended in colatitude with 36 cells spanning $\pm 2H$ around the midplane (a logarithmic spacing is used in colatitude with finer grid cells near the midplane). Opacities are calculated using Mie theory, assuming a dust mixture comprised of 30% astrosilicates and 70% water ices, which corresponds to a mean internal density of ~ 1.7 g cm^{-3}, close to that assumed in the hydrodynamical simulations. We use the Bruggeman formula to obtain the optical constants of the mixture (the optical constants of water ices are from the Jena database, those of astrosilicates are from Draine & Lee, 1984). We assume the disk to be located at 150 pc, with zero inclination relative to the line of sight, and a central star with a radius of 2 $R_\odot$ and effective temperature of 7000 K. We use 10^9 photon packages for

the thermal Monte-Carlo calculations. Scattering of dust grains is discarded. Since our disk model is rather optically thick at 1.3 mm, discarding scattering significantly decreases the computation time of the radiative transfer calculations. We will verify this assumption in section 6.4.2. Finally, knowing the disk distance, the specific intensity is convolved with a 0.02" beam in order to obtain a synthetic flux map of continuum emission.

We begin this chapter with an overview of our results of hydrodynamical simulations in section 6.2, which delineates the region of parameter space for which intermittent planetary migration is obtained. We then focus in sections 6.3 and 6.4 on two simulations in which intermittent migration results in the formation of multiple dark and bright rings of emission at millimeter wavelengths. In section 6.5, we explore the impact of some key parameters in the setting up of intermittent migration, followed in section 6.6 by a study of the longevity of these aforementioned bright rings. We discuss the results in section 6.7.

6.2 OVERVIEW

We present in Fig. 6.2.1 a general view of twelve simulations characterized by the parameters h_0, α and Σ_0 described in section 6.1. In this figure, we plot the evolution of the planet's orbital radius as a function of time, with a panel for each value of h_0. For both values of h_0, we remark that the graphs can be separated into three specific areas depending on Σ_0:

- *Fast migration:* for the most massive disk model ($\Sigma_0 = 3 \times 10^{-3}$), the four curves (in yellow) almost lie on top of one another, which shows that the migration rate hardly depends on α and h_0. It indicates that migration is mostly driven by a strong dynamical corotation torque, rather than by the the wave (Lindblad) torque and the static corotation torque (both of which scale as h_0^{-2} for low-mass planets). The very fast inward migration stalls when the planet ($\mathcal{P}$) reaches the inner damping zone of the grid, where its migration is no longer determined by the physical properties of the disk. This migration regime is so fast that the interaction between $\mathcal{P}$ and the dust particles remains limited, as is illustrated in the first row of Fig. 6.B.1 in Appendix 6.B. As $\mathcal{P}$ moves inwards, most dust particles inside the orbit of $\mathcal{P}$ perform indeed an outer horseshoe U-turn relative to $\mathcal{P}$ and end up forming a dust band behind $\mathcal{P}$ that is similar to the initial one. Some of the particles embarking onto horseshoe U-turns also become trapped around the L4 Lagrange point in front of $\mathcal{P}$ in the azimuthal direction. We will come back in section 7.5 to this particles trapping in L4 due to fast inward migrating planets. Once the dust band is formed again, it drifts and diffuses radially due to gas drag and turbulence, respectively.

- *Slow migration:* for the least massive disk model ($\Sigma_0 = 3 \times 10^{-4}$, blue curves), migration is slow and the dust rings generated by $\mathcal{P}$ display little evolution over the duration of the simulations. $\mathcal{P}$ actually forms three dust rings: one on each side of its partial gap in the gas, and one that stays coorbital with $\mathcal{P}$. As $\mathcal{P}$ moves

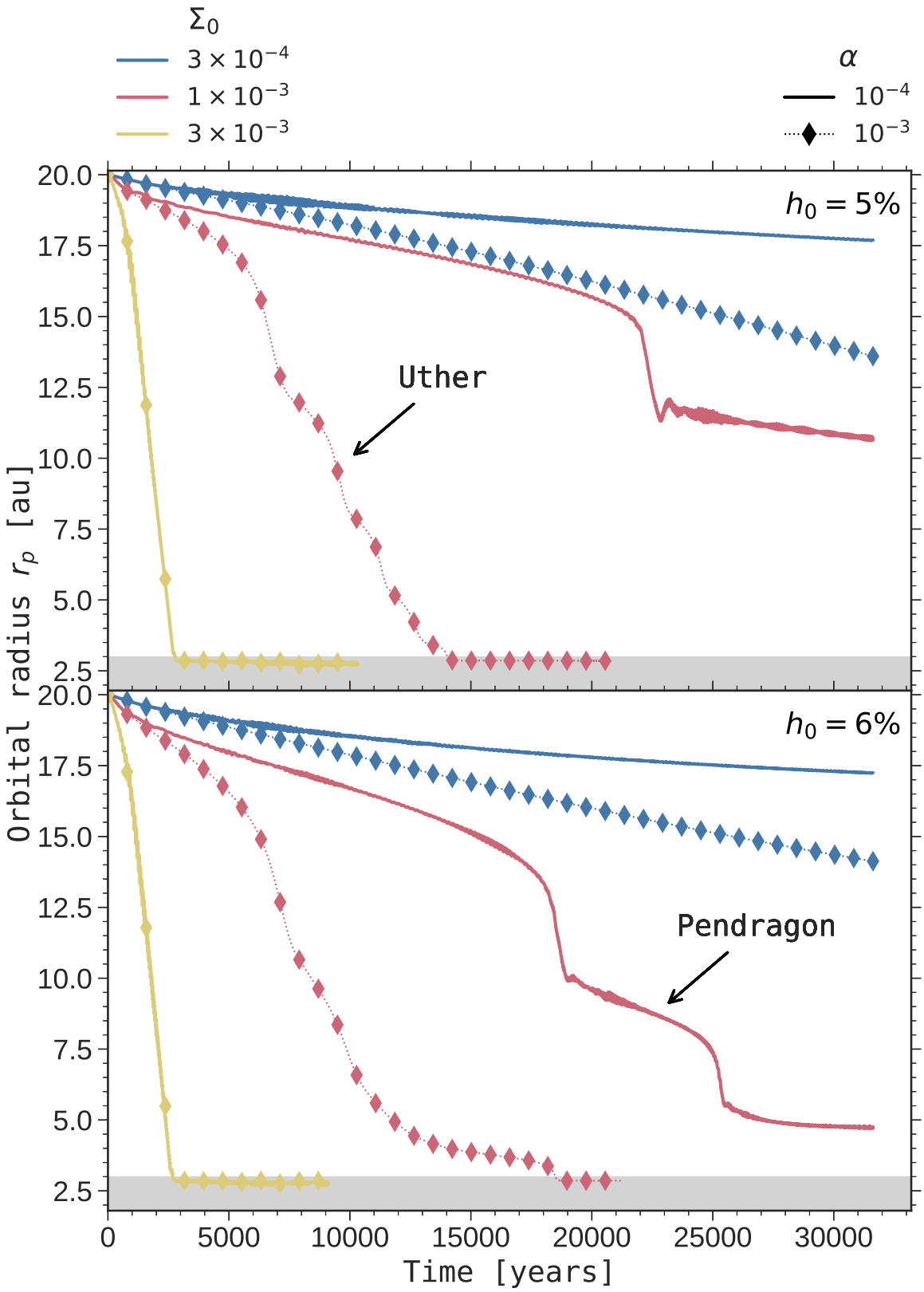

Figure 6.2.1: Overview of our results of hydrodynamical simulations: time evolution of the planet's orbital radius for three values of the gas surface density (Σ_0), two values of the alpha turbulent viscosity (α) and of the disk's aspect ratio (h_0). **Top:** $h_0 = 5\%$. **Bottom:** $h_0 = 6\%$. The gray bands correspond to the inner wave-killing zone. The results for the Uther and Pendragon runs are presented respectively in sections 6.3 and 6.4.

inwards, the inner and coorbital dust rings move inward with $\mathcal{P}$ while the outer ring roughly stays at its initial location (Pérez et al., 2019; Meru et al., 2019, see also section 4.5, section 6.4.1 and the second row of Fig. 6.B.1 in Appendix 6.B). This implies that the mutual separation between the three rings increases as $\mathcal{P}$ migrates. This effect may well be observed in the outer parts of the HD 169142 disk, where the radial asymmetry between the three fine bright rings located between $\sim 0''.5$ and $\sim 0''.7$ (see left part of Fig. 4.1.2) has been interpreted as the signature of an inward-migrating mini-Neptune planet (Pérez et al., 2019).

- *Intermittent migration:* the intermediate curves for $\Sigma_0 = 10^{-3}$ (in red) show non-steady (or non-smooth) orbital evolution, with several short stages of runaway migration which impart a stair-case shape to the curves. Lin & Papaloizou (2010) and McNally et al. (2019) have reported results of hydrodynamical simulations with similar multiple episodes of runaway migration, which were obtained in inviscid or low-viscosity disk models. These intermittent stages of runaway migration are related to the time evolution of the coorbital vorticity-weighted mass deficit of the planet (Masset & Papaloizou, 2003). This quantity close to the one defined in section 3.3.3.2 basically compares the inverse vortensity[1] of the gas crossing the planet's orbit with that of the gas trapped in the planet's horseshoe region (see Eq. 103 below). Although it has the dimension of a mass, the coorbital vorticity-weighted mass deficit should rather be considered a coorbital vortensity deficit, especially for the low-mass planets considered in our study (Paardekooper, 2014). Note in particular that δm may be either positive or negative, depending on the background vortensity profile. We will now call δm the coorbital vortensity deficit. When δm exceeds the mass of the planet (M_p) plus that of its circumplanetary disk (M_{cpd}), $\mathcal{P}$ enters a regime of runaway migration[2] (see Masset & Papaloizou, 2003; Masset, 2008, and section 3.3.3.2). However, as will be shown via one of our simulations in section 6.3, δm may decrease during runaway migration, with the consequence that runaway ceases and the migration of $\mathcal{P}$ proceeds at a slower pace. We will show that during this phase of reduced migration, the vortensity inside the horseshoe region gets mixed and runaway can start again.

In the following, we focus on the results of two simulations, which are labeled Uther and Pendragon in Fig. 6.2.1, for which $\mathcal{P}$ displays intermittent runaway migration. The results of both simulations are described in sections 6.3 and 6.4.

6.3 UTHER SIMULATION ($h_0 = 0.05$, $\alpha = 10^{-3}$)

The simulation that we refer to as Uther displays four episodes of runaway migration in the upper panel of Figure 6.2.1. We begin in section 6.3.1 by showing that these

1 we recall that the gas vortensity, or potential vorticity, refers in this study to the ratio between the vorticity and the surface density, with the vorticity being the z-component of the curl of the 2D velocity.

2 we have checked that M_{cpd} is always smaller than M_p in our simulations, by typically an order of magnitude. Thus, we will now simply use $\delta m > M_p$ to define the onset of runaway migration (see Fig. 6.A.1 in Appendix 6.A).

Parameter	Symbol	Value
Gas surface density at r_0 [code units]	Σ_0	10^{-3}
Disk's aspect ratio at r_0	h_0	0.05
Alpha turbulent viscosity	α	10^{-3}
Planet to primary mass ratio	q_p	2.5×10^{-4}
Number of dust super-particles	N_{part}	50000
Dust's initial location	$\in [r_{d,min} - r_{d,max}]$	$\in [14 - 21]$ au

Table 6.3.1: Parameters of simulation Uther (section 6.3)

intermittent stages of runaway migration are due to oscillations in the planet's coorbital vortensity deficit. We then examine the impact of these successive jolts of the planet on the dust's spatial distribution in section 6.3.2, and on the dust's thermal emission at millimeter wavelengths in section 6.3.3. The main parameters of the simulation are summarized in Table 6.3.1.

6.3.1 *Coorbital vorticity-weighted deficit*

As recalled in the previous section and in section 3.3.3.2, the coorbital vortensity deficit δm is key to define when migration runs away. When $\delta m < M_p$, the dynamical corotation torque is not large enough to trigger runaway migration. On the contrary, when $\delta m > M_p$, $\mathcal{P}$ enters a runaway migration regime for which small perturbations to the position of the planet are rapidly amplified. The coorbital vortensity deficit reads (Masset & Papaloizou, 2003):

$$\delta m = 4\pi r_p \omega(r_p) \times \left[x_s \frac{\Sigma}{\omega}(r_p - x_s) - \int_{r_p - x_s}^{r_p} \frac{\Sigma}{\omega}(r)\, dr \right], \tag{103}$$

with ω the gas vorticity and x_s the radial half-width of the planet's horseshoe region. The first term in the square brackets features the inverse vortensity of the gas entering the horseshoe region at orbital radius $r_p - x_s$, the second term the inverse vortensity of the gas trapped in libration inside the horseshoe region. Eq. (103) is valid while the planet's migration timescale over a radial distance x_s remains much longer than the half-libration timescale of fluid elements at the horseshoe separatrices, located at $r_p \pm x_s$. In other words, δm can be expressed by Eq. (103) so long as the migration speed $\dot{a}$ is slow compared to the critical speed $\dot{a}_c$:

$$|\dot{a}| \ll \dot{a}_c = \frac{3 x_s^2 \Omega_p}{4\pi r_p}, \tag{104}$$

with Ω_p the orbital frequency of $\mathcal{P}$. When this is the case, the horseshoe region can be approximated as a rectangle in polar cylindrical coordinates, with a radial width of $2x_s$ and an azimuthal width of nearly 2π. We will also assume that the gas vortensity trapped in libration with $\mathcal{P}$ is uniform (see, e.g., Paardekooper, 2014, and Fig. 6.3.3 below). Further denoting by $\mathcal{I}_\mathcal{V}$ the inverse vortensity Σ/ω, by $\mathcal{I}_{\mathcal{V}_e}$ the inverse

vortensity of the gas entering the horseshoe region ($\mathcal{I}_{\mathcal{V}e} = \mathcal{I}_{\mathcal{V}}(r_p - x_s)$), and by $\mathcal{I}_{\mathcal{V}\text{lib}}$ that of the gas trapped in libration, Eq. (103) can thus be recast as

$$\delta m \approx 4\pi r_p \omega(r_p) x_s \times [\mathcal{I}_{\mathcal{V}e} - \mathcal{I}_{\mathcal{V}\text{lib}}]\,, \tag{105}$$

which agrees with the simplified version of δm obtained in Lin & Papaloizou (2010) (see their section 6.1.1). When Eq. (104) is no longer satisfied, both the material trapped in libration with $\mathcal{P}$ and the orbit-crossing flow have an azimuthal extent $\Delta\theta < 2\pi$. Assuming that the expression of δm in Eq. (103) remains valid even when $|\dot{a}| \sim \dot{a}_c$, we show in Appendix 6.C that the approximated expression for δm in Eq. (105) gets multiplied by $\Delta\theta/2\pi$ (see Eq. 110). A schematic illustration of $\mathcal{I}_{\mathcal{V}e}$ and $\mathcal{I}_{\mathcal{V}\text{lib}}$ can be found in the top-middle panel of Fig. 6.3.3.

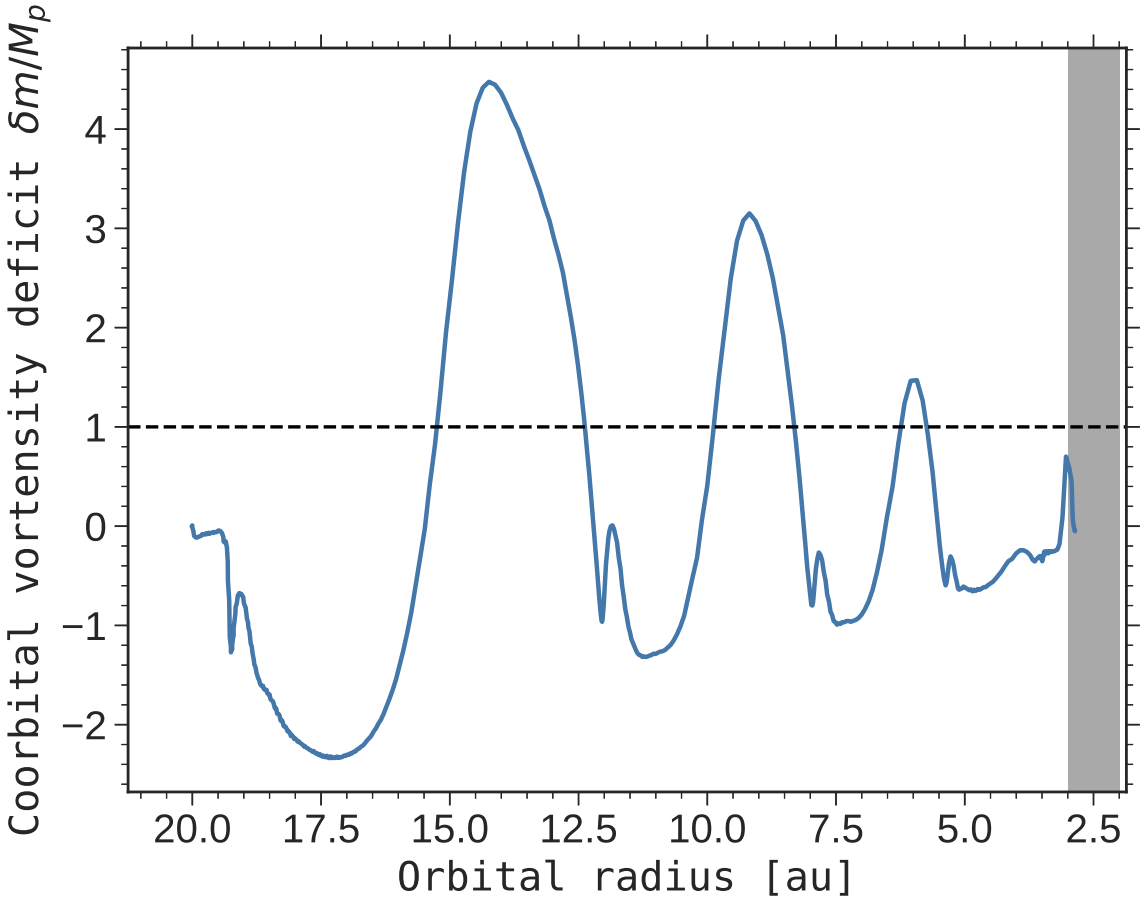

Figure 6.3.1: Numerical estimation of the coorbital vortensity deficit (δm) during the inward migration of $\mathcal{P}$ in the Uther simulation. δm is normalized by the planet's mass M_p. The horizontal dashed line separates the regimes of runaway migration ($\delta m/M_p \geqslant 1$) and non-runaway migration ($\delta m/M_p \leqslant 1$). The gray band corresponds to the inner wave-killing zone.

We display in Fig. 6.3.1 the coorbital vortensity deficit normalized by the planet's mass M_p. For simplicity, δm is calculated via Eq. (105) instead of Eq. (110), as an automatic determination of $\Delta\theta$ from the simulation outputs would be quite cumbersome.

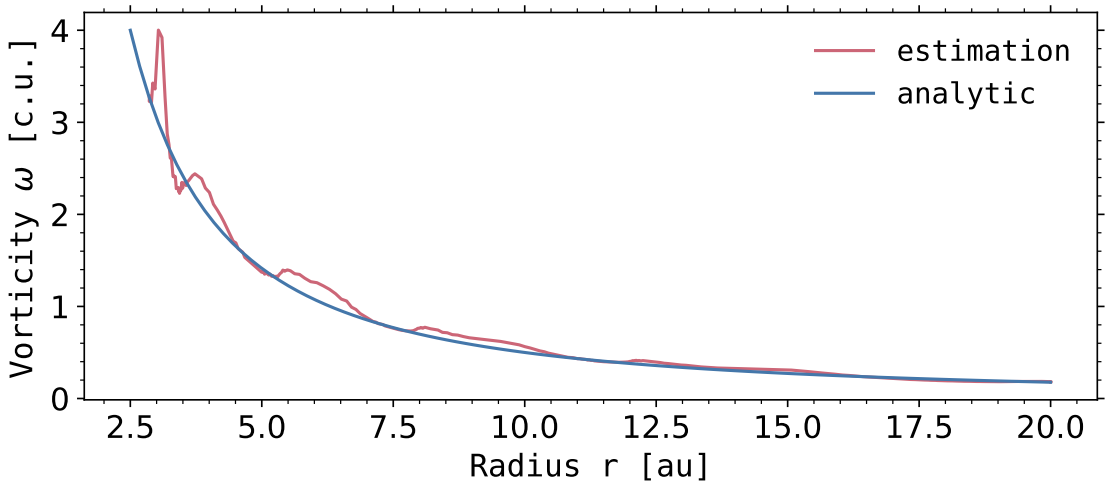

Figure 6.3.2: Numerical estimation of the vorticity $\omega(r_p)$ of the material trapped in libration (red curve), during the inward migration of $\mathcal{P}$ in the Uther simulation. The blue curve is the unperturbed initial profile $\omega(r) = \Omega_K(r)/2$, with $\Omega_K(r)$ the Keplerian frequency.

For $\omega(r_p)$, it can be approximated as the unperturbed (initial) value of the gas vorticity at $r = r_p$, which is demonstrated in Fig. 6.3.2.

For x_s, we use $x_s \approx 2.45 r_p \times (q_p/3)^{1/3}$, which applies to planets with $q_p/h^3(r_p) \gtrsim 2$ on fixed circular orbits (Masset et al., 2006; Jiménez & Masset, 2017). We have checked by a streamline analysis that this expression still works correctly in our simulations. A systematic determination of $\mathcal{I}_{\mathcal{V}e}$ and $\mathcal{I}_{\mathcal{V}\text{lib}}$ from the simulation outputs would also be a little tricky. For $\mathcal{I}_{\mathcal{V}e}$, we approximate it as the inverse vortensity radially averaged over horseshoe U-turns just behind the planet in azimuth (since the planet migrates inward), using the fact that the inverse vortensity over a radial U-turn remains essentially unaltered for the range of viscosities in our disk models. This method works generally well, except at the initiation and termination of the runaway stages, where a streamline analysis would be required to estimate $\mathcal{I}_{\mathcal{V}e}$ more accurately. For the quantity $\mathcal{I}_{\mathcal{V}\text{lib}}$, it is estimated as the average inverse vortensity of gas in front of the planet in azimuth around $r = r_p$, using the fact that, as already stated below, the vortensity of the gas trapped in libration with the planet is roughly uniform. This method is less robust at the termination of runaway stages because of vortensity mixing within the horseshoe region.

Fig. 6.3.1 clearly shows that δm oscillates around M_p, which indicates that $\mathcal{P}$ alternates between stages of runaway and non-runaway migration, and which explains the steps obtained in the migration pattern (Fig. 6.2.1). Note that when the planet runs away, the material that remains in corotation (or in libration) with $\mathcal{P}$ shrinks to a trapezoidal region ('tadpole' region) in the radius-azimuth plane, either ahead or behind the planet in azimuth depending on the direction of migration (Masset, 2002; Pepliński et al., 2008a,b). The trapezoidal region, which in our case is ahead of the planet as the latter migrates inwards, has an azimuthal width $\Delta\theta < 2\pi$ when migration

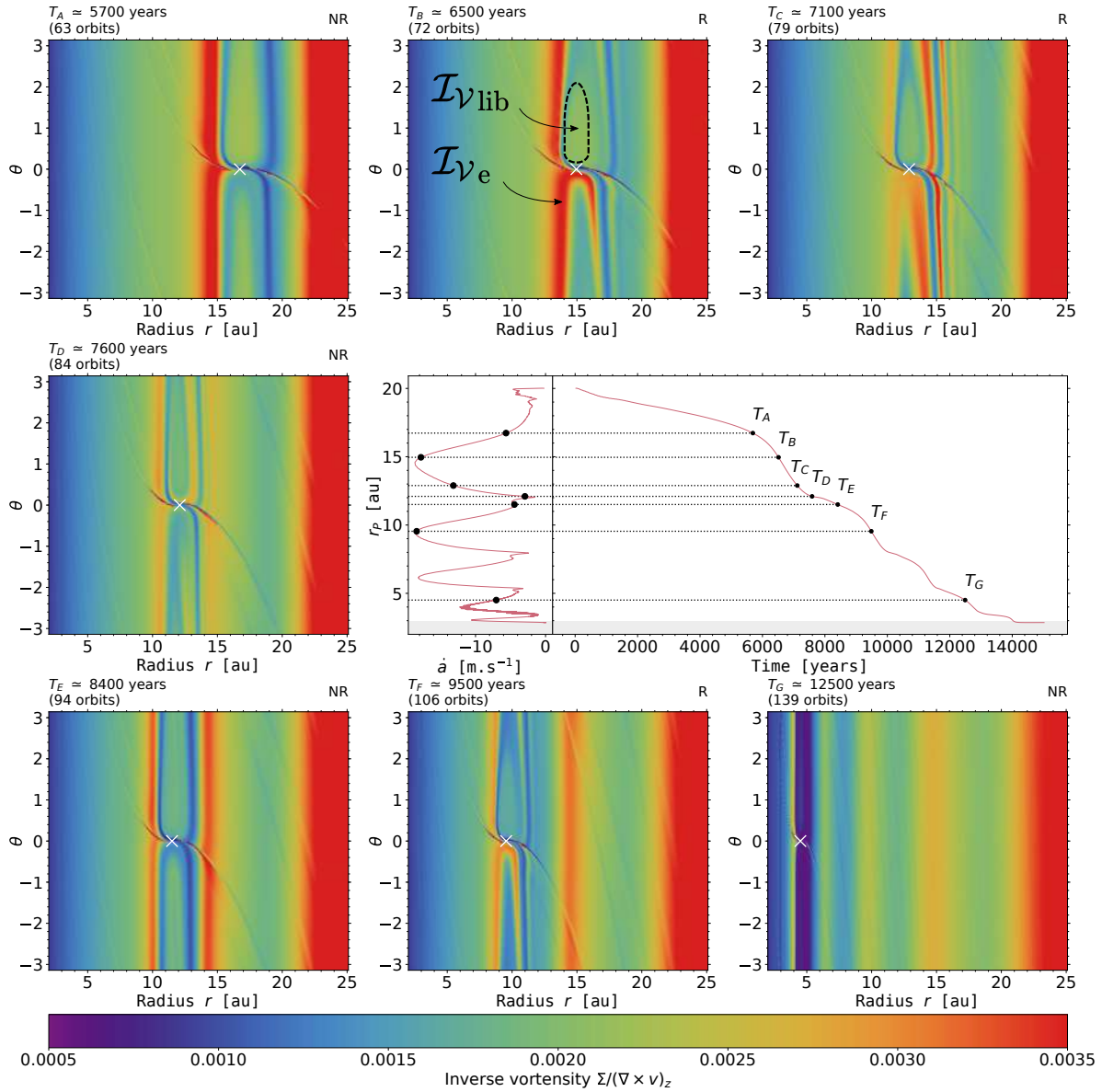

Figure 6.3.3: Results of the Uther simulation: time evolution of the planet's orbital radius and migration rate (middle-right panel; the gray band corresponds to the inner wave-killing zone), and screenshots of the inverse vortensity ($\mathcal{I}_\mathcal{V}$) at seven times denoted by T_A to T_G in the panel showing the planet's orbital evolution. In each screenshot, $\mathcal{I}_\mathcal{V}$ is expressed in code units and shown in polar cylindrical coordinates between the inner boundary at 2 au and 25 au, and the number of orbits indicated in the upper-left corner corresponds to the number of orbital periods at the planet's initial location (20 au). Note that one orbital period at this location corresponds to ≈90 years. In the upper-right corner of each $\mathcal{I}_\mathcal{V}$ panel, we specify with 'R' or 'NR' whether the planet is undergoing runaway or non-runaway migration. The planet's position is marked by a white cross.

runs away, as will be illustrated in Fig. 6.3.3 (see the libration region labeled with $\mathcal{I}_{\mathcal{V}\mathrm{lib}}$ in the top middle panel). Therefore, δm is actually overestimated in Fig. 6.3.1 when $\delta m \gtrsim M_p$ (see Eq. 110). But in this case, the hypothesis of slow migration (see

Eq. 104) required to express δm via Eqs. (103), (105) or (110) may not be verified in the simulation.

To understand what stops and reinstates runaway migration intermittently, we display in Fig. 6.3.3 seven screenshots of the gas inverse vortensity ($\mathcal{I}_\mathcal{V}$) taken at times T_A to T_G indicated in the middle-right panel of the same figure, which shows the temporal evolution of the planet's orbital radius (r_p) and migration speed ($\dot{a}$). $\mathcal{I}_\mathcal{V}$ is calculated in the inertial frame. We now describe each panel of $\mathcal{I}_\mathcal{V}$ separately:

- T_A (top-left panel): $\mathcal{P}$ being quite massive ($q_p/h^3(r_{p,o}) \sim 1.5$, see section 3.3.2), its wakes turn into shocks within their excitation region (Goodman & Rafikov, 2001) and create $\mathcal{I}_\mathcal{V}$ maxima on both sides of the planet orbit (Lin & Papaloizou, 2010). (Note that the background profile of $\mathcal{I}_\mathcal{V}$ increases as $r^{1/2}$, which reflects its initial profile. Note also the $\mathcal{I}_\mathcal{V}$ perturbations in the planet's wakes which arise because $q_p/h^3(r_{p,o}) > 1$.) We observe an asymmetry in the radial location of the $\mathcal{I}_\mathcal{V}$ maxima with respect to $\mathcal{P}$, which comes about because of the inward migration of $\mathcal{P}$ (see section 4.5). Around the gap's inner edge, the synodic period of the gas relative to the planet remains shorter than the migration timescale of $\mathcal{P}$ across its gap region. The inner wake of $\mathcal{P}$ can therefore shock the gas near the gap's inner edge multiple times, and sustain an $\mathcal{I}_\mathcal{V}$ maximum there (it is like a cumulative effect). Because of the inward migration, the outer wake of $\mathcal{P}$ cannot shock the same fluid elements repetitively near the gap's outer edge, which explains the lack of an $\mathcal{I}_\mathcal{V}$ maximum at this location. The $\mathcal{I}_\mathcal{V}$ maximum that is visible at around 24 au was triggered by the outer wake of $\mathcal{P}$ when its migration rate was smaller near the beginning of the simulation.

- T_B (top-middle panel): as migration proceeds, the material that crosses the planet's orbit has increasing inverse vortensity, which therefore increases the dynamical corotation torque and the migration rate (Masset & Papaloizou, 2003, and see Eq. 105). As the migration rate increases, $\mathcal{P}$ enters the runaway migration regime ($\delta m \gtrsim M_p$). At some point, migration is fast enough that the synodic period of the gas near the gap's inner edge becomes longer than the migration timescale of $\mathcal{P}$ across its gap. The cumulative shocks of the inner wake brought about above no longer operate, or, said differently, the inner wake of $\mathcal{P}$ can no longer sustain an $\mathcal{I}_\mathcal{V}$ maximum inside the orbit. When the entering inverse vortensity takes its maximum value, $\mathcal{P}$ reaches its maximum migration rate. This is the case shown in this panel (see the "red" stream of high $\mathcal{I}_\mathcal{V}$ executing an outward U-turn relative to $\mathcal{P}$ at $\theta \lesssim 0$). Meanwhile, the azimuthal extent $\Delta\theta$ of the libration region decreases, which saturates the runaway process by limiting the increase in δm (see the $\Delta\theta$ term in Eq. 110).

- T_C (top-right panel): after the gas with maximum $\mathcal{I}_\mathcal{V}$ has crossed the orbit, $\mathcal{P}$ keeps on migrating and now forces material with unperturbed (and thus smaller) $\mathcal{I}_\mathcal{V}$ to execute outward U-turns. The feedback on migration due to the coorbital vortensity deficit now acts in the opposite way: the inverse vortensity of the material entering the horseshoe region ($\mathcal{I}_{\mathcal{V}_e}$) decreases, δm decreases, and so does the migration rate.

- T_D (middle-left panel): migration is now slow enough that part of the high $\mathcal{I}_\mathcal{V}$ material that previously entered the horseshoe region becomes trapped in libration and performs multiple horseshoe U-turns. This panel actually highlights a secondary inward U-turn of high $\mathcal{I}_\mathcal{V}$ material in front of the planet in azimuth. Because the gas executing inward U-turns has a higher $\mathcal{I}_\mathcal{V}$ than the gas doing outward U-turns, a positive corotation torque applies to $\mathcal{P}$, which slows down even more its migration, until the vortensity in the horseshoe region gets progressively mixed. These secondary U-turns will be examined in more detail in section 6.5.1.

- T_E (bottom-left panel): $\mathcal{P}$ is now in a non-runaway migration regime and its wakes can trigger new $\mathcal{I}_\mathcal{V}$ maxima on both sides of the planet's orbit. Inward migration resumes, and a radial asymmetry in the position of the $\mathcal{I}_\mathcal{V}$ maxima with respect to $\mathcal{P}$ can be seen again in this panel, which is similar to the one shown at time T_A. A new cycle of runaway migration begins. The comparison with the panel at T_A highlights that the radial location of the $\mathcal{I}_\mathcal{V}$ maximum outside the planet at T_E (~ 14 au) nearly coincides with that of the $\mathcal{I}_\mathcal{V}$ maximum inside the planet at T_A, i.e. just before the onset of runaway migration. We will come back to this point in section 6.7.

- T_F (bottom-middle panel): as previously, runaway stalls as the inner wake ultimately fails to maintain an $\mathcal{I}_\mathcal{V}$ maximum inside the planet's orbit and the azimuthal width of the libration region shrinks. This panel is very similar to the one shown at time T_B, and we notice that the migration rate takes very similar values at both times. A new maximum of $\mathcal{I}_\mathcal{V}$ will form outside the planet's orbit when the migration rate has reached again its minimum value.

- T_G (bottom-right panel): at the end of the simulation, when migration stalls near the grid's inner boundary, multiple bands of high-$\mathcal{I}_\mathcal{V}$ material are formed, including one inside the planet's orbit. The bands beyond the planet's orbit trace the transition stages between fast and slow migration. The longevity of these bands will be discussed in sections 6.3.2 and 6.6.

As already stated in section 6.2, Lin & Papaloizou (2010) and McNally et al. (2019) have obtained a similar scenario of intermittent migration. Although in these models gas vortices form at the edges of the planet gap due to the Rossby-Wave Instability (see section 2.3.4), the intermittent episodes of runaway migration can also be accounted for by the time evolution of the inverse vortensity of the gas crossing the planet's orbit.

6.3.2 *Dust spatial distribution*

We have seen in section 6.3.1 that intermittent planet migration gives structure to the disk gas, with the formation of new maxima in the inverse vortensity profile on each side of the planet's orbit at the end of each stage of runaway migration. These inverse vortensity maxima are intimately related to pressure maxima triggered by the planet wakes when migration decelerates, as we illustrate below (the reader is referred to, e.g., Eq. 32 in Casoli & Masset, 2009 for a formal link between maxima of inverse

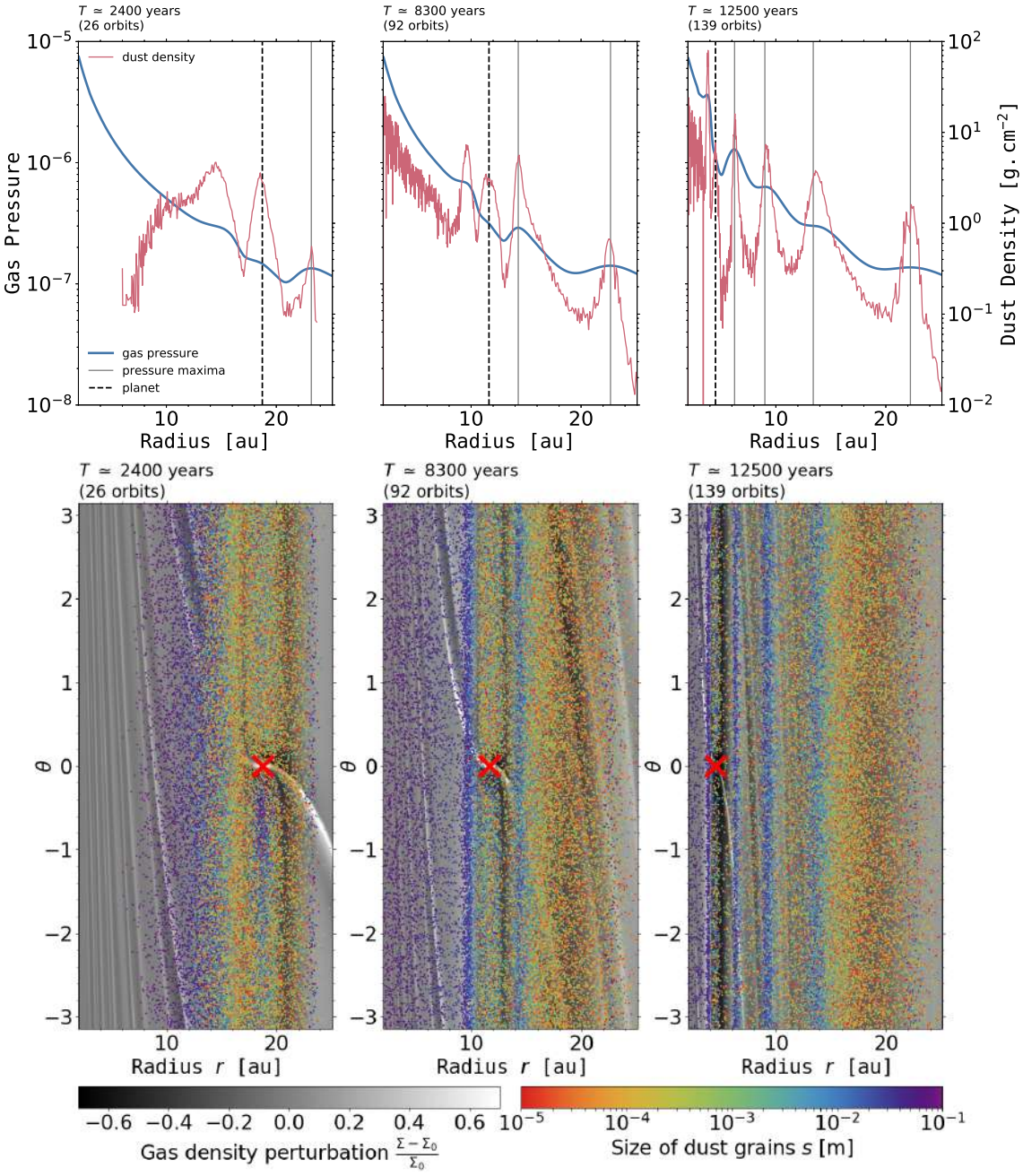

Figure 6.3.4: Results of the Uther simulation: gas structure and dust spatial distribution in polar cylindrical coordinates in the disk region between the inner boundary at 2 au and 25 au. Results are shown at 2400 years in the left panels, at 8300 years in the middle panels, and at 12500 years in the right panels (same time as in Fig. 6.3.3, bottom right). **Top:** azimuthally-averaged radial profiles of the gas pressure (*blue*) and of the dust's surface density (*red*). The planet's orbital radius is spotted by a vertical dashed line. Pressure maxima outside the planet position are depicted by the thick gray lines. **Bottom:** perturbed gas surface density relative to its initial profile, $(\Sigma - \Sigma_0)/\Sigma_0$, in black and white. The location of dust particles is overlaid by colored dots. The rainbow color bar shows dust size in meters, with purple dots for the largest particles (10 cm) and red dots for the smallest (10 μm). In each panel, the red cross at zero azimuth marks the position of the planet.

vortensity and of pressure). We then study how intermittent migration impacts the dust distribution. For the simulation Uther, we use 5×10^4 Lagrangian test particles with initial orbital radius $r_d \in [14 - 21]$ au. This is meant to maximize the particles resolution at the dust structures that form during the inward migration of $\mathcal{P}$.

The upper panels in Fig. 6.3.4 show three snapshots of the azimuthally-averaged radial profiles of the gas pressure (in blue) and of the dust's surface density (in red). The dust's surface density is calculated with the dust's size distribution and total mass adopted in the radiative transfer calculations (see section 6.1). We note in passing that the dust-to-gas surface density ratio does not exceed ~ 0.1 throughout the simulation, which justifies that dust feedback on the gas can be safely discarded for the Uther disk model. The thick gray lines in Fig. 6.3.4 show the location of the pressure maxima **beyond** the planet's orbital radius. We do not mark eventual inner pressure maxima in this graph. The location of the planet is marked by the dashed line.

Shortly after the beginning of the simulation (Fig. 6.3.4, top left), there is only one pressure maximum at the outer edge of the planet's gap, which is built up by the outer wake of $\mathcal{P}$ before the first episode of runaway migration (see also the Appendix A of Meru et al., 2019). At the end of the first cycle of runaway migration, when $\mathcal{P}$ has decelerated, a new pressure maximum forms outside the planet orbit (see Fig. 6.3.4, top middle, which corresponds approximately to Fig. 6.3.3, bottom left, for the inverse vortensity). At the end of the third episode of runaway migration (Fig. 6.3.4, top right, corresponding to Fig. 6.3.3, bottom right), we obtain four pressure maxima outside the planet orbit, and one inside the orbit. More precisely, at the position of $\mathcal{P}$ in this last snapshot (~ 5 au), the planet braked three times, which gave it time to create three pressure maxima in addition to the initial pressure maximum outside the original position of $\mathcal{P}$ (near 22 au). The pressure maxima that are not sustained by the planet wakes progressively turn into inflection points under the action of turbulent viscosity.

As we have seen in section 2.2.2, at a given location in the disk, dust and gas do not have the same orbital speed due to the pressure-gradient force acting on the gas. This velocity difference induces an aerodynamic force from the gas to the dust, which eventually leads to the radial drift of the dust. At a pressure maximum, there is no relative motion of the dust and the gas, therefore no aerodynamic force and no resulting drift. A pressure maximum thus defines an equilibrium position where dust accumulates and is trapped in rings. We thus expect an accumulation of dust at each bump in the pressure profile, and this is precisely what can be seen in the upper panels in Fig. 6.3.4 by comparing the location of the maxima in the dust surface density (red curves) and in the gas pressure (thick gray lines) beyond the planet.

The bottom panels of Fig. 6.3.4 display in black and white the perturbed gas surface density ($\Sigma - \Sigma_0$) relative to its initial profile Σ_0 at the same times as the top panels in the same figure. The red cross spots the location of $\mathcal{P}$. We depict dust super-particles as colored dots; color varies with particles size, from red (10 µm) to purple (10 cm). The inward drift of the largest ($s \gtrsim 1$ cm) particles is clearly visible between the bottom left and bottom middle panels of Fig. 6.3.4. Note that the small particles are not present in the inner disk due to the choice of initial particles location and the fact that there has not been enough time for the small particles to drift. In the bottom-right panel of Fig. 6.3.4, we see that dust particles are trapped in axisymmetric rings at the location of the pressure maxima (around 22, 14, 9, 6 and 4 au for this simulation

at 12500 years), and that larger particles get more concentrated at these locations on account of their larger Stokes number (larger particles, with Stokes number $\lesssim 1$, drift more rapidly towards equilibrium locations).

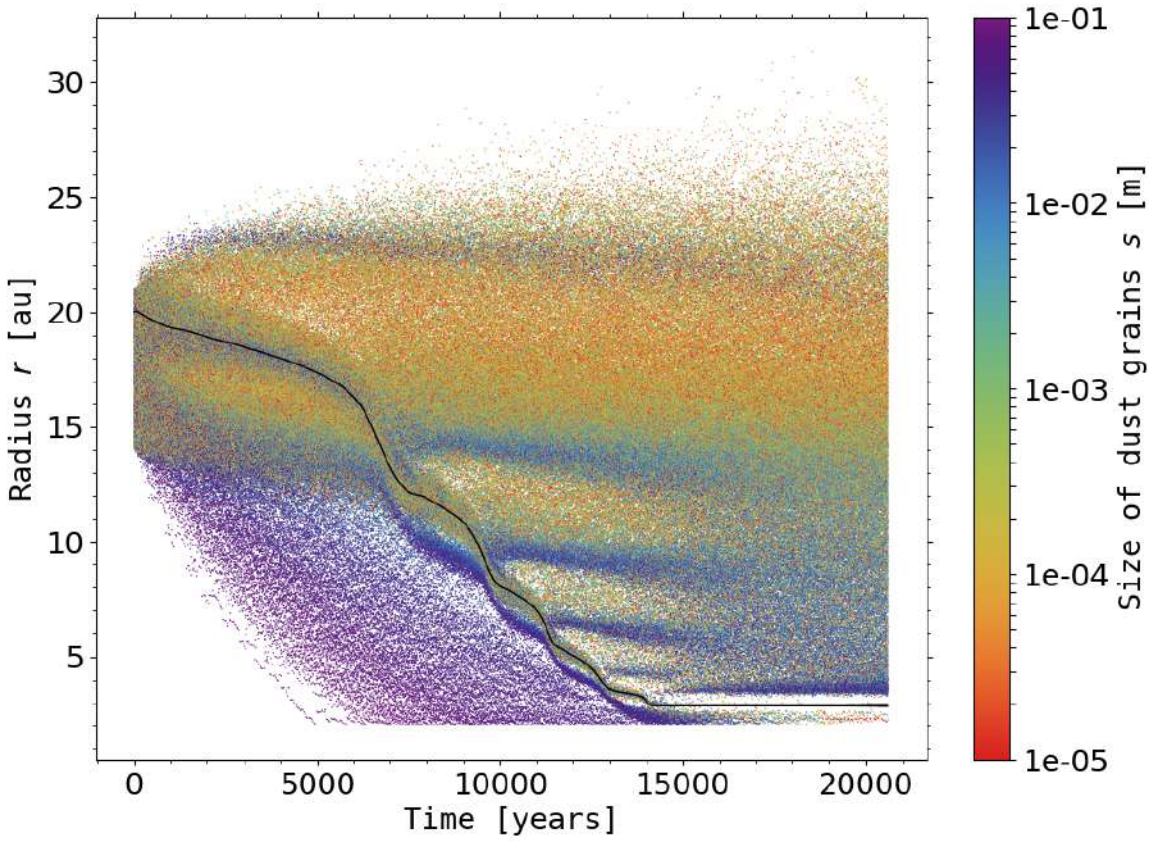

Figure 6.3.5: Space-time diagram for the Uther simulation, illustrating the longevity of dust rings formed by multiple stages of runaway planet migration. This panel displays the orbital radius of a sample of super-particles as a function of time, with color varying with particles size. The planet's orbital radius is shown by a black curve.

To examine the longevity of the dust rings, we display in Fig. 6.3.5 the space-time diagram of the dust's radial location versus dust size for the Uther simulation. Each dot marks the orbital radius of a sample of super-particles as a function of time, with color varying with particles size (see color bar on the right-hand side). This graph clearly shows the progressive disappearance of the dust rings formed prior to each stage of inward runaway migration. Dust rings typically last between 3000 and 10000 years. It is also instructive to examine the time evolution of the radial location of the largest particles (dark-blue dots). Some of these large particles are initially located around the planet's orbital radius before the first episode of runaway migration at $\sim$ 6000 years, and going back to the bottom-left panel in Fig. 6.3.4 we see that these correspond to the particles trapped around the L5 Lagrange point behind the planet in azimuth. As the runaway proceeds, these particles escape the Lagrange point and a large fraction of them become trapped at the pressure maximum outside the planet's

Parameter	Symbol	Value
Wavelength	λ	1.3 mm
Dust's size range	$\in [s_{min} - s_{max}]$	$\in [10^{-5} - 10^{-1}]$ m
Dust size distribution	$n(s)$	$\propto s^{-3.5}$
Dust-to-gas mass ratio	μ_d	10^{-2}
Dust composition	—	30% silicates, 70% water ices
Scattering	—	discarded
Disk distance	d	150 pc
Stellar radius	$r_\star$	2 $R_\odot$
Star effective temperature	T_{eff}	7000 K
Beam	—	$0''.02 \times 0''.02$

Table 6.3.2: Parameters of the dust radiative transfer calculations

orbit which forms at the end of this first runaway. Similarly, close inspection at the second stage of runaway migration at ~ 9000 years shows that the large particles that become trapped at the newly formed pressure maximum outside the planet's orbit mainly originate from the reservoir of large particles initially inside the orbit. A similar observation can be made with the subsequent stages of runaway migration. It is interesting to realize that not all the reservoir of large particles inside the orbit ends up populating the dust trap triggered outside the orbit. Part of the particles embarking onto outward U-turns perform secondary U-turns inward, the same secondary U-turns that we have illustrated on the gas inverse vortensity in the middle left panel (T_D) of Fig. 6.3.3. This process allows to maintain a contingent of large particles inside the planet's orbit which will progressively fill the dust traps outside the planet's orbit formed after each jolt of the planet. We will illustrate this phenomenon in section 7.7 via a particle tracking methodology. We finally notice that the dust traps formed outside the planet's orbit seem to have a geometrical radial spacing (there is a factor ~ 1.5 between the radial locations of successive dust rings, we will come back to this point in section 6.7).

6.3.3 *Continuum emission*

The dust spatial distribution obtained in the Uther simulation was post-processed with the 3D radiative transfer code `RADMC3D` to produce synthetic flux maps of continuum emission at $\lambda = 1.3$ mm according to the procedure detailed in section 5.2.1. The main parameters of the dust radiative transfer calculations are summed up in Table 6.3.2.

The synthetic flux map of continuum emission based on the results of the Uther simulation at 12500 years is displayed in the top-left panel in Fig. 6.3.6. Three bright rings of emission are clearly visible in the flux map. The outermost visible ring, which is located at ~ $0''.09$ (~ 14 au), corresponds to the maximum in the dust's surface density located near 14 au in the top-right panel in Fig. 6.3.4. The dust density maximum located near 22 au does not produce a visible bright ring in the flux map. The second visible ring in the top-left panel of Fig. 6.3.6 mostly corresponds to the dust density maximum located near 9 au in the top-right panel in Fig. 6.3.4. Finally, the innermost

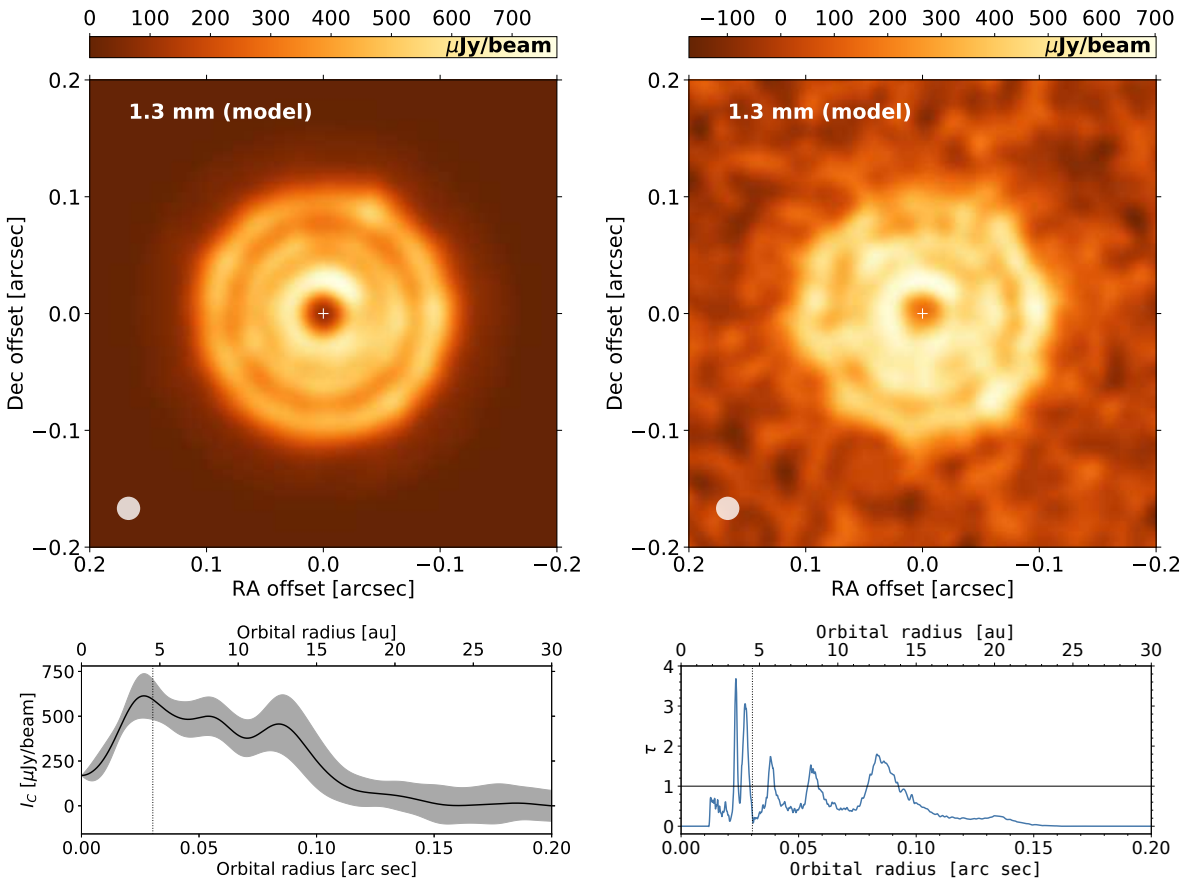

The vertical dotted line in the bottom panels shows the location of the planet.

Figure 6.3.6: Predicted continuum emission at 1.3 mm for the Uther simulation at 12500 years (or 139 planet orbits). **Top-left:** Synthetic flux map obtained after convolution with a 0.″02 circular beam. The beam is shown by the circle in the bottom-left corner. The x- and y-axes indicate the offset from the stellar position in the RA and DEC in arcseconds, i.e., north is up and west is to the right. **Top-right:** Same as top-left panel, but with white noise of 50 μJy/beam standard deviation added to the raw flux maps (prior to beam convolution). **Bottom-left:** Azimuthally averaged convolved intensity as a function of distance to the star. The gray shaded area around the profile corresponds to $\pm 2\sigma$ dispersion around the mean. **Bottom-right**: Optical depth τ as a function of distance to the star. The medium is marginally optically thick ($\tau \in [1.5, 2.0]$) near the three bright rings beyond 4 au. The horizontal black line highlights $\tau = 1$.

bright ring corresponds to the beam dilution of the three dust density maxima which are located at the planet's orbital radius and on both sides of the planet's gap. The top-right panel in Fig. 6.3.6 shows the same flux map obtained by adding white noise to the raw flux map prior to beam convolution. It is clear that the three bright rings are still discernible despite the realistic level of noise that we consider. These rings are also clearly visible in the bottom-left panel of Fig. 6.3.6, where we display the azimuthally-averaged radial profile of the convolved intensity. At the location of the bright rings, the dust's thermal emission is optically thick: near the emission peaks, the absorption optical depth varies between about 1.5 and 4 (bottom-right panel of

Parameter	Value
Planet to primary mass ratio q_p	4.3×10^{-4}
Disk's aspect ratio h_0 at 10 au	0.06
Alpha turbulent viscosity	10^{-4}
Gas surface density Σ_0 at 10 au [code units]	10^{-3}
Number of dust super-particles	100000
Dust's initial location	$\in [14 - 23]$ au

Table 6.4.1: Parameters of simulation Pendragon (section 6.4)

Fig. 6.3.6). Furthermore, we notice azimuthal variations of the flux along the bright rings, which are of the order of 50 µJy/beam. These azimuthal variations in the intensity thus convey azimuthal variations in the dust temperature obtained by the thermal Monte-Carlo calculation. We have noticed that by increasing the number of dust super-particles, in particular 200000 instead of 50000, it is much more difficult to distinguish the multiple bright rings in the continuum map: the convolved intensity is maximal at the innermost dust ring, and the variations in intensity near the outer dust rings are much smaller. This may be due to the radial drift of a significant number of large particles in the inner disk that 'block' the star's radiation, resulting in a weaker dust thermal emission further away in the disk. This wall effect from inner particles is to be studied in more details.

6.4 PENDRAGON SIMULATION ($h_0 = 0.06$, $\alpha = 10^{-4}$)

We now present the results of the Pendragon simulation, which differs from the Uther simulation by a slightly increased disk's aspect ratio ($h_0 = 0.06$ instead of 0.05) and a reduced alpha turbulent viscosity ($\alpha = 10^{-4}$ instead of 10^{-3}). Having a smaller α implies that the structures that we obtain in the dust spatial distribution are sharper and less subject to turbulent diffusion, which leads to structures that last longer in the disk. However, because a low turbulence favors the Rossby wave instability (RWI, see section 2.3.4), the formation of vortices that can interact with $\mathcal{P}$ makes the interpretation of the planet's orbital evolution a priori harder. These vortices can appear for example when a stream of high $\mathcal{I}_\mathcal{V}$ material mixes with low $\mathcal{I}_\mathcal{V}$ non-perturbed regions, which is typical of the fast migration stages presented in section 6.3.1. Nevertheless, the important quantities presented in that same section, mainly the coorbital vortensity deficit and the inverse vortensity of the orbit-crossing material, allow a good understanding of what happens in the low turbulent case that we present in this section. For the dust, we use this time 10^5 Lagrangian test particles initially distributed in a larger band $r_d \in [14 - 23]$ au, in order to have more particles trapped at the outermost pressure maximum formed by the planet shortly after the beginning of the simulation. Table 6.4.1 sums up the main parameters of this simulation.

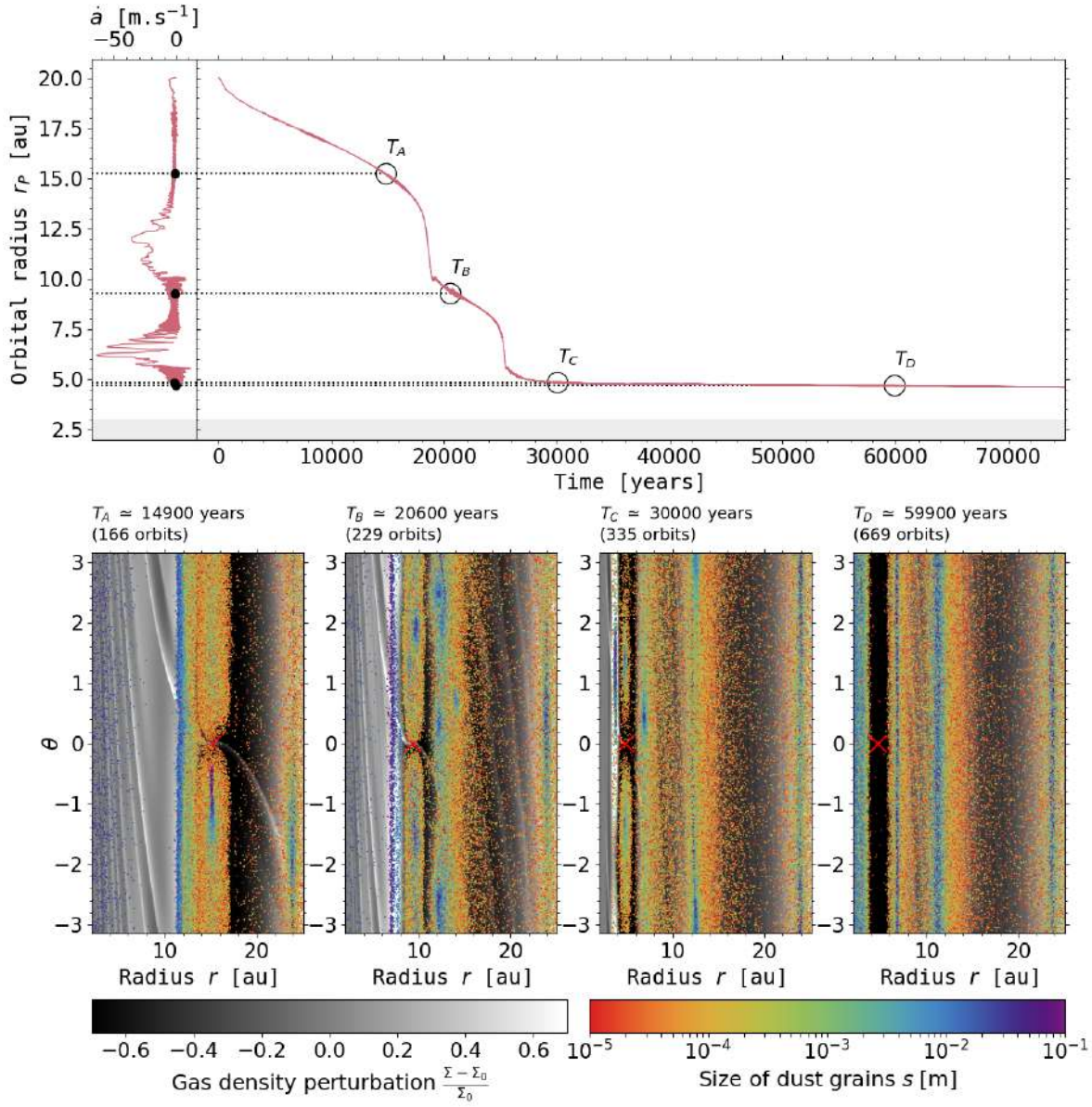

Figure 6.4.1: Results of the Pendragon simulation : planet's orbital evolution, gas structure and dust spatial distribution in the disk region between the inner boundary at 2 au and 25 au. **Top right:** evolution of the planet's orbital radius as a function of time. The four circles indicate four different times in the simulation : $T_A = 14900$, $T_B = 20600$, $T_C = 30000$ and $T_D = 59900$ years. **Top left:** evolution of the planet's migration speed as a function of its position in the disk. The gray band corresponds to the inner wave-killing zone. **Bottom:** same as lower panel of Fig. 6.3.4, but for the four aforementioned times in the Pendragon simulation.

6.4.1 *Dust spatial distribution*

The upper panel in Fig. 6.4.1 shows the time evolution of the planet's orbital radius (right-hand side) and its migration speed (left-hand side). The migration pattern is similar to that in the Uther simulation, with a succession of fast (runaway) and slow (non-runaway) migration episodes. Compared to the Uther simulation, the steps occur

at a later time because of a slower initial migration due to a deeper gap. Also, the steps are less numerous and more pronounced, foretelling there should be less bright rings in the continuum emission.

In the lower part of Fig. 6.4.1 is shown the dust spatial distribution (colored dots) superimposed on the perturbed gas surface density (black and white contours) at the four times marked by black circles in the upper panel: $T_A = 14900$ years, $T_B = 20600$ years, $T_C = 30000$ years and $T_D = 59900$ years. Initially, $\mathcal{P}$ migrates slowly. Due to this slow migration, the dust structures in the disk follow the planet's orbital motion. We can highlight two important behaviors: first, $\mathcal{P}$ forms a dust ring ($\mathcal{R}_p$) centered on its orbital radius with an accumulation of particles around the Lagrange point L5 behind the planet in azimuth. The ring $\mathcal{R}_p$ is surrounded by two rings: an internal ring $\mathcal{R}_i$ and an external ring $\mathcal{R}_{e,1}$. Secondly, we observe the rapid inward drift of the largest grains. While $\mathcal{P}$ migrates inward gently, it gets closer to $\mathcal{R}_i$ as it pushes particles inwards. Particles that were initially trapped at $\mathcal{R}_{e,1}$ drift slowly because the location of the corresponding pressure maximum does not change much. This progressively leads to a radial asymmetry of $\mathcal{R}_i$ and $\mathcal{R}_{e,1}$ compared to $\mathcal{R}_p$ (Pérez et al., 2019; Meru et al., 2019). For instance, at time T_A, $\mathcal{R}_i$, $\mathcal{R}_p$ and $\mathcal{R}_{e,1}$ are located at around 12 au, 15 au and 24 au, respectively. As we have seen in section 6.3.1, this asymmetry enables material with higher $\mathcal{I}_\mathcal{V}$ to enter the coorbital region, making $\mathcal{P}$ move faster inward. When the fast migration regime is triggered, $\mathcal{P}$ overtakes the internal ring $\mathcal{R}_i$ at around 10 au, and part of the dust that was trapped at $\mathcal{R}_i$ and at the Lagrange points perform a horseshoe U-turn. These particles then follow a complex dynamics due to the presence of small vortices arising because of the Rossby-Wave Instability, and form a new outer dust ring $\mathcal{R}_{e,2}$ at 12 au (see second lower panel from the left at time T_B). The same behavior happens again during each jolt in the planet migration. During this evolution, the external rings $\mathcal{R}_e$ that are left behind $\mathcal{P}$ do not drift significantly. After the Nth jump, N+1 outer dust rings have been created. Since two stages of runaway migration occur in the simulation, three dust rings form outside the planet's location (here at around 7, 12 and 24 au).

Each jolt is associated with an increase in the migration speed (Fig. 6.4.1, top left): between T_A and T_B, and between T_B and T_C. The rather large amplitude oscillations in the planet's migration speed are most probably due to the formation of several vortices that carry away sporadically high $\mathcal{I}_\mathcal{V}$ material from the inner to the outer edges of the planet's gap (T_B, see Lin & Papaloizou, 2010). These vortices interact with the planet before merging and forming a single large-scale vortex (T_C) in which dust particles larger than about a millimeter are trapped. The vortex gradually disappears and becomes an axisymmetric dust ring. At the time T_D shown in the lower-right panel of Fig. 6.4.1, which is a long time after the planet has stalled its migration upon reaching the inner wave-killing zone, the three dust rings are still present. The external ring created last ($\mathcal{R}_{e,3}$ at 7 au) is located at the outer edge of the final planet's position $\mathcal{R}_p \sim 5$ au.

We display in Fig. 6.4.2 the space-time diagram for the Pendragon simulation, which shows that the dust rings have a much longer lifetime than in the Uther simulation, since some dust rings are maintained over more than 10^5 years. We notice that the dust ring at $\sim$ 12 au gets disrupted at $\sim$ 60000 years onward and the largest dust particles that were initially trapped there start drifting inward. They ultimately reach the dust

trap at ~ 7 au. Similarly, the dust ring initially at ~ 24 au disappears after ~ 200000 years. As will be further emphasized in section 6.6, the longevity of the dust rings is intimately related to the sharpness of the pressure profile around the maxima, which turbulent viscosity progressively smooths out. It therefore depends on how strong the shock of the outer planet's wake is initially during each stage of non-runaway migration. The shorter this stage, the weaker the shock will be, and the earlier the dust ring formed beyond the planet's orbit will disappear. We finally point out that, for the size distribution and total mass of dust in the radiative transfer calculation, the dust-to-gas surface density ratio can reach up to 0.5-0.6 throughout the Pendragon simulation, and discarding dust feedback remains a safe approximation for this disk model (see section 6.5.5 for some simulations with feedback of dust fluids onto the gas).

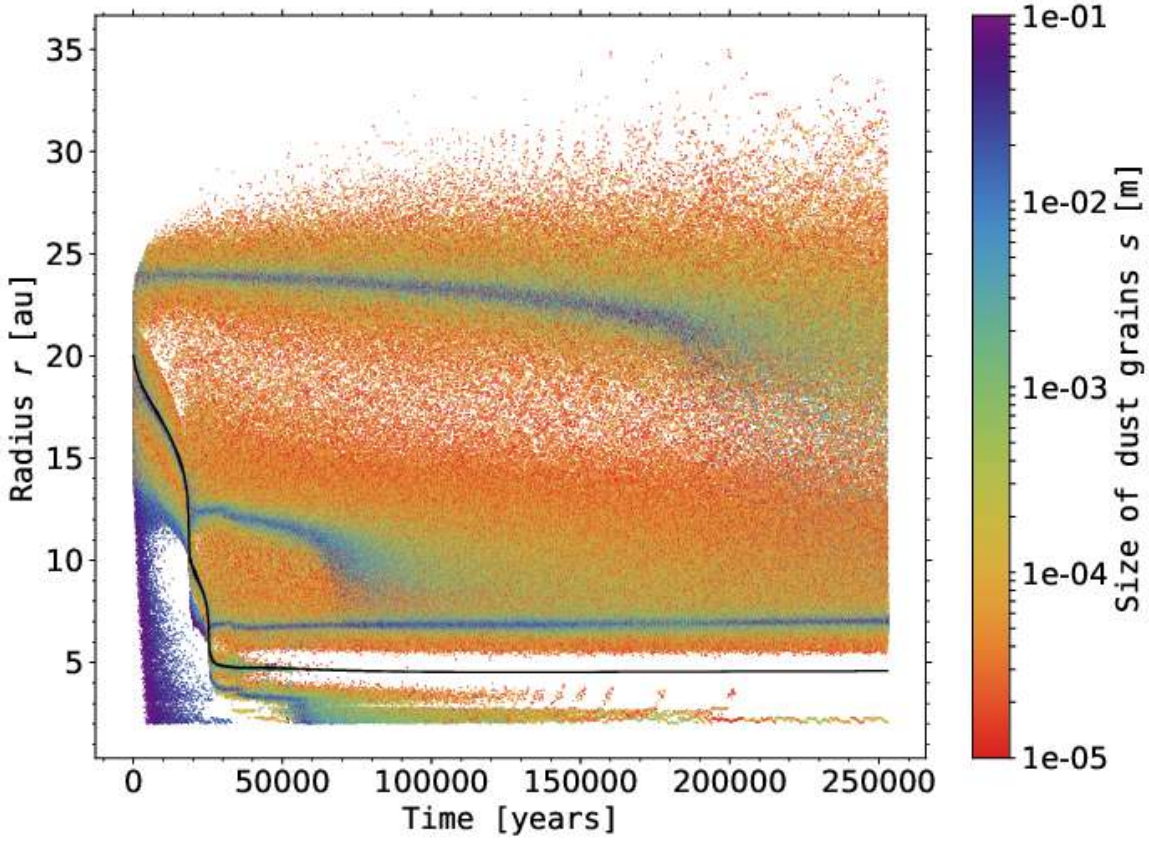

Figure 6.4.2: Same as Fig. 6.3.5 for the Pendragon simulation.

6.4.2 *Continuum emission*

The synthetic map of the 1.3 mm continuum emission obtained from the Pendragon simulation at 59900 years is displayed in the top-left panel in Fig. 6.4.3. The low level of turbulence in this simulation implies sharp structures in the continuum emission. Four bright rings of emission are clearly visible in the synthetic flux map. The two

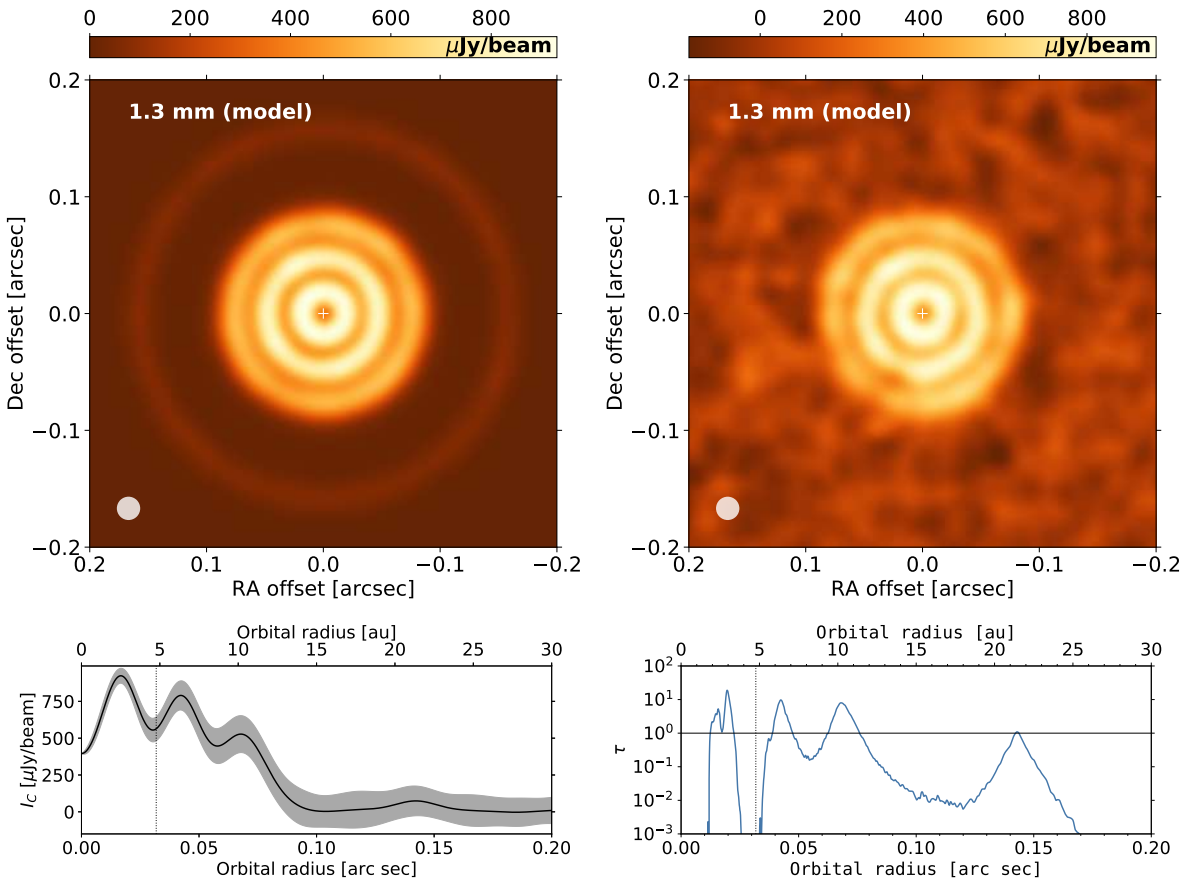

Figure 6.4.3: Same as Fig. 6.3.6, but for the Pendragon simulation at 59900 years (669 planet orbits). The optical depth τ in the bottom-right panel is this time displayed in logarithmic scale. The horizontal black line highlights $\tau = 1$.

innermost bright rings correspond to the dust rings at the pressure maxima located on both sides of the planet's orbit (which are at around 4 and 7 au, see bottom-right panel of Fig. 6.4.1). The two outermost bright rings correspond to the dust rings that formed outside the planet's orbit prior to each stage of runaway inward migration (they are at about 12 and 24 au, see again the bottom-right panel of Fig. 6.4.1).

We notice that the flux along the bright rings decreases with increasing distance from the star, which mostly reflects the radial decrease in the dust temperature. The emission is indeed optically thick at the three innermost bright rings ($\tau \sim 10$), and marginally optically thick in the outermost one ($\tau \sim 1$). The intensity of the outermost bright ring at around 24 au is actually quite low (around 100 μJy/beam). Thus, when white noise with a rms level of 50 μJy/beam is added to the raw flux map, the outermost ring is almost not visible anymore, whereas the innermost rings are still clearly visible (see top-right and bottom-left panels of Fig. 6.4.3).

Scattering in these dust radiative transfer calculations is discarded, as it is found to have a small impact on our final synthetic images. We have checked this by dedicated `RADMC3D` calculations including anisotropic scattering with the Henyey-Greenstein approximation for the scattering phase function. See Fig. 6.4.4 for a comparison of the azimuthally averaged convolved intensity as a function of distance to the star, without (blue curve) and with (red curve) dust scattering. For the simulation presented in

this figure, inclusion of anisotropic scattering results in a relative difference between ~ 5% and ~ 15% for the flux of continuum emission compared to a calculation without scattering. The fact that dust scattering can decrease the intensity if τ is sufficiently large ($\tau \gtrsim 10^{-1}$) is coherent with theoretical predictions from (Miyake & Nakagawa, 1993, see their Fig. 22 in Appendix C) and depends on the albedo, and therefore on the dust composition.

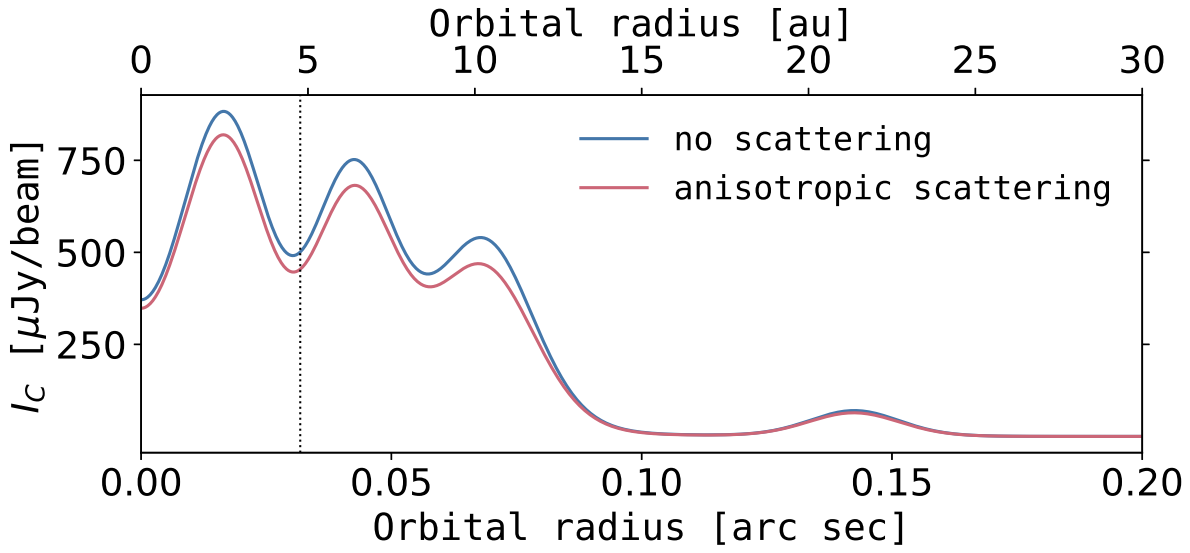

Figure 6.4.4: Impact of dust anisotropic scattering in the dust radiative transfer calculations at 1.3 mm in the Pendragon case.

6.5 PARAMETER SPACE AND BEYOND THE FIDUCIAL CASES

6.5.1 *Initial gas surface density profile*

We have seen in Fig. 6.2.1 that increasing the initial surface density Σ_0 from 3×10^{-4} to 3×10^{-3} radically changes the migration pattern of $\mathcal{P}$, as well as the dust spatial distribution (Fig. 6.B.1). According to Figure 14 of Masset & Papaloizou (2003), which shows the occurrence of runaway migration as a function of disk mass and planet mass, the slow migration case in Fig. 6.2.1 (section 6.2) corresponds to non-runaway type I migration, whereas the intermittent and fast cases correspond to type III runaway migration. We now show in this section that, for a given value of Σ_0, inward runaway migration can also be smooth or discontinuous depending on the slope of the initial gas density profile.

By varying the power-law exponent of the initial surface density profile of the gas, that is σ in $\Sigma_0(r) = \Sigma_0 \times (r/r_0)^{-\sigma}$, we change the unperturbed (i.e., initial) inverse vortensity profile, $\mathcal{I}_{\mathcal{V}0}(r) = \Sigma_0(r)/\omega_0(r) \propto r^{3/2-\sigma}$, and thus the inverse vortensity of the material entering the horseshoe region ($\mathcal{I}_{\mathcal{V}_e}$) as the planet migrates. To examine how different values of σ impact our results, we performed two additional simulations with the Uther disk model for $\sigma = 0$ and $\sigma = 2$, the fiducial Uther simulation presented in section 6.3 having $\sigma = 1$. In the following, we refer to these simulations as the σ_0, σ_1

and σ_2 runs. The upper panel of Fig. 6.5.1 compares the time evolution of the planet's orbital radius (r_p) and migration speed ($\dot{a}$) in these three simulations.

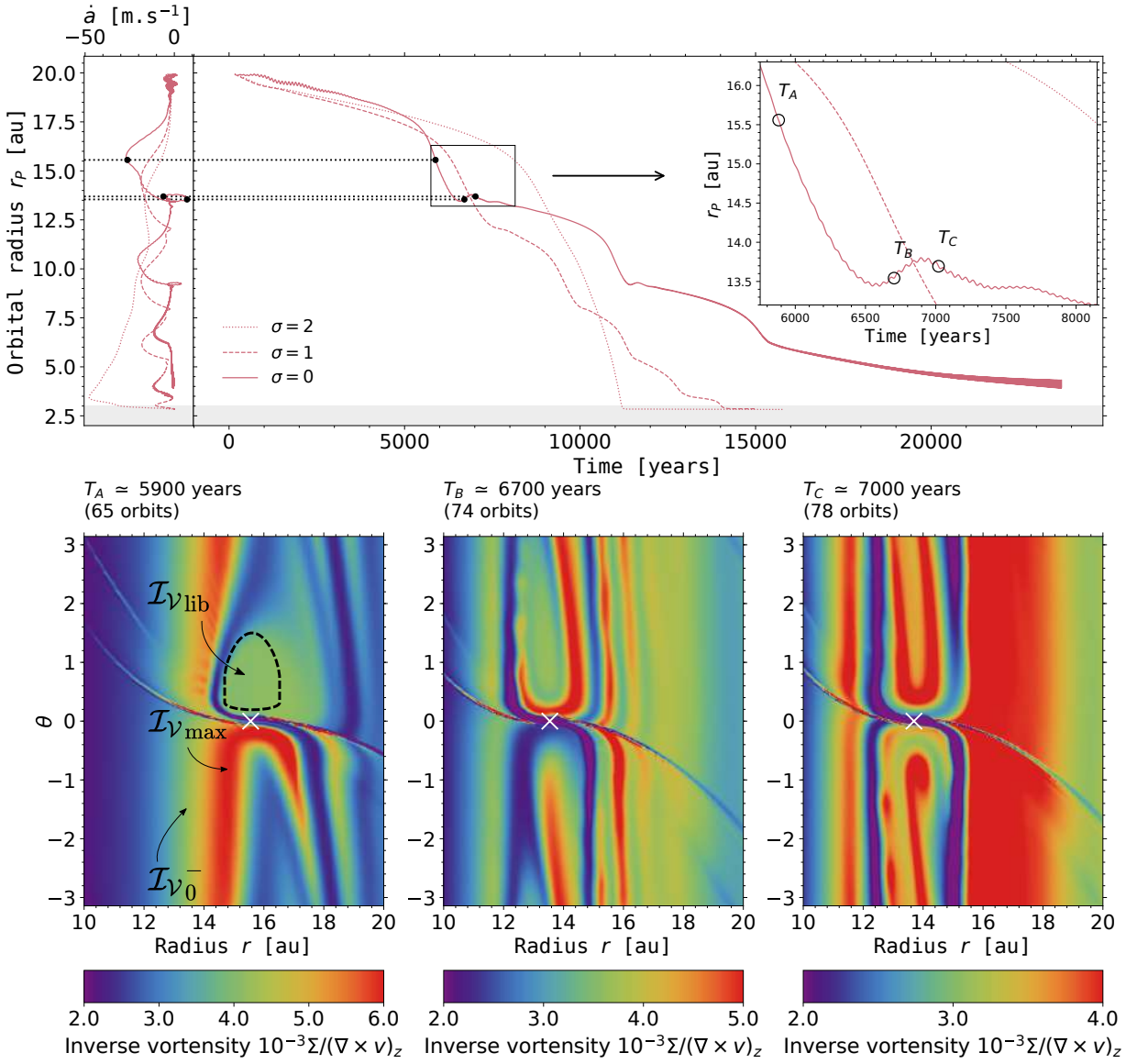

Figure 6.5.1: Impact of the initial surface density profile of the gas ($\Sigma_0(r) \propto r^{-\sigma}$) on the planet's orbital evolution in the Uther disk model. The upper panel compares the time evolution of the planet's orbital radius and migration rate in the simulation presented in section 6.3 (dashed curves, $\sigma = 1$), with those obtained in two additional simulations for $\sigma = 0$ (solid curves) and $\sigma = 2$ (dotted curves). The gray band corresponds to the inner wave-killing zone. The lower panels display three screenshots of the gas inverse vortensity in the $\sigma = 0$ simulation at the three times denoted by T_A, T_B and T_C in the upper panel. The planet's position is marked by a white cross.

We see that, initially, $|\dot{a}|$ takes very similar values in all three runs ($|\dot{a}| \sim 2$ m.s^{-1}). From this we argue that the static corotation torque plays a minor role in the initial migration rate. This is confirmed by inspection at Eq. (51) of Paardekooper et al. (2011a), which indicates that the static corotation torque saturates for the values of

q_p, h_0 and α in the Uther simulation. The migration behavior changes dramatically, however, after the first episode of runaway: in the σ_2 run, migration remains smooth and fast, whereas in the σ_0 run migration is intermittent, with stages of decelerated migration that last longer than in the σ_1 run. These behaviors boil down again to the radial profile of inverse vortensity.

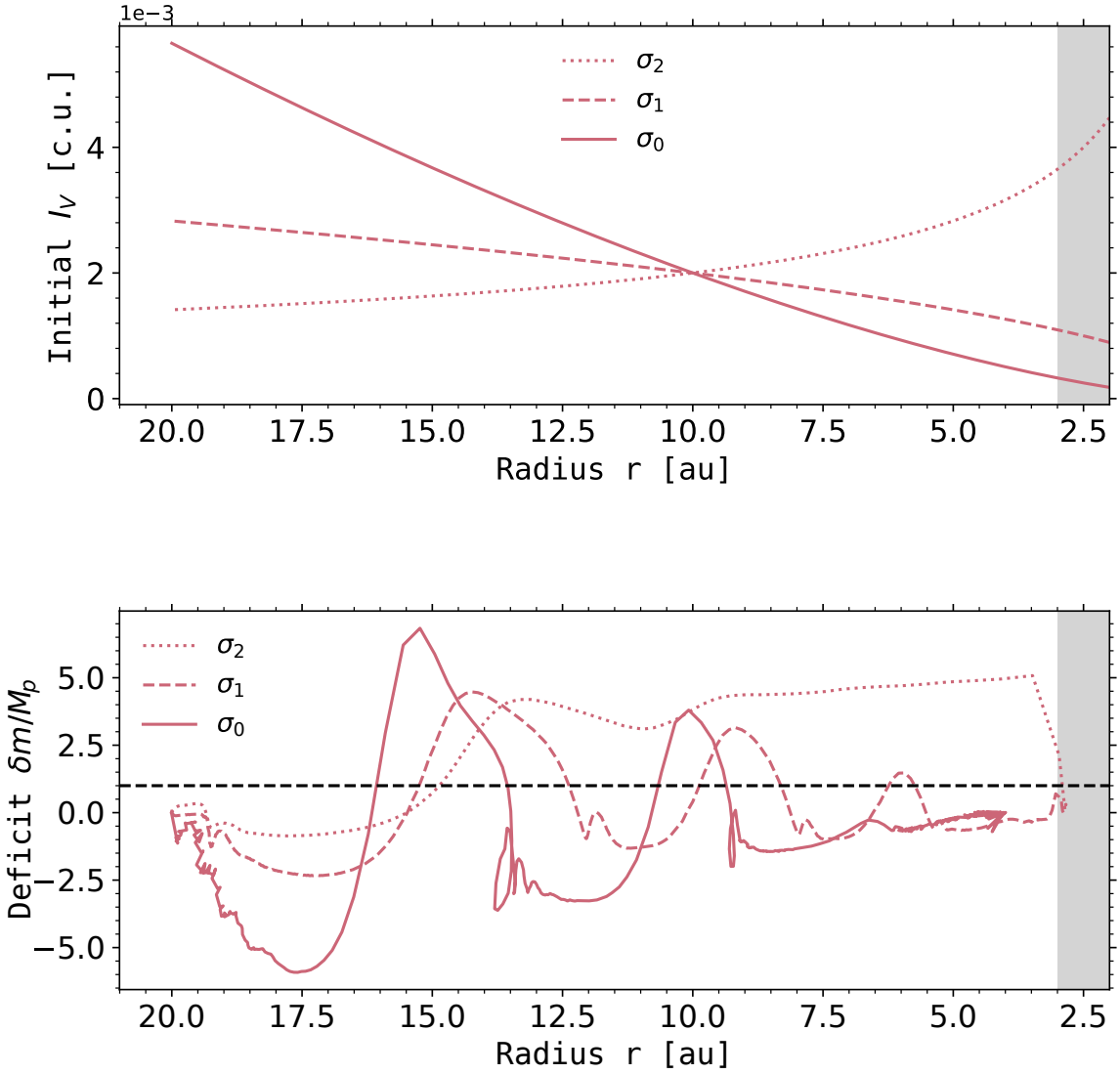

Figure 6.5.2: **Top panel**: Initial (non-perturbed) inverse vortensity profile [in code units] in the inner disk, for the three runs σ_2 (dotted line), σ_1 (dashed line) and σ_0 (solid line). The initial inverse vortensity profile decreases with radius for the σ_2 run only. **Bottom panel**: Numerical estimation of the normalized coorbital vortensity deficit δm in the σ_2 (dotted line), σ_1 (dashed line) and σ_0 (solid line) runs. The horizontal dashed line separates the non-runaway regime from the runaway regime. The gray band corresponds to the inner wave-killing zone. **Be careful** that the x-axis starts near the initial position of the planet ($r_{p,0} = 20$ au) and follows the planet during its inward migration until the inner wave-killing zone ($r = 3$ au).

In the σ_2 run, the background inverse vortensity profile decreases with radius as $r^{-1/2}$ (see the dotted curve in the top panel of Fig. 6.5.2). The unperturbed material that crosses the orbit has an inverse vortensity comparable to, if not larger than that of the gas initially shocked by the inner wake. The coorbital vortensity deficit thus does not decrease when the planet starts interacting with the unperturbed gas inside its orbit ($\delta m \simeq 4$ from 14 to 3 au, see the dotted curve in the bottom panel of Fig. 6.5.2), and migration does not decelerate. Shock formation is impeded, and runaway migration is fueled solely by the increasing inverse vortensity of the background material that crosses the orbit as $\mathcal{P}$ moves inwards. A similar result was predicted by Lin & Papaloizou (2010) (their section 6.1.1). Consequently, migration becomes increasingly fast, and it is clear in the upper panel of Fig. 6.5.1 that $|\dot{a}|$ increases nearly continuously in the σ_2 simulation until $\mathcal{P}$ reaches the grid's inner boundary.

On the contrary, in the σ_0 and σ_1 runs, the background inverse vortensity increases with radius (see respectively the solid and dashed curve in the top panel of Fig. 6.5.2). The unperturbed material crossing the orbit has an inverse vortensity smaller than that of the gas initially shocked by the inner wake. The coorbital vortensity deficit therefore decreases when $\mathcal{P}$ starts interacting with this unperturbed material (see respectively the solid and dashed curve in the bottom panel of Fig. 6.5.2), runaway stalls, and $\mathcal{P}$ is able to generate an $\mathcal{I}_\mathcal{V}$ maximum inside its orbit that fuels the next episode of runaway migration.

The maximum migration rate is determined by the difference between the $\mathcal{I}_\mathcal{V}$ maximum of the gas shocked by the inner wake (which we denote by $\mathcal{I}_{\mathcal{V}\mathrm{max}}$) and $\mathcal{I}_{\mathcal{V}\mathrm{lib}}$ (which is close to $\mathcal{I}_{\mathcal{V}0}(r_p)$). Both quantities are annotated in the lower-left panel of Fig. 6.5.1. This difference of inverse vortensity increases upon lowering σ, and we see in the upper-left panel of Fig. 6.5.1 that the maximum migration rate increases for smaller σ, at least in the first episode of runaway migration. Likewise, the braking is determined by the difference between $\mathcal{I}_{\mathcal{V}\mathrm{max}}$ and the $\mathcal{I}_{\mathcal{V}0}$ of the material orbiting inside the shocked gas (denoted by $\mathcal{I}_{\mathcal{V}_0^-}$ in the lower-left panel of Fig. 6.5.1). Again, this difference increases (in absolute value) for smaller σ. The braking also depends on the ability of the material entering the horseshoe region to perform secondary U-turns, which slows down migration by adding a positive corotation torque.

We have already mentioned the existence of secondary U-turns for the Uther simulation in section 6.3 (see the panel at time T_D in Fig. 6.3.3). A smaller σ favors multiple U-turns of the material entering the horseshoe region, a larger induced corotation torque, and therefore a more abrupt braking of the migration. A short episode of outward migration is even observed at the end of the first runaway in the σ_0 run, as highlighted by the inset plot in the upper panel of Fig. 6.5.1. The three panels of inverse vortensity in Fig. 6.5.1 help understand this short episode. The left panel at time $T_A = 5900$ years is when $|\dot{a}|$ is maximum. A trapezoidal region of material trapped in libration with $\mathcal{P}$ forms at $0 \lesssim \theta \lesssim 2$ rad, whereas the inner material with maximum $\mathcal{I}_\mathcal{V}$ executes primary U-turns outwards, contributing to the planet's runaway. Part of this material with maximum $\mathcal{I}_\mathcal{V}$ crosses the orbit, but when $\mathcal{P}$ starts slowing down, part of it stays in the horseshoe region and performs secondary U-turns. This situation is illustrated in the middle panel at time $T_B = 6700$ years, where the $\mathcal{I}_\mathcal{V}$ difference of the gas just in front of the planet in azimuth (high $\mathcal{I}_\mathcal{V}$) and just behind it (low $\mathcal{I}_\mathcal{V}$) is large enough for the (positive) corotation torque to allow outward migration.

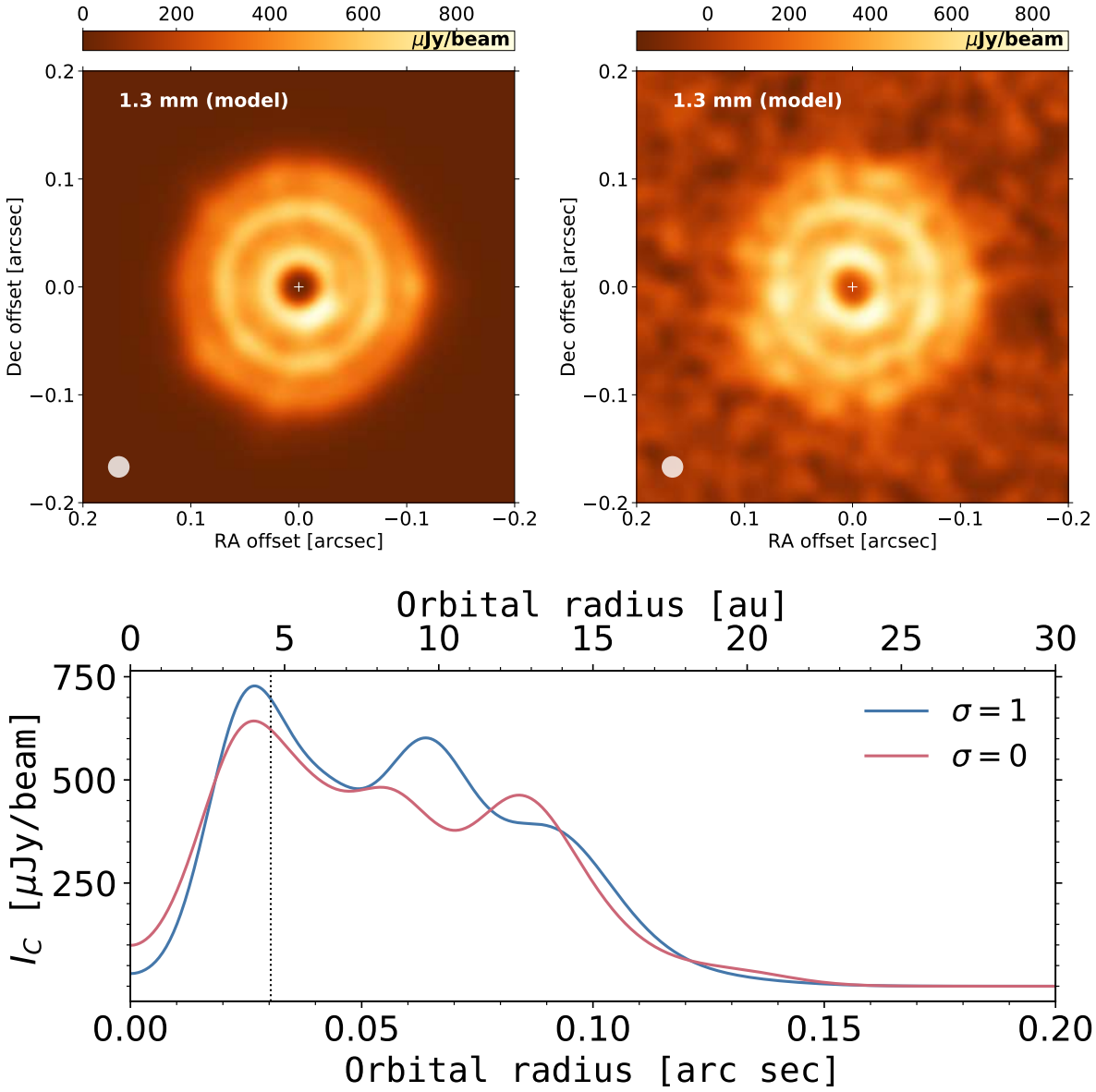

Figure 6.5.3: **Top panels**: same as the top panels of Fig. 6.3.6, but for the σ_0 run. The dust radiative transfer calculations are carried out just after the third phase of runaway migration, at ~ 18700 years, in order to compare with the calculations presented for the σ_1 run in section 6.3.3. The **bottom panel** compares the azimuthally-averaged convolved intensity versus distance to the star in the σ_0 and σ_1 runs.

This $\mathcal{J}_\nu$ difference changes sign in the right panel at time $T_C = 7000$ years. Progressive advection-diffusion of vortensity in the horseshoe region, and shock formation inside the gap's inner edge, reinstate inward migration. The oscillations in the planet's orbital radius described by McNally et al. (2019) after each runaway phase correspond in our work to secondary U-turns of high-$\mathcal{J}_\nu$ material in the coorbital region. These secondary U-turns help at once brake the planet's migration and replenish the reservoir of dust particles ahead of the planet before the pending runaway phase (see section 7.7 for the tracking of this reservoir of particles during the simulation).

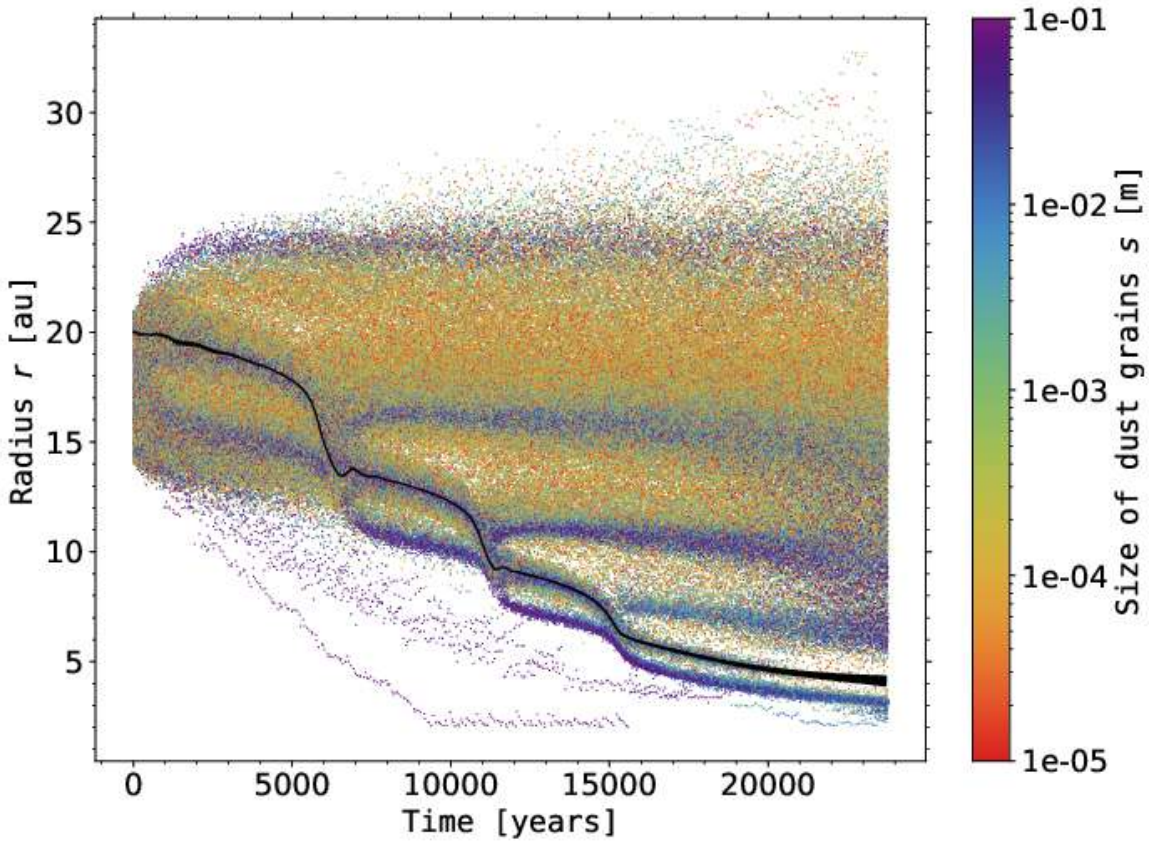

Figure 6.5.4: Same as Fig. 6.3.5 for the σ_0 run.

Concerning the impact of σ on the dust, we point out that the number of rings is smaller in the σ_0 run than in the σ_1 run, due to the reduced number of episodes of runaway migration. Moreover, because the phases of non-runaway migration last longer for σ_0, the pressure maxima are sharper, and the intensity ratio between bright and dark rings is larger, especially for the outermost bright ring. We have checked this by a dedicated dust radiative transfer calculation for the σ_0 run (see Fig. 6.5.3). The sharper pressure maxima in the σ_0 run also imply longer-lived dust rings, which is visible in the space-time diagram of Fig. 6.5.4: the rings of large particles are still distinguishable in the σ_0 run at 23000 years, whereas these rings are almost not visible anymore after 17000 years in the σ_1 run (see space-time diagram in Fig. 6.3.5).

To conclude this section, we stress again that, for a given planet mass and disk's aspect ratio, inward runaway migration comes in two flavors: (i) smooth and fast, or (ii) intermittent and globally slower. Getting one behavior or the other depends on the profile of inverse vortensity in the disk, in particular across the inner edge of the planet gap. As we have seen, a low turbulent viscosity and a shallow gas surface density profile favor intermittent runaway with sharper stairs in the migration pattern.

6.5.2 *Self-Gravity*

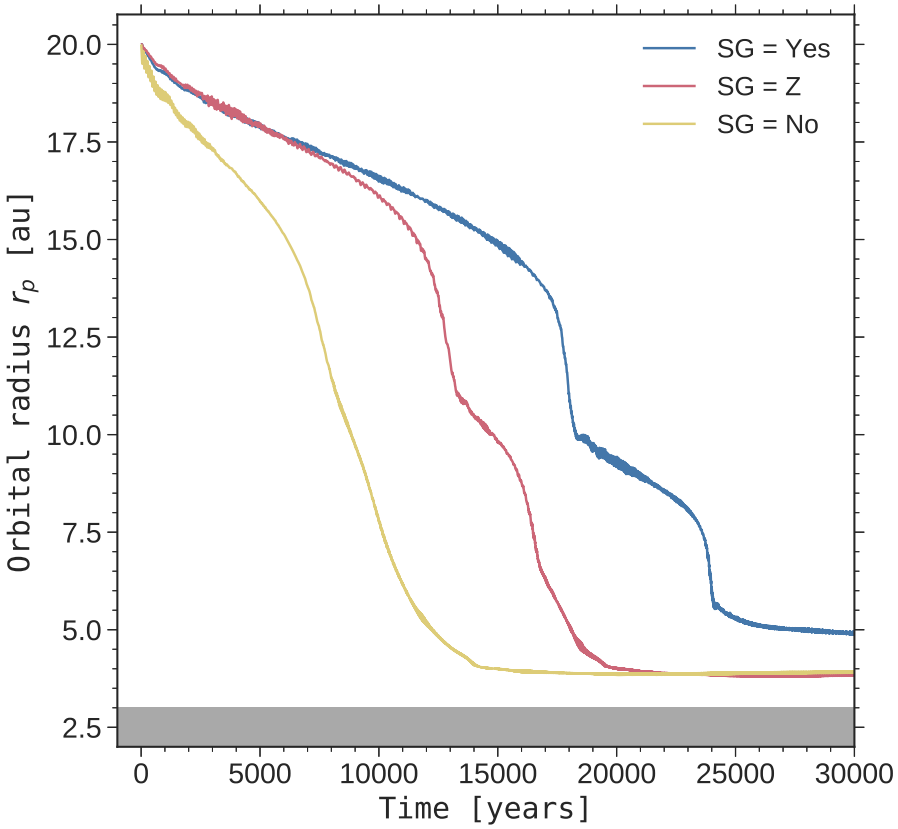

Figure 6.5.5: Impact of including gas self-gravity on the planet's orbital evolution in the Pendragon simulation. Results are shown with full inclusion of the gas self-gravity (blue curve labeled as SG = Yes), with only the axisymmetric part of the gas self-gravity (red curve, SG = Z), and without self-gravity (yellow curve, SG = No). The gray band shows the inner wave-killing zone.

Depending on the disk's aspect ratio h_0, the disk models for which intermittent runaway migration is observed in Fig. 6.2.1 have an initial Toomre Q-parameter in the range $[16-19]$ at 10 au, which is about half way between the planet's initial location and the outer edge of the inner damping boundary. These values of Q are large enough to wonder whether gas self-gravity should be included in the simulations. To show that gas self-gravity actually matters despite these rather large Q values, we compare in Fig. 6.5.5 the planet's orbital evolution in the Pendragon run (blue curve, section 6.4) with that in two additional simulations: one that discards gas self-gravity (yellow curve), and another one where only the axisymmetric part of the gas self-gravity is accounted for (red curve, see Baruteau & Masset, 2008b). These two additional simulations use otherwise the same setup as Pendragon.

We see that the initial migration rate is substantially larger in the run without self-gravity. This is due to a spurious inward shift of the Lindblad resonances when the planet feels the gravitational potential of the disk but the disk does not feel its

own potential (Pierens & Huré, 2005; Baruteau & Masset, 2008b). This inward shift causes an increase in the magnitude of the net Lindblad torque that scales with $(Qh)^{-1}$, and which becomes significant when $Qh \lesssim 1$, as is the case in the Pendragon and Uther simulations (see Baruteau & Masset, 2008b, whose results were obtained for non gap-opening planets). As a consequence of the faster (initial) migration, the steps in the migration pattern are much less visible in the run without self-gravity (see section 6.5.1). To understand why this is the case, one has to dwell again on the inverse vortensity profile ($\mathcal{I}_\mathcal{V}$). Without self-gravity, we find that the planet is able to maintain a small $\mathcal{I}_\mathcal{V}$ bump inside its orbit all over its migration course. The orbit-crossing gas has an $\mathcal{I}_\mathcal{V}$ which is high enough to sustain runaway migration, but not high enough that the planet can overcome this $\mathcal{I}_\mathcal{V}$ bump, which would cause gas with unperturbed, smaller $\mathcal{I}_\mathcal{V}$ to start crossing the orbit, and which would therefore cease runaway, as explained in section 6.3.1. The smaller amplitude of the $\mathcal{I}_\mathcal{V}$ bump inside the planet orbit without self-gravity is due to the artificially faster migration rate in that case, which weakens the shock driven by the planet's inner wake (the synodic period of the gas around the gap's inner edge being too short in comparison to the planet's migration timescale over its horseshoe region). In the run without self-gravity, the planet's migration rate ($|\dot{a}|$) stays around 10 $m.s^{-1}$, while with self-gravity $|\dot{a}|$ oscillates between approximately 0 and 20 $m.s^{-1}$.

In the simulation with the axisymmetric part of the gas self-gravity, the initial migration rate is very similar to that with full self-gravity, in agreement again with past studies on the Lindblad torque (Pierens & Huré, 2005; Baruteau & Masset, 2008b). We notice, however, that runaway migration starts earlier in the run with axisymmetric self-gravity. Comparison with full self-gravity points to the presence of stronger (high-$\mathcal{I}_\mathcal{V}$) vortices in the the run with axisymmetric self-gravity, in particular along the inner separatrix of the horseshoe region, which fuels the runaway process. This is due to the fact that the non-axisymmetric part of the gas self-gravity significantly damps large-scale vortices induced by the Rossby-Wave Instability (with azimuth wavenumber $m = 1$) when $Q \times h \lesssim 1$, as is the case in these simulations (e.g., Lovelace & Hohlfeld, 2013; Zhu & Baruteau, 2016).

We finally point out that, in some of our simulations with full self-gravity, growth of a global $m = 1$ mode is observed (hints of this behavior can be seen in the σ_0 run displayed in Fig. 6.5.1, through oscillations of increasing amplitude visible in the planet's orbital radius after $\sim$ 18000 years). Similar findings have been recently reported (Pierens & Lin, 2018; Pérez et al., 2019; Baruteau et al., 2019). The nature and implications of such mode growth require a dedicated study.

6.5.3 *Energy equation*

As already stated in section 6.1, a locally isothermal equation of state is more relevant to the outer parts of protoplanetary disks, typically beyond a few tens of au, where the radiative diffusion and/or cooling timescales become shorter than the orbital timescale. In the following, simulations that include the above energy equation are referred to as radiative simulations, those that do not as isothermal simulations. Ziampras et al. (2020) found that radiative effects can prevent a planet from efficiently

carve secondary gaps in its protoplanetary disk. They showed that this overestimation of the gap-opening capabilities of a single planet in the isothermal case is due to a higher contrast of the spiral arms with respect to the disk. Said differently, the density perturbations due to the planet wakes are stronger in the isothermal case than in the radiative case. This discrepancy is even more critical for the planet's inner wake (see their Fig. 4), which induces a smaller local perturbation in the disk. This section aims therefore at examining the impact of an energy equation on the results of the Pendragon simulation, in particular the intermittent runaway migration and the formation of multiple bright rings. The energy equation solves the time evolution of the gas thermal energy density, and it includes viscous heating, radiative cooling and stellar irradiation. However, radiative diffusion is discarded for simplicity. Our energy equation is thus the same as, e.g., Equation 1 of Pierens & Raymond (2016), but without the radiative diffusion term. The Rosseland mean opacity is taken from Bell & Lin (1994). The gas adiabatic index is set to 5/3, and for our fiducial profiles of initial surface density and temperature, the initial entropy profile happens to be nearly flat ($\propto r^{-1/30}$). Since viscous heating is small in the Pendragon disk model ($\alpha = 10^{-4}$), the gas temperature very quickly evolves towards the temperature profile set by stellar irradiation. For comparison purposes, the radial profile of the irradiation temperature (T_{irr}) is chosen such that the radial profile of the gas adiabatic sound speed approximately matches that of the isothermal sound speed in the Pendragon run, which led us to adopt $T_{irr}(r) = 80\,K \times (r/r_0)^{-0.7}$ (recall that $r_0 = 10$ au).

In the top-left panel of Fig. 6.5.6, we compare the time evolution of the planet's orbital radius in the isothermal and radiative Pendragon simulations. The migration pattern of $\mathcal{P}$ is similar in both simulations, with basically two stages of runaway migration that cease at about the same locations in the disk (near 10 and 5 au). The initial migration rate is somewhat higher in the radiative run, however, and the first runaway occurs earlier. The origin of this behavior is not entirely clear. One possible lead is the absence of vortices observed in the radiative run, or the fact the planetary shocks appear to be smoother in that run. This enhanced inward migration in the radiative simulation is coherent with the results in Ziampras et al. (2020): because the contrast for the planet's inner wake is smaller in their radiative simulation, we would expect a faster inward migration of their planet due to an enhanced Lindblad torque. In order to verify this statement, a detailed investigation would be required. In agreement with the results presented in section 6.5.1, this overall faster migration results in smoother stairs. Nonetheless, the similar pattern of intermittent migration leads to the formation of similar dust structures at the end of the radiative simulation, and therefore a similar sequence of bright and dark rings of continuum emission, as illustrated in the middle and bottom panels in Fig. 6.5.6. Because the stage of decelerated migration at $\sim$ 10 au lasts shorter in the radiative simulation, the dust ring that forms at the pressure maximum outside the planet (near 12 au) fades away faster than in the isothermal simulation. The lower panel in Fig. 6.5.6 actually makes it clear that the bright ring of continuum emission near 12 au is broader in the radiative simulation.

For the sake of completeness, we also performed a radiative simulation with the Uther disk model ($\alpha = 10^{-3}$). The profile of irradiation temperature was chosen as $T_{irr}(r) = 60\,K \times (r/r_0)^{-0.7}$. Although not shown here, the migration pattern in this

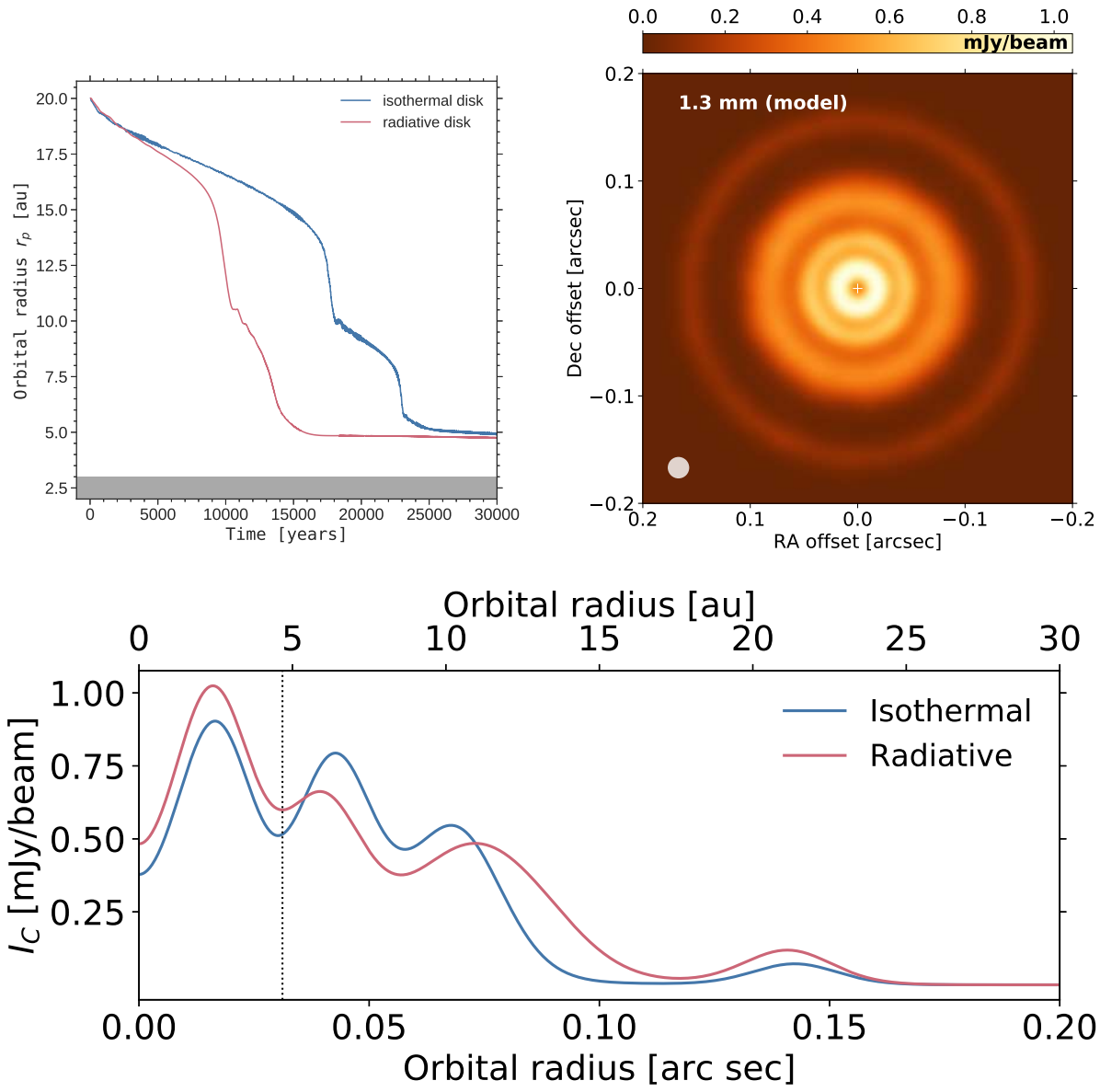

Figure 6.5.6: **Top-left:** Time evolution of the planet's orbital radius in the Pendragon run (blue curve, labeled as isothermal disk) and in an additional run that includes an energy equation (red curve, labeled as radiative disk; see text). The gray band shows the inner wave-killing zone. **Top-right:** Synthetic flux map of the continuum emission at $\lambda = 1.3$ mm in the radiative run, convolved with a 0.″02 circular beam, at ~ 40000 years (~ 25000 years after migration halted). **Bottom:** Azimuthally-averaged convolved intensity versus distance to the star in the isothermal and radiative runs. The intensity of the isothermal run is at 59900 years (also ~ 25000 years after migration stopped in that run). The vertical dotted line shows the planet location.

radiative simulation is very smooth, and the absence of clear steps in the migration, along with the higher level of disk turbulence, preclude the formation of well-defined dust rings in the disk. Still, we have checked that intermittent migration and the formation of multiple dust rings are recovered in the Uther radiative simulation by simply increasing the planet mass.

6.5.4 *Resolution*

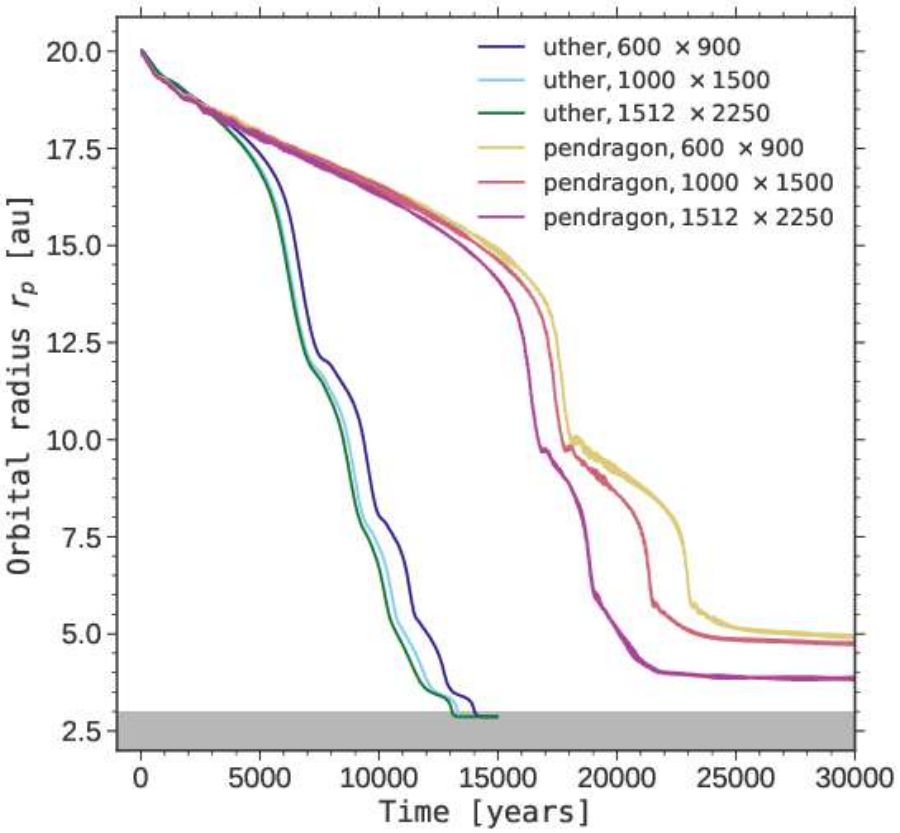

Figure 6.5.7: Impact of increasing grid resolution on the planet's orbital evolution in the Uther and Pendragon simulations. Results are shown for three grid resolutions : 600×900 (fiducial), 1000×1500 and 1512×2250. The gray band shows the inner wave-killing zone.

When the grid resolution is increased, we find that the planet migrates globally faster, and that, as we have seen in section 6.5.1, the stages of decelerated migration last shorter. This is illustrated in Fig. 6.5.7 for the Uther and Pendragon simulations, where the fiducial grid resolution is increased to 1000×1500 and 1512×2250. The convergence in resolution is more easily achieved in the Uther run due to the larger disk's turbulent viscosity. Increasing resolution allows to better resolve small-scale structures in the gas vortensity within or near the planet's horseshoe region. This is particularly critical to the simulations at low viscosity, like in the Pendragon run with $\alpha = 10^{-4}$, for which increasing resolution tends to form smaller, high-$\mathcal{J}_V$ vortices along the inner separatrix of the horseshoe region, which therefore embark more easily onto U-turns, and boost the planet's migration rate. These small-scale vortices, which are better resolved in the 1512×2250 simulation, thus tend to extend the runaway phase, and bring the planet closer to the grid's inner boundary. Similar results have been obtained by McNally et al. (2019), who examined intermittent runaway migration in

low-viscosity and inviscid disk models, and found that convergence in resolution was increasingly difficult to achieve, if achievable at all, upon decreasing viscosity.

Although, in our simulations, stages of decelerated migration last shorter when increasing resolution, a pressure maximum does form when migration decelerates, but it is smoother, the density of dust trapped at this location is therefore smaller, and so is the intensity of the corresponding bright ring. For Pendragon, for instance, when the number of grid cells is increased from 600×900 to 1000×1500, the intensity of the 3 innermost bright rings is decreased by a few percent up to 30%, depending on the ring. Concerning the longevity of dust rings, for example the ring at 12 au in the Pendragon simulation, its lifetime is shorter when increasing resolution because the preceding stage of slow migration is shorter and the corresponding pressure maximum therefore smoother. For the 1512×2250 run, the ring's disruption starts at ~ 50000 years, while it does so at ~ 70000 years at 600×900.

6.5.5 *Dust backreaction*

We carried out multifluid numerical simulations in 2D with FARGO3D. The aim was in particular to test the hypothesis that the backreaction of dust on the gas is not dominant in the intermittent runaway migration of a Saturn-like planet, for the parameters that we tested. We based these multifluid simulations on the parameters for our fiducial case Pendragon. The results of seven simulations are presented in Fig. 6.5.8. For five of them, we just consider two fluids (the gas and one dust fluid) that can interact with the planet and with themselves via dust and gas feedback. The five dust sizes for these dust fluids are chosen from s_{min} to s_{max}, more specifically $s_d = 10$ µm (dark blue curve), 100 µm (light blue curve), 1 mm (dark green curve), 1 cm (yellow curve), 10 cm (red curve). Note that we consider for these individual simulations the same initial dust-to-gas density ratio $\epsilon = 0.05$. The other two simulations correspond to these five dust fluids with the gas, discarding (purple curve) and taking into account (light green curve) the feedback. For these two simulations, we chose an initial dust-to-gas mass ratio $\mu = 0.05$, and therefore a more realistic dust size distribution for these five fluids ($q = 3.5$, see the "size distribution" methodology in section 5.1.2.2).

The first remark on Fig. 6.5.8 concerns the staircase migration pattern that is present in all seven simulations, regardless of the particle size, with and without dust feedback. Results are therefore qualitatively similar to the fiducial case presented in section 6.4, with a few differences on when the stages of runaway migration occur. In particular, we can highlight the fact that the impact of the feedback seems rather negligible by comparing the purple and the light green curves which show a very similar migration pattern as long as the planet is beyond $4-5$ au, with the phases of slow and fast migration that occur at approximately the same time. The main difference comes from the individual simulations (gas + one dust fluid). In order to grasp what is happening, let us compare two simulations with one individual dust fluid: $s_d = 1$ cm and $s_d = 10$ cm. For a physical quantity X, we use thereafter the subscripts X_1 and X_10 to refer to these specific simulations. X_g refers to the physical quantity in the gas. For these two simulations, we would like to interpret the fact that the runaway migration phase occurs earlier in the case of a 10 cm dust fluid (end of the first runway regime at

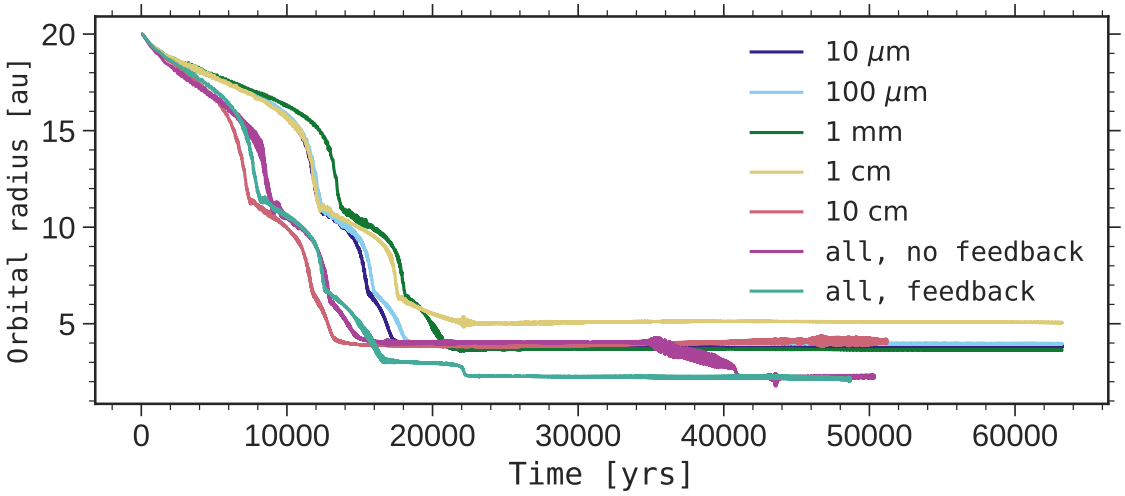

Figure 6.5.8: Impact of the torques from the dust fluids on the runaway intermittent migration of the Saturn-like planet in the Pendragon case. Dust feedback is included in most cases. Seven cases are show in this graph. Five dust sizes are considered individually, from 10 μm to 10 cm. For the two remaining simulations, we include all five dust fluids with and without feedback.

$\lesssim$ 8000 years) compared to a 1 cm dust fluid (end of the runway regime at $\gtrsim$ 12000 years).

In order to simplify the calculations, we use here the simplified expression of the coorbital mass deficit presented from Eq. (90) in section 3.3.3.2:

$$\delta m_g = 4\pi\Sigma_{S,g} r_p x_s - M_{HS,g}, \tag{106}$$

with $\Sigma_{S,g}$ the uniform gas surface density in the inner separatrix (because the migration is inward), and $M_{HS,g}$ the mass of the horseshoe region. If we want to understand the impact of the dynamical corotation torque from the dust fluid, we assume in a first step that the backreaction of the dust fluid on the gas is negligible, which is indeed verified in Fig. 6.5.8. This amounts to say that the gas dynamical corotation torque is the same in the two simulations, as well as the coorbital mass deficit $\delta m_{g,10} \simeq \delta m_{g,1}$. We can therefore compare the total coorbital mass deficits in the two simulations, by looking at the following quantity:

$$\delta m_{10} - \delta m_1 = 4\pi \left(\Sigma_{S,10} - \Sigma_{S,1}\right) r_p x_s - \left(M_{HS,10} - M_{HS,1}\right), \tag{107}$$

where ($\Sigma_{S,10}$,$\Sigma_{S,1}$) are the values of the dust density near the inner separatrix, and ($M_{HS,10}$,$M_{HS,10}$) the values of the mass of dust material trapped in libration with the planet. In order to roughly estimate these four quantities, we display in Fig.6.5.9 the dust surface density for the '$s_d = 1$ cm' simulation (left panel) and the '$s_d = 10$ cm' simulation (right panel). In agreement with the corresponding curves in Fig. 6.5.8, the planet (black vertical dashed line) in the second case is closer to the star ($\sim$ 15 au) than in the first case ($\sim$ 17 au), because of a globally faster migration. We can try to qualitatively constrain $\Sigma_{S,d}$ and $M_{HS,d}$ in the two simulations, at the same time. By

looking at the inner separatrix, at ~ 12 au for the largest particles and at ~ 14 au for the smallest particles, we notice that $\Sigma_{S,10} \simeq \Sigma_{S,1}$, which reduces Eq. 107:

$$\delta m_{10} - \delta m_1 \simeq (M_{HS,1} - M_{HS,10}) \tag{108}$$

Finally, we also notice that larger particles (10 cm, right panel) have started to leave the Lagrange points of the planet, and more generally its corotation region. The mean density in the horseshoe region is thus significantly lower in the '$s_d = 10$ cm' case compared to the '$s_d = 1$ cm' case. By integrating the density in the corotation region, we can therefore write $M_{HS,10} < M_{HS,1}$ and $\delta m_{10} > \delta m_1$. From that simple analysis of the surface density fields, we find that the coorbital mass deficit is larger for the simulation with largest particles. Because a larger deficit favors the runaway of the planet, we find qualitatively the result of Fig. 6.5.8, with a globally faster migration if the planet is immersed in a fluid of larger particles.

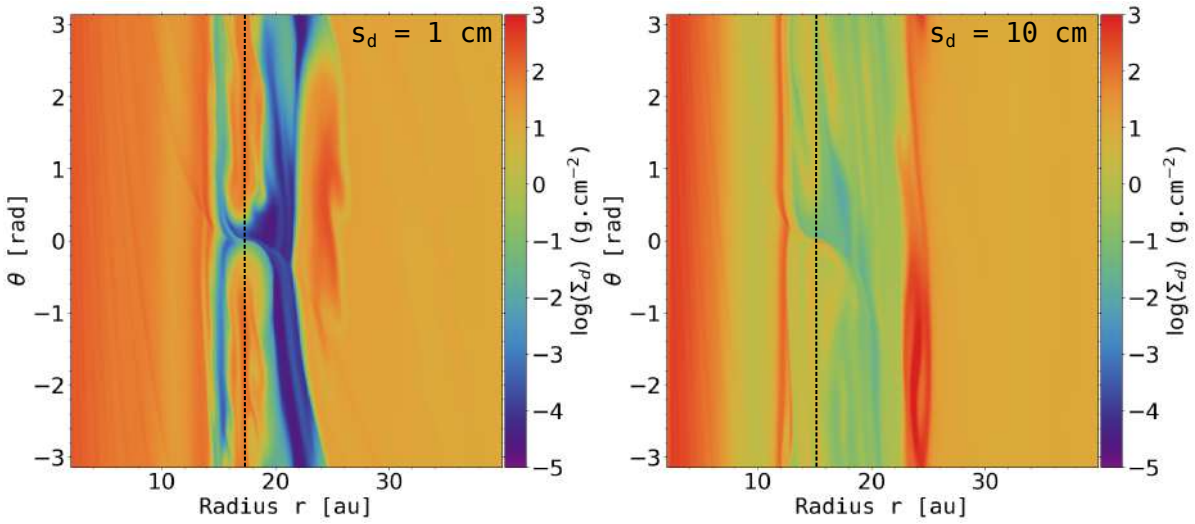

Figure 6.5.9: Results of two 2D numerical simulations with FARGO3D, which models dust as pressure-less fluids: a $s_d = 1$ cm dust fluid is coupled to the gas in the left panel, whereas a $s_d = 10$ cm dust fluid is coupled to the gas in the right panel. We display the dust surface density in these two cases, in logarithmic scale. The radial location of the planet is marked with the black vertical dashed line.

Note that dust feedback may actually have a stronger impact on the intermittent runaway migration of the planet. By comparing the gas surface density in the two aforementioned cases, we notice the presence of a large-scale vortex in the gas, outside the planet location, for '$s_d = 1$ cm' (you can infer the presence of this vortex in the left panel of Fig. 6.5.9, at r ~ 25 au). This vortex is not as strong for larger particles. This absence of vortices for larger particles has already been stated in Fu et al. (2014), and is a direct consequence of dust feedback. In any case, the absence or presence of such large vortex near the gap's outer edge can modify the migration of the planet. More simulations and analyses are needed in order to fully determine the impact of each fluid and the feedback on the intermittent runaway migration scenario.

6.5.6 *Inner planet and resonance*

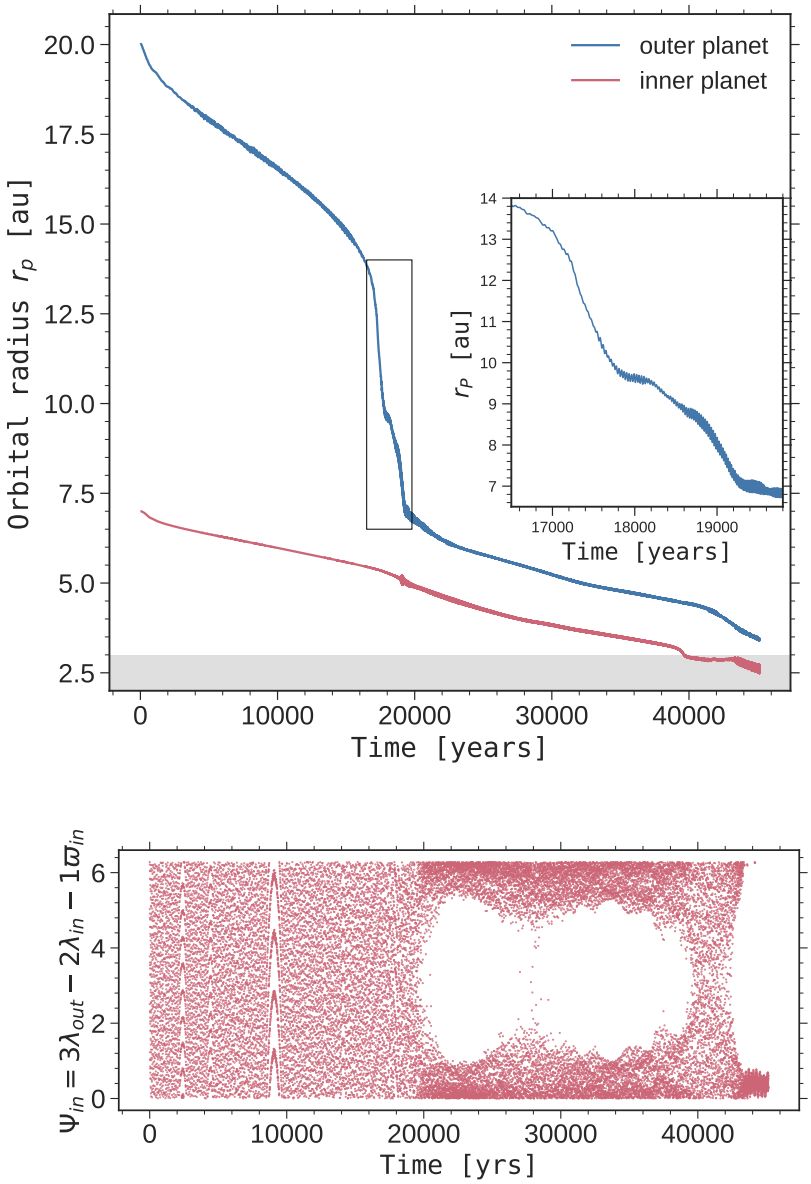

Figure 6.5.10: **Top panel**: Time evolution of the orbital radius of two planets, the inner planet in red and the outer one in blue. The outer ~ 1.5 M_{Saturn} planet is in an intermittent runaway migration regime, whereas the inner ~ 0.5 M_{Saturn} planet is rather in a type-I migration regime. The grey band corresponds to the inner wave-killing zone. **Bottom panel**: Time evolution of the 3:2 resonant angle for the inner planet. The convergent inward migration leads to the capture of the two planets into the 3:2 mean-motion resonance.

We chose also to study the evolution of an outer planet $\mathcal{P}_o$, with the same parameters as those presented in the low turbulent case Pendragon in section 6.4, but with an inner planet $\mathcal{P}_i$ with a mass ratio $q_{pi} = 1.4 \times 10^{-4}$, that is a third of q_{pe}, and initially

at 7 au. If the planets are able to interact between each other and become resonant, the results related to the presence of this second planet are twofold. Firstly, it is a more natural way of stopping the migration of $\mathcal{P}_e$, rather than expecting that the outer planet reaches the inner boundary of the simulation grid. Secondly, $\mathcal{P}_i$ is massive enough to create a natural barrier that prevents large particles of disappearing inside the inner boundary of the grid, due to the fast drift of these dust grains. The top panel of Fig. 6.5.10 displays the orbital evolution of the two planets in the protoplanetary disk, in blue for the outer planet and in red for the inner planet. Because $q_{pi}/h^3 < 1$, $\mathcal{P}_i$ is not in a type III migration regime, it therefore does not know any fast migration stage, unlike $\mathcal{P}_e$. Indeed, the latter reaches a runaway regime before breaking at around 18000 yr (see inset panel in Fig. 6.5.10). When we consider the inverse vortensity profile, we notice the horseshoe U-turn of high $\mathcal{I}_\mathcal{V}$ material, which speeds the outer planet up. The maximum of $\mathcal{I}_\mathcal{V}$ that is formed at the inner planet's outer edge takes part in the acceleration of $\mathcal{P}_e$ when the corresponding material starts its U-turn. After the braking, a new $\mathcal{I}_\mathcal{V}$ maximum appears between the two planets' orbits. $\mathcal{P}_e$ then enters a second runaway phase, before its migration is suddenly stopped due to a common gap shared by $\mathcal{P}_i$ and $\mathcal{P}_e$ at around 20000 yr. At this time, we checked that one of the resonant angles of the planets is librating. In this simulation, the resonant angle of $\mathcal{P}_i$ dynamically librates around $\theta = 0$ (see bottom panel of Fig. 6.5.10). More simulations have to be carried out, in particular to see the impact of an inner planet on the dust thermal emission and the formation of multiple bright rings. We considered in this section the impact of an inner planet in the intermittent runaway migration. In section 7.4, we will deal with the orbital evolution of an outer low-mass planet once a Saturn-mass planet has migrated intermittently. In particular, we will focus on the impact of inverse vortensity maxima on the planet migration.

6.6 LONGEVITY OF THE DUST RINGS

We discuss in this section the longevity of the dust rings induced by intermittent runaway migration. When the planet starts a new episode of runaway migration, the pressure maximum that the planet has formed beyond its orbit is no longer sustained by the planet's outer wake. The pressure maximum is therefore progressively smoothed out by the disk's turbulent viscosity, and so is the dust ring that coincides with the pressure maximum. As we have seen in Figs. 6.3.5 and 6.4.2, the dust rings last between 3000 and 10000 years in the Uther simulation ($\alpha = 10^{-3}$), whereas some dust rings survive for more than 10^5 years in the Pendragon simulation ($\alpha = 10^{-4}$).

This comparison highlights that the lifetime of the dust rings does not simply scale inversely proportional to the gas turbulent viscosity. The main reason is that the lifetime of a dust trap partly depends on how sharp the radial pressure profile is around the pressure maximum, which is related to the duration of the stage of decelerated migration between two successive runaways. This duration is sensitive to the disk's turbulent viscosity, but also to the disk's physical model (e.g., the background gas density profile, see section 6.5.1) and the numerical resolution (see section 6.5.4).

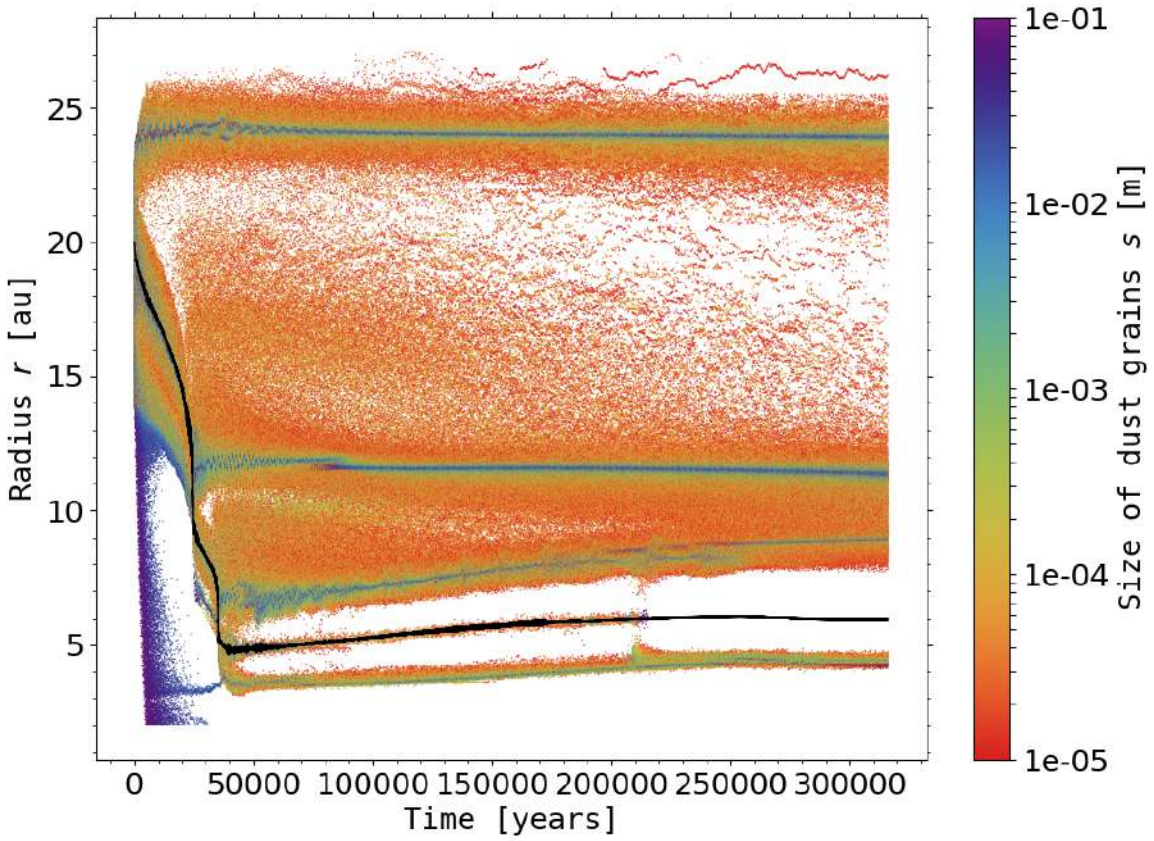

Figure 6.6.1: Same as in Fig. 6.3.5 for an extra run with the same setup as Pendragon but with a turbulent viscosity $\alpha = 10^{-5}$.

Finally, Fig. 6.6.1 presents the space-time diagram of the dust's radial location for an additional simulation with a setup identical to that of the Pendragon run, but a turbulent viscosity reduced to $\alpha = 10^{-5}$. It shows that all dust rings, except the one coorbital with the planet, last over the entire duration of the simulation ($\gtrsim 3 \times 10^5$ years). We notice in this case that the planet slowly migrates outwards after having reached the proximity of the inner wave-killing zone, and so do the dust rings formed inside and outside the planet's orbit after the last episode of runaway migration.

6.7 GEOMETRICAL SPACING

Starting from our fiducial case Uther, we performed additional simulations in order to test the robustness of the intermittent runaway migration, and its ability to form multiple bright rings in the dust thermal emission. In particular, we varied the initial gas surface density profile (Σ_0 and σ), the initial position of the planet d_0, the α parameter and the aspect ratio h_0 at r_0. We will come back more in depth to the results shown in Fig. 6.7.1, but the legend of the first five panels (panels A to E) indicates some values of the parameters for which we retrieve the intermittent runaway migration. In each simulation, we start from the parameters of the Uther run and modify just

one quantity. Note that (i) the region of parameter space for which the intermittent runaway migration scenario occurs is actually larger, and more simulations have to be performed in order to better delineate this region. In particular, we find that intermittence is also favored for larger planet-to-primary mass ratios q_p (but still in the partial gap opening regime). We have checked the latter dependence for the Uther disk model by increasing the planet mass from 0.9 M_{Saturn} to 2.7 M_{Saturn} (i.e 0.8 $M_{Jupiter}$). (ii) Other simulations show a staircase migration pattern, but we conserve only the simulations for which at least four outer pressure maxima/bumps are generated in the disk.

Let us now consider the first five panels of Fig. 6.7.1, which display the radial distribution of the pressure maxima or pressure bump in the disk, when varying the parameters indicated in the previous paragraph. For example in panel D, four simulations are considered with $\alpha = 3 \times 10^{-4}$, 5×10^{-4}, 8×10^{-4} and 10^{-3}. We display the radial location of the outer pressure maxima near the end of the simulations. Note that a more accurate approach would be to consider the radial location of the bright rings after dust radiative transfer calculations. We therefore assume that each pressure bump or maximum efficiently traps particles and generate bright rings in the dust thermal emission, which has been valid in almost all our simulations in this chapter (as long as the inner disk is resolved). In panel D, four outer pressure maxima are obtained and their radial locations depend little on α (see also Fig. 11 in Lin & Papaloizou, 2010). By fitting the distribution of the rings in the disk, we find that the rings have a geometric spacing $\delta = r_{i+1}/r_i \sim 1.5$, with r_i the radial location of the ith bright ring. Interestingly, the additional simulations indicate that, when intermittent runaway migration is at work, this geometric spacing mainly depends on the disk's aspect ratio h_0 (panel E of Fig. 6.7.1), but hardly on q_p, the initial location of the planet $d_0 = r_{p,o}$ (panel C), Σ_0 (panel A and Fig. 18 in Lin & Papaloizou, 2010), and even σ (panel B). In all these panels, the value of δ is written in the legends as the slope of the best fit. In order to derive the δ, note that we removed the outermost pressure maximum of the fit, as it almost always located slightly beyond its expected position. We will come back to this point later on in this section.

A simple estimate of δ can be obtained with two assumptions.

- **Ideal staircase migration pattern**: a planet that follows an ideal staircase migration pattern is at rest during the slow migration phases, and migrates instantaneously to its new position during the runaway phases.

- The radial location of the $\mathcal{J}_\nu$ maximum outside the planet just after runaway migration **coincides** with that of the $\mathcal{J}_\nu$ maximum inside the planet just before runaway migration. Remember that we noticed such a behavior between panels T_E and T_A in Fig. 6.3.3 in section 6.3.1.

With these assumptions, we can write $\delta = (r_p + \xi)/(r_p - \xi)$, with ξ the radial separation between the planet and the $\mathcal{J}_\nu$ maxima. The precise value of ξ is uncertain, but roughly $\xi \gtrsim x_s$ (recall that x_s denotes the radial half-width of the planet's horseshoe region). We thus expect $\xi \propto r_p$, and therefore δ independent of r_p, which accounts for the geometric spacing of the dust rings. By adopting $\xi = x_s$, we obtain $\delta \approx 1.25$. This is smaller than the typical value ~ 1.5 found in our simulations, which is due in

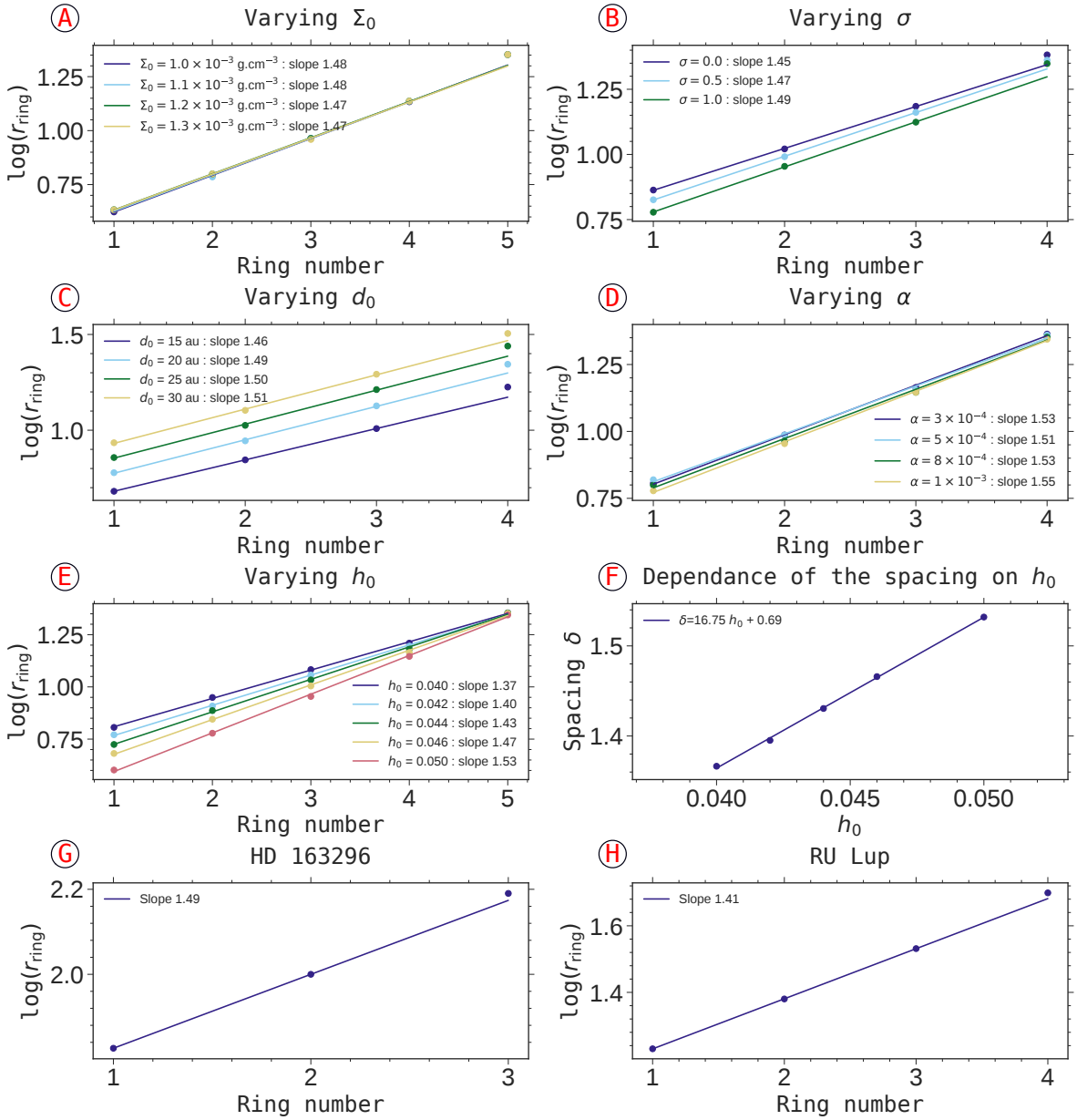

Figure 6.7.1: Robustness of the intermittent runaway migration scenario, and geometrical spacing. In all panels except for panel F, we display the locations of the pressure maxima outside the planet location (in logarithmic scale) as a function of their rank. Said differently, these panels show the distribution of the rings throughout the disk for various simulations, by varying the initial gas surface density profile via Σ_0 (panel A) and σ_0 (panel B), the initial position of the planet d_0 (panel C), the turbulent viscosity α (panel D) and the aspect ratio h_0 (panel E). If there are N rings, the lines show the best fits for the N−1 first rings. The slope of these fits defines a constant geometrical spacing between successive rings, close to 1.5 in almost all the simulations. Panel F shows how the geometrical spacing depends on the aspect ratio h_0. Finally, the bottom row displays the location of the bright rings and the corresponding fitted geometrical spacing for two observations from Huang et al. (2018a): HD 163296 (panel G) and RU Lup (panel H).

part to the fact that the migration pattern is not an ideal staircase (due to the stages of non-runaway migration in-between the runaway phases). Note that in panels A, B and C the mass of the planet gradually increases over its first 5 orbits while it migrates: initially, the planet therefore migrates inward in a type-I migration regime, leading to a displacement that is not taken into account in the model of an ideal staircase migration pattern. On the contrary, in panels D and E, the planet is immediately put in the disk with its final mass ($q_p = 2.5 \times 10^{-4}$) and migrates consequently. In these two panels, we do not see any displacement of the outermost pressure maximum compared to its expected position given the constant geometrical spacing. It suggests that the behavior we are discussing is due to the artificial initial planet growth in our simulations.

Interestingly, some protoplanetary disks display a very similar geometric spacing for the radial location of successive bright rings in the continuum emission. For HD 163296 (panel G), we infer $\delta \sim 1.49$ by selecting the three outermost rings in Huang et al. (2018a), and for RU Lup (panel H), we infer $\delta \sim 1.41$ by considering the four bright rings reported in Huang et al. (2018a). Among all the panels of Fig. 6.7.1, panel E shows that the geometrical spacing depends mainly on the aspect ratio h_0 and little on the other parameters. The dependency of δ in h_0 is in fact linear, as shown in panel F. We can thus write $\delta \simeq \delta(h_0) = a h_0 + b$, with $a \simeq 16.75$ and $b = 0.69$, where we neglected the small contribution of the other parameters. As long as the geometrical spacing is comprised between 1.37 and 1.53, it is therefore possible to have a rough estimate of the aspect ratio h_0. Assuming that this direct link between aspect ratio and geometrical spacing is valid for HD 163296 and RU Lup, we obtain respectively $h_0 \simeq 0.048$ and $h_0 \simeq 0.043$. Note that, to be more exhaustive in this estimation, we should also consider the impact of the flaring index. In any case, the spacing could be a promising quantity to look at in future works to discriminate between different models of multiple rings formation, for a given disk observation. Let us conclude this section and chapter with a last remark on Fig. 6.7.1. Similarly to our results of simulations, we did not take into account the outermost bright ring in the estimation of δ for HD 163296 and RU Lup, as it is located slightly beyond its expected position. This interesting displacement of the outermost bright ring may actually reveal the formation region of a planet of a few Saturn masses that subsequently migrated inward in an intermittent runaway fashion.

APPENDIX

6.A MASS OF THE CIRCUMPLANETARY DISK

In this chapter, we assumed that the criterion $\delta m > M_p$ defines if the planet is in a runaway migration regime. This assumption is valid if the mass of the circumplanetary disk M_{cpd} can be neglected with respect to the mass of the planet M_p. We verify this hypothesis via Fig. 6.A.1, by displaying an upper boundary of the value of $q_{cpd} = M_{cpd}/M_\star$ relative to the planet-to-primary mass ratio $q_p = M_p/M_\star$, as a function of the planet semi-major axis in our two fiducial cases Uther and Pendragon. q_{hill} is the mass included inside the Hill radius, which is usually larger than the typical size of the circumplanetary disk (Crida et al., 2009). q_{hill} is therefore an upper limit for q_{cpd}. In the two fiducial cases, the mass of the circumplanetary disk rarely exceeds 10% of the mass of the planet q_p during the simulations.

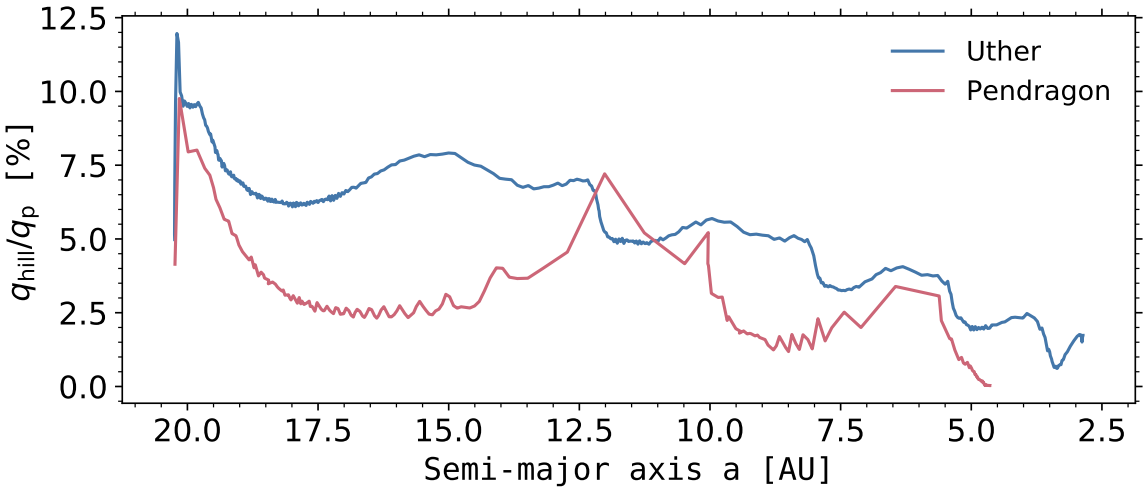

Figure 6.A.1: Numerical estimation of the mass inside the Hill sphere during the inward migration of $\mathcal{P}$ in the Uther (blue curve) and Pendragon (red curve) simulations. The hill-to-primary mass ratio q_{hill} is normalized by the planet-to-primary mass ratio q_p.

6.B ADDITIONAL RESULTS FOR FAST AND SLOW MIGRATION

We have seen in section 6.2 via Fig. 6.2.1 that for our disk model and range of planet masses, migration could be either fast, slow or intermittent, depending on the background surface density of the gas. While the main body of this chapter focuses on intermittent migration, we illustrate in this section our main findings in the fast

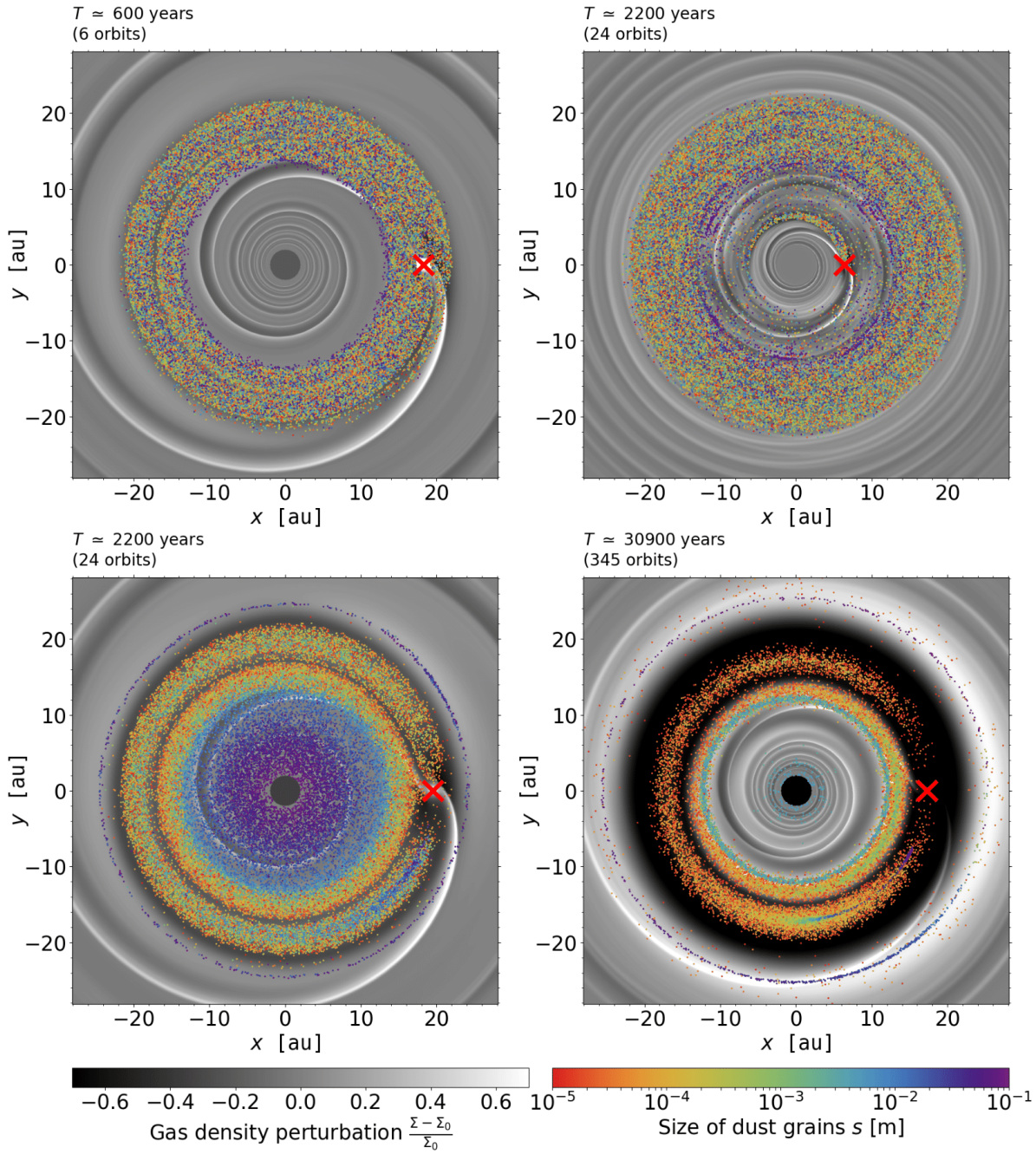

Figure 6.B.1: Perturbed gas surface density relative to its initial profile, $(\Sigma - \Sigma_0)/\Sigma_0$, in black and white and in Cartesian coordinates. The location of the dust particles is overlaid by colored dots (see rainbow color bar below the bottom-right panel). In each panel, the red cross marks the position of the planet. Results are shown for a simulation with a disk setup similar to that of the Pendragon run, but for two different initial surface densities: $\Sigma_0 = 3 \times 10^{-3}$ (upper panels, fast planet migration) and $\Sigma_0 = 3 \times 10^{-4}$ (lower panels, slow migration).

and slow migration regimes. Results are shown in Fig. 6.B.1 for the same disk setup as in the Pendragon simulation (see Table 6.4.1), but for different initial surface densities of the gas at 10 au (Σ_0).

The upper panels are for $\Sigma_0 = 3 \times 10^{-3}$, that is for the fast migration case highlighted in section 6.2. After $\mathcal{P}$ has moved through the initial dust band (upper-left panel), some particles get trapped around the L4 Lagrange point located ahead of $\mathcal{P}$ in the azimuthal direction, which is clearly seen in the upper-right panel. Comparison between both panels shows that, apart from the dust trapped near L4, most of the dust particles ultimately form a band behind $\mathcal{P}$ that is similar to the initial one, except that it drifts radially due to gas drag, and diffuses radially due to turbulence.

The lower panels are for $\Sigma_0 = 3 \times 10^{-4}$ (slow migration). The bottom-right panel shows that the planet forms three rings: (i) an outer ring that is mostly comprised of large particles, and which roughly stays at its initial location (compare with the bottom-left panel), (ii) a coorbital ring, and (iii) an inner ring that builds up at the pressure maximum between the main gap around the planet orbit and a secondary gap inside the orbit. Concerning the outer ring, a different choice of initial particles location could have led to more particles being trapped there, which would have made this ring more visible and/or thicker. Both the coorbital and the inner rings move inward together with the planet. Note that the inner ring only forms at low viscosities (it does not form for $\alpha = 10^{-3}$). The bottom-right panel indicates that some large particles remain in the inner disk parts. We attribute this seeming trapping to a numerical artifact of the grid's inner wave-killing zone rather than to a physical pressure maximum arising from a tertiary gap carved by the planet's inner wake.

6.C A SIMPLE MODIFICATION TO THE EXPRESSION OF THE COORBITAL VORTENSITY DEFICIT FOR FAST MIGRATION

The aim of this section is to propose a simple generalized expression for the coorbital vortensity deficit δm when the assumption of slow migration in Eq. (104) is not satisfied. We shall still assume, however, that δm can be defined by Eq. (103). By dividing the right-hand side of Eq. (103) by $2\pi r_p$, and integrating over θ, we get

$$\delta m \approx 4\pi r_p \omega(r_p) \times \left[\frac{x_s}{2\pi r_p} \int_{\theta_1}^{\theta_2} \mathcal{I}_\mathcal{V} \left(r_p - x_s, \theta \right) r_p \, d\theta - \frac{1}{2\pi r_p} \int_{\theta_1}^{\theta_2} \int_{r_p - x_s}^{r_p} \mathcal{I}_\mathcal{V} \left(r, \theta \right) r_p \, d\theta dr \right], \tag{109}$$

which assumes $r \approx r_p$, and where $[\theta_1, \theta_2]$ defines the azimuthal extent of the material trapped in libration with $\mathcal{P}$ and of the orbit-crossing flow ($\Delta\theta = \theta_2 - \theta_1$). Further assuming that the material trapped in libration has uniform $\mathcal{I}_\mathcal{V}$ over a rectangular domain of extent $2x_s \times \Delta\theta$ in polar cylindrical coordinates, and that $\mathcal{I}_\mathcal{V}\left(r_p - x_s, \theta\right)$ is

independent of θ over $[\theta_1, \theta_2]$ (see Fig. 6.3.3 and lower-left panel in Fig. 6.5.1), Eq. (103) can be recast as

$$\begin{aligned} \delta m &\approx 4\pi r_p \omega(r_p) \times \left[\frac{x_s}{2\pi r_p} \mathcal{I}_{\mathcal{V}e} r_p \Delta\theta - \frac{1}{2\pi r_p} \mathcal{I}_{\mathcal{V}\text{lib}} r_p \Delta\theta x_s \right] \\ &\approx 4\pi r_p \omega(r_p) x_s \times \frac{\Delta\theta}{2\pi} \times \left[\mathcal{I}_{\mathcal{V}e} - \mathcal{I}_{\mathcal{V}\text{lib}} \right]. \end{aligned} \tag{110}$$

Recall that $\mathcal{I}_{\mathcal{V}e}$ is the inverse vortensity of the gas entering the horseshoe region ($\mathcal{I}_{\mathcal{V}e} = \mathcal{I}_{\mathcal{V}}(r_p - x_s)$), and $\mathcal{I}_{\mathcal{V}\text{lib}}$ that of the gas trapped in libration with $\mathcal{P}$. The r.h.s. of Eq. (110) is therefore that of Eq. (105) multiplied by $\Delta\theta/2\pi$.

7

FURTHER OBSERVATIONAL DIAGNOSTICS OF PLANET FORMATION AND MIGRATION: ONGOING PROJECTS

In this chapter, I present current advances in several ongoing projects on various observational diagnostics linked to the presence and migration of planets in protoplanetary disks. We can tackle these projects from two different angles. From a planet perspective, additional work on the intermittent runaway migration scenario is presented, in particular what is the impact of annular substructures on the migration of low-mass planets (section 7.4), or the premises of 3D simulations (section 7.6). In addition, we present an ongoing study which intends to introduce and search for the origin of velocity kinks (section 7.3). From a dust dynamics perspective, we discuss the temporal evolution of dust substructures (section 7.2), the link between spectral index and dust size distribution (section 7.1) and the impact of planet migration on Lagrange points (section 7.5). Finally, we apply a particle tracking methodology to a key group of particles during the intermittent runaway migration of a Saturn-like planet (section 7.7).

CONTENT

7.1 Spectral index and dust size distribution 175
7.2 Spotlighting the temporal evolution of substructures 179
7.3 Velocity kinks due to the presence of a giant planet 182
7.4 Orbital evolution of an outer low-mass planet in a disk with pre-formed annular substructures 191
7.5 Dust dynamics and emission at the Lagrange points of a migrating planet 195
7.6 Preliminary work on intermittent runaway migration in 3D 202
7.7 Tracking a group of particles 206

8 CONCLUSION AND FUTURE PROSPECTS 209

Conclusion et perspectives 215

Bibliography 221

As we have seen in chapter 4, several mechanisms could explain observed substructures in protoplanetary disks, whether in the dust thermal emission, the scattered light or the spectral line emission (via the velocity kinks for example). Planets, zonal flows, snowline mechanisms, ... each of these phenomena may account for one or more bright rings in the dust emission, but this does not mean that the observational signposts of each of these mechanisms are exactly the same. The primary objective of all the ongoing works described in this chapter is to be able to provide observational predictions that would allow to discriminate between the different models, especially those that invoke planets. Several gaps can be generated by a single fixed planet (Zhang et al., 2018), by a single migrating planet (Wafflard-Fernandez & Baruteau, 2020, and chapter 6), but also by several fixed planets within them (NGNP model, see for example Lodato et al., 2019). Moreover, a single gap can be generated by several planets that have opened a common gap (see, e.g., Baruteau & Papaloizou, 2013). If we only look at the radial intensity profile of the dust continuum of a disk with substructures, it may seem impossible to discriminate which planetary mechanisms may be at the origin of radial variations in the intensity. However, one can be reassured by considering the multiplicity of observational tools at our disposal. For example, one can use several more or less optically thin observations to probe the emission at different altitudes in the disk. One can consider the azimuthal structure of the disks: are the sub-structures axisymmetric or localized? One can also for example analyze multi-wavelength observations to derive the spectral index. One can also use the large number of disks with annular substructures to see a possible temporal evolution of the substructures: do a bright crescent and an axisymmetric bright ring reflect the temporal evolution of the same substructure? It is certainly a possibility, as numerical simulations predict that dust vortices generally end up forming axisymmetric structures in the gas and the dust. Although all of these aspects obviously go hand in hand with observational biases, they can be used to portray the multiplicity of substructures from different angles, in order to catch both their generic and specific nature.

7.1 SPECTRAL INDEX AND DUST SIZE DISTRIBUTION

In chapter 6, synthetic maps of continuum emission have been computed at $\lambda = 1.3$ mm from the Pendragon simulation at 59900 years. We present in this section additional dust radiative transfer calculations, this time at $\lambda = 0.87$ mm. The aim is here to derive the spectral index α_ν (see Eq. 4 for the expression of the spectral index). We recall here that $\alpha_\nu = 2$ in an optically thick medium, and $\alpha_\nu = 2 + \beta_\nu$ in an optically thin medium, with β_ν the absorption opacity spectral index. The top panel of Fig. 7.1.1 shows the azimuthally averaged convolved intensity for $\lambda = 1.3$ mm (solid line) and $\lambda = 0.87$ mm (dashed line). Both synthetic profiles show radial variations, which indicate the presence of bright and dark rings (four bright rings encompassing three dark rings). By computing the spectral index α_ν in the middle panel of Fig. 7.1.1, we obtain its evolution as a function of the distance to the star. For the substructures in the inner disk (< 10 au), whether it be for the bright rings or for the dark rings, α_ν is close to 2, which in this case confirms the fact that the inner disk is optically thick, or marginally optically thick (see also the bottom-right panel of Fig.6.4.3, with

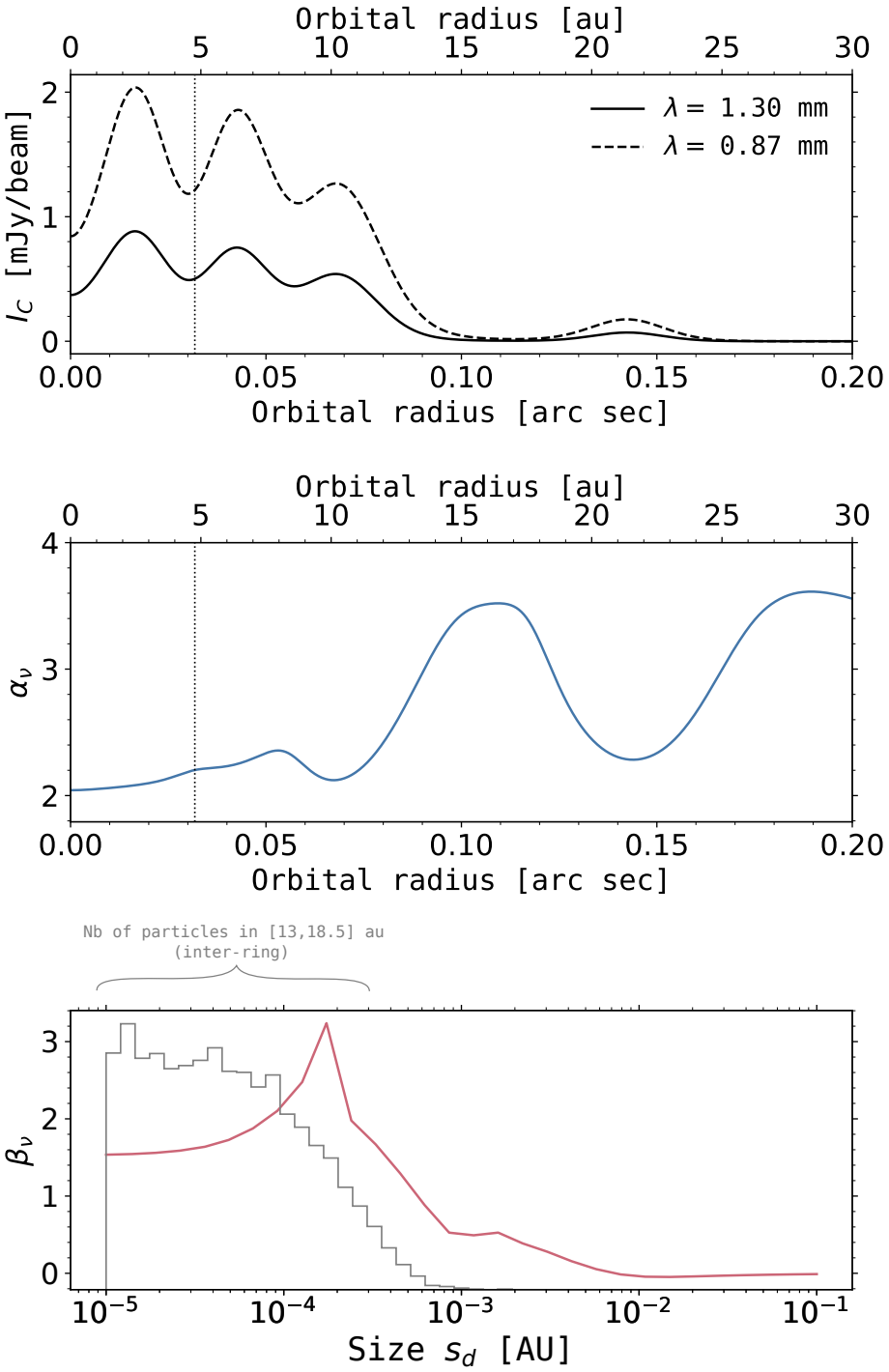

Figure 7.1.1: **Top panel**: azimuthally averaged convolved intensity as a function of the distance to the star in the Pendragon simulation, for the synthetic maps at $\lambda = 1.3$ mm (solid black line, same as in Fig. 6.4.3) and $\lambda = 0.87$ mm (dashed black line). **Middle panel**: spectral index (between 0.87 and 1.3 mm) $\alpha_\nu = \log\left(\frac{I_{1.3}}{I_{0.87}}\right) / \log\left(\frac{\lambda_{0.87}}{\lambda_{1.3}}\right)$ as a function of the distance to the star. **Bottom panel**: absorption opacity spectral index (between 0.87 and 1.3 mm) $\beta_\nu = \log\left(\frac{\kappa_{\nu,1.3}}{\kappa_{\nu,0.87}}\right) / \log\left(\frac{\lambda_{0.87}}{\lambda_{1.3}}\right)$ as a function of the particle size s_d. The gray histogram shows a normalized number of particles as a function of their size in the dark ring between 13 and 18.5 au. The vertical dotted line shows the location of the planet.

$\tau \gg 1$ in particular in the inner bright rings). For the outer disk, the analysis is a bit more complicated. In the bright ring at $\simeq$ 22 au, $\alpha_\nu \gtrsim 2$, whereas on both sides of the bright ring, α_ν is actually larger (up to $\sim$ 3.5). There are two possibilities. Either the medium is optically thick in the bright ring, which is marginally verified by an optical depth $\tau \sim 1$ (see again the bottom-left panel of Fig.6.4.3), near the location of the outermost bright ring, or the medium is optically thin and the spectral index provides valuable information on the size range of the particles that emit the most between 0.87 and 1.3 mm, via a value of β_ν close to zero. If $\beta_\nu \simeq 0$ in an optically thin medium, it suggests that the dust particles that dominate the emission are at least centimeter-sized particles. It is due to the fact that, for sufficiently large (spherical) particles, their absorption opacity does not depend on the wavelength of observation. This is actually what is shown in the bottom part of Fig. 7.1.1 for the evolution of β_ν as a function of the particle size, between 0.87 and 1.3 mm. The predominance of large ($\gtrsim$ cm-sized) particles in the outer ring is actually something we find in the Pendragon simulation at the time when the synthetic maps are computed (see the bottom-right panel of Fig. 6.4.1 and the space-time diagram in Fig. 6.4.2).

For a given particles composition with a given internal density, the spectral index gives a rough idea of the particle size distribution in an optically thin medium (outside the bright rings for example). On the one hand, the particles that dominate the emission at the center of dark rings (beyond 10 au) are such that $\alpha_\nu \simeq 3.5$, i.e. for $\beta_\nu \simeq 1.5$, which corresponds to particles typically smaller than 100 µm (red curve in the bottom part of Fig. 7.1.1). This size range of particles indeed predominates in the corresponding numerical simulation at the radial location of the dark rings. To be convinced of this, one can look at the gray histogram shown on top of the bottom part of Fig. 7.1.1 which shows a normalized number of particles as a function of their size within the radial interval [13-18.5] au, i.e. in the gap between the two outermost bright rings. This histogram shows a majority of particles with size < 100 µm in that region. Note that, unlike radiative transfer calculations which use a 'realistic' dust size distribution (see chapter 5), the one used in our numerical simulations is such that $n(s) \propto 1/s$, i.e. there is the same number of particles per logarithmically-spaced size bin. The absence of large particles in the gap therefore attests to a real deficit in this zone compared to the initial size distribution, and explains why α_ν is $\sim$ 3.5 around this location.

On the other hand, by gradually moving away from the dark rings to the edges of the bright rings (as long as the disk remains optically thin, see the variations of the optical depth in Fig. 6.4.3), one can also have a good idea of the particle size distribution in these transition zones. For example, between 16 au and 11 au, α_ν falls continuously from $\simeq$ 3.5 to $\simeq$ 2.2, i.e. β_ν falls continuously from $\simeq$ 1.5 to $\simeq$ 0.2. Using the red curve at the bottom of Fig. 7.1.1, this drop in the spectral index corresponds to a maximum dust size between a few 10^{-4} m at the center of the gap, to a maximum dust size larger than $\sim 10^{-2}$ at the edges of the bright ring around 11 au. Considering the dust spatial distribution in this area (between 16 au in the center of the gap and 11 au at the outer edge of the bright ring), we obtain as well a radial segregation of particle sizes similar to that estimated by looking at α_ν and β_ν. Fig. 7.1.2 shows the dust spatial distribution between the bright ring at $\sim$ 11 au and the center of the gap, with the mean size $\overline{s_d}$ of particles in that region (dashed black curve). To estimate

$\overline{s_d}$, we use the size distribution from the numerical simulation ($n(s) \propto 1/s$), define 50 bins of position and calculate the total number N_{tot} and mass M_{tot} of particles in each position bin. Using a mean internal density of $\rho_{int} = 2$ g.cm^{-3}, we can obtain $\overline{s_d} = \left(\frac{M_{tot}}{N_{tot}} \frac{3}{4\pi\rho_{int}}\right)^{1/3}$ in each position bin. In order to do that, we use a particle tracking method (see the methodology in section 7.7). It is just a post-processing of FARGO-ADSG output files in order to make the particles discernible and thus be able to track a group of particles subject to specific conditions.

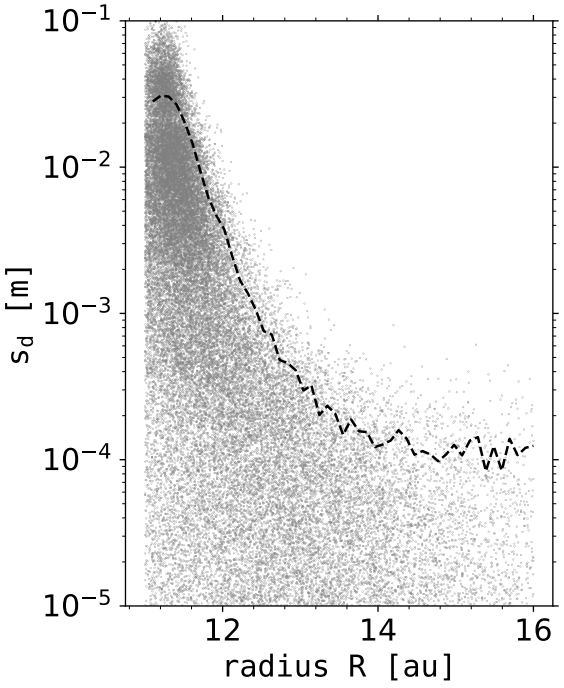

Figure 7.1.2: Dust spatial distribution between the edges of a bright ring (~ 11 au) and the center of a gap (~ 17 au), from the FARGO-ADSG output files. The dashed black line shows the mean particle size $\overline{s_d}$ in that region (see text). Large particles accumulate near the location of the bright ring, whereas the gap is filled with smaller particles ($< 10^{-4}$m).

We simply illustrate in Fig. 7.1.2 that large particles accumulate more efficiently at pressure maxima than smaller particles, which are more easily subject to turbulent diffusion (see, e.g., Ataiee et al., 2018). Laboratory experiments and cometary dust recovery allow to better determine dust grains properties (in particular their size distribution, their shape and their internal density). With a more thorough knowledge of these dust properties, it could be interesting to use the spectral index to better constrain the dust spatial distribution in protoplanetary disks. This would require the use of multi-wavelength observations, for example of the DSHARP sample at 0.87 mm. This kind of study requires a better understanding of the link between dust size distribution and spectral index, using simplified numerical simulations and radiative transfer calculations for example. A possible extension of this work would be to determine whether it is possible to derive the sharpness of the pressure maximum at the origin of particle accumulation, by considering the sharpness of the spectral index around a dark ring. Such study would be interesting to help discriminate between the various mechanisms able to generate one or multiple dust rings. As we discussed in chapter 6, the outer pressure maxima that result from an intermittent runaway migration are progressively smoothed out by turbulent viscosity, unlike the sharp pressure maxima at the outer edge of a massive planet. Note that, in addition to assumptions about the composition and properties of the emitting dust, this kind of study makes sense only if bright rings in disks reflect an actual accumulation of dust

particles. Furthermore, this type of measurement is particularly sensitive to the radial resolution and contrast sensitivity of the substructures in the disks. To demonstrate this beam size issue, Fig. 7.1.3 shows two spectral index maps, with a 0.″02 circular beam (left panel) and a 0.″01 circular beam (right panel). We can directly compare the spectral index map in the left panel of Fig. 7.1.3 with its radial profile in the middle panel of Fig. 7.1.1. This comparison demonstrates that the small variations of α_ν in the inner disk ($\alpha_\nu \simeq 2$ for $r < 10$ au) are in fact partially due to the beam dilution of the innermost bright rings in that region. From the high resolution map in the right panel of Fig. 7.1.3, we would indeed expect thin peaks of α_ν near the inner dark rings.

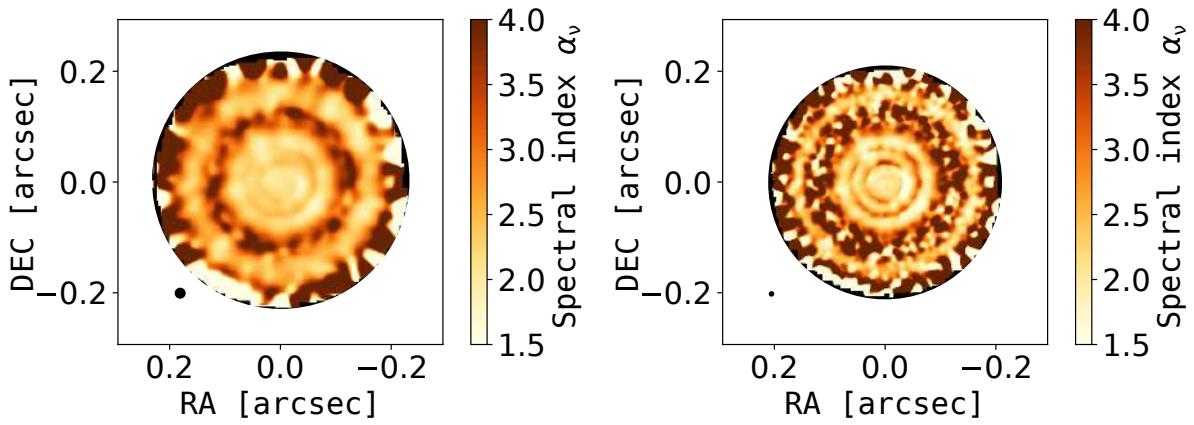

Figure 7.1.3: Spectral index α_ν maps between 0.87 and 1.3 mm from the Pendragon simulation for two beam sizes: a 0.″02 circular beam (**left panel**) and a 0.″01 circular beam (**right panel**).

7.2 SPOTLIGHTING THE TEMPORAL EVOLUTION OF SUBSTRUCTURES

As briefly discussed in section 4.2 with the example of disk vortices turned axisymmetric, substructures in protoplanetary disks result from dynamical processes in the dust and gas. They are therefore expected to evolve over time. We show in the left panels of Fig. 7.2.1 the dust continuum emission maps at 1.3 mm of three DSHARP targets, all of which harboring various substructures (Andrews et al., 2018; Huang et al., 2018a) : crescent-like and asymmetric structures (HD 143006, HD 163296), bright and dark rings (HD 143006, HD 163296, Elias 24) or diffuse rings (Elias 24). In the right panels of Fig. 7.2.1, the intermittent migration scenario described in length in chapter 6 comes back into play to unveil the temporal evolution of its substructures. The panels show indeed the results of the **same** simulation (Pendragon) at different times (after 327, 669 and 1122 planet orbits, that is after ~ 20000, ~ 60000 and ~ 100000 years) post-processed with dust radiative transfer calculations in order to follow the temporal evolution of substructures, like bright and dark rings. Recall that the inner part of the disk is not simulated, hence the drop of the intensity in the inner disk in all the synthetic dust continuum maps. Note also that the post-processing in these three synthetic maps is not exactly the same, in particular the disk inclination, the beam size, the level of noise, or the radial extent of the observational window.

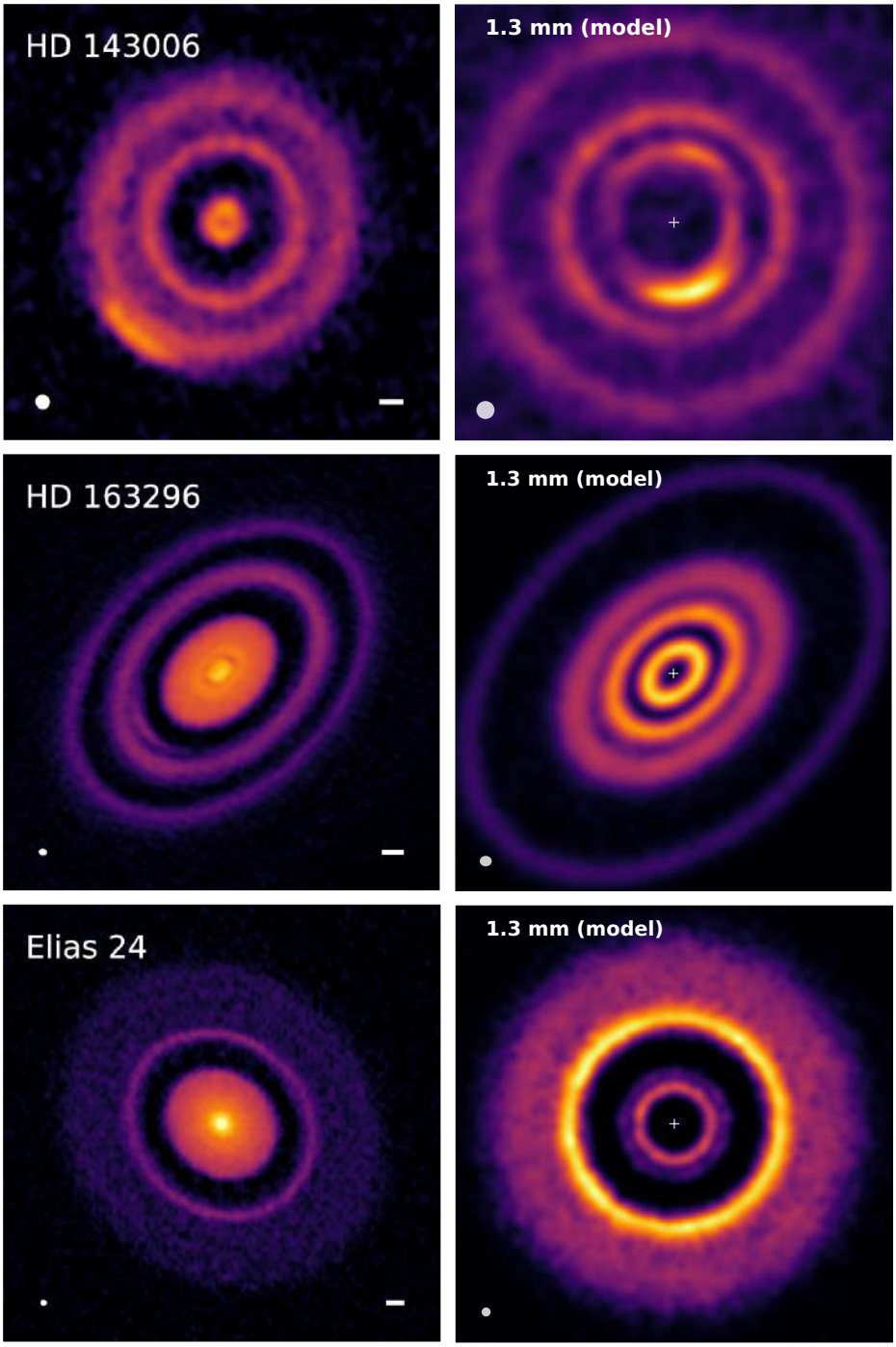

Figure 7.2.1: Left panels: dust continuum emission images for three disks in the DSHARP sample (top: HD143006, middle: HD163296, bottom: Elias 24), from Andrews et al. (2018). Right panels: synthetic maps of dust continuum emission calculated with `RADMC3D` from one **single** 2D gas+dust hydrodynamical simulation performed with `FARGO-ADSG`, but at different times (the Pendragon run presented in section 6.4). The right panels are arranged chronologically from top to bottom. Note that in the maps created by `RADMC3D` there are some small differences in the choice of the beam size, the noise level, and the disk inclination.

Here is a quick summary of what can be seen in the right panels of Fig. 7.2.1. A massive planet is able to form vortices and a dust concentration around its Lagrange points, which are local pressure maxima where large particles can be trapped. In particular, the bright asymmetric substructure in the top-right panel of Fig. 7.2.1 is due to a dust trapping in a Lagrange point, as we will see later in this section. The sequence of dark and bright rings in this panel is here due to the intermittent runaway migration of the planet, and is also present and even more visible in the middle-right panel of Fig. 7.2.1. All the asymmetries seen in this middle-right panel have become axisymmetric and form a multiple-ring system. Finally, in the bottom-right panel of Fig. 7.2.1, one of the pressure maxima triggered by one of the episodes of slowed migration, and causing a local dust accumulation, is progressively smoothed out by turbulent viscosity. As we have seen in chapter 6, this pressure maximum is no longer sustained by the planet which has migrated further inward in the disk. Dust trapping there is no longer as effective as before. Particles therefore begin to drift radially until they reach the next inward pressure maximum. The drift starts from the outermost diffuse ring, and the new accumulation of particles occurs in the brightest ring on this bottom-right panel.

Note that the aim of the synthetic dust continuum maps presented in the right panels of Fig. 7.2.1 is not to model specific observations, but rather to highlight some important planet-induced dust substructures that can also be visible in real dust continuum maps. The goal here is neither to call upon the intermittent migration scenario at every opportunity, but just to illustrate that the same mechanism can generate different substructures at different times. More precisely, the aim is here to use the knowledge provided by all or part of a specific mechanism to suggest physical interpretations to the observed substructures. Here are some examples.

- The **diffuse ring** beyond the bright ring in Elias 24 may be due to the viscous spreading of a pre-existing pressure maximum which is no longer able to efficiently trap particles. These particles then start to drift radially towards the next pressure maximum, closer to the star. It would actually be interesting for this disk to have a high resolution observation at a different wavelength in order to derive the spectral index and determine if a radial segregation of particle sizes is detectable between the bright ring and the diffuse ring (see section 7.1.1, and the space-time diagram of Pendragon in Fig. 6.4.2, at ~ 100000 years near 10 au). It is indeed expected that the largest particles (as long as $S_t < 1$) will drift first as the pressure maximum is progressively smoothed out by viscosity.

- **Azimuthal asymmetries**: if a planet is not massive enough, it will not be able to sustain long formation and presence of vortices. They will eventually form axisymmetric structures. For a given planet mass, the timescale over which vortices decay in 2D models depends in a complex way on the disk's physical properties. Besides the turbulent viscosity and the disk's aspect ratio, it also depends on radiative processes (Les & Lin, 2015), gas self gravity (Lin & Papaloizou, 2011) or dust backreaction (Fu et al., 2014). In any case, less massive planets are probably not ideal candidates to generate strong asymmetries in disks, since vortices related to their presence are expected to rapidly form axisymmetric structures. However, if planetary migration alternates between fast and slow

phases, this may change the situation. Numerous vortices are indeed created during each episode of rapid migration and are channeled towards the new outer pressure maximum generated by the planet during the subsequent episode of slow migration. Jolts in the planet migration, whatever their origin, can therefore easily be at the origin of vortices that are constantly regenerated.

- **Azimuthal asymmetries - other interpretation**: As we will see later in section 7.5, an azimuthal asymmetry close to a bright ring can be due to the emission of particles that are trapped in one of the Lagrange points of a (migrating) planet. In particular, we have noticed in numerous numerical simulations that the Lagrange point L5 (behind the planet in azimuth) efficiently traps large particles, whether the planet is migrating or not, and mostly independently of whether migration is directed inward or outward. Furthermore, if we take into account the radial asymmetry of the bright rings encompassing the planet's location, asymmetry that is related to the planet migration (see section 4.5), the asymmetries detected in HD 143006 and HD 163296 could be due to the emission of particles in L5 from an inward migrating planet and an outward migrating planet respectively (in one case, the asymmetry is closer to an inner ring, in the other to an outer ring). As stated earlier, this situation is in fact exactly what happens in the top-right panel of Fig. 7.2.1: the Neptune-like planet has entered an episode of slow inward migration that indirectly generates, in the planet's Lagrange point L5, this bright crescent-like structure close to an inner ring.

7.3 VELOCITY KINKS DUE TO THE PRESENCE OF A GIANT PLANET

This section presents results of gas radiative transfer calculations of a protoplanetary disk that features a massive planet. My aim was first to have a better understanding of how a massive planet generate velocity kinks in the channel maps of gas emission (see section 4.4.3), and then to explore the impact of planet migration on those velocity kinks. The methodology here is similar to the one presented in chapter 6: first we perform 3D numerical simulations with `FARGO3D`, then we carry out dust and line radiative transfer calculations in order to compute dust continuum emission maps and channel maps of the gas emission, but also gas intensity maps (0th moment, computed by integrating all the contributions from individual channel maps along the velocity axis) and intensity-weighted velocity maps (1st moment). The 0th and 1st moment maps are all integrated between $\Delta v = -4$ km/s and $\Delta v = 4$ km/s from systemic velocity, and sampled every 0.2 km/s. Moments of higher order (in particular the 2nd moment, i.e. the velocity dispersion map) can also be computed from the channel maps, but we only considered for now the intensity and velocity maps. The main fiducial parameters of the numerical simulations and radiative transfer calculations are presented in Table 7.3.1. These parameters are close to those used in Pinte et al. (2019) adapted for `FARGO3D` with a 5 $M_{\rm Jupiter}$ planet and different migration scenarios. Note that Pinte et al. (2019) performed their simulations with the `PHANTOM SPH` code.

For a 5 $M_{\rm Jupiter}$ planet on a fixed circular orbit, Fig. 7.3.1 displays the results of the radiative transfer calculations with `RADMC3D`. The top-left panel shows the dust continuum maps at $\lambda = 1.3$ mm, with a realistic $0''.11 \times 0''.07$ elliptic beam. Three bright

Parameter	Symbol	Value
Numerical simulations		
Code's unit of length	r_0	130 au
Code's unit of mass	$M_\star$	$2.4 M_\odot$
Initial Toomre parameter at r_0	Q	> 50
Self-Gravity	—	BMo8
Energy equation	—	No
Gas surface density at r_0 [code units]	Σ_0	10^{-3}
Gas surface density slope	σ	0.5
Disk's aspect ratio at r_0	h_0	~ 0.09
Flaring index	f	0.375
Alpha turbulent viscosity	α	10^{-3}
Planet to primary mass ratio	q_p	5×10^{-3}
Planet's initial location	$r_{p,o}$	$1.1 r_0 = 143$ au
—	$q/h^3(r_{p,o})$	~5.2
Number of dust fluids	`NFLUIDS`	4
Dust's size range	$\in [s_{min} - s_{max}]$	$\in [1\ \mu m - 1$ mm$]$
Dust size distribution	$n(s)$	$\propto s^{-3.5}$
Dust-to-gas mass ratio	μ_d	0.05
Dust's internal density	ρ_{int}	1.2 g cm^{-3}
Number of radial cells	N_r	300
Number of azimuthal cells	N_ϕ	200
Number of colatitudinal cells	N_θ	$20 - 40$
Dust radiative transfer		
Wavelength	λ	1.3 mm
Dust composition	—	30% silicates, 70% water ices
Scattering	—	discarded
Disk distance	d	185 pc
Disk inclination	i	40 deg
Stellar radius	$R_\star$	$2.25\ R_\odot$
Star effective temperature	T_{eff}	10000 K
Beam	—	$0\farcs11 \times 0\farcs07$
Line radiative transfer		
Gas molecules	—	^{13}CO, C^{18}O
Abundances	χ	7×10^{-5}, 7×10^{-7}, 2×10^{-8}

Table 7.3.1: Main fiducial parameters for the 3D numerical simulations, dust and line radiative transfer calculations presented in section 7.3.

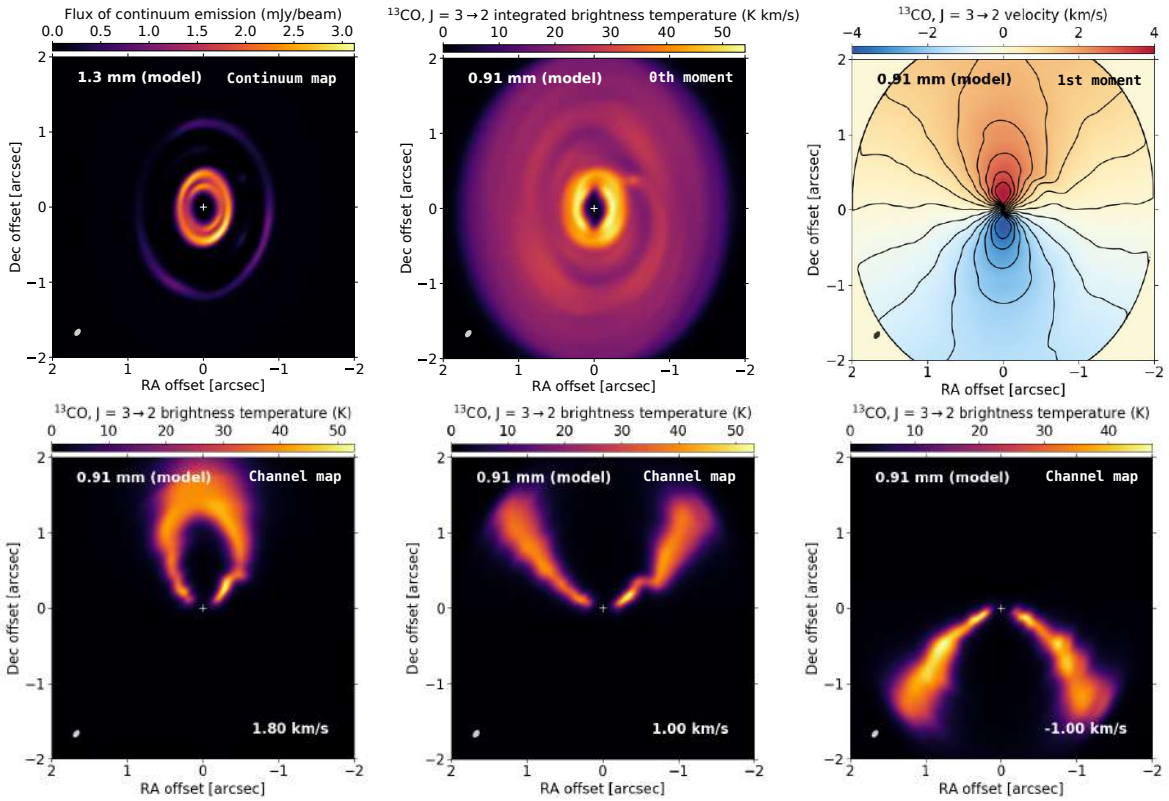

Figure 7.3.1: Results of 3D multifluid simulations with FARGO3D post-processed with RADMC3D, for a 5 $M_{Jupiter}$ non-migrating planet. **Top-left panel**: Synthetic flux map of the dust continuum emission at $\lambda = 1.3$ mm, convolved with a $0''.11 \times 0''.07$ elliptic beam. **Top-middle panel**: ^{13}CO J $= 3 \rightarrow 2$ synthetic intensity map (0th moment, in brightness temperature units). **Top-right panel**: Synthetic velocity map (1st moment) from ^{13}CO J $= 3 \rightarrow 2$ emission which shows perturbed non-Keplerian flows at RA $\simeq -1''$. The black curves show the isovelocity contours every 0.5 km/s. **Bottom panels**: ^{13}CO J $= 3 \rightarrow 2$ synthetic emission channel maps that show velocity kinks, in particular in the right wing at $\Delta v = 1.00$ km/s from systemic velocity, absent in $\Delta v = -1.00$ km/s.

rings of emission are detected: a faint external ring at the outer pressure maximum of the massive planet, and two close internal rings in the inner disk. The innermost ring may be due to the opening of a secondary gap (Zhang et al., 2015), or the inner boundary condition. More specifically, a maximum of dust density is formed in our simulation at ~ 52 au, just outside the inner wave-killing zone that extends from ~ 39 au to ~ 46 au, hence the uncertainty on the physical or numerical origin of this radial substructure. This dust ring gives then rise to the innermost bright ring visible in the continuum emission. During this step, the dust temperature T_d is computed from a thermal Monte-Carlo calculation. To compute the ^{13}CO J $= 3 \rightarrow 2$ moment maps for intensity (0th moment) and velocity field (1st moment) in the top-middle and top-right panels, we assume that the gas temperature T_g is equal to the dust temperature T_d, with $\chi_{^{13}CO} = 7 \times 10^{-7}$ (value chosen by Pinte et al. (2019)). Note that in the channel maps and the 0th moment maps, the convolved intensity I is displayed in terms of

'brightness temperature' T_B. The conversion between I and T_B is as follows (see also Eq. 1 in Boehler et al., 2017):

$$T_B = \frac{hc}{\lambda k_B} \frac{1}{\ln\left(1 + \frac{2hc}{\lambda^3 I}\right)}, \tag{111}$$

with λ the wavelength of observation. To convert between I and T_B with this formula, the convolved intensity I must be converted from Jy/pixel to erg.s^{-1}.cm^{-2}.Hz^{-1}.sr^{-1} using the solid angle subtended by one pixel.

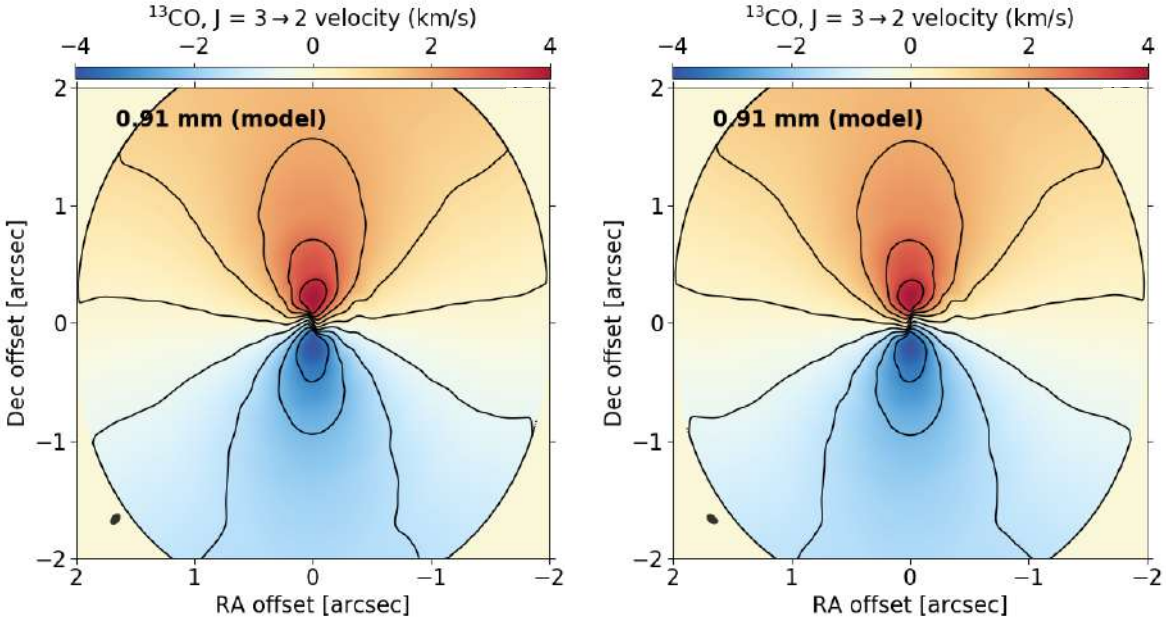

Figure 7.3.2: Synthetic velocity maps (1st moment) from ^{13}CO J = 3 → 2 emission. Between the two maps, the beam has been rotated by 90 degrees. The impact of the shape of the beam on the inner structures of the 1st moment is particularly visible close to the disk center.

What do we see in the 0th and 1st moment maps of Fig. 7.3.1? In the 0th moment map, one can guess the planet at RA offset $\simeq -0.5$, DEC offset $\simeq 0.5$, via the emission of its circumplanetary disk. One can also detect slight radial variations ($\sim$ 10%) in the integrated intensity, with a bright diffuse ring at the location of the outermost continuum ring, and a dark diffuse ring at the location of the gap carved by the planet. Note that the outer planet wake seems to be marginally visible, propagating from the point-like source to and through the bright diffuse ring. Regarding the 1st moment map, we see the dipole-like morphology which is characteristics of a nearly Keplerian structure in the disk. Two main non-Keplerian perturbations can be detected. First there is a tilt in the isovelocity contours near the disk center, and secondly there are 'wiggles' mainly visible in the right part of the panel, i.e. at RA offset < 0 and close to the planet. The wiggles in the isovelocity contours seem also to partly follow the location of the portion of the outer wake closest to the planet. Finally, the three channel maps in the bottom of Fig. 7.3.1 mostly show velocity kinks at $\Delta v = 1.8$ and $\Delta v = 1.0$ km/s from systemic velocity, at RA offset < 0 near the expected position of

the planet. The velocity kink is not clearly visible at $\Delta v = -1.0$ km/s, despite some slight perturbations in the Keplerian flow. In Fig. 7.3.2, we show that the tilt in the isovelocity contours near the disk center, visible in the 1st moment map of Fig. 7.3.1, is actually artificial and due to the shape of the beam. Because the beam is not circular but elliptic, we rotated the beam with different angles and noted its impact on the isovelocity contours close to the inner disk. In particular, the beam has been rotated by 90 degrees between the two 1st moment maps of Fig. 7.3.2, leading to a different tilt in the inner disk's isovelocity contours.

We present in Fig. 7.3.3 the impact of several parameters on the CO 0th moment maps and channel maps, in particular the assumption $T_g = T_d$, the CO-to-H_2 abundance ratio, and the choice of the isotopologue.

- The **second raw** in Fig. 7.3.3 is used as a reference and corresponds to the parameters chosen in Fig. 7.3.1: $T_g = T_d$ and $\chi_{^{13}CO} = 7 \times 10^{-7}$. All comparisons in this paragraph are made with respect to this reference.

- The **first raw** in Fig. 7.3.1 considers the impact of the choice of the gas temperature, in particular if we do not use the dust temperature but the hydrodynamical gas temperature directly given by `FARGO3D` output files. In our run, recall that the gas is supposed locally isothermal, therefore the gas temperature is fixed by the initial conditions: $T(r) \simeq 41\ \mathrm{K}\,(r/130\ \mathrm{au})^{-1/4}$. The assumption that we choose for the gas temperature does not seem to have a strong influence on the development of structures in the 0th moment and channel maps. The main difference is actually a global deviation of $\sim 20\%$ in the intensity (larger intensity for $T_g = T_d$). The deviation is even larger in the bright inner disk. This behavior is not clear, as it is not directly related to a similar deviation of the temperature, nor of the Planck function. In any case, the structure of the velocity kink in the channel map is not modified by our choice of how the gas temperature is computed in the radiative transfer calculations.

- In the **third raw**, the abundance of ^{13}CO is multiplied by 100, i.e. the number density of this gas molecule is 100 times larger. This is equivalent to artificially increasing the optical depth of the medium. It implies in practice that the CO emission comes from more superficial regions of the disk (see Fig. 1.2.3 for the contribution of more or less rare CO isotopologues in the zones of emission). In the 0th moment map, the radial variations in the intensity are weaker, which suggests that the ability of the planet to generate deficits and excesses in the ^{13}CO is in principle larger in the midplane than in the surface of the disk. The vertical structure of the disk is actually visible in the channel map, with the emission of both the front side and the rear side of the disk for a large ^{13}CO abundance. It is also possible that, because the optical depth is larger, we are more sensitive to variations in the gas temperature in the upper layers of the disk than variations in the CO density in the disk surface. Regardless of the abundance value, the velocity kink is clearly visible in both cases, with a more extended ^{13}CO emission for a larger $\chi_{^{13}CO}$.

- Finally, the **last raw** in Fig. 7.3.1 focuses on the emission of the rarer isotopologue C^{18}O, which is in principle sensitive to regions closer to the midplane, as

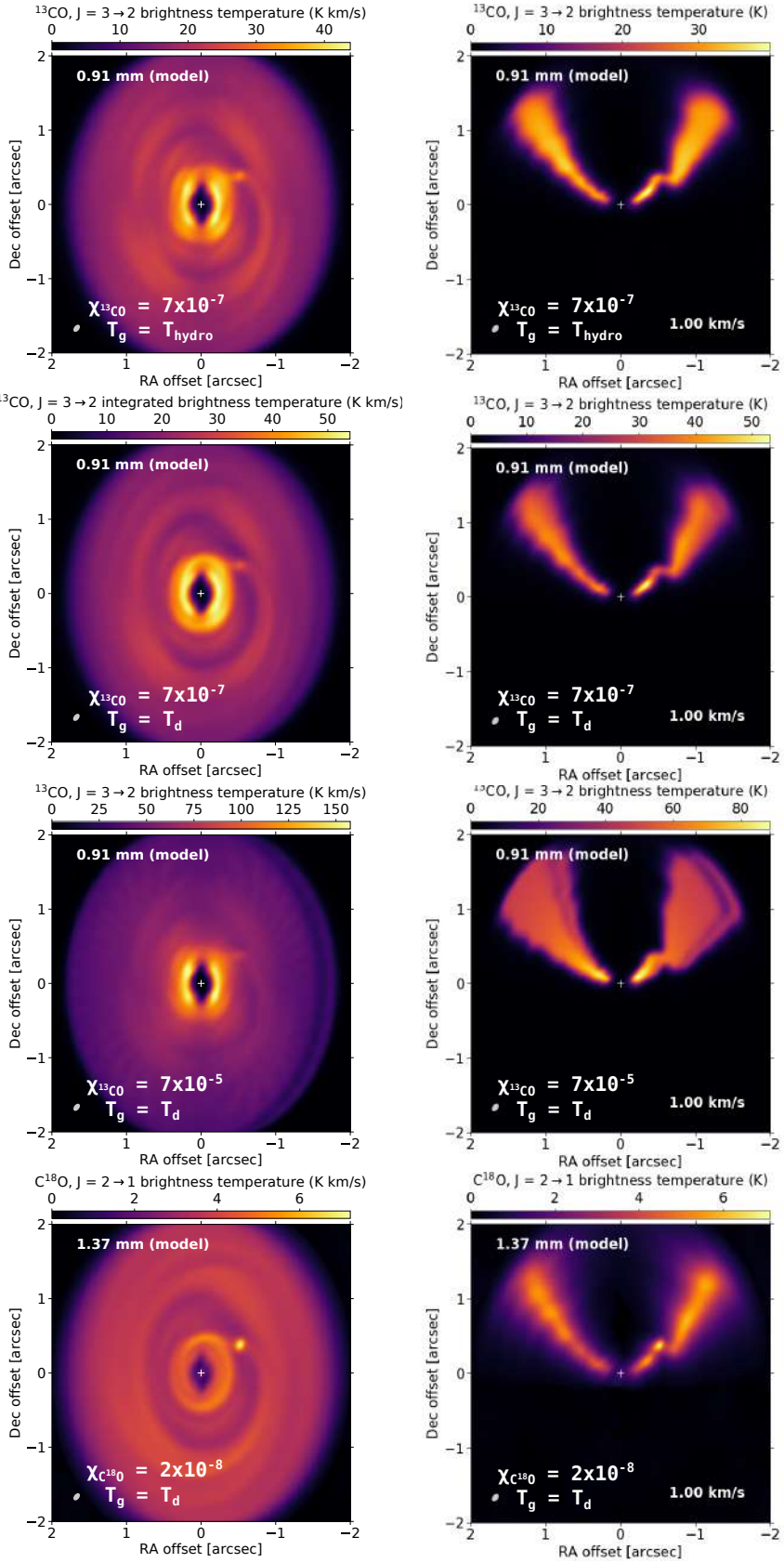

Figure 7.3.3: Collection of intensity maps (0th moment) and corresponding channel maps at $\Delta v = 1.00$ km/s. **First row**: we use the hydrodynamical temperature T_{hydro} as the gas temperature T_g to compute the ^{13}CO J $= 3 \rightarrow 2$ emission maps, with an abundance ratio $\chi_{^{13}CO} = 7 \times 10^{-7}$. **Second row**: we use this time the dust temperature T_d as the gas temperature. **Third row**: the only difference with the second row is that $\chi_{^{13}CO} = 7 \times 10^{-5}$, i.e. 100 times larger. **Fourth row**: we compute here the C^{18}O J $= 2 \rightarrow 1$ emission maps, with $\chi_{C^{18}O} = 2 \times 10^{-8}$ and $T_g = T_d$.

presented in Fig 1.2.3. We were focusing in the third raw on zones of emission in the surface of the disk, and we are here sensitive to zones of emission at lower altitudes, with steeper radial variations in the intensity and the presence of the velocity kink in the channel map. Note here the particularly strong emission of the circumplanetary envelope, both in the 0th moment map and in the channel map. Two important caveats are to be pointed out here for this kind of very optically thin emission maps. On the one hand, because the gas temperature is lower in the midplane, freeze-out onto dust grains can occur whenever the local gas (and dust) temperature falls below 19K. With $T_g = T_{hydro}$, the disk never reaches such a low temperature. Concerning the case $T_g = T_d$, $C^{18}O$ could indeed be subject to freeze-out in our simulation, but only in the outer disk (typically beyond 230 au). On the other hand, photo-dissociation by UV irradiation can also occur when the local gas column density falls below a certain threshold (Simon et al., 2015; Flaherty et al., 2017). In practice, these two phenomena reduce the abundance of the gas molecules and therefore their number density, which decreases the intensity of emission. Since the $C^{18}O$ emission flux is very weak and potentially very noisy (see the values of the integrated brightness temperature < 7Kkm/s) due to the scarcity of $C^{18}O$, taking into account these phenomena with a realistic noise level would make the emission maps even more noisy. The detection of circumplanetary emission is therefore more likely in the $C^{18}O$, but also more difficult to access because of this significant noise. Taking into account freeze-out and photo-dissociation is the next step to improve the models presented in this section.

In the next paragraph, we present a set of numerical experiments whose goal is to determine whether velocity kinks are rather due to velocity perturbations imparted by the planet wakes or by the circumplanetary flow. For the fiducial simulation of this paragraph, the main parameters are presented in Table 7.3.1. In addition to these parameters, the planet can freely migrate in the disk, and we adopt a turbulent velocity of $v_{turb} = 50$ m/s in the line radiative transfer calculations. It is actually a larger value than expected (Flaherty et al., 2015) given the choice of α in the simulation, set to 10^{-3}:

$$v_{turb}(r_0) = h_0\sqrt{\alpha}\sqrt{\frac{GM_\star}{r_0}}. \tag{112}$$

For the parameters in Table 7.3.1, this expression corresponds approximately to $v_{turb} \simeq 10$ m/s at 130 au.

The procedure to determine the origin of velocity kinks is simple. We start from the FARGO3D output files, in particular the gas velocity fields v_r, v_ϕ and v_θ. Just before any line radiative transfer calculations, we modify these velocity fields by azimuthally averaging specific zones in the disk. The aim is to determine which area contributes most to the development of velocity kinks, whether it be the circumplanetary system or the planet wakes. This averaging procedure artificially enhances some structures in the velocity fields by smoothing out other structures. Fig. 7.3.4 illustrates eight different cases with the corresponding channel maps, labeled from a to h. The gray shapes picture the zones where the velocity fields are azimuthally averaged.

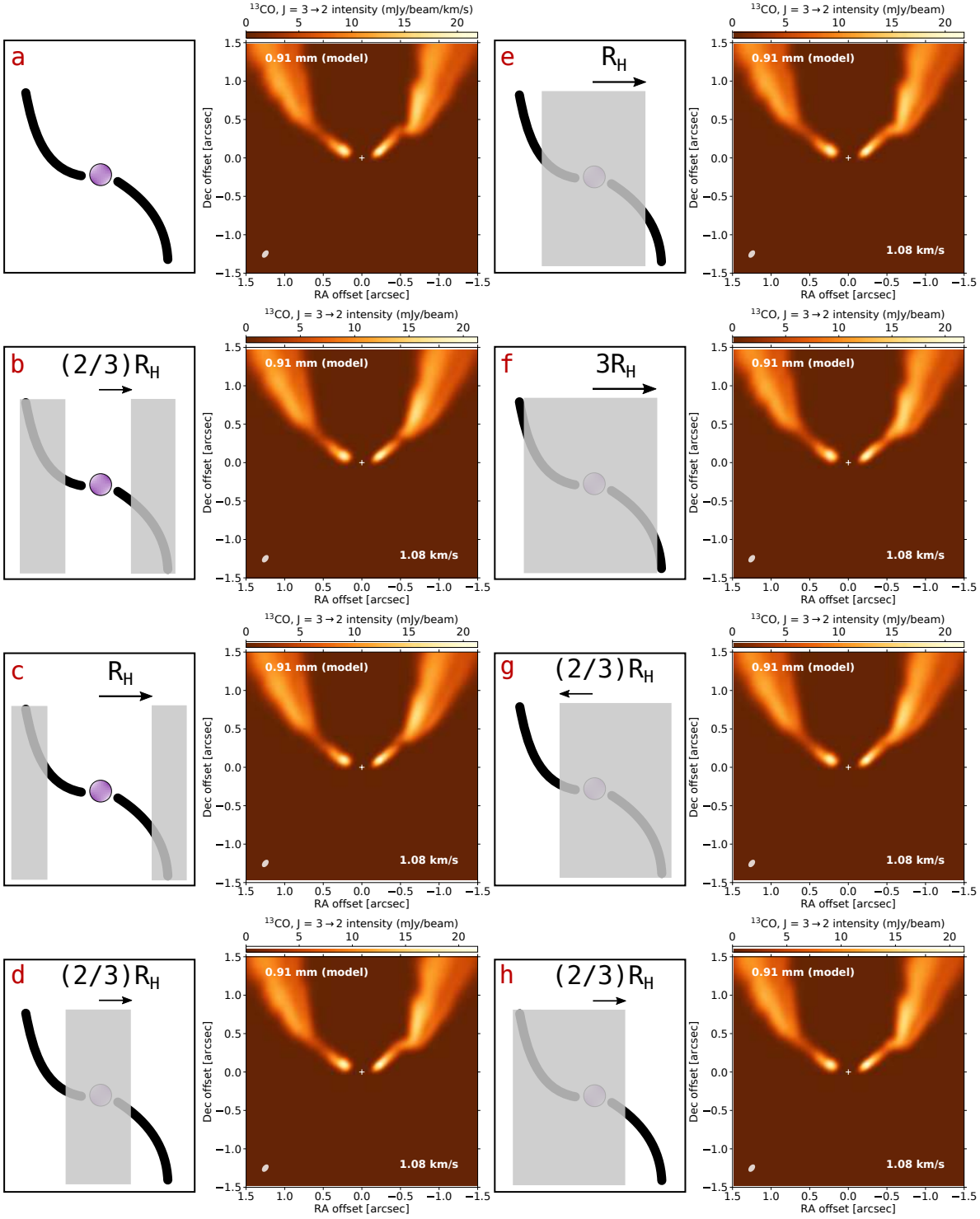

Figure 7.3.4: Eight sketches which represent numerical experiments, with corresponding ^{13}CO J = 3 → 2 synthetic emission channel maps. In all cases, the planet can freely migrate in the disk. Each sketch can be associated with the channel map directly to its right. In the sketches, the purple circle represents the planet with eventually its circumplanetary disk. The thick black lines propagating from the planet represent the inner and outer planet wakes. The gray translucent rectangles represent areas in the simulated disk where we azimuthally average the gas velocity fields ($v_{g,r}$, $v_{g,\phi}$ and $v_{g,\theta}$) in order to artificially enhance different asymmetrical structures in these fields. R_H is the Hill radius of the planet. See body of the text for the analysis and more details about the procedure.

- **Panel** a: reference channel map which shows a strong velocity kink in the right wing at RA $\mathrm{offset} < 0$ and DEC $\mathrm{offset} \simeq 0.4$. There is a strong asymmetry between the left wing of emission and the right wing of emission. From this channel map, it is difficult to disentangle the contribution of the circumplanetary system and the planet wakes.

- **Panel** b: the velocity fields for the regions beyond $(2/3)R_H$ from the planet are azimuthally averaged, with R_H the Hill radius of the planet defined in Eq. 78. We are therefore focusing on the impact of velocity perturbations close to the planet (in particular the circumplanetary system). By looking at the corresponding channel map, we find that the velocity kink is almost absent (compared to panel a just above). To be convinced of this, one can also compare in panel b the left wing of emission with the right wing of emission: the two wings are almost symmetrical. It seems to suggest that planet wakes are responsible for the velocity kink.

- **Panel** c: this panel is quite similar to panel b, but this time the velocity fields are azimuthally averaged for regions beyond R_H from the planet. We thus focus on a slightly larger region around the planet's radial location. We obtain a similar result, without a clear detection of velocity kink.

- **Panel** d: this case is the opposite of panel b, i.e. we focus on the planet wakes by smoothing out the contribution of the regions close to the planet ($< (2/3)R_H$). Because we recover the velocity kink, it suggests that planet wakes are responsible for it.

- **Panel** e **and** f: now that we know the importance of planet wakes, increasingly larger regions are averaged (respectively inside R_H and $3R_H$). We find from panel d to panel f that the velocity kink is less and less visible. It suggests that the main contribution from the planet wakes are relatively close to the planet, where their perturbations on fluid elements are stronger.

- **Panel** g: we this time focus on the inner wake ($> (2/3)R_H$ from the planet), by averaging both the circumplanetary system and all the outer disk. The impact of the outer planet wake is therefore smoothed out as well. Compared to the original velocity kink in panel a, we do not find clear evidence of a velocity kink here.

- **Panel** h: we finally focus on the impact of the outer wake ($> (2/3)R_H$ from the planet) by averaging everything else, and we retrieve the detection of the velocity kink, by comparing with the channel map in panel a.

From the numerical experiment presented in Fig. 7.3.4, we propose that the main contribution to the velocity kinks in our disk model and numerical setup comes from the outer planet wake. Furthermore, fluid elements are increasingly perturbed by the planet's outer wake when they are closer to the planet. Besides the inclusion of freeze-out and photo-dissociation that can potentially affect CO emission regardless of the chemical abundance, other improvements are possible and have to be considered later

on. For example, it could be interesting to consider the effect of dust scattering, in order to estimate slightly more accurately the dust temperature in our disk model. Moreover, note that the grid resolution does not properly resolve the circumplanetary disk flow. A higher resolution may show higher velocity perturbations in the circumplanetary flow and thus a visible effect on the velocity kinks. One of the possible projects concerning velocity kinks is to consider the impact of a potential vortex at the outer edge of a planet gap. Such problem has recently been studied by Robert et al. (2020) via 2D hydrodynamical simulations and idealized line-of-sight velocity maps. It would be interesting to analyze it with 3D numerical simulations and 3D radiative transfer calculations, specifically in the channel maps of the gas emission. In addition, several simulations with different migration scenarios are in progress, in particular a forced inward migration and a forced outward migration. The aim is indeed to consider the impact of planet migration on the structure of velocity kinks, even if it could probably face strong resolution issues.

7.4 ORBITAL EVOLUTION OF AN OUTER LOW-MASS PLANET IN A DISK WITH PRE-FORMED ANNULAR SUBSTRUCTURES

We have seen in chapter 6 the impact of a rather massive planet on its environment, in particular on the formation of multiple dust related to the formation of multiple pressure (or inverse vortensity $\mathcal{I}_\mathcal{V}$) maxima. We are now interested in the impact of these structures, in particular the $\mathcal{I}_\mathcal{V}$ maxima, back on the orbital evolution of outer, low-mass planets (typically $< 16\ M_{Earth}$). The scenario is as follows: after the intermittent migration of a Saturn-like planet, a low-mass planet forms far away in the disk. What is its orbital evolution near an $\mathcal{I}_\mathcal{V}$ maximum? The objective is actually more general, as we want to assess the impact of any $\mathcal{I}_\mathcal{V}$ maximum in a disk, whatever its origin. Note however that this study focuses on an $\mathcal{I}_\mathcal{V}$ maximum that is not sustained by a nearby massive planet.

To do so, we use the parameters of the fiducial case 'Pendragon' presented in chapter 6, and we include a new planet in the outer disk after the migration of the Saturn-like planet. We choose three different planet masses (2,8 and 16 M_{Earth}) initially located beyond the outermost $\mathcal{I}_\mathcal{V}$ maximum at ~ 24 au. The outer planet can freely migrate in the disk. Because we consider a low-mass planet, it is expected to be in a Type-I migration regime. Note that 16 M_{Earth} actually correspond to 1 $M_{Neptune}$. In addition to the planet mass, we also vary α between two values: 10^{-5} and 10^{-4}.

Fig. 7.4.1 shows the time evolution of the planet's semi-major axis for these three values of planet mass and two values of α turbulent viscosity. We find that, regardless of α, all the planets are initially in a phase of fast inward migration. The initial migration rate actually increases with the planet mass. This is expected, because the torques at the origin of Type-I migration (see section 3.3.1) scale with the square of the planet mass ($\propto q_p^2$). Then, whatever the planet-to-star mass ratio q_p and α, planets have their migration stalled, or nearly stalled, when they reach the radial location of the outermost $\mathcal{I}_\mathcal{V}$ maximum. It seems to suggest that $\mathcal{I}_\mathcal{V}$ maxima are planet traps, as long as the planet is not too massive to perturb the background disk. Moreover, the planet trapping is more efficient when the turbulent viscosity is weaker. Within 0.1

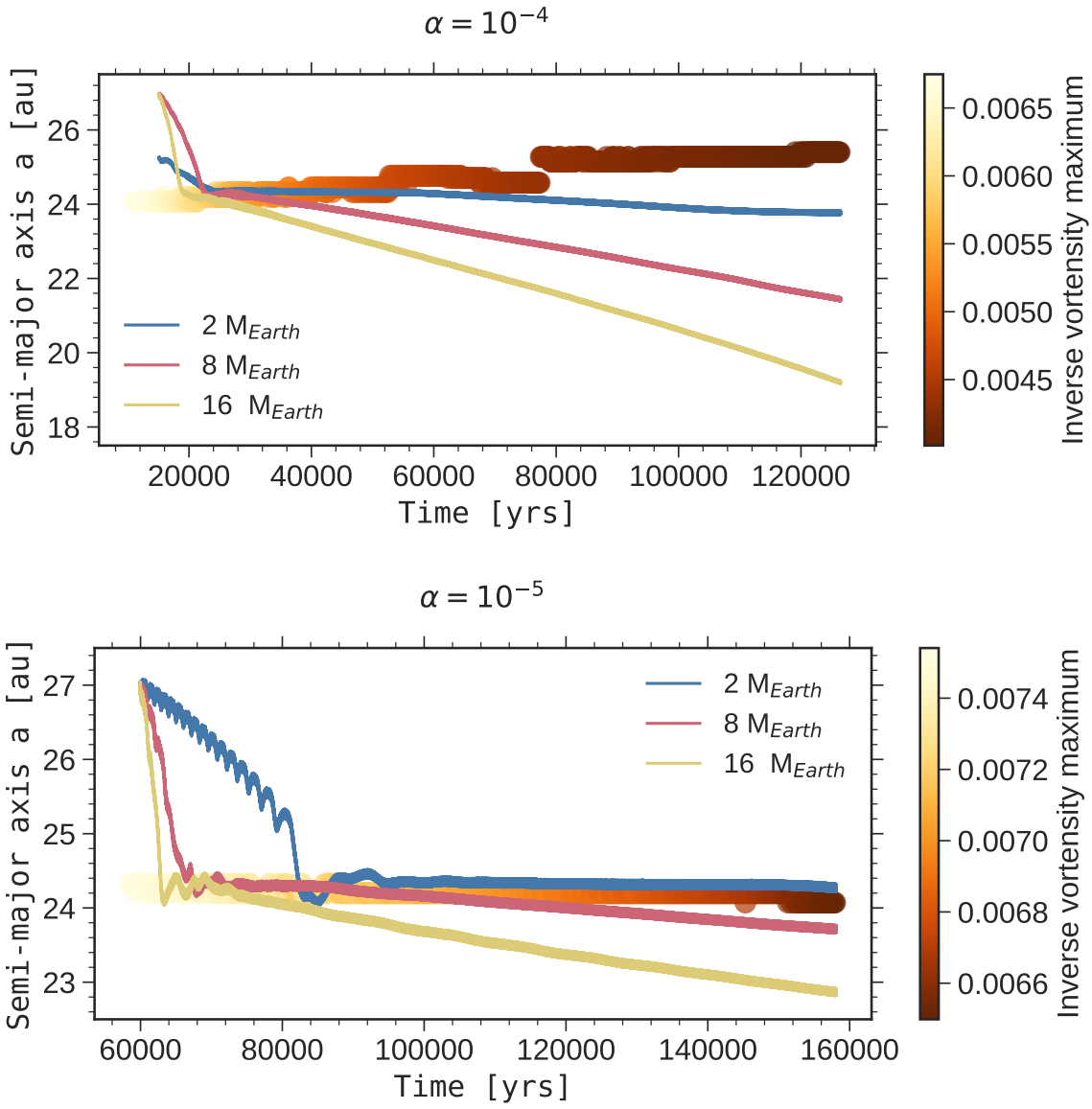

Figure 7.4.1: Time evolution of the planet's semi-major axis for a second planet included initially beyond the outermost $\mathcal{I}_\mathcal{V}$ maximum in the Pendragon simulation (see section 6.4). Three values of planet mass are considered (2 M_{Earth} for the blue curves, 8 M_{Earth} for the red curves and 16 M_{Earth} for the yellow curves) and two values of the α turbulent viscosity ($\alpha = 10^{-4}$ for the **top panel** and $\alpha = 10^{-5}$ for the **bottom panel**). In both panels, the colored circles show the radial location, and value of the outermost $\mathcal{I}_\mathcal{V}$ maximum. A brighter color pinpoints a stronger $\mathcal{I}_\mathcal{V}$ maximum.

Myrs, planets migrate inward by no more than 5 au (top panel of Fig. 7.4.1, yellow curve) for the $\alpha = 10^{-4}$ case and the most massive planet, with almost no migration for the 2 M_{Earth} planet (top panel of Fig. 7.4.1, blue curve). Regarding the $\alpha = 10^{-5}$ case and on the same timescale, planets move less than 1 au inward (bottom panel).

To better grasp why the low-mass planets are trapped at or near inverse vortensity maxima, one can consider Eq. 18 of Paardekooper (2014) (see also the expression of the coorbital vortensity deficit in Eq. 105 of section 6.3.1), which gives the expression of

the dynamical corotation torque for low-mass planets. This torque strongly depends on the inverse vortensity gradient and the migration rate $\dot{a}$, as it is proportional to $(\delta\mathcal{I})\,\dot{a} \equiv \left(1 - \frac{\mathcal{I}_{\mathcal{V}\mathrm{lib}}}{\mathcal{I}_{\mathcal{V}e}}\right)\dot{a}$, with $\mathcal{I}_{\mathcal{V}\mathrm{lib}}$ the averaged inverse vortensity in the corotation region, and $\mathcal{I}_{\mathcal{V}e}$ the inverse vortensity of the material near the separatrix (inner separatrix for an inward migration). Starting from this equation, two cases can be identified.

- if $\mathcal{I}_{\mathcal{V}\mathrm{lib}} < \mathcal{I}_{\mathcal{V}e}$: the low-mass planet migrates towards higher values of $\mathcal{I}_{\mathcal{V}}$, that is to say it migrates towards an $\mathcal{I}_{\mathcal{V}}$ maximum. In that case, $\delta\mathcal{I} > 0$ and the dynamical corotation torque has the same sign as the migration rate $\dot{a}$. It corresponds to a positive feedback (which accelerates migration). Note that we clearly observe in the top panel of Fig. 7.4.1 ($\alpha = 10^{-4}$ case) a slight acceleration of the planet migration as the planet gets closer to the $\mathcal{I}_{\mathcal{V}}$ maximum, i.e. when the $\mathcal{I}_{\mathcal{V}}$ gradient gets higher.

- if $\mathcal{I}_{\mathcal{V}\mathrm{lib}} > \mathcal{I}_{\mathcal{V}e}$: for example, the planet is located at the radial location of an $\mathcal{I}_{\mathcal{V}}$ maximum and migrates towards regions with lower values of $\mathcal{I}_{\mathcal{V}}$. In that case, $\delta\mathcal{I} < 0$ and the dynamical corotation torque acts against migration (the dynamical corotation torque and the migration rate have opposite signs). It corresponds to a negative feedback which impedes the migration. It is actually what we see in Fig. 7.4.1 when the planets reach the $\mathcal{I}_{\mathcal{V}}$ maximum and start to migrate in a negative $\mathcal{I}_{\mathcal{V}}$ gradient (in the sense that $\mathcal{I}_{\mathcal{V}e} - \mathcal{I}_{\mathcal{V}\mathrm{lib}}$ is negative).

Turbulent viscosity has two closely linked consequences. On the one hand it smooths out any radial perturbation in the disk, on the other hand it is the cause of an outward radial drift (viscous drift) of $\mathcal{I}_{\mathcal{V}}$ maxima. These two phenomena are all the faster and stronger as α is large. For $\alpha = 10^{-5}$, the outermost $\mathcal{I}_{\mathcal{V}}$ maximum stays approximately at $\sim$ 24 au, and its value decreases only by $\sim$ 15% in 0.1 Myrs. On the contrary, for $\alpha = 10^{-4}$, the outermost $\mathcal{I}_{\mathcal{V}}$ maximum radially drifts to $\sim$ 25.5 au, and its value decreases by $\sim$ 40% in 0.1 Myrs. This behavior is particularly visible in the top panel of Fig. 7.4.1 with the ocher colormap that shows the space-time diagram of the outermost $\mathcal{I}_{\mathcal{V}}$ maximum. Once a planet is trapped close to an $\mathcal{I}_{\mathcal{V}}$ maximum, it slowly continues to migrate inward (depending on the disk and planet properties). If the $\mathcal{I}_{\mathcal{V}}$ maximum is drifting outwards while being less and less intense, the planet evolves in areas where the $\mathcal{I}_{\mathcal{V}}$ gradient is less and less negative (in the sense that the difference between $\mathcal{I}_{\mathcal{V}e}$ and $\mathcal{I}_{\mathcal{V}\mathrm{lib}}$ is less and less negative), which is supposed to decrease the impact of the negative feedback and gradually speeds up the migration. For the rather low values of α presented here, this trend is visible for the most massive planets but is not dominant, and we mainly see the strong slowdown of planet migration by the presence of this sharp $\mathcal{I}_{\mathcal{V}}$ maximum.

Note that a more massive planet has a stronger impact on its environment, and in particular on the inverse vortensity profile. The evolution of the $\mathcal{I}_{\mathcal{V}}$ maximum presented in the two panels of Fig. 7.4.1 has been computed for the least massive planet. Things are actually a bit different for the most massive planet. In particular, as the planet's migration rate is reduced, we notice that the $\mathcal{I}_{\mathcal{V}}$ maximum slowly drifts along with the planet. More specifically, the 16 $M_{\mathtt{Earth}}$ planet gradually spreads $\mathcal{I}_{\mathcal{V}}$

maximum as it slowly migrates. We also noticed in the $\alpha = 10^{-5}$ case the presence of a vortex that interacts with the planets during their initial type-I migration. This interaction is particularly visible in the blue curve (2 M_{Earth}) of the bottom panel of Fig. 7.4.1, with the oscillations in the planet's orbital motion between $\sim$ 60000 and$\sim$ 80000 years. When the planet reaches the location of the $\mathcal{I}_\mathcal{V}$ maximum, the vortex performs multiple secondary U-turns in the planet's horseshoe region. Each outward/inward secondary U-turn leads to a positive/negative corotation torques that makes the planet oscillate around the radial location of the $\mathcal{I}_\mathcal{V}$ maximum. The planet eventually cohabits with the vortex, but in phase opposition (i.e. the azimuthal location of the vortex seems to be shifted by π compared to the azimuthal location of the planet.) This behavior has previously been seen in Ataiee et al. (2014).

There are several interesting implications to these $\mathcal{I}_\mathcal{V}$ planet traps.

- If there is an $\mathcal{I}_\mathcal{V}$ maximum without planet-planet interaction (no massive planet nearby), the inward migration of a low-mass planet is slowed down or halted at the vicinity of this $\mathcal{I}_\mathcal{V}$ maximum. It may favor rapid planet growth, given the presence of a dust ring close to this radial location. These dust particles are trapped in a pressure maximum which is also subject to turbulent viscosity (smoothing out and slow inward drift). This slow radial drift of the dust is interesting, because particles drift towards the same direction as the slow migration of a low-mass planet in a negative $\mathcal{I}_\mathcal{V}$ gradient, further extending the time of interaction between planet and dust. With this scenario, a bright ring in the continuum emission could actually hide the presence of a low-mass planet, contrary to the classical picture of a dark ring hosting a massive planet.

- One can also consider this $\mathcal{I}_\mathcal{V}$ planet trap from another perspective. We know that there is a strong link between dust trapping pressure maxima and inverse vortensity maxima (Casoli & Masset, 2009). If planetary formation takes place in a dust ring, then it means that a planet forms near the radial location of an $\mathcal{I}_\mathcal{V}$ maximum. This planet will therefore not migrate (or not much) until it has reached a mass sufficient to generate strong structures in the gas (partial gap, shock wakes,...) that will trigger a faster migration. It can considerably increase planetary formation timescale and potentially favor the formation of gas giants, which starts typically when protoplanetary cores reach $\sim$ 10 M_{Earth} (though it also depends on the Rosseland mean opacity and the accretion rate of solids (Ikoma et al., 2000; Lissauer & Stevenson, 2007). An interesting study would be to investigate planetary formation and migration at the vicinity of a dust ring and an $\mathcal{I}_\mathcal{V}$ maximum, and in particular under which conditions $\mathcal{I}_\mathcal{V}$ planet trapping takes place (for instance the impact of the disk mass, the aspect ratio, the energy equation, in 2D and 3D numerical simulations).

One of the objectives of my future postdoctoral work (MHDiscs project, IPAG) is to study the evolution of planets in a disk with MHD winds, and to predict observational signatures of this planet-disk-wind interaction. The results of Béthune et al. (2017); Riols & Lesur (2019); Riols et al. (2020) show that dust particles can accumulate near pressure maxima generated via a wind instability. I expect that $\mathcal{I}_\mathcal{V}$ maxima are associated with these pressure maxima, and that the migration of a low-mass planet

can be hindered by such structures in the disk. It will be the opportunity to verify this statement in a disk whose radial perturbations are not due to planets but to other physical processes.

7.5 DUST DYNAMICS AND EMISSION AT THE LAGRANGE POINTS OF A MIGRATING PLANET

The main motivation behind all the simulations presented in this section was initially to investigate the differences between the formation of multiple dust rings by the NGNP scenario (N Gaps N Planets, see section 4.3.2) and by the intermittent migration of a single massive planet. We focus on the Pendragon simulation, in which three dark rings form before the pressure maxima triggered by the intermittent migration pattern get smoothed out by turbulent viscosity ($\alpha = 10^{-4}$, see section 6.4.2). The goal was therefore to carry out numerical simulations with three planets on fixed circular orbits at the same location as the three aforementioned dark rings (namely at $R \sim 5$, ~ 9 and ~ 16 au), and to investigate the differences between the NGNP model and the intermittent runaway migration scenario. Note that the idea was to reuse the exact same parameters for the disk model (initial gas surface density profile, aspect ratio, α, ...), and just vary the mass of the three fixed planets such that they open annular gaps in the disk gas around their orbit with similar depths and widths as the gaps in the Pendragon simulation. However, in the 2D numerical simulations performed with `FARGO-ADSG`, we noticed that the planets do not efficiently clear their coorbital region, even for 1 M_{Jupiter} planets. Dust particles tend indeed to be trapped in one or both of the planets' Lagrange points. This is one major difference between the NGNP and the intermittent migration scenarios. The problem is thus the following: can we detect planets' Lagrange points in the dust thermal emission? What is the impact of planet migration on the dynamics and the possible emission of Lagrange points?

The parameters of the numerical simulations presented here are rather close to the ones used in chapter 6 for the Pendragon fiducial case (see Table 6.1.1 and Table 6.4.1). The main difference is the dust's initial location, here in a large band around the planet between 6 and 32 au, and the fact that the 1.5 M_{Saturn} planet is forced to migrate at a fixed migration rate. Several migration scenarios are considered here: inward migration ($\dot{a} = -17.6, -5.8, -1.7, -0.4$ m/s), no migration ($\dot{a} = 0$ m/s) and outward migration ($\dot{a} = 0.4, 1.7, 5.8, 17.6$ m/s). Some of these simulations were actually used in Fig. 3.3.3 (section 3.3.2) to highlight the impact of planetary migration on the carving of a gap in the gas of a protoplanetary disk. The dust spatial distribution obtained in the simulations are then post-processed with `RADMC3D` to produce synthetic flux maps of continuum emission at $\lambda = 1.3$ mm according to the procedure detailed in section 5.2.1. The main parameters of the dust radiative transfer calculations are summed up in Table 6.3.2. We use 10^8 photon packages for the thermal Monte-Carlo and ray-tracing calculations.

Fig. 7.5.1 shows the maps of dust continuum emission for these nine migration scenarios. The time in orbits is indicated in each panel, and is constrained by the migration speed of the planet. The case without migration is displayed in the center of the figure, the others are distributed around it (the migration rate is indicated

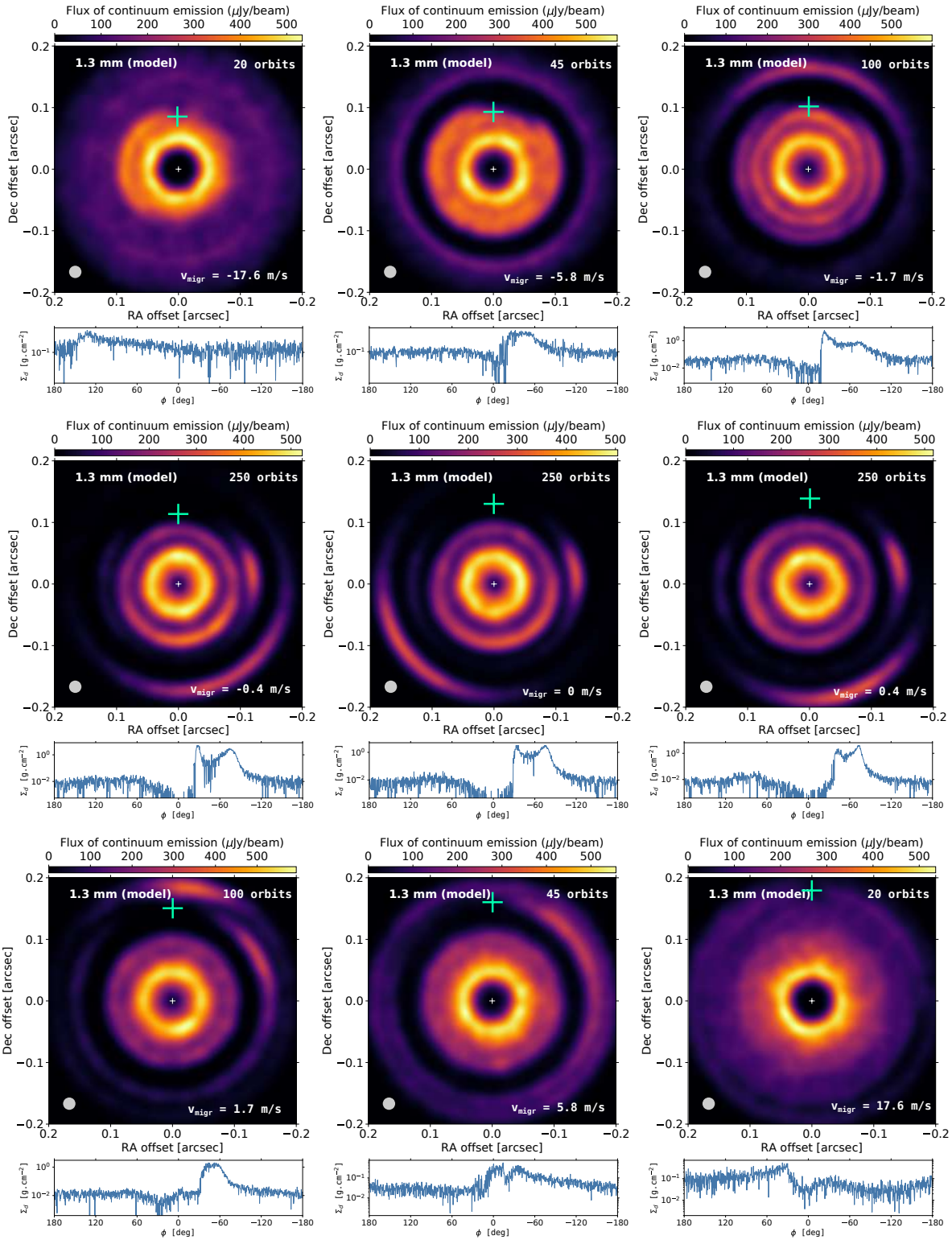

Figure 7.5.1: Results of numerical simulations and dust radiative transfer calculations. Each panel shows the continuum maps at 1.3 mm for different migration scenarios: inward migration at different migration rates (−17.6, −5.8, −1.7 and −0.4 m/s), no migration and outward migration (0.4, 1.7, 5.8 and 17.6 m/s). The turquoise cross marks the position of the Saturn-like planet. Each map of continuum emission is associated with a blue curve which shows the dust density averaged radially in the corotation region as a function of the azimuthal angle. The Lagrange point L5 is such that $\phi < 0$, whereas the Lagrange point L4 is such that $\phi > 0$.

in the bottom-right corner of each panel). Below each continuum map, we display the radially-averaged dust density in the corotation region (between $r_p - x_s$ and $r_p + x_s$, with x_s the half-width of the planet's horseshoe region) as a function of the azimuthal angle ϕ, assuming a dust size distribution $n(s) \propto s^{-3.5}$ and a total dust mass $M_{dust} = 10^{-2}\ M_{gas}$. Several features can be stressed out.

Radial asymmetry: we find again the radial asymmetry between the inner, coorbital and outer rings relative to the planet's radial location (as pointed out in section 4.5 and studied in Weber et al. (2019); Pérez et al. (2019)). It is even more visible in Fig. 7.5.2 with the polar deprojection of three synthetic maps after 100 planet orbits, in the cases $v_{migr} = -1.7, 0, 1.7$ m/s. The planet location is pinpointed with the turquoise cross, and defines the coorbital ring in each panel. The three rings are marked with horizontal dashed lines. Their mutual separation is approximately symmetric for $v_{migr} = 0$ m/s and asymmetric in the two other cases, with the coorbital ring closer to the inner (outer) ring for an inward (outward) migration. Note that the location of the two rings at the edges of the corotation region slightly depends on the scenario, as they marginally follow the direction of planet migration. In addition to this radial asymmetry, the inner and outer rings are less sharp and intense in the dust continuum maps if the planet migrates faster. It is due to the fact that the planet wakes of a fast migrating planet are not as efficient at carving gaps and pressure bumps as the planet wakes of a non-migrating planet, owing to the cumulative effect presented in section 6.3.1. We already mentioned this aspect in section 3.3.2 when describing Fig. 3.3.3. Note that a fainter outer ring for a faster inward migration is also an important signature of planet migration stressed in Meru et al. (2019) (see section 4.5).

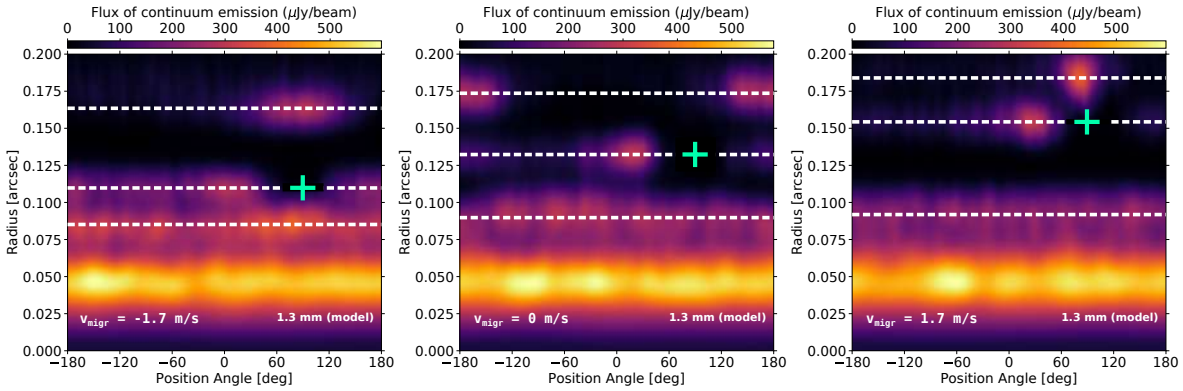

Figure 7.5.2: Radial asymmetry in the polar deprojection of three synthetic maps after 100 orbits of the Saturn-like planet. From left to right, we consider an inward migration at $v_{migr} = -1.7$ m/s, no migration and an outward migration at $v_{migr} = 1.7$ m/s. The turquoise cross marks the position of the planet. The white dashed lines show the radial locations of the three bright rings surrounding the planet.

Lagrange points: In most of the panels that show the azimuthal variations of Σ_d in the corotation region (blue curves in Fig. 7.5.1), particles seem to accumulate more efficiently around the L5 Lagrange point that is located behind the planet's orbit in the azimuthal direction ($\phi < 0$). From a dust thermal emission perspective, this trend

is more visible for the slowest migration regimes. The visibility of L5 emission will be discussed at the end of this paragraph. The only exceptions to this accumulation around L5 are the two extreme migration rates: for fast migration scenarios, whether outward or inward, particles seem to accumulate around the L4 Lagrange point located in front of the planet's orbit in the azimuthal direction ($\phi > 0$). This L4 accumulation is real for the fastest inward migration at $v_{migr} = -17.6$ m/s, and is visible both in the dust continuum map and in the $\Sigma_d(\phi)$ diagram (top-left panel in Fig. 7.5.1). For such fast inward migration, the corotation region shrinks to a trapezoidal region in the radius-azimuth plane ahead of the planet in azimuth, as seen in chapter 6. This phenomenon leads to an accumulation of dust particles close to the L4 Lagrange point. Note the similarities of such structure in the dust continuum map with observations of crescent-like structures just outside bright rings, in HD 135344 B for example (see Fig. 4.3.0). Regarding the fastest outward migration scenario ($v_{migr} = 17.6$ m/s, bottom-right panel), one could arguably suspect an accumulation of particles around L4 by just looking at $\Sigma_d(\phi)$. In reality, what we see is an inward horseshoe U-turn of large particles initially located outside the planet location. This U-turn leads to an over-density of particles at $\phi > 0$. It is however a transient phenomenon, as the only particles that remain in the corotation region eventually accumulate in L5. Outside the corotation region, note that most particles end up drifting radially in the inner disk. The horseshoe U-turn is illustrated in the right panel of Fig. 7.5.3 ($\phi > 0$) which shows the dust spatial distribution on top of the gas surface density perturbation, in the $v_{migr} = 17.6$ m/s case. We also clearly see the tadpole region in L5 ($\phi < 0$) that will accumulate particles later in the simulation. Note the clear presence of double peaks in $\Sigma_d(\phi)$ for the low migration cases (in particular for $v_{migr} = -0.4$, 0 or 0.4 m/s). This behavior is due to the azimuthal segregation of particle sizes in the Lagrange point L5, and therefore on the dust size distribution that we chose initially for the particles. It has been previously reported by Baruteau & Zhu (2016). We will see in the next paragraph that these double peaks are more sharped when particles spend more time trapped in the Lagrange point L5, because the azimuthal segregation is accentuated as particles reach their azimuthal position of equilibrium in the Lagrange point, according to their size. Though this temporal aspect is essential to detect double peaks in $\Sigma_d(\phi)$, the impact of planet migration should not be neglected and should be studied more in depth later on. We introduced earlier the formation of a tadpole region for the fast migration scenarios. We noticed in the dust spatial distribution that particles are trapped in libration there, but do not seem to be able to reach their equilibrium azimuthal position due to the planet's fast orbital motion. It would be interesting to study the large-scale fast migration of a planet in order to investigate the long-term evolution of particles in Lagrange points, and therefore to study only the impact of fast migration once particles have reached their equilibrium position. We noticed that the shape of the double peak is different for a different choice of q (recall that $q = -3.5$ in the estimation of $\Sigma_d(\phi)$ presented in this section). One question to be asked concerns the emission counterpart of these double peaks. One could imagine to carry out multi-wavelength radiative transfer calculations, at 1.3 mm and 0.87 mm for example, derive the spectral index close to the L5-induced crescent-like structure, estimate a size distribution and compare with our choice of q. If such study shows that we can infer azimuthal segregation and size distribution near crescent-like

structures from the spectral index azimuthal profile, we could apply this technique to real observations. If the double peak is present in the inferred $\Sigma_d(\phi)$, we could have access to a dust size distribution near the asymmetric structure. If the double peak is absent in the inferred $\Sigma_d(\phi)$, it could for example suggest (if it is due to planet-dust interaction) that the asymmetric structure is recent or the planet is in a fast migrating regime. The feasibility of such study still needs to be addressed, in particular due to the resolution issues and the uncertainties on the dust properties (shape, porosity, ...).

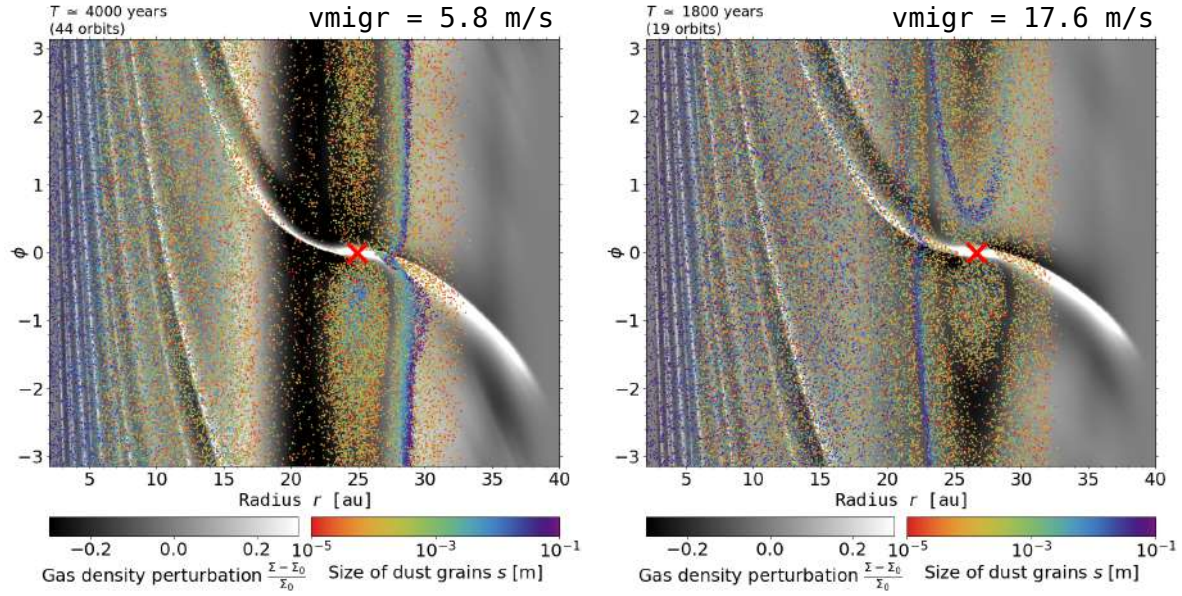

Figure 7.5.3: Dust spatial distribution in polar cylindrical coordinates for two cases presented in Fig. 7.5.1: outward migrating planets at a migration rate +5.8 m/s (left panel) and +17.6 m/s (right panel). The perturbed gas surface density relative to its initial profile, $(\Sigma - \Sigma_0)/\Sigma_0$, is shown in black and white. The location of dust particles is overlaid by colored dots. The rainbow color bar shows dust size in meters, with purple dots for the largest particles (10 cm) and red dots for the smallest (10 μm). In each panel, the red cross at zero azimuth marks the position of the planet.

Temporal evolution: by looking at the coorbital structures in the emission maps of Fig. 7.5.1, the emission around the Lagrange point L5 seems to be more localized when the migration is slower. It is particularly visible in the outward migration cases, by comparing the panels $v_{migr} = 0, 0.4, 1.7, 5.8$ m/s, where the emission around L5 is more and more extended. However, we need here to take into account the temporal evolution of dust accumulation in the Lagrange points. Fig. 7.5.4 displays this evolution for the non-migrating planet scenario, after 100 (left panel) and 250 (right panel) planet orbits. The comparison between these two continuum maps highlights the fact that the emission in the Lagrange points is highly dependent on how long it takes for the dust to be efficiently trapped in these positions of equilibrium. In order to determine the impact of migration on the azimuthal extent of the Lagrange points emission, there is an additional constraint on the migration timescale of the planet in the disk. For a small protoplanetary disk, as considered here ($r_{max} = 40$ au),

fast migration leaves little time for Lagrange points to efficiently accumulate particles. A possible extension of this study to better compare continuum maps would be to carry out radiative transfer calculations for a planet at a given location (e.g. $r_p = 1$), and after the same number of orbits. To do this, simulations would have to be run for a larger disk. The $\Sigma_d(\phi)$ profiles below the continuum maps demonstrate an accumulation of particles around L5. The main difference between these two graphs is the presence of a double peak at 250 orbits, whereas this structure is hardly detectable at 100 orbits. As already mentioned in the previous paragraph about Lagrange points, this behavior is due to a stronger azimuthal segregation when particles spend more time trapped in the Lagrange point L5.

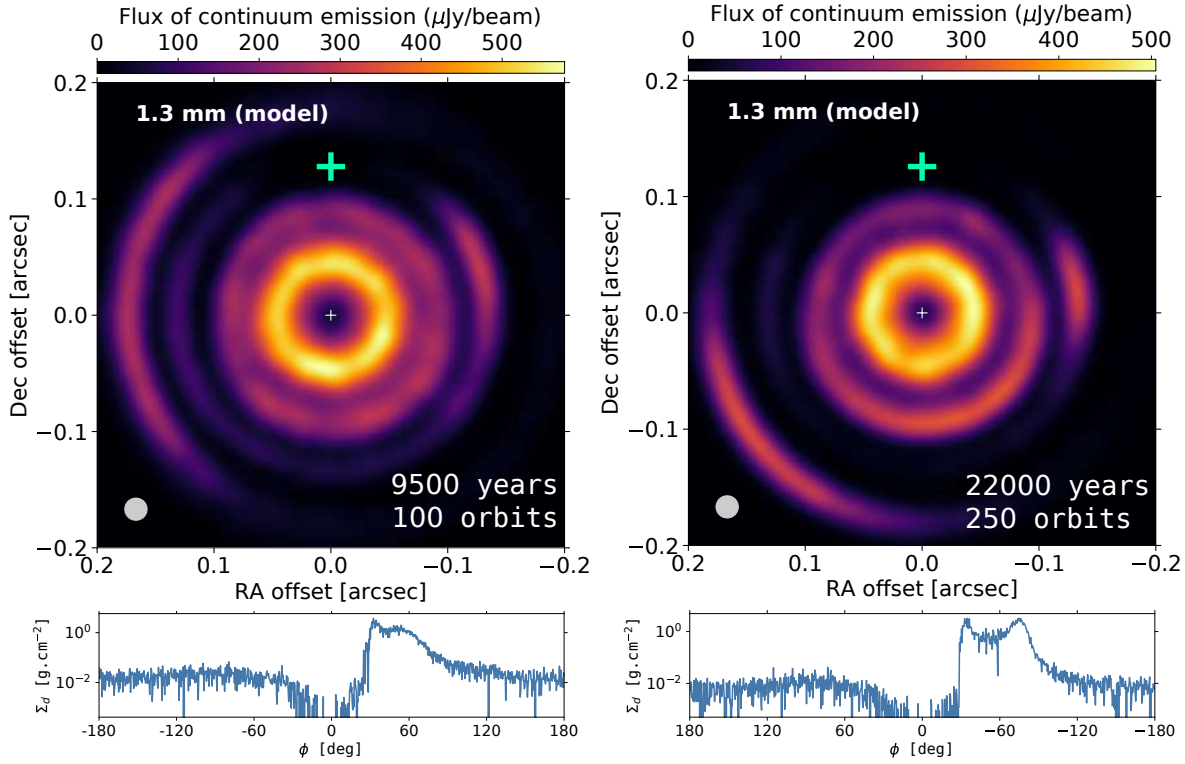

Figure 7.5.4: Temporal evolution of the dust continuum map in the simulation without migration (middle panel in Fig. 7.5.1). The emission of the asymmetric coorbital ring is more extended in the left panel (after 100 planet orbits) than in the right panel (after 250 planet orbits). The turquoise cross marks the position of the Saturn-like planet.

In summary, the emission in the coorbital region of a Saturn-like planet is generally dominated by L5, as long as this planet is not in a fast inward migration regime.

Emission at wake-driven kicks: if the angular resolution of the synthetic maps is increased, i.e. if the raw flux maps are convolved with a 0.″01 circular beam instead of a 0.″02 beam, an interesting structure can be detected in the scenarios with strong radial asymmetries. A kick (small deviation) in the emission is visible in the ring closest to the planet, whether it be the inner ring for an inward migrating planet or the outer ring for an outward migrating planet. Fig. 7.5.5 shows the polar deprojection of two

synthetic maps, for $v_{migr} = -5.8$ m/s (left panel) and $v_{migr} = 5.8$ m/s (right panel). The emission kicks are pinpointed with the turquoise dashed V-shaped segment, respectively in the inner ring and the outer ring.

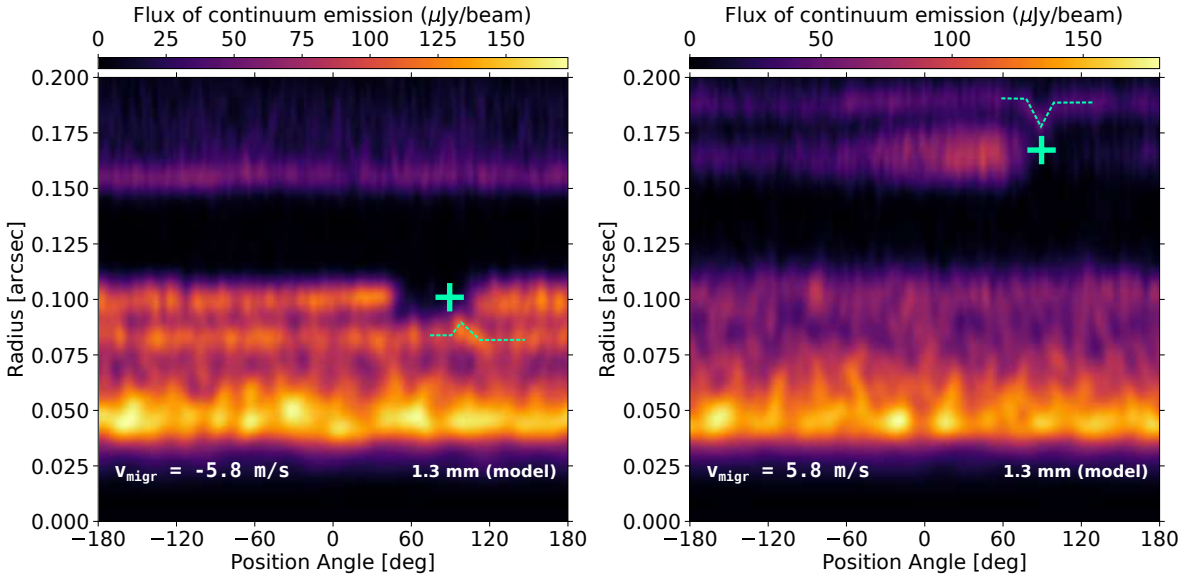

Figure 7.5.5: Emission kicks due to the planet wakes in the polar deprojection of two synthetic maps after 44 orbits of the Saturn-like planet, visible at a higher resolution (circular beam $0''.01 \times 0''.01$ instead of $0''.02 \times 0''.02$). The planet migrates at $v_{migr} = -5.8$ m/s (left panel) and $v_{migr} = 5.8$ m/s (right panel). The turquoise cross marks the position of the planet, and the turquoise dashed V-curves highlight the emission kicks, in the inner (outer) ring for an inward (outward) migrating planet.

These kicks result from the deflection of large particles by the planet wake (outer wake if the migration is outward, inner wake if the migration is inward). The perturbation is more visible in the outward migration case, for various reasons. Firstly, the intensity in the outer ring is not polluted by the emission of large particles drifting in the inner disk. Secondly, because emission kicks are due to the perturbations of the planet wakes, the impact of the outer wake in the right panel is better resolved than the impact of the inner wake in the left panel. In addition to that, the inner pressure bump where inner particles accumulate is not as strong as the outer pressure maximum where outer particles are trapped. The inner wake perturbation thus concerns particles that are scattered in a diffuse inner ring, leading to a less compact emission kick. To confirm the impact of the outer wake on the emission kick, we display in the left panel of Fig. 7.5.3 the dust spatial distribution on top of the gas surface density perturbation, in the $v_{migr} = 5.8$ m/s case. Note the accumulation of particles in L5, also visible in the continuum map (right panel of Fig. 7.5.5). From these emission kicks, we deduce a stronger structure due to the outer wake close to the planet. Note the analogy with our results in section 7.3 which seem to indicate that the main contribution to the velocity kinks in our disk model and numerical setup also comes from the outer wake close to the planet.

To conclude this section, if planets are indeed responsible for bright rings and gaps, many other substructures at smaller scales should be detected by using increasingly resolved observations. In the NGNP model, if some of the dark rings commonly observed in protoplanetary disks are due to intermediate-mass planets that carve gaps, is the absence of emission in these gaps due to efficient dust growth in Lagrange points ? This statement requires dedicated numerical simulations in the vicinity of the Lagrange points of a planet, including dust growth, dust backreaction and dust self-gravity.

7.6 PRELIMINARY WORK ON INTERMITTENT RUNAWAY MIGRATION IN 3D

Parameter	Symbol	Value
Code's unit of length	r_0	—
Initial Toomre parameter at r_0	Q	~ 13
Self-Gravity	—	No
Indirect term	—	Yes (planet) / No (gas)
Energy equation	—	No
Gas surface density at r_0 [code units]	Σ_0	1.91×10^{-3}
Gas surface density slope	σ	1.5
Disk's aspect ratio at r_0	h_0	0.08
Flaring index	f	0.5
Alpha turbulent viscosity	α	0
Planet to primary mass ratio	q_p	4×10^{-4}
Planet's initial location	$r_{p,o}$	r_0
—	$q/h^3(r_0)$	~0.78
Number of dust fluids	NFLUIDS	0
Number of radial cells	N_r	138
Number of azimuthal cells	N_ϕ	348
Number of colatitudinal cells	N_θ	40
Radial extension	$[r_{min}, r_{max}]$	$[0.15r_0, 2.4r_0]$
Azimuthal extension	$[\phi_{min}, \phi_{max}]$	$[-\pi, +\pi]$
Colatitudinal extension	$[\theta_{min}, \theta_{max}]$	$[\pi/2 - 0.15, \pi/2 + 0.15]$

Table 7.6.1: Main fiducial parameters for the 3D numerical simulations presented in section 7.6. We simulate the full disk in latitude, from −0.15 rad to 0.15 rad.

In this section, we briefly present the first 3D simulations that we carried out with FARGO3D, with the aim to test to what extent intermittent migration occurs similarly in 3D than in 2D. More simulations are in progress, with a higher resolution or more robust sets of parameters. We present here preliminary (low-resolution, no self-gravity, and no indirect term related to the gravitational acceleration of the disk onto the star[1]) inviscid simulations with the disk and planet parameters inspired by McNally et al. (2019) (see Table 7.6.1). In the simulations, we adopt a spherical coordinate system

1 the indirect term due to the disk is neglected by default in FARGO3D, and it is likely that it was also not included in McNally et al. (2019).

(r, θ,ϕ), with r the radial spherical coordinate measured from the central star, θ the colatitude angle, and ϕ the azimuthal angle.

In Fig. 7.6.1, we show the orbital evolution of the Saturn-like planet for two simulations with different smoothing lengths, $\epsilon_{smooth} = 0.4$ H and 0.1 H. In 3D simulations, ϵ_{smooth} is used in the expression of the planet gravitational potential $\Phi_p(\vec{r})$ in order to avoid a numerical divergence if the planet is at the center of a grid cell:

$$\Phi_p(\vec{r}) = -\frac{GM_p}{\sqrt{|\vec{r} - \vec{r_p}|^2 + \epsilon^2_{smooth}}}, \tag{113}$$

with r_p and M_p respectively the planet location and the planet mass. ϵ_{smooth} is in general taken relatively small in 3D simulations (typically close to the size of a grid cell), in order not to alter too much the exact expression of the 3D gravitational potential.

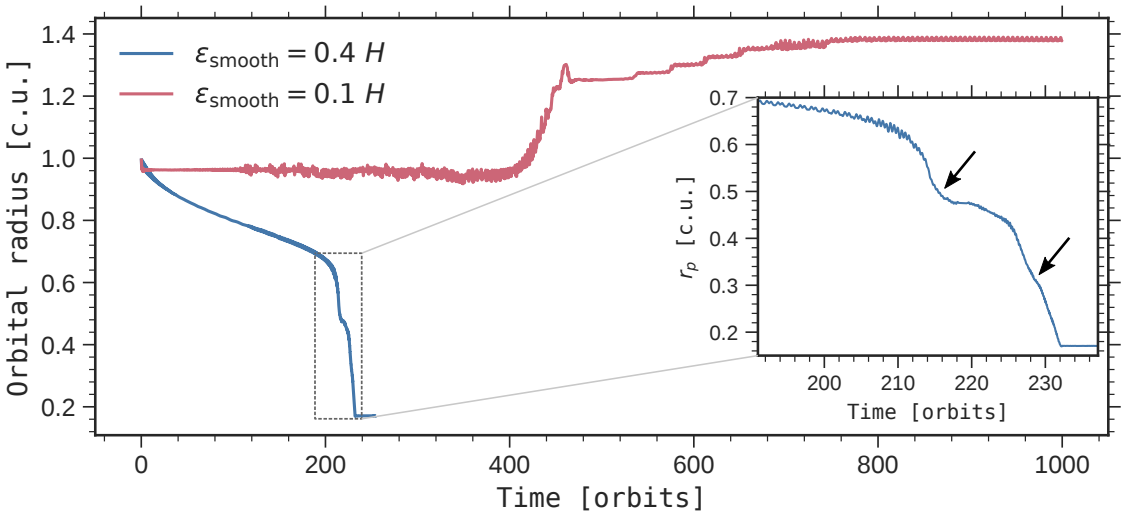

Figure 7.6.1: Results of 3D hydrodynamical simulations: time evolution of the planet's orbital radius for two values of the thickness smoothing: $\epsilon_{smooth} = 0.4$ H (blue curve) and 0.1 H (red curve). The black arrows in the inset plot highlight the phases of migration slow-down between two phases of fast runaway migration.

- For a large value of ϵ_{smooth} (blue curve), which is actually very similar to that adopted in the 2D simulations presented in chapter 6, we find an evolution of the planet's orbital radius that looks a lot like intermittent runaway migration, with three inward jumps. We therefore expect four outer rings in the gas density perturbation. This is actually the case when we consider the top panels of Fig. 7.6.2, which display in cartesian coordinates (X,Y,Z)[2] the gas density perturbation in the midplane (Z = 0, top-left panel) and in the (X-Z) plane

2 with $X = r\sin(\theta)\cos(\phi)$, $Y = r\sin(\theta)\sin(\phi)$ and $Z = r\cos(\theta)$. Note that in the midplane ($\theta = \pi/2$), $X = r\cos(\phi)$, $Y = r\sin(\phi)$ and $Z = 0$. In the plane such that $\phi = 0$, $X = r\sin(\theta)$, $Y = 0$ and $Z = r\cos(\theta)$. In that case, X is the cylindrical radius.

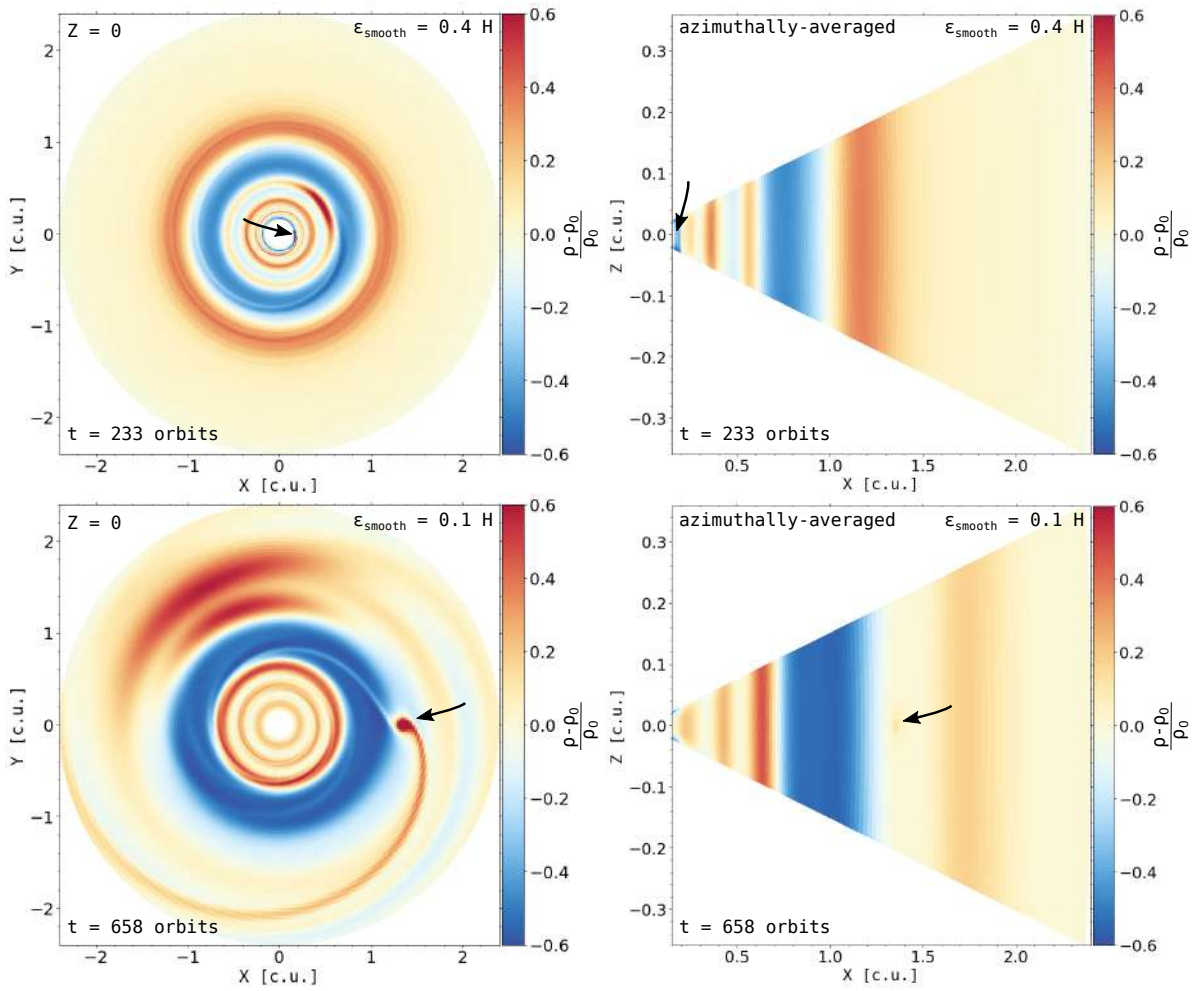

Figure 7.6.2: Perturbed gas volume density relative to its initial profile, $(\rho - \rho_0)/\rho_0$, in red and blue and in Cartesian coordinates, for $\epsilon_{smooth} = 0.4$ H at 233 orbits (top panels) and 0.1 H at 658 orbits (bottom panels). Over-densities show up in red, under-densities in blue. For each case, the gas volume density perturbation is displayed in the midplane (left panels) and azimuthally-averaged in the (X-Z) plane. The black arrows show the location of the planet.

(azimuthally-averaged, top-right panel). The four rings of over-density are in red in these panels. Because we consider inviscid simulations, any jump in the planet migration will irremediably lead to a long-lasting ring in the gas surface density field. Note also the presence of a vortex in the top-left panel at $r \sim 0.5 r_0$, due to the extremely low viscosity.

- For a lower value of ϵ_{smooth}, a powerful vortex (`Vortex1`), initially external to the planet, creates a positive dynamical corotation torque that leads to a phase of type-III rapid outward migration, perhaps similar to what Rometsch et al. (2020) observed in their simulations. Interestingly, after this phase of outward runaway migration, `Vortex1` is now trapped in the L4 Lagrange point of the planet. There is only one planet here, so there is no resonance with an internal planet that would make it jump back to a location closer to the star, as observed

in Rometsch et al. (2020). The planet thus remains approximately at $r = 1.4r_0$ and creates a second vortex (`Vortex2`), external to its new position. The outer and coorbital vortices are visible in the bottom-left panel of Fig. 7.6.2. In this panel, the planet outer wake is clearly visible (as well as an outer wake launched from `Vortex2`), but also spirals in the inner disk which may be visible in the integrated gas intensity maps (0th moment). Note in the bottom-right panel the presence of four rings of over-density close to the position of the four over-dense rings in the top-right panel. They are not created by the same process. The three inner rings at low ϵ_{smooth} are indeed probably due to the opening of a secondary and a tertiary gap, as observed in the simulations of (Zhang et al., 2018). These multiple rings are clearly visible because the viscosity is extremely low.

The significant discrepancy in the behavior of the planet for two values of the smoothing length is probably related to the strong impact of the torques exerted by the gas material very close to the planet, in particular in the circumplanetary disk. It would therefore be appropriate to carry out simulations at higher resolution, ideally with self-gravity, or to partly exclude the impact of the Hill sphere in the torques calculation (Crida et al., 2009). This approach is valid when gas self-gravity is neglected and the planet can migrate, which is the case here.

Other simulations have been carried out, with a set of parameters closer to the one used in section 6.4, with multiple dust fluids and at two resolutions ($N_r \times N_\phi \times N_\theta$), but for a smoothing length set to 0. In the low resolution case ($216 \times 288 \times 20$), the planet migration shows a slight intermittent runaway pattern, but not in the higher resolution case ($612 \times 900 \times 20$). In this latter case, the planet gradually migrates outward. Additional simulations have to be carried out in order to determine if this behavior is physical or due to numerical processes. For example, it can be due to the choice of the smoothing length and the fact that the torque calculation does not discard material within the planet's circumplanetary environment. We also noticed the development of the VSI (see section 2.3.3), and we are not sure yet what its impact is on the planet migration in our simulations. Furthermore, McNally et al. (2020) showed that the dynamical corotation torque does not act the same way in 2D and in 3D, with in particular the presence of buoyancy resonances that tend to speed up the inward migration of low-mass planets. We can therefore wonder what the effect of such resonances is on the 3D migration of intermediate-mass planets, for which the dynamical corotation torque already plays a very important role in 2D. In any case, as we saw in chapter 6, the triggering and 'sharpness' of intermittent runaway migration depends in particular on the mass of the planet and the disk's thermal properties (see section 6.5.3 about the impact of the energy equation). Its study in 3D would thus require to scan the parameter space.

Among the possible extensions of this work, it would be interesting to examine how the formation of multiple dust rings and gaps due to intermittent runaway migration would look like in scattered light at near-IR wavelengths. This question would probably be best addressed by dust radiative transfer calculations based on 3D gas+dust hydrodynamical simulations, necessary to properly model the vertical behavior of very small dust particles. Before post-processing our results of simulations with dust radiative transfer calculations to infer the polarized light that results from the

annular substructures, we thus needed to develop the necessary tools (`fargo23radmc3d` in particular) to analyze 3D simulations. It is possible that intermittent migration may leave imprints in scattered light as radial minima and maxima in the polarized intensity, which would reflect more or less the radial variations of the gas density in the superficial layers of the disk.

7.7 TRACKING A GROUP OF PARTICLES

To finish this chapter, we show an example of application of the particle tracking methodology. This methodology is actually just a post-processing of the FARGO-ADSG `dustsystatX.dat` output files, with X the output number, which makes the test particles discernible. To do this, we first order the dust size array at X. Then we consider the 'final size distribution', i.e. the particles that survive till the end of the simulation. We therefore remove all particles that disappear outside the active mesh. Usually, it corresponds mainly to particles subject to a strong radial drift and which leave the computational grid through its radial inner edge. Ultimately, all particles that have by chance the same 'ID card' (i.e. the same size) are also removed in the post-processing. Several aspects have to be noted here. On the one hand, this method is valid if dust growth is discarded, because particles are here identified only by their size. On the other hand, large particles are slightly disadvantaged, as they are usually more affected by radial drift. However, as long as we are aware of this bias, we can still correct it if needed.

For the case study that we present here, we spotlight a specific group of particles during the intermittent runaway migration of chapter 6. We highlighted in that chapter that some particles perform an outward horseshoe U-turn from an inner ring to the coorbital region of a runaway migrating Saturn-like planet, noted $\mathcal{P}$. After a phase of mixing in the corotation region, and during a slowing down of $\mathcal{P}$, some of these particles actually perform an inward horseshoe U-turn and eventually replenish the reservoir of dust particles ahead of the planet before the pending runaway phase. What is the dynamics of such specific pack of particles, their history and their future ? The answer can be found in Fig. 7.7.1.

We start initially with 100000 particles, and $\sim$ 93% of them are kept after the post-processing methodology presented in the previous paragraph. Among these $\sim$ 93000 particles, we consider only the particles that replenish the inner ring from the corotation region of $\mathcal{P}$.

- To understand this particle selection, let us consider the inset panel of Fig.7.7.1. We represent here (at $t = 6102$ years) with the black dots the size of the particles as a function of their position in a narrow region around the planet **compared** to the planet location r_p (in this diagram, particles at $r_d/r_p = 1$ are thus at the same location as the planet). We also see in this diagram an accumulation of large particles ($> 10^{-2}$ m) in an inner ring (at $r_d/r_p = 0.8$). At this moment ($t = 6102$ years), $\mathcal{P}$ just recovers from a phase of fast inward migration and enters a phase of slow migration during which some particles accumulate in this new inner ring. As we said earlier, we are interested specifically in these particles that were a few orbits earlier in the corotation region (then closer to $r_d/r_p = 1$).

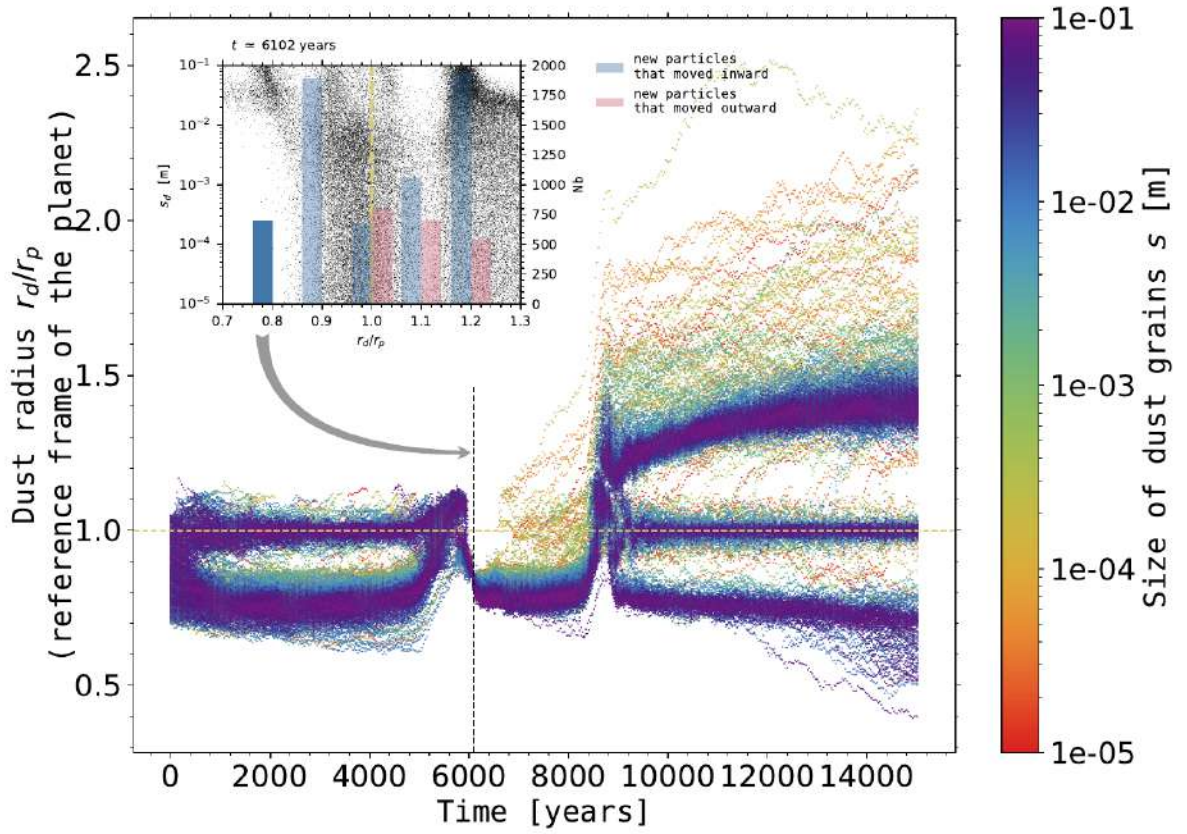

Figure 7.7.1: **Inset panel**: spatial distribution of particles (black dots) in the reference frame of the planet. The y-axis shows the size of the particles. The blue histogram shows the particles at $t = 6102$ years and at a given location that were closer to the planet a few orbits earlier. Similarly, the red histogram shows the particles at $t = 6102$ years and at a given location that were further away from the planet a few orbits earlier. We select particles in the deep blue bin, i.e. particles at $r_d/r_p = 0.8$ and $t = 6102$ years that were closer to the planet a few orbits earlier. **Rest of the panel**: space-time diagram of the particles within the aforementioned deep blue bin, compared to the planet location. The colorbar shows the size of the particles that we are looking at.

- The role of the histograms presented in the inset panel of Fig.7.7.1 is to discriminate, at a given location, between particles that are moving inward (blue bars), particles that are moving outward (red bars), and particles that were already at this location a few orbits earlier (not represented in the histograms). From these histograms, we select only particles that **were** in the corotation region and are **now** in the inner ring at $r_d/r_p = 0.8$ (deep blue bar).

- We can now consider the space-time diagram of this specific pack of particles, in the rest of Fig.7.7.1. The y-axis corresponds to the particles location r_d compared to the planet location r_p. The x-axis corresponds to the time in the simulation.

The colorbar shows the particle size. A vertical black dashed line highlights the time $t = 6102$ years, at which we select our group of particles. We see indeed that particles at that time are all in a narrow region in the disk (actually in the inner ring), between $r_d/r_p = 0.75$ and $r_d/r_p = 0.85$, in accordance with our selection method. The left side of this vertical line shows the pas evolution of these selected particles, while the right side shows their future. From the 'past' portion, we learn that part of these particles were in the corotation region, and the rest of them were already in an inner ring before performing single outward+inward horseshoe U-turns. From the 'future' portion, we see that these particles stay in the inner ring until the following episode of runaway inward migration, at $t \simeq 8500$ years. From that point onward, particles separate into three distinct groups: particles in an outer ring, in a coorbital ring and in an inner ring. Two interesting remarks can be made. Firstly, the oscillations in the coorbital ring are actually due to the motion of particles that are mixing in the corotation region before being trapped in the planet's Lagrange points. Secondly, we see that a large fraction of particles remains trapped in an inner ring throughout the simulation, with the exception of two brief visits in the corotation region during the phases of runaway migration. Such particles are necessary in order to generate the multiple annular substructures visible in the dust thermal emission (see Fig.6.4.3).

8

CONCLUSION AND FUTURE PROSPECTS

Since the beginning of my PhD thesis, my main focus has been to study the orbital evolution of planetary systems in a protoplanetary disk made of gas and dust around a young star (the first ten million years after the star formation). Recent observations of spatially resolved protoplanetary disks, in particular with the radio interferometer ALMA, have revealed a large diversity of substructures, in the dust thermal emission (sequences of dark rings (gaps) and bright rings, asymmetries, spirals, ...). Various mechanisms have been proposed to generate these substructures, and one possibility is to invoke the presence of planets. With this hypothesis, I examine what the impact of planetary migration is on the spatial distribution and the emission of dust particles, and what the observed substructures could tell us about the early formation and evolution of planetary systems.

The observation of N dark rings of emission is often interpreted as evidence for the presence of N planets which clear dust gaps around their orbit and form dust-trapping pressure maxima in the disk (N Gaps N Planets model). In general, these models assume planets on fixed orbits. During my first PhD project, I have gone a different route and have examined how the large-scale inward migration of a single planet structures the dust content of a massive disk.

In many circumstances, the migration of a partial gap-opening planet with a mass comparable to Saturn is found to run away (Masset & Papaloizou, 2003), with multiple stages of intermittent runaway migration (Lin & Papaloizou, 2010; McNally et al., 2019). By means of 2D gas and dust hydrodynamical simulations carried out with the code `Dusty FARGO-ADSG`, with dust grains modeled as Lagrangian test particles, I have shown that these multiple stages of intermittent runaway migration lead to the formation of several dust rings and therefore sequences of dark and bright rings in the (sub)mm continuum. With this scenario, planet-induced bright rings can be obtained without expecting planets in the vicinity of gaps in the continuum emission. As already stated by McNally et al. (2019), an intermittently migrating planet can wind up close to the star and be unresolved for the current observing facilities, and still have given rise to lasting multiple rings, depending on the disk's turbulent viscosity.

The jolts in the staircase migration pattern are intimately related to the perturbed gas surface density (more specifically the inverse potential vorticity). These perturbations in the gas depend on the ability of the planet to generate efficient shocks during its

migration in the disk. This ability is linked to the migration rate: a slowly migrating planet repetitively shocks the gas located on both sides of its orbit through its wakes (it is like a cumulative effect), which thus increases the gas surface density there. By contrast, a rapidly migrating planet cannot shock the gas around its orbit as efficiently. At low migration rate, a pressure maximum or an inflection point therefore builds up on both sides of the planet's orbit. In particular, before each episode of runaway migration, a pressure maximum forms outside the planet orbit. Because a pressure maximum defines an equilibrium position for the dust, large particles are efficiently trapped there. After the last episode of runaway migration, we thus end up with multiple concentric dust rings. The longevity of the dust structures mainly depends on how the pressure maxima are formed and how they are smoothed out by the disk's turbulent viscosity. In particular, a longer stage of slow migration, or a low level of turbulent viscosity, lead to a sharper pressure maximum, and therefore a longer-lived dust ring.

Our simulations results, more specifically the dust spatial distribution, are then post-processed with 3D dust radiative transfer calculations. These calculations are carried out with the code `RADMC3D`, for a face-on disk at 1.3 mm wavelength, which is the same wavelength as in the ALMA DSHARP survey (Huang et al., 2018a). I used the publicly available python program `fargo2radmc3d` (Baruteau et al., 2019) to compute synthetic images of the continuum emission from the outputs of `FARGO`. This requires to specify a total mass, a size distribution as well as a composition for the disk dust, so as to compute the dust's opacities, its temperature and eventually its intensity of emission after convolution with a synthetic beam (which we take similar to the best angular resolution currently achievable with ALMA at our working wavelength). Our dust radiative transfer calculations confirm that concentric dust rings induced by intermittent runaway migration can lead to the formation of multiple sets of bright and dark rings of continuum emission in the (sub)millimeter beyond the planet location. More importantly, the intensity contrast between bright and dark rings is detectable with the current sensitivity of ALMA. We have written a press release about this scenario, available in English at this address, and in French at this address.

Other projects are in progress, most of which are described in chapter 7, with possible extensions. Here is a non-exhaustive list.

- **Observational signatures of intermittent runaway migration scenario in various observational tracers**:
  - With the intermittent migration scenario, we found that the dust rings have a geometrical spacing in their radial position. More specifically, the radial location of successive pressure maxima follows a power law (in $r^{[1.4,1.5]}$). Furthermore, we noticed a similar behavior in the radial position of bright rings for some disks observed with ALMA, with a similar geometrical spacing. We could better delineate the region of parameter space for which this scenario occurs, and then use the geometrical spacing between bright rings to extract valuable information from specific disk observations (aspect ratio, temperature, presence of a putative planet, ...).
  - Most of the radiative transfer calculations were carried out at 1.3 mm. At this wavelength, the specific intensity is sensitive to the thermal emission of large

dust particles (with a size comparable to the wavelength of observation), which are cold and rather located in the midplane of protoplanetary disks. A possibility would be to consider the light scattered by smaller and hotter particles located in the superficial layers of protoplanetary disks, in order to examine how the formation of multiple dust rings and gaps due to intermittent runaway migration would look like at near-IR wavelengths. To do that, 3D gas and dust hydrodynamical simulations are necessary, using for instance `FARGO3D`, as small particles are located off the midplane.

  - Another possible extension would be to be able to discriminate between the N Gaps N Planets model and the intermittent runaway migration scenario through gas kinematic signatures (in particular by looking at the deviation of the gas azimuthal velocity from Keplerian rotation or velocity kinks in channel maps of the gas emission), via line transfer calculations with `RADMC3D`. Our primary results in our disk model and numerical setup regarding velocity kinks seem to suggest that their origin is linked to the deflection of fluid elements by outer wakes close to the planets. We would therefore expect multiple velocity kinks for the NGNP model, and no kink at all in our intermittent runaway migration scenario (except in the inner region close to the star, if spatially resolved). The origin of velocity kinks should be studied more in depth with increased numerical resolution. Furthermore, more simulations on the impact of planet migration on velocity kinks are in progress.

- **Emission of Lagrange points**:
  - we have noticed in various numerical simulations that the Lagrange point L5 (behind the planet in azimuth) is an efficient trap for large particles, whether the planet is migrating or not, and mostly independently of whether migration is directed inward or outward. Such result has also been found by Montesinos et al. (2020). More simulations should be performed to test this behavior of L5. In any case, it could be used to infer the location of planets in disks that show azimuthal substructures, along with the radial asymmetry of bright rings that could inform us on the direction of migration of such planet.
  - We can expect that particles trapped in Lagrange points L4/L5 of massive planets should be bright in the continuum emission. But these features do not seem to be as frequent in ALMA observations (we do not see point-source-like emissions within every dark ring in the dust continuum emission maps). We could therefore study the dust dynamics and dust growth inside the Lagrange points of a (migrating or not) massive planet. The aim would be to understand if the scarcity of detection of crescent-like structures between two bright rings of emission is due to an absence of planets at the center of dark rings, an efficient removal of particles in planets' horseshoe region, or a diminished dust thermal emission due to efficient dust growth.

- **Dust growth**: All our simulations assume a fixed dust size distribution. It would be interesting to study the coagulation+fragmentation of these particles with

dust growth models. Ideally, we could for example study dust coagulation and fragmentation by resolving the Smoluchowski equation in 1D (Birnstiel et al., 2010; Pinilla et al., 2012) or 2D (Drążkowska et al., 2019) models. We could also use an analytical prescription for the evolution of the grain size as a function their relative velocity, and use a simple model for fragmentation (see, e.g., Stepinski & Valageas, 1997; Laibe et al., 2008; Gonzalez et al., 2015).

- **Spectral index and dust size distribution**:
  - First, we could estimate the efficiency of particle trapping as a function of the sharpness of pressure maxima, and study the expected radial segregation of particle sizes. Then, using multi-wavelength synthetic dust continuum maps, we could analyze more in depth the link between spectral index and dust size distribution, in particular regarding the radial segregation of particle sizes. The aim would be to estimate the sharpness of pressure maxima behind the bright rings, and then have other constraints on the mechanism(s) behind their formation.
  - Another project concerns the spectral index near bright crescent-like structures. Again, inferring a dust size distribution from the azimuthal spectral index profile could give an insight on the azimuthal segregation of particle sizes. From their we could have constraints on the mechanism(s) behind crescent-like structures, for example concerning the migration of a nearby planet.

- **Wind-driven accretion model**: I am currently working on the interaction between a planet and a viscously evolving disk through hydrodynamical simulations, with no magnetic field. However, the observations of thin substructures, in particular in the (sub)mm continuum, suggest that turbulence in the midplane of protoplanetary disks is weaker than usually thought (see, e.g., Pinte et al., 2016), and that wind-driven accretion may therefore play a major role in the dynamical evolution of protoplanetary disks. It would therefore be interesting to determine through magneto-hydrodynamical simulations the impact of these MHD winds on planetary migration, and to predict observational signatures of planet-disk-wind interactions in various observational tracers. This will be the main topic of my post-doctoral work within the MHDiscs project team at IPAG.

- **Orbital evolution of an outer low-mass planet in a disk with pre-formed annular substructures**:
  - Implications to $\mathcal{I}_\mathcal{V}$ planet traps are numerous (see section 7.4), in particular if a planet forms near a dust rings, and if this dust ring is located close to an $\mathcal{I}_\mathcal{V}$ maximum. The migration of such planet is expected to be hampered until it has grown enough to generate strong structures in the gas that will trigger a faster migration. An interesting study would be to investigate planetary formation and migration near $\mathcal{I}_\mathcal{V}$ planet traps via 2D or 3D numerical models, and post-process the results with dust+line radiative transfer calculations in order to hunt down signposts of low-mass planets in the bright rings.

– We could also investigate if planet $\mathcal{I}_\nu$ traps are a generic process, for example in the case of MHD winds able to induce zonal flows which take the form of axisymmetric rings (see, e.g., Béthune et al., 2017; Riols & Lesur, 2019). Dust particles can accumulate near pressure maxima generated via this process (Riols et al., 2020), and I would expect that $\mathcal{I}_\nu$ maxima are associated with these pressure maxima. The migration of a low-mass planet could therefore be hindered by such structures in the disk. My post-doctoral work will be the opportunity to verify this statement in a disk whose annular substructures are not due to planets but to other physical processes.

Ultimately, the common thread between all these possible projects is to develop a collection of tools in order to have at one's disposal a set of observational predictions for a given model. Starting from an output of a simulation, the aim would be to derive a series of predictions, either in the thermal dust emission (dust continuum maps, spectral index), or in the spectral line emission (channel maps, intensity maps, velocity maps) for example. To be more complete, another area to develop and study concerns therefore scattered light at near-IR wavelengths.

CONCLUSION ET PERSPECTIVES

Depuis le début de ma thèse de doctorat, un des principaux objectifs a été d'étudier l'évolution orbitale de planètes dans un disque protoplanétaire constitué de gaz et de poussières autour d'une jeune étoile (quelques dizaines de millions d'années après sa formation). Les observations récentes de disques protoplanétaires spatialement résolus, en particulier avec l'interféromètre radio ALMA, ont révélé une grande diversité de sous-structures dans l'émission thermique de la poussière, que ce soient des séquences d'anneaux sombres (sillons) et d'anneaux brillants, des asymétries ou des spirales. Différents mécanismes ont été proposés pour générer ces sous-structures, et une possibilité est d'invoquer la présence de planètes. En se basant sur cette hypothèse, j'examine quel est l'impact de la migration planétaire sur la distribution spatiale et l'émission de particules de poussière, et ce que les sous-structures observées pourraient nous apprendre sur la formation et l'évolution des systèmes planétaires.

Selon un modèle répandu, chaque anneau sombre dans un disque protoplanétaire correspondrait au sillon ouvert par une planète en orbite fixe autour de son étoile. Si N anneaux sombres sont détectés, alors N planètes sont proposées (modèle NGNP). Ces planètes, à l'origine de maxima de pression dans le disque, seraient favorables au piégeage de la poussière sous forme d'anneaux. Au cours de mon premier projet de doctorat, j'ai emprunté une voie différente et ai examiné comment la migration grande échelle vers l'étoile d'une seule planète peut structurer la poussière d'un disque massif.

Dans bien des cas, pour une planète capable d'ouvrir un sillon partiel et dont la masse est comparable à celle de Saturne, on constate un emballement de la migration (Masset & Papaloizou, 2003) qui se caractérise notamment par plusieurs étapes de migration intermittente, 'en escalier' (Lin & Papaloizou, 2010; McNally et al., 2019). Au moyen de simulations hydrodynamiques 2D modélisant l'évolution du gaz et des poussières d'un disque réalisées avec le code `Dusty FARGO-ADSG`, nous avons constaté que ces multiples étapes de migration intermittente conduisent à la formation de plusieurs anneaux de poussières. Le post-traitement de ces résultats de simulations par des calculs de transfert radiatif dans la poussière au moyen du code public `RADMC3D` a montré que les anneaux de poussières multiples se caractérisent par une alternance d'anneaux sombres et brillants dans le continuum d'émission en radio. Avec ce scénario, il est ainsi possible d'obtenir des séquences d'anneaux sombres et brillants par la migration d'une seule planète dans un disque protoplanétaire. Comme proposé par McNally et al. (2019), une planète en migration intermittente peut s'approcher suffisamment près de l'étoile pour ne pas être détectable à la résolution actuelle des téléscopes, et tout de même être à l'origine d'anneaux multiples durables, selon la viscosité turbulente du disque.

Les à-coups dans la migration en escalier sont intimement liés aux perturbations induites par la planète dans la densité de surface du gaz (plus précisément dans l'inverse de la vorticité potentielle). Ces perturbations du gaz dépendent essentiellement de la capacité de la planète à générer des chocs efficaces lors de sa migration

dans le disque, et donc à sa vitesse de migration. Les sillages d'une planète qui migre lentement choquent de façon répétitive le gaz situé de part et d'autre de l'orbite planétaire (c'est un effet cumulatif), ce qui augmente la densité de surface du gaz à cet endroit. En revanche, les sillages d'une planète qui migre rapidement ne peuvent pas choquer le gaz aussi efficacement. À faible vitesse de migration, des maxima de pression (ou points d'inflexion) se forment donc des deux côtés de l'orbite de la planète. En particulier, avant chaque épisode de migration emballée, un maximum de pression se forme à l'extérieur de l'orbite de la planète. Ce n'est pas le cas lors d'une phase de migration plus rapide. Etant donné qu'un maximum de pression définit une position d'équilibre pour la poussière, les grandes particules y sont efficacement piégées. Après le dernier épisode de migration emballée, nous nous retrouvons donc avec de multiples anneaux de poussières concentriques. La longévité des structures de poussières dépend principalement de la façon dont les maxima de pression sont formés et de la façon dont ils sont lissés par la viscosité turbulente du disque. En particulier, une étape plus longue de migration lente, ou un faible niveau de viscosité turbulente, conduisent à un maximum de pression plus marqué, et donc à une plus grande longévité des anneaux de poussières.

Les résultats de nos simulations, plus précisément la distribution spatiale de la poussière, ont été post-traités avec des calculs de transfert radiatif dans la poussière en 3D. Ces calculs sont effectués avec le code `RADMC3D`, pour un disque vu de face à 1.3 mm de longueur d'onde, qui est la même longueur d'onde que celle utilisée pour les observations avec ALMA des disques du projet DSHARP (Huang et al., 2018a). J'ai utilisé le programme python `fargo2radmc3d` (Baruteau et al., 2019) pour calculer des cartes synthétiques de l'émission du continuum à partir des résultats de mes simulations hydrodynamiques. La procédure nécessite de spécifier une masse totale, une distribution de taille ainsi qu'une composition pour la poussière du disque, afin de calculer la température, les opacités et l'intensité d'émission de la poussière après convolution par un beam synthétique (que nous choisissons en fonction de la résolution angulaire actuelle d'ALMA à la longueur d'onde considérée). Nos calculs de transfert radiatif des poussières confirment que les anneaux de poussières concentriques induits par la migration intermittente d'une planète peuvent conduire à la formation d'anneaux brillants et sombres dans l'émission (sub-)millimétrique. Plus important encore, le contraste d'intensité entre les anneaux brillants et sombres est détectable avec la sensibilité actuelle d'ALMA. Nous avons rédigé un communiqué de presse sur ce scénario, disponible en anglais à cette adresse, et en français à cette adresse.

D'autres projets sont en cours, dont la plupart sont décrits au chapitre 7, avec des extensions possibles. En voici une liste non exhaustive.

- **Signatures du scénario de migration intermittente dans divers traceurs observationnels** :
  - Avec le scénario de migration intermittente, nous avons vu que la position radiale des anneaux brillants de poussières ont un espacement géométrique. Plus précisément, la position radiale des maxima de pression successifs suit une loi de puissance en $r^{[1,4,1,5]}$. De plus, nous avons remarqué un espacement géométrique similaire dans la position radiale des anneaux brillants

de certains disques observés avec ALMA. Il serait intéressant de mieux délimiter la région de l'espace des paramètres pour laquelle ce scénario se produit, et ensuite utiliser l'espacement géométrique entre les anneaux brillants pour extraire des informations précieuses des observations de disques spécifiques (rapport d'aspect, température, présence d'une éventuelle planète, ...).

- La plupart des calculs de transfert radiatif ont été effectués à 1.3 mm. À cette longueur d'onde, l'intensité spécifique est sensible à l'émission thermique de grandes particules de poussière (d'une taille comparable à la longueur d'onde d'observation), qui sont froides et plutôt situées dans le plan médian des disques protoplanétaires. Une possibilité serait de considérer la lumière diffusée par les particules plus petites et plus chaudes situées dans les couches superficielles des disques protoplanétaires, afin d'examiner les signatures de la migration intermittente en infrarouge proche. Pour ce faire, des simulations hydrodynamiques 3D (les petites particules sont situées hors du plan médian) du gaz et des poussières sont nécessaires, en utilisant par exemple FARGO3D.
- Une autre extension possible serait de pouvoir différencier le modèle NGNP et le scénario de migration intermittente par le biais des signatures cinématiques du gaz (en particulier en examinant la déviation de la vitesse azimuthale du gaz par rapport à la rotation képlérienne ou les *velocity kinks* dans les channel maps de l'émission de gaz), grâce à des calculs de raies d'émission avec `RADMC3D`. Nos résultats préliminaires concernant les *velocity kinks* semblent suggérer que leur origine est liée à la déflection des éléments fluides par le sillage externe des planètes. Nous nous attendons donc à de multiples *velocity kinks* pour le modèle NGNP, et à aucun velocity kink dans notre scénario de migration intermittente (sauf si le disque interne très proche de l'étoile est spatialement résolu). Pour étudier plus en détail l'origine des velcoty kinks, il faudrait réaliser des simulations numériques à plus grande résolution. D'autre part, des simulations concernant l'impact de la migration planétaire sur les *velocity kinks* sont en cours.

- **Emission des points de Lagrange** :
  - Nous avons remarqué dans diverses simulations numériques que le point de Lagrange L5 (situé derrière la planète dans la direction azimutale) est un piège efficace pour les grandes particules, avec ou sans migration, et ce indépendamment du fait que la migration soit dirigée vers l'intérieur ou vers l'extérieur. Ce phénomène a également été mis en évidence par Montesinos et al. (2020), et pourrait être utilisé pour déduire l'emplacement d'éventuelles planètes dans les disques qui présentent des sous-structures azimuthales. L'asymétrie radiale des anneaux brillants pourrait quant à elle nous renseigner sur la direction de la migration planétaire.
  - Les particules piégées au niveau des points de Lagrange L4/L5 de planètes massives devraient être brillantes dans le continuum d'émission. Or, ce type d'asymétries dans les anneaux sombres ne semble pas être fréquemment

observé avec ALMA. Un projet possible serait donc d'étudier la dynamique et la croissance des poussières à l'intérieur des points de Lagrange d'une planète massive (en migration ou non). L'objectif serait de comprendre si la rareté des détections de structures en forme de croissant entre deux anneaux brillants est due à l'absence de planètes au centre des anneaux sombres, à une évacuation efficace des particules dans la région coorbitale des planètes, ou à une diminution de l'émission thermique des poussières due à une croissance efficace des grains au niveau des points de Lagrange.

- **Croissance des poussières** : Toutes nos simulations supposent une distribution fixe de la taille des poussières. Il serait intéressant d'étudier la coagulation+fragmentation de ces particules avec des modèles de croissance des poussières. Idéalement, nous pourrions par exemple étudier la coagulation et la fragmentation des poussières en résolvant l'équation de Smoluchowski dans des modèles 1D (Birnstiel et al., 2010; Pinilla et al., 2012) ou 2D (Drążkowska et al., 2019). Nous pourrions également utiliser une prescription analytique pour l'évolution de la taille des grains en fonction de leur vitesse relative, et utiliser un modèle simple pour la fragmentation (voir, par exemple, Stepinski & Valageas, 1997; Laibe et al., 2008; Gonzalez et al., 2015)

- **Indice spectral et distribution de taille des poussières** :
  - Premièrement, nous pourrions estimer l'efficacité du piégeage des particules en fonction de la pente des maxima de pression, et étudier la ségrégation radiale en taille des particules. Ensuite, à l'aide de cartes synthétiques multi-longueurs d'onde du continuum d'émission des poussières, nous pourrions analyser plus en profondeur le lien entre l'indice spectral et la distribution en taille de poussières, en particulier en ce qui concerne la ségrégation radiale. L'objectif serait alors d'estimer la pente des maxima de pression à l'origine des anneaux brillants, et d'ainsi avoir des contraintes sur le(s) mécanisme(s) derrière leur formation.
  - Un autre projet concerne l'indice spectral près des structures brillantes en forme de croissant. Là encore, déduire une distribution de taille des poussières à partir du profil cette fois azimuthal d'indice spectral pourrait donner un aperçu de la ségrégation azimuthale en taille de particules. A partir de celle-ci, nous pourrions avoir des contraintes sur le(s) mécanisme(s) à l'origine des structures en croissant.

- **Modèle d'accrétion par des vents magnétiques** : Les modèles numériques que j'utilise reposent sur une évolution visqueuse turbulente du disque protoplanétaire, sans champ magnétique. Cependant, les observations de sous-structures fines, en particulier dans le continuum d'émission en radio, suggèrent que la turbulence dans le plan médian des disques protoplanétaires est plus faible qu'attendu (voir par exemple Pinte et al., 2016), et que l'accrétion due à des vents magnétisés pourrait jouer un rôle majeur dans l'évolution dynamique des disques protoplanétaires. Il serait donc intéressant de déterminer par des simulations magnétohydrodynamiques l'impact de ces vents MHD sur la migration

planétaire, et de prédire les signatures des interactions planète-disque-vent dans divers traceurs observationnels. Ce sera d'ailleurs le sujet principal de mon travail post-doctoral au sein de l'équipe MHDiscs à l'IPAG à partir de Janvier 2021.

- **Évolution orbitale d'une planète externe de faible masse dans un disque avec des sous-structures annulaires préexistantes** :
  - La formation de plusieurs maxima d'inverse de la vorticité potentielle du gaz $\mathcal{I}_V$ (ou de sa pression) par la migration d'une planète massive a de nombreuses implications (voir section 7.4), notamment en ce qui concerne l'évolution orbitale d'autres planètes dans le même disque. La migration d'une telle planète devrait être entravée jusqu'à ce qu'elle ait atteint une masse suffisante pour altérer la structure du disque. Une étude intéressante consisterait à étudier la croissance et la migration de planètes à proximité de tels maxima de $\mathcal{I}_V$ au moyen de simulations hydrodynamiques gaz+poussières en 2D ou 3D, et à post-traiter les résultats avec des calculs de transfert radiatif dans la poussière et le gaz afin de chercher les signatures de planètes de faible masse dans les anneaux brillants.
  - Nous pourrions également étudier si la capacité des maxima d'$\mathcal{I}_V$ à ralentir la migration de planètes de faible masse est un processus générique. Par exemple, les vents MHD sont capables d'induire également des anneaux axisymétriques de densité (voir, par exemple, Béthune et al., 2017; Riols & Lesur, 2019). Les particules de poussière peuvent s'accumuler près des maxima de pression générés par ce processus (Riols et al., 2020), et je m'attendrais à ce que des maxima d'$\mathcal{I}_V$ soient associés à ces maxima de pression. La migration d'une planète de faible masse pourrait donc être entravée par de telles structures dans le disque. Mon travail post-doctoral sera l'occasion de vérifier cette proposition dans un disque dont les sous-structures annulaires ne sont pas dues à des planètes mais à d'autres processus physiques.

Au final, le fil conducteur de tous ces projets possibles est de développer une collection d'outils afin de disposer d'un ensemble de prédictions observationnelles pour un modèle donné. A partir des résultats de simulations numériques 2D ou 3D, l'objectif serait d'avoir une série de prédictions, soit dans l'émission thermique des poussières (cartes du continuum d'émission, indice spectral), soit dans l'émission de raies spectrales (cartes d'intensité, cartes de vitesse) par exemple. Pour être plus complet, un autre domaine à développer et à étudier concerne la lumière diffusée dans le proche infrarouge.

BIBLIOGRAPHY

ALMA Partnership et al., 2015, ApJ, 808, L3

Alexander R., et al., 2014, in Beuther H., et al., eds, Protostars and Planets VI. p. 475 (arXiv:1311.1819), doi:10.2458/azu_uapress_9780816531240-ch021

Alibert Y., et al., 2005, A&A, 434, 343

Alibert Y., Mordasini C., Benz W., 2011, A&A, 526, A63

Andrews S. M., 2015, PASP, 127, 961

Andrews S. M., 2020, arXiv e-prints, p. arXiv:2001.05007

Andrews S. M., et al., 2018, ApJ, 869, L41

Ansdell M., et al., 2018, ApJ, 859, 21

Arlt R., Urpin V., 2004, A&A, 426, 755

Armitage P. J., 2007, arXiv e-prints, pp astro–ph/0701485

Ataiee S., et al., 2014, A&A, 572, A61

Ataiee S., et al., 2018, A&A, 615, A110

Avenhaus H., et al., 2017, AJ, 154, 33

Avenhaus H., et al., 2018, ApJ, 863, 44

Bae J., Zhu Z., 2018a, ApJ, 859, 118

Bae J., Zhu Z., 2018b, ApJ, 859, 119

Bae J., Zhu Z., Hartmann L., 2016, ApJ, 819, 134

Bae J., Zhu Z., Hartmann L., 2017, ApJ, 850, 201

Bai X.-N., 2013, ApJ, 772, 96

Bai X.-N., Stone J. M., 2013, ApJ, 769, 76

Balbus S. A., Hawley J. F., 1991, ApJ, 376, 214

Barge P., Sommeria J., 1995, A&A, 295, L1

Barker A. J., Latter H. N., 2015, MNRAS, 450, 21

Baruteau C., 2008, PhD thesis, CEA Saclay, Service d'Astrophysique, 91191 Gif/Yvette Cedex, France

Baruteau C., Masset F., 2008a, ApJ, 672, 1054

Baruteau C., Masset F., 2008b, ApJ, 678, 483

Baruteau C., Papaloizou J. C. B., 2013, ApJ, 778, 7

Baruteau C., Zhu Z., 2016, MNRAS, 458, 3927

Baruteau C., Meru F., Paardekooper S.-J., 2011, MNRAS, 416, 1971

Baruteau C., et al., 2014, Protostars and Planets VI, pp 667–689

Baruteau C., et al., 2016, Space Sci. Rev., 205, 77

Baruteau C., et al., 2019, MNRAS, 486, 304

Batygin K., Bodenheimer P. H., Laughlin G. P., 2016, ApJ, 829, 114

Bell K. R., Lin D. N. C., 1994, ApJ, 427, 987

Benisty M., et al., 2015, A&A, 578, L6

Benisty M., et al., 2017, A&A, 597, A42

Benítez-Llambay P., Pessah M. E., 2018, ApJ, 855, L28

Benítez-Llambay P., et al., 2016, ApJ, 826, 13

Benítez-Llambay P., Krapp L., Pessah M. E., 2019, ApJS, 241, 25

Bentley M. S., et al., 2016, Nature, 537, 73

Bergin E. A., et al., 2013, in Kawabe R., Kuno N., Yamamoto S., eds, Astronomical Society of the Pacific Conference Series Vol. 476, New Trends in Radio Astronomy in the ALMA Era: The 30th Anniversary of Nobeyama Radio Observatory. p. 185

Béthune W., Lesur G., Ferreira J., 2017, A&A, 600, A75

Birnstiel T., Dullemond C. P., Brauer F., 2010, A&A, 513, A79

Birnstiel T., Klahr H., Ercolano B., 2012, A&A, 539, A148

Birnstiel T., Fang M., Johansen A., 2016, Space Sci. Rev., 205, 41

Bitsch B., et al., 2013, A&A, 549, A124

Bitsch B., Lambrechts M., Johansen A., 2015, A&A, 582, A112

Bjorkman J. E., Wood K., 2001, ApJ, 554, 615

Blandford R. D., Payne D. G., 1982, MNRAS, 199, 883

Blum J., 2018, Space Sci. Rev., 214, 52

Blum J., Wurm G., 2000, Icarus, 143, 138

Bodenheimer P., Hubickyj O., Lissauer J. J., 2000, Icarus, 143, 2

Boehler Y., et al., 2017, ApJ, 840, 60

Boehler Y., et al., 2018, ApJ, 853, 162

Bohren C. F., Huffman D. R., 1983, Absorption and scattering of light by small particles

Boley A. C., et al., 2010, Icarus, 207, 509

Briceño C., et al., 2019, AJ, 157, 85

Calcino J., et al., 2020, MNRAS, 498, 639

Carmona A., 2010, Earth Moon and Planets, 106, 71

Carmona A., et al., 2017, A&A, 598, A118

Casoli J., Masset F. S., 2009, ApJ, 703, 845

Cazzoletti P., et al., 2018, A&A, 619, A161

Cébron D., et al., 2013, Icarus, 226, 1642

Chatterjee S., et al., 2008, ApJ, 686, 580

Chen J.-W., Lin M.-K., 2018, MNRAS, 478, 2737

Crida A., Morbidelli A., Masset F., 2006, Icarus, 181, 587

Crida A., et al., 2009, A&A, 502, 679

Cuello N., et al., 2019, MNRAS, 483, 4114

Cuello N., et al., 2020, MNRAS, 491, 504

Currie T., et al., 2014, ApJ, 796, L30

D'Angelo G., Henning T., Kley W., 2003, ApJ, 599, 548

Dipierro G., Laibe G., 2017, MNRAS, 469, 1932

Dipierro G., et al., 2015, MNRAS, 453, L73

Dipierro G., et al., 2018, MNRAS, 479, 4187

Donati J. F., et al., 2016, Nature, 534, 662

Dong R., et al., 2017, ApJ, 843, 127

Dong R., et al., 2018, ApJ, 860, 124

Draine B. T., Lee H. M., 1984, ApJ, 285, 89

Drążkowska J., et al., 2019, ApJ, 885, 91

Dubrulle B., Morfill G., Sterzik M., 1995, Icarus, 114, 237

Dullemond C., et al., 2015, RADMC3D, `http://www.ita.uni-heidelberg.de/~dullemond/software/radmc-3d/`

Fabrycky D., Tremaine S., 2007, ApJ, 669, 1298

Facchini S., Lodato G., Price D. J., 2013, MNRAS, 433, 2142

Facchini S., et al., 2019, A&A, 626, L2

Fedele D., et al., 2010, A&A, 510, A72

Fedele D., et al., 2017, A&A, 600, A72

Flaherty K. M., et al., 2015, ApJ, 813, 99

Flaherty K. M., et al., 2017, ApJ, 843, 150

Flock M., et al., 2015, A&A, 574, A68

Follette K. B., et al., 2017, AJ, 153, 264

Forgan D. H., Ilee J. D., Meru F., 2018, ApJ, 860, L5

Fouchet L., Gonzalez J. F., Maddison S. T., 2010, A&A, 518, A16

Fricke K., 1968, Mitteilungen der Astronomischen Gesellschaft Hamburg, 25, 129

Fromang S., Lesur G., 2019, in EAS Publications Series. pp 391–413, doi:10.1051/eas/1982035

Fu W., et al., 2014, ApJ, 795, L39

Fuente A., et al., 2017, ApJ, 846, L3

Gammie C. F., 2001, ApJ, 553, 174

Garufi A., et al., 2020, A&A, 633, A82

Goldreich P., Schubert G., 1967, ApJ, 150, 571

Gonzalez J. F., et al., 2015, Planet. Space Sci., 116, 48

Gonzalez J. F., Laibe G., Maddison S. T., 2017, MNRAS, 467, 1984

Goodman J., Rafikov R. R., 2001, ApJ, 552, 793

Guzmán V. V., et al., 2018, ApJ, 869, L48

Haffert S. Y., et al., 2019, Nature Astronomy, 3, 749

Hansen B. M. S., Murray N., 2013, ApJ, 775, 53

Harris R. J., et al., 2012, ApJ, 751, 115

Heese S., et al., 2017, A&A, 604, A5

Heinemann T., Papaloizou J. C. B., 2009a, MNRAS, 397, 52

Heinemann T., Papaloizou J. C. B., 2009b, MNRAS, 397, 64

Hennebelle P., Lesur G., Fromang S., 2016, A&A, 590, A22

Hennebelle P., Lesur G., Fromang S., 2017, A&A, 599, A86

Hernández J., et al., 2007a, ApJ, 662, 1067

Hernández J., et al., 2007b, ApJ, 671, 1784

Hsieh H.-F., Lin M.-K., 2020, MNRAS, 497, 2425

Huang J., et al., 2018a, ApJ, 869, L42

Huang J., et al., 2018b, ApJ, 869, L43

Ikoma M., Nakazawa K., Emori H., 2000, ApJ, 537, 1013

Isella A., et al., 2018, ApJ, 869, L49

Jiménez M. A., Masset F. S., 2017, MNRAS, 471, 4917

Johansen A., Klahr H., 2005, ApJ, 634, 1353

Johansen A., et al., 2014, in Beuther H., et al., eds, Protostars and Planets VI. p. 547 (arXiv:1402.1344), doi:10.2458/azu_uapress_9780816531240-ch024

Jurić M., Tremaine S., 2008, ApJ, 686, 603

Kataoka A., et al., 2014, A&A, 568, A42

Keppler M., et al., 2018, A&A, 617, A44

Keppler M., et al., 2019, A&A, 625, A118

Klahr H., Pfeil T., Schreiber A., 2018, Instabilities and Flow Structures in Protoplanetary Disks: Setting the Stage for Planetesimal Formation. p. 138, doi:10.1007/978-3-319-55333-7_138

Kley W., 1999, MNRAS, 303, 696

Kley W., Bitsch B., Klahr H., 2009, A&A, 506, 971

Knutson H. A., et al., 2014, ApJ, 785, 126

Koepferl C. M., et al., 2013, MNRAS, 428, 3327

Kokubo E., Ida S., 2000, in Lemarchand G., Meech K., eds, Astronomical Society of the Pacific Conference Series Vol. 213, Bioastronomy 99. p. 51

Kuiper G. P., 1938, ApJ, 88, 472

Laibe G., et al., 2008, A&A, 487, 265

Langevin Y., et al., 2016, Icarus, 271, 76

Les R., Lin M.-K., 2015, MNRAS, 450, 1503

Lesur G., 2020, arXiv e-prints, p. arXiv:2007.15967

Lesur G., Kunz M. W., Fromang S., 2014, A&A, 566, A56

Lesur G., Hennebelle P., Fromang S., 2015, A&A, 582, L9

Li H., et al., 2000, ApJ, 533, 1023

Li H., et al., 2001, ApJ, 551, 874

Lin M.-K., Papaloizou J. C. B., 2010, MNRAS, 405, 1473

Lin M.-K., Papaloizou J. C. B., 2011, MNRAS, 415, 1426

Lin C. C., Shu F. H., 1964, ApJ, 140, 646

Lissauer J. J., Stevenson D. J., 2007, in Reipurth B., Jewitt D., Keil K., eds, Protostars and Planets V. p. 591

Lodato G., 2007, Nuovo Cimento Rivista Serie, 30, 293

Lodato G., et al., 2019, MNRAS, 486, 453

Long F., et al., 2018, ApJ, 869, 17

Long F., et al., 2019, ApJ, 882, 49

Lovelace R. V. E., Hohlfeld R. G., 2013, MNRAS, 429, 529

Lovelace R. V. E., Romanova M. M., 2014, Fluid Dynamics Research, 46, 041401

Lovelace R. V. E., et al., 1999, ApJ, 513, 805

Lynden-Bell D., Pringle J. E., 1974, MNRAS, 168, 603

Lyra W., Lin M.-K., 2013, ApJ, 775, 17

Lyra W., Umurhan O. M., 2019, PASP, 131, 072001

Lyra W., et al., 2009, A&A, 497, 869

Lyra W., Turner N. J., McNally C. P., 2015a, A&A, 574, A10

Lyra W., Turner N. J., McNally C. P., 2015b, A&A, 574, A10

Malik M., et al., 2015, ApJ, 802, 56

Marino S., Perez S., Casassus S., 2015, ApJ, 798, L44

Masset F., 2000, A&AS, 141, 165

Masset F. S., 2002, A&A, 387, 605

Masset F. S., 2008, in Goupil M. J., Zahn J. P., eds, EAS Publications Series Vol. 29, EAS Publications Series. pp 165–244, doi:10.1051/eas:0829006

Masset F. S., Benítez-Llambay P., 2016, ApJ, 817, 19

Masset F. S., Papaloizou J. C. B., 2003, ApJ, 588, 494

Masset F. S., D'Angelo G., Kley W., 2006, ApJ, 652, 730

Mathis J. S., Rumpl W., Nordsieck K. H., 1977, ApJ, 217, 425

Matsuyama I., Johnstone D., Hollenbach D., 2009, ApJ, 700, 10

Mayor M., et al., 2011, arXiv e-prints, p. arXiv:1109.2497

McNally C. P., et al., 2019, MNRAS, 484, 728

McNally C. P., et al., 2020, MNRAS, 493, 4382

Meheut H., et al., 2012, A&A, 542, A9

Menou K., Goodman J., 2004, ApJ, 606, 520

Meru F., et al., 2017, ApJ, 839, L24

Meru F., et al., 2019, MNRAS, 482, 3678

Miyake K., Nakagawa Y., 1993, Icarus, 106, 20

Montesinos M., et al., 2020, arXiv e-prints, p. arXiv:2009.10768

Mordasini C., Alibert Y., Benz W., 2009a, A&A, 501, 1139

Mordasini C., et al., 2009b, A&A, 501, 1161

Müller T. W. A., Kley W., 2013, A&A, 560, A40

Müller T. W. A., Kley W., Meru F., 2012, A&A, 541, A123

Müller A., et al., 2018, A&A, 617, L2

Musiolik G., Wurm G., 2019, ApJ, 873, 58

Musiolik G., et al., 2016, ApJ, 827, 63

Nakagawa Y., Sekiya M., Hayashi C., 1986, Icarus, 67, 375

Nayakshin S., 2017, PASA, 34, e002

Nazari P., et al., 2019, MNRAS, 485, 5914

Nelson R. P., Gressel O., Umurhan O. M., 2013, MNRAS, 435, 2610

Ngo H., et al., 2015, ApJ, 800, 138

Öberg K. I., et al., 2011, ApJ, 734, 98

Ogihara M., Morbidelli A., Guillot T., 2015, A&A, 578, A36

Okuzumi S., et al., 2016, ApJ, 821, 82

Owen J. E., 2016, PASA, 33, e005

Paardekooper S. J., 2014, MNRAS, 444, 2031

Paardekooper S. J., et al., 2010, MNRAS, 401, 1950

Paardekooper S. J., Baruteau C., Kley W., 2011a, MNRAS, 410, 293

Paardekooper S.-J., Baruteau C., Meru F., 2011b, MNRAS, 416, L65

Papaloizou J. C. B., 2011, Celestial Mechanics and Dynamical Astronomy, 111, 83

Pepliński A., Artymowicz P., Mellema G., 2008a, MNRAS, 386, 179

Pepliński A., Artymowicz P., Mellema G., 2008b, MNRAS, 387, 1063

Pérez S., Casassus S., Benítez-Llambay P., 2018, MNRAS,

Pérez S., et al., 2019, AJ, 158, 15

Pérez S., et al., 2020, ApJ, 889, L24

Pierens A., 2015, MNRAS, 454, 2003

Pierens A., Huré J.-M., 2005, A&A, 433, L37

Pierens A., Lin M.-K., 2018, MNRAS, 479, 4878

Pierens A., Raymond S. N., 2016, MNRAS, 462, 4130

Pinilla P., Benisty M., Birnstiel T., 2012, A&A, 545, A81

Pinilla P., et al., 2018, ApJ, 868, 85

Pinte C., et al., 2016, ApJ, 816, 25

Pinte C., et al., 2019, Nature Astronomy, 3, 1109

Pinte C., et al., 2020, ApJ, 890, L9

Poppe T., 2003, Icarus, 164, 139

Quanz S. P., et al., 2015, ApJ, 807, 64

Rafikov R. R., 2002, ApJ, 572, 566

Ribas Á., Bouy H., Merín B., 2015, A&A, 576, A52

Riols A., Lesur G., 2019, A&A, 625, A108

Riols A., Lesur G., Menard F., 2020, A&A, 639, A95

Robert C. M. T., Méheut H., Ménard F., 2020, A&A, 641, A128

Rodenkirch P. J., et al., 2020, A&A, 633, A21

Rometsch T., et al., 2020, arXiv e-prints, p. arXiv:2009.03090

Scally A., Clarke C., 2001, MNRAS, 325, 449

Seizinger A., Krijt S., Kley W., 2013, A&A, 560, A45

Shakura N. I., Sunyaev R. A., 1973, A&A, 24, 337

Shallue C. J., Vanderburg A., 2018, AJ, 155, 94

Simon J. B., et al., 2013, ApJ, 775, 73

Simon J. B., et al., 2015, MNRAS, 454, 1117

Simon M., et al., 2017, ApJ, 844, 158

Stepinski T. F., Valageas P., 1997, A&A, 319, 1007

Stolker T., et al., 2016, A&A, 595, A113

Stoll M. H. R., Kley W., 2014, A&A, 572, A77

Suzuki T. K., et al., 2016, A&A, 596, A74

Tanaka H., Takeuchi T., Ward W. R., 2002, ApJ, 565, 1257

Tazzari M., et al., 2017, A&A, 606, A88

Teague R., et al., 2018a, ApJ, 860, L12

Teague R., et al., 2018b, ApJ, 868, 113

Testi L., et al., 2014, in Beuther H., et al., eds, Protostars and Planets VI. p. 339 (arXiv:1402.1354), doi:10.2458/azu_uapress_9780816531240-ch015

Urpin V., 2003, A&A, 404, 397

Urpin V., Brandenburg A., 1998, MNRAS, 294, 399

Varnière P., Tagger M., 2006, A&A, 446, L13

Villenave M., et al., 2020, arXiv e-prints, p. arXiv:2008.06518

Wafflard-Fernandez G., Baruteau C., 2020, MNRAS, 493, 5892

Wang J., Zhong Z., 2018, A&A, 619, L1

Weaver E., Isella A., Boehler Y., 2018, ApJ, 853, 113

Weber P., et al., 2019, arXiv e-prints, p. arXiv:1909.01661

Weidenschilling S. J., 1977, Ap&SS, 51, 153

Williams J. P., Cieza L. A., 2011, ARA&A, 49, 67

Woitke P., Kamp I., Thi W. F., 2009, A&A, 501, 383

Wright J. T., et al., 2012, ApJ, 753, 160

Youdin A. N., Goodman J., 2005, ApJ, 620, 459

Youdin A. N., Lithwick Y., 2007, Icarus, 192, 588

Yu L., et al., 2017, MNRAS, 467, 1342

Zhang K., Blake G. A., Bergin E. A., 2015, ApJ, 806, L7

Zhang K., et al., 2017, Nature Astronomy, 1, 0130

Zhang S., et al., 2018, ApJ, 869, L47

Zhu Z., Baruteau C., 2016, MNRAS, 458, 3918

Zhu Z., et al., 2011, ApJ, 729, 47

Ziampras A., Kley W., Dullemond C. P., 2020, A&A, 637, A50

de Val-Borro M., et al., 2007, A&A, 471, 1043

de Valon A., et al., 2020, A&A, 634, L12

van der Marel N., et al., 2013, Science, 340, 1199

van der Marel N., et al., 2018, ApJ, 854, 177